North Carolina Agricultural and Technical State University
Aggie Digital Collections and Scholarship

Theses | Electronic Theses and Dissertations

2015

Synthesis, X-Ray Crystallography, Characterization And Luminescence Studies Of Selected Tertiary Phosphine Gold (I) Complexes

George Agbeworvi
North Carolina Agricultural and Technical State University

Follow this and additional works at: https://digital.library.ncat.edu/theses

Recommended Citation

Agbeworvi, George, "Synthesis, X-Ray Crystallography, Characterization And Luminescence Studies Of Selected Tertiary Phosphine Gold (I) Complexes" (2015). *Theses*. 336.
https://digital.library.ncat.edu/theses/336

This Thesis is brought to you for free and open access by the Electronic Theses and Dissertations at Aggie Digital Collections and Scholarship. It has been accepted for inclusion in Theses by an authorized administrator of Aggie Digital Collections and Scholarship. For more information, please contact iyanna@ncat.edu.

SYNTHESIS, X-RAY CRYSTALLOGRAPHY, CHARACTERIZATION AND LUMINESCENCE STUDIES OF SELECTED TERTIARY PHOSPHINE GOLD (I) COMPLEXES

George Agbeworvi

North Carolina A&T State University

A thesis submitted to the graduate faculty

in partial fulfillment of the requirements for the degree of

MASTER OF SCIENCE

Department: Chemistry

Major: Chemistry

Major Professor: Dr. Zerihun Assefa

Greensboro, North Carolina

2015

The Graduate School
North Carolina Agricultural and Technical State University

This is to certify that the Master's Thesis of

George Agbeworvi

has met the thesis requirements of
North Carolina Agricultural and Technical State University

Greensboro, North Carolina
2015

Approved by:

Dr. Zerihun Assefa Major Professor	Dr. Mufeed Basti Committee Member
Dr. Margaret Kanipes-Spinks Department Chair	Dr. Jahangir Emrani Committee Member

Dr. Sanjiv Sarin
Dean, The Graduate School

© Copyright by

George Agbeworvi

2015

Biographical Sketch

George Agbeworvi was born on April 4, 1987, in Accra, Ghana. He graduated from Keta Senior High School in 2004. He received the Bachelor of Science degree in Chemistry from Kwame Nkrumah University of Science and Technology, Ghana in 2009. In the fall 2013 he was accepted to North Carolina Agricultural and Technical State University to obtain his Masters of Science degree in Chemistry.

Dedication

This thesis is dedicated to God Almighty, my dear mother, Ms Ellen Mensah, my brother Norbert Agbeworvi, my relatives Ms Dzigbordi Tsifoaka, Ms Virginia Dawu and Mr. Emmanuel Amekuedzi.

Acknowledgments

Thus far the good Lord has brought me. I am indeed much grateful unto the most high God for his kind blessings, goodness, guidance and protection throughout my two years at the North Carolina A&T State University so far as my graduate studies is concern. My profound gratitude goes to my mother and my brother for their support, encouragement and prayers during my trying moments in pursuance of my graduate studies. Sincere gratitude goes to my advisor Dr. Assefa for his guidance, tolerance, constructive criticisms, support and patience he had for reading through all the scripts and in ensuring also that I carry this research work to its logical conclusion. May the good Lord bless you and reward your efforts. To my committee Dr. Basti and Dr. Emrani, thank you. A special appreciation goes to Carlos Crawford who has been with me from the first day of my research till the end. Thank you. I have to acknowledge my group members who have been there to keep me on track and have helped me from the beginning to the end. Finally, I thank those who have shown me a lot of love throughout my stay here at A&T, especially Dr. Kanipes, Mr. King, Dr. Richard Abrokwah, William Dade, Derick Jones, Taylor Davis, Emmanuel Ampiah, and Hope Kumakli.

Table of Contents

List of Figures xv

List of Tables xxxi

Abstract 1

CHAPTER ONE Introduction 2

1.1 Luminescence 2

1.2 Photoluminescence 3

1.3 Gold Chemistry 9

1.3.1 History 9

1.3.2 Chemical and Physical Properties 10

1.3.3 Theoretical Considerations 11

1.3.4 Chemistry 13

1.3.5 Photochemistry of d^{10} Gold (I) Complexes 14

1.4 Ligands 16

1.4.1 Phosphine Ligands 16

CHAPTER TWO Experimental Methods 20

2.1 Physical measurements and instrumentations 20

2.1.1 NMR Spectroscopic Measurements 20

2.1.2 FT-IR Spectroscopic Measurements 20

2.1.3 Raman Spectroscopic Measurements 20

2.1.4 Ultraviolet and Visible (UV-Vis) Spectroscopic Measurements 20

2.1.5 Photoluminescence Spectroscopic Measurements 21

2.1.6 X-ray Crystallography Studies 21

2.1.7 Group Theoretical analysis (Nuclear Site Group Analysis) 21

2.1.8 Computational Studies 22

2.2 Chemical Reagents 22

2.3 Reagent Preparation 23

2.4 Syntheses 24

CHAPTER THREE Synthesis and Characterization of mono-, bis-, tris-, and tetrakis-{tris(3, 5-dimethylphenyl)phosphine} gold(I) complexes 25

3.1 Syntheses 25

3.1.1 Tris(3,5-dimethylphenyl)phosphine gold (I) chloride (**2**). 25

3.1.2 Bis{Tris(3,5-dimethylphenyl)phosphine} gold (I) chloride (**3**) 25

3.1.3 Tris{Tris(3,5-dimethylphenyl)phosphine} gold (I) chloride (**4**). 25

3.1.4 Tetrakis-{Tris(3,5-dimethylphenyl)phosphine} gold (I) chloride (**5**) 26

3.2 Results 26

3.2.1 X-ray Crystallography 26

3.2.2 Infrared Spectroscopy 31

3.2.3 Nuclear Magnetic Resonance 34

3.2.4 UV-Vis Spectroscopy 37

3.2.5 Luminescence 43

3.2.6 Raman Spectroscopy 56

3.3 Discussion 58

3.3.1 X-ray Crystallography 58

3.3.2 Infrared Spectroscopy (Vibrational Studies) 58

3.3.3 Nuclear Magnetic Resonance 59
3.3.4 UV-Vis Spectroscopy 60
3.3.5 Luminescence 61
3.3.6 Raman Spectroscopy 63
3.3.7 Computational Studies 63
3.3.7.1 Structural Comparison 63
3.3.7.2 Spectroscopic Comparison. 64
3.3.7.3 Electronic Comparison 64
3.3.7.3.1 Luminescence 64
3.3.7.3.2 UV-Vis 65
CHAPTER FOUR Synthesis and Characterization of mono-, bis-, tris-, and tetrakis-{tris(2, 6-dimethoxyphenyl)phosphine} gold(I) complexes 66
4.1 Syntheses 66
4.1.1 Tris(2,6-dimethoxyphenyl)phosphine gold (I) chloride (**6**). 66
4.1.2 Bis{Tris(2,6-dimethoxyphenyl)phosphine} gold (I) chloride (**7**) 66
4.1.3 Tris{tris(2,6-dimethoxyphenyl)phosphine} gold (I) chloride (**8**) 66
4.1.4 Tetrakis{Tris(2,6-dimethoxyphenyl)phosphine} gold (I) chloride (**9**) 67
4.2 Results 67
4.2.1 X-ray Crystallography 67
4.2.2 Infrared Spectroscopy 70
4.2.3 Nuclear Magnetic Resonance 74
4.2.4 UV-Vis Spectroscopy 77
4.2.5 Luminescence 82
4.2.6 Raman Spectroscopy 90

4.3 Discussion 93
4.3.1 X-ray Crystallography 93
4.3.2 Infrared Spectroscopy (Vibrational Studies) 93
4.3.3 Nuclear Magnetic Resonance 94
4.3.4 UV-Vis Spectroscopy 95
4.3.5 Luminescence 96
4.3.6 Raman Spectroscopy 97
4.3.7 Computational Studies 98
4.3.7.1 Structural Comparison 98
4.3.7.2 Spectroscopic Comparison. 98
4.3.7.3 Electronic Comparison 98
4.3.7.3.1 Luminescence 98
4.3.7.3.2 UV-Vis 99
CHAPTER FIVE Synthesis and Characterization of mono-, bis-, tris-, and tetrakis-{tris(4-methoxyphenyl)phosphine} gold(I) complexes 101
5.1. Syntheses 101
5.1.1 Tris(4-methoxyphenyl)phosphine gold (I) chloride (**10**) 101
5.1.2 Bis{tris(4-methoxyphenyl)phosphine} gold (I) chloride (**11**) 101
5.1.3 Tris{Tris(4-methoxyphenyl)phosphine} gold (I) chloride (**12**) 101
5.1.4 Tetrakis{tris(4-methoxyphenyl)phosphine} gold (I) chloride (**13**) 102
5.2 Results 102
5.2.1 X-ray Crystallography 102
5.2.2 Infrared Spectroscopy 102
5.2.3 Nuclear Magnetic Resonance 105

5.2.4 UV-Vis Spectroscopy 108

5.2.5 Luminescence 112

5.3 Discussion 121

5.3.1 Infrared Spectroscopy (Vibrational Studies) 121

5.3.2 Nuclear Magnetic Resonance 122

5.3.3 UV-Vis Spectroscopy 123

5.3.4 Luminescence 124

5.3.5 Computational Studies 125

5.3.5.1 Spectroscopic Comparison 125

5.3.5.2 Electronic Comparison 126

5.3.5.2.1 Luminescence 126

5.3.5.2.2 UV-Vis 126

CHAPTER SIX Synthesis and Characterization of mono-, bis-, tris-, and tetrakis-{tert-butyldiphenyl)phosphine} gold(I) complexes 128

6.1 Syntheses 128

6.1.1 Tert-butyldiphenylphosphine gold (I) chloride (**14**) 128

6.1.2 Bis{Tert-butyldiphenylphosphine} gold (I) chloride (**15**) 128

6.1.3 Tris-{Tert-butyldiphenylphosphine} gold (I) chloride (**16**) 128

6.1.4 Tetrakis{tert-butyldiphenylphosphine} gold (I) chloride (**17**) 129

6.2 Results 129

6.2.1 X-ray Crystallography 129

6.2.2 Infrared Spectroscopy 132

6.2.3 Nuclear Magnetic Resonance 136

6.2.4 UV-Vis Spectroscopy 139

6.2.5 Luminescence 145
6.3 Discussion 154
6.3.1 X-ray Crystallography 154
6.3.2 Infrared Spectroscopy (Vibrational Studies) 154
6.3.3 Nuclear Magnetic Resonance 155
6.3.4 UV-Vis Spectroscopy 156
6.3.5 Luminescence 157
6.3.6 Computational Studies 158
6.3.6.1 Structural Comparison 158
6.3.6.2 Spectroscopic Comparison 159
6.3.6.3 Electronic Comparison 159
6.3.6.3.1 Luminescence 159
6.3.6.3.2 UV-Vis 160
CHAPTER SEVEN Synthesis and Characterization of mono-, bis-, tris-, and tetrakis-{tris(4-fluorophenyl)phosphine} gold(I) complexes 161
7.1 Syntheses 161
7.1.1 Tris(4-fluorophenyl)phosphine gold (I) chloride (**18**) 161
7.1.2 Bis{tris(4-fluorophenyl)phosphine} gold (I) chloride (**19**) 161
7.1.3 Tris(4-fluorophenyl)phosphine gold (I) chloride (**20**) 161
7.1.4 Bis{tris(4-fluorophenyl)phosphine} gold (I) chloride (**21**) 162
7.2 Results 162
7.2.1 X-ray Crystallography 162
7.2.2 Infrared Spectroscopy 162
7.2.3 Nuclear Magnetic Resonance 165

7.2.4 UV-Vis Spectroscopy 168
7.2.5 Luminescence 173
7.3.2 Infrared Spectroscopy (Vibrational Studies) 185
7.3.3 Nuclear Magnetic Resonance 186
7.3.4 UV-Vis Spectroscopy 187
7.3.5 Luminescence 188
7.3.6 Computational Studies 189
7.3.6.1 Spectroscopic Comparison. 189
7.3.6.2 Electronic Comparison 190
7.3.6.2.1 Luminescence. 190
7.3.6.2.2 UV-Vis. 190
CHAPTER EIGHT Synthesis and Characterization of mono-, bis-, tris-, and tetrakis-{tris(pentafluorophenyl)phosphine} gold(I) complexes 192
8.1 Syntheses 192
8.1.1 Tris(pentafluorophenyl)phosphine gold (I) chloride (**22**) 192
8.1.2 Bis{tris(pentafluorophenyl)phosphine} gold (I) chloride (**23**) 192
8.1.3 Tris{tris(pentafluorophenyl)phosphine} gold (I) chloride (**24**) 192
8.1.4 Tetrakis{tris(pentafluorophenyl)phosphine} gold (I) chloride (**25**). 193
8.2 Results 193
8.2.1 X-ray Crystallography 193
8.2.2 Infrared Spectroscopy 193
8.2.3 Nuclear Magnetic Resonance 196
8.2.4 UV-Vis Spectroscopy 197
8.2.5 Luminescence 202

8.3 Discussion 210
8.3.1 Infrared Spectroscopy (Vibrational Studies). 210
8.3.2 Nuclear Magnetic Resonance 211
8.3.3 UV-Vis Spectroscopy 212
8.3.4 Luminescence 213
8.3.5 Computational Studies 214
8.3.5.1 Spectroscopic Comparison 214
8.3.5.2 Electronic Comparison 214
8.3.5.2.1 Luminescence 214
8.3.5.2.2 UV-Vis 215
CHAPTER NINE Comparison Between the Various Ligands and Their Complexes 216
9.1 Phosphorus NMR 216
9.2 UV-Vis Spectroscopy 216
CHAPTER TEN Conclusion 218
Conclusion 218
References 219

List of Figures

Figure 1.1. Electron configurations for (a) a singlet ground state; (b) a singlet excited state; and (c) a triplet excited state. 5

Figure 1.2. Energy level diagram for a molecule showing pathways for the deactivation of an excited state: *vr* is vibrational relaxation; *ic* is internal conversion; *ec* is external conversion; and *isc* is an intersystem crossing. 7

Figure 3.1. Thermal ellipsoid diagram of the $AuP(C_8H_9)_3Cl$ complex. 26

Figure 3.2. IR spectrum for $P(C_8H_9)_3$ calculated theoretically using Gaussian 09 31

Figure 3.3. IR spectrum for $P(C_8H_9)_3$ 31

Figure 3.4. IR spectrum for $AuP(C_8H_9)_3Cl$ 32

Figure 3.5. IR spectrum for $AuP(C_8H_9)_3Cl$ calculated theoretically using Gaussian 09 32

Figure 3.6. IR spectrum for $Au(P(C_8H_9)_3)_2Cl$ 33

Figure 3.7. ^1H NMR spectrum of $P(C_8H_9)_3$ 34

Figure 3.8. ^1H NMR spectrum of $AuP(C_8H_9)_3Cl$ 34

Figure 3.9. ^1H NMR spectrum of $Au(P(C_8H_9)_3)_2Cl$ 35

Figure 3.10. $^{31}P\{^1H\}$ NMR spectrum of $P(C_8H_9)_3$ 35

Figure 3.11. $^{31}P\{^1H\}$ NMR spectrum of $AuP(C_8H_9)_3Cl$ 35

Figure 3.12. $^{31}P\{^1H\}$ NMR spectrum of $Au(P(C_8H_9)_3)_2Cl$ 36

Figure 3.13. ^1H NMR spectrum of $P(C_8H_9)_3$ obtained from theoretical calculation using Gaussian 09 program 36

Figure 3.14. ^1H NMR spectrum of $AuP(C_8H_9)_3Cl$ obtained from theoretical calculation using Gaussian 09 program 37

Figure 3.15. UV-Vis spectrum of $P(C_8H_9)_3$ 38

Figure 3.16. UV-Vis spectrum of $AuP(C_8H_9)_3Cl$ 38

Figure 3.17. UV-Vis spectrum of $Au(P(C_8H_9)_3)_2Cl$ 39

Figure 3.18. Calculated UV-Vis spectrum of $AuP(C_8H_9)_3Cl$ using Gaussian 09 program 39

Figure 3.19. Calculated UV-Vis spectrum of $P(C_8H_9)_3$ using Gaussian 09 program 40

Figure 3.20. Excitation spectrum of TDMPP ligand collected at room temperature by monitoring the emission at 450 nm 44

Figure 3.21. Excitation spectrum of TDMPP ligand collected at room temperature by monitoring the emission at 540 nm 44

Figure 3.22. Excitation spectrum of TDMPP ligand collected at room temperature by monitoring the emission at 412 nm 45

Figure 3.23. Excitation spectrum of $AuP(C_8H_9)_3Cl$ collected at room temperature by monitoring the emission at 554 nm 45

Figure 3.24. Excitation spectrum of $AuP(C_8H_9)_3Cl$ collected at room temperature by monitoring the emission at 473 nm 46

Figure 3.25. Excitation spectrum of $AuP(C_8H_9)_3Cl$ collected at room temperature by monitoring the emission at 527 nm 46

Figure 3.26. Excitation spectrum of $AuP(C_8H_9)_3Cl$ collected at room temperature by monitoring the emission at 542 nm 47

Figure 3.27. Excitation spectrum of $AuP(C_8H_9)_3Cl$ collected in liquid nitrogen by monitoring the emission at 450 nm 47

Figure 3.28. Excitation spectrum of $AuP(C_8H_9)_3Cl$ collected in liquid nitrogen by monitoring the emission at 437 nm 48

Figure 3.29. Excitation spectrum of $AuP(C_8H_9)_3Cl$ collected in liquid nitrogen by monitoring the emission at 471 nm 48

Figure 3.30. Excitation spectrum of $AuP(C_8H_9)_3Cl$ collected in liquid nitrogen by monitoring the emission at 512 nm 49

Figure 3.31. Emission spectrum of TDMPP ligand collected at room temperature upon excitation at 287 nm..... 49

Figure 3.32. Emission spectrum of TDMPP ligand collected at room temperature upon excitation at 287 nm..... 50

Figure 3.33. Emission spectrum of TDMPP ligand collected at room temperature upon excitation at 362 nm..... 50

Figure 3.34. Emission spectrum of TDMPP ligand collected at room temperature upon excitation at 388 nm..... 51

Figure 3.35. Emission spectrum of $AuP(C_8H_9)_3Cl$ collected at room temperature upon excitation at 296 nm..... 51

Figure 3.36. Emission spectrum of $AuP(C_8H_9)_3Cl$ collected at room temperature upon excitation at t 389 nm 52

Figure 3.37. Emission spectrum of $AuP(C_8H_9)_3Cl$ collected at room temperature upon excitation at 460 nm..... 52

Figure 3.38. Emission spectrum of $AuP(C_8H_9)_3Cl$ collected at room temperature upon excitation at 366 nm..... 53

Figure 3.39. Emission spectrum of $AuP(C_8H_9)_3Cl$ collected in liquid nitrogen upon excitation at 325 nm 53

Figure 3.40. Emission spectrum of $AuP(C_8H_9)_3Cl$ collected in liquid nitrogen upon excitation at 376 nm 54

Figure 3.41. Emission spectrum of $AuP(C_8H_9)_3Cl$ collected in liquid nitrogen upon excitation at 340 nm 54

Figure 3.42. Raman spectrum for $P(C_8H_9)_3$ obtained from theoretical calculation using Gaussian 09 program 56

Figure 3.43. Raman spectrum for $P(C_8H_9)_3$ 57

Figure 3.44. Raman spectrum for $AuP(C_8H_9)_3Cl$ obtained from theoretical calculation using Gaussian 09 program 57

Figure 3.45. Raman spectrum for $AuP(C_8H_9)_3Cl$ 58

Figure 4.1. Thermal ellipsoid diagram of the $AuP(C_8H_9O_2)_3Cl$ complex. 67

Figure 4.2. IR spectrum for $P(C_8H_9O_2)_3$ calculated theoretically using Gaussian 09 software .. 71

Figure 4.3. IR spectrum for $P(C_8H_9O_2)_3$ 71

Figure 4.4. IR spectrum for $AuP(C_8H_9O_2)_3Cl$ 72

Figure 4.5. IR spectrum for $AuP(C_8H_9O_2)_3Cl$ calculated theoretically using Gaussian 09 software 72

Figure 4.6. IR spectrum for $Au(P(C_8H_9O_2)_3)_2Cl$ 73

Figure 4.7. ^1H NMR spectrum of $P(C_8H_9O_2)_3$ 74

Figure 4.8. ^1H NMR spectrum of $AuP(C_8H_9O_2)_3Cl$ 74

Figure 4.9. ^1H NMR spectrum of $Au(P(C_8H_9O_2)_3)_2Cl$ 75

Figure 4.10. $^{31}P\{^1H\}$ NMR spectrum of $P(C_8H_9O_2)_3$ 75

Figure 4.11. $^{31}P\{^1H\}$ NMR spectrum of $AuP(C_8H_9O_2)_3Cl$ 75

Figure 4.12. $^{31}P\{^1H\}$ NMR spectrum of $AuP((C_8H_9O_2)_3)_2Cl$ 76

Figure 4.13. ^{1}H NMR spectrum of $P(C_8H_9O_2)_3$ calculated theoretically using Gaussian 09 software 76

Figure 4.14. ^{1}H NMR spectrum of $AuP(C_8H_9O_2)_3Cl$ calculated theoretically using Gaussian 09 software 77

Figure 4.15. UV-Vis spectrum of $P(C_8H_9O_2)_3$ 78

Figure 4.16. UV-Vis spectrum of $AuP(C_8H_9O_2)_3Cl$ 78

Figure 4.17. UV-Vis spectrum of $AuP((C_8H_9O_2)_3)_2Cl$ 79

Figure 4.18. UV-Vis spectrum of $AuP(C_8H_9O_2)_3Cl$ calculated theoretically using Gaussian 09 software 79

Figure 4.19. UV-Vis spectrum of $P(C_8H_9O_2)_3$ calculated theoretically using Gaussian 09 software 80

Figure 4.20. Excitation spectrum of TDMOPP ligand collected at room temperature by monitoring the emission at 481 nm 82

Figure 4.21. Excitation spectrum of TDMOPP ligand collected at room temperature by monitoring the emission at 450 nm 83

Figure 4.22. Excitation spectrum of $AuP(C_8H_9O_2)_3Cl$ collected at room temperature by monitoring the emission at 550 nm 83

Figure 4.23. Excitation spectrum of $AuP(C_8H_9O_2)_3Cl$ collected at room temperature by monitoring the emission at 473 nm 84

Figure 4.24. Excitation spectrum of $AuP(C_8H_9O_2)_3Cl$ collected at room temperature by monitoring the emission at 527 nm 84

Figure 4.25. Excitation spectrum of $AuP(C_8H_9O_2)_3Cl$ collected in liquid nitrogen by monitoring the emission at 450 nm 85

Figure 4.26. Emission spectrum of TDMPP ligand collected at room temperature upon excitation with the 346 nm wavelength 85

Figure 4.27. Emission spectrum of TDMPP ligand collected at room temperature upon excitation with the 291 nm wavelength 86

Figure 4.28. Emission spectrum of $AuP(C_8H_9O_2)_3Cl$ collected at room temperature upon excitation with the 358 nm wavelength 86

Figure 4.29. Emission spectrum of $AuP(C_8H_9O_2)_3Cl$ collected at room temperature upon excitation with the 362 nm wavelength 87

Figure 4.30. Emission spectrum of $AuP(C_8H_9O_2)_3Cl$ collected at room temperature upon excitation with the 384 nm wavelength 87

Figure 4.31. Emission spectrum of $AuP(C_8H_9O_2)_3Cl$ collected at room temperature upon excitation with the 414 nm wavelength 88

Figure 4.32. Emission spectrum of $AuP(C_8H_9O_2)_3Cl$ collected in liquid nitrogen upon excitation with the 380 nm wavelength 88

Figure 4.33. Emission spectrum of $AuP(C_8H_9O_2)_3Cl$ collected in liquid nitrogen upon excitation with the 341 nm wavelength 89

Figure 4.34. Raman spectrum for $P(C_8H_9O_2)_3$ obtained from the theoretical calculation using the Gaussian 09 software program 91

Figure 4.35. Raman spectrum for $P(C_8H_9O_2)_3$ 91

Figure 4.36. Raman spectrum for $AuP(C_8H_9O_2)_3Cl$ obtained from the theoretical calculation using the Gaussian 09 software program 92

Figure 4.37. Raman spectrum for $AuP(C_8H_9O_2)_3Cl$ 92

Figure 5.1. Theoretically calculated IR spectrum for $P(C_7H_7O)_3$ measured using Gaussian 09 software. 103

Figure 5.2. IR spectrum for $P(C_7H_7O)_3$ 103

Figure 5.3. IR spectrum for $AuP(C_7H_7O)_3Cl$ 104

Figure 5.4. Theoretically calculated IR spectrum for $AuP(C_7H_7O)_3Cl$ using Gaussian 09 program. 104

Figure 5.5. ^1H NMR spectrum of $P(C_7H_7O)_3$ 106

Figure 5.6. ^1H NMR spectrum of $AuP(C_7H_7O)_3Cl$ 106

Figure 5.7. $^{31}P\{^1H\}$ NMR spectrum of $P(C_7H_7O)_3$ 106

Figure 5.8. $^{31}P\{^1H\}$ NMR spectrum of $AuP(C_7H_7O)_3Cl$ 106

Figure 5.9. ^1H NMR spectrum of $P(C_7H_7O)_3$ calculated theoretically using Gaussian 09 software 107

Figure 5.10. ^1H NMR spectrum of $AuP(C_7H_7O)_3Cl$ calculated theoretically using Gaussian 09 software 107

Figure 5.11. UV-Vis spectrum of $P(C_7H_7O)_3$ 108

Figure 5.12. UV-Vis spectrum of $AuP(C_7H_7O)_3Cl$ 109

Figure 5.13. UV-Vis spectrum of $P(C_7H_7O)_3$ calculated theoretically using Gaussian 09 program 109

Figure 5.14. UV-Vis spectrum of $AuP(C_7H_7O)_3Cl$ calculated theoretically using Gaussian 09 110

Figure 5.15. Excitation spectrum of $P(C_7H_7O)_3$ collected at room temperature by monitoring the emission at 480 nm 112

Figure 5.16. Excitation spectrum of $AuP(C_7H_7O)_3Cl$ collected at room temperature by monitoring the emission at 492 nm 113

Figure 5.17. Excitation spectrum of $AuP(C_7H_7O)_3Cl$ collected at room temperature by monitoring the emission at 480 nm..... 113

Figure 5.18. Excitation spectrum of $AuP(C_7H_7O)_3Cl$ collected at room temperature by monitoring the emission at 467 nm..... 114

Figure 5.19. Excitation spectrum of $AuP(C_7H_7O)_3Cl$ collected at room temperature by monitoring the emission at 450 nm..... 114

Figure 5.20. Excitation spectrum of $AuP(C_7H_7O)_3Cl$ collected in liquid nitrogen by monitoring the emission at 421 nm 115

Figure 5.21. Excitation spectrum of $AuP(C_7H_7O)_3Cl$ collected in liquid nitrogen by monitoring the emission at 485 nm 115

Figure 5.22. Excitation spectrum of $AuP(C_7H_7O)_3Cl$ collected in liquid nitrogen by monitoring the emission at 450 nm 116

Figure 5.23. Emission spectrum of $P(C_7H_7O)_3$ collected at room temperature upon excitation at 385 nm 116

Figure 5.24. Emission spectrum of $AuP(C_7H_7O)_3Cl$ collected at room temperature upon excitation at 360 nm..... 117

Figure 5.25. Emission spectrum of $AuP(C_7H_7O)_3Cl$ collected at room temperature upon excitation at 356 nm..... 117

Figure 5.26. Emission spectrum of $AuP(C_7H_7O)_3Cl$ collected at room temperature upon excitation at 389 nm..... 118

Figure 5.27. Emission spectrum of $AuP(C_7H_7O)_3Cl$ collected in liquid nitrogen upon excitation at 305 nm..... 118

Figure 5.28. Emission spectrum of $AuP(C_7H_7O)_3Cl$ collected in liquid nitrogen upon excitation at 338 nm..... 119

Figure 5.29. Emission spectrum of $AuP(C_7H_7O)_3Cl$ collected in liquid nitrogen upon excitation at 348 nm..... 119

Figure 5.30. Emission spectrum of $AuP(C_7H_7O)_3Cl$ collected in liquid nitrogen upon excitation at 361 nm..... 120

Figure 6.1. Thermal ellipsoid diagram of $AuP(C_6H_5)_2(C_4H_9)Cl$ complex..... 129

Figure 6.2. Theoretically calculated IR spectrum for $P(C_6H_5)_2(C_4H_9)$ using Gaussian 09 software..... 133

Figure 6.3. IR spectrum for $P(C_6H_5)_2(C_4H_9)$..... 133

Figure 6.4. Theoretically calculated IR spectrum for $AuP(C_6H_5)_2(C_4H_9)Cl$ using Gaussian 09 software..... 134

Figure 6.5. IR spectrum for $AuP(C_6H_5)_2(C_4H_9)Cl$..... 134

Figure 6.6. IR spectrum for $Au(P(C_6H_5)_2(C_4H_9))_2Cl$..... 135

Figure 6.7. ^1H NMR spectrum of $P(C_6H_5)_2(C_4H_9)$..... 136

Figure 6.8. ^1H NMR spectrum of $AuP(C_6H_5)_2(C_4H_9)Cl$..... 136

Figure 6.9. ^1H NMR spectrum of $Au(P(C_6H_5)_2(C_4H_9))_2Cl$..... 137

Figure 6.10. $^{31}P\{^1H\}$ NMR spectrum of $P(C_6H_5)_2(C_4H_9)$..... 137

Figure 6.11. $^{31}P\{^1H\}$ NMR spectrum of $AuP(C_6H_5)_2(C_4H_9)Cl$..... 137

Figure 6.12. $^{31}P\{^1H\}$ NMR spectrum of $AuP(C_6H_5)_2(C_4H_9)Cl$..... 138

Figure 6.13. Theoretically calculated ^1H NMR spectrum of $P(C_6H_5)_2(C_4H_9)$ using Gaussian 09 software..... 138

Figure 6.14. Theoretically calculated ^{1}H NMR spectrum of $AuP(C_6H_5)_2(C_4H_9)Cl$ using Gaussian 09 software 139

Figure 6.15. UV-Vis spectrum of $P(C_6H_5)_2(C_4H_9)$ 140

Figure 6.16. UV-Vis spectrum of $AuP(C_6H_5)_2(C_4H_9)Cl$ 140

Figure 6.17. UV-Vis spectrum of $Au(P(C_6H_5)_2(C_4H_9))_2Cl$ 141

Figure 6.18. Theoretically calculated UV-Vis spectrum of $AuP(C_6H_5)_2(C_4H_9)Cl$ using Gaussian 09 software 141

Figure 6.19. Theoretically calculated UV-Vis spectrum of $AuP(C_6H_5)_2(C_4H_9)Cl$ using Gaussian 09 software 142

Figure 6.20. Excitation spectrum of $P(C_6H_5)_2(C_4H_9)$ collected at room temperature by monitoring the emission at 418 nm 145

Figure 6.21. Excitation spectrum of $AuP(C_6H_5)_2(C_4H_9)Cl$ collected at room temperature by monitoring the emission at 450 nm 146

Figure 6.22. Excitation spectrum of $AuP(C_6H_5)_2(C_4H_9)Cl$ collected at room temperature by monitoring the emission at 424 nm 146

Figure 6.23. Excitation spectrum of $AuP(C_6H_5)_2(C_4H_9)Cl$ collected at room temperature by monitoring the emission at 490 nm 147

Figure 6.24. Excitation spectrum of $AuP(C_6H_5)_2(C_4H_9)Cl$ collected at room temperature by monitoring the emission at 467 nm 147

Figure 6.25. Excitation spectrum of $AuP(C_6H_5)_2(C_4H_9)Cl$ collected in liquid nitrogen by monitoring the emission at 450 nm 148

Figure 6.26. Excitation spectrum of $AuP(C_6H_5)_2(C_4H_9)Cl$ collected in liquid nitrogen by monitoring the emission at 411 nm 148

Figure 6.27. Emission spectrum of $P(C_6H_5)_2(C_4H_9)$ collected at room temperature upon excitation at 364 nm 149

Figure 6.28. Emission spectrum of $AuP(C_6H_5)_2(C_4H_9)Cl$ collected at room temperature upon excitation at 347 nm 149

Figure 6.29. Emission spectrum of $AuP(C_6H_5)_2(C_4H_9)Cl$ collected at room temperature upon excitation at 350 nm 150

Figure 6.30. Emission spectrum of $AuP(C_6H_5)_2(C_4H_9)Cl$ collected at room temperature upon excitation at 303 nm 150

Figure 6.31. Emission spectrum of $AuP(C_6H_5)_2(C_4H_9)Cl$ collected in liquid nitrogen upon excitation at 381 nm 151

Figure 6.32. Emission spectrum of $AuP(C_6H_5)_2(C_4H_9)Cl$ collected in liquid nitrogen upon excitation at 370 nm 151

Figure 6.33. Emission spectrum of $AuP(C_6H_5)_2(C_4H_9)Cl$ collected in liquid nitrogen upon excitation at 353 nm 152

Figure 6.34. Emission spectrum of $AuP(C_6H_5)_2(C_4H_9)Cl$ collected in liquid nitrogen upon excitation at 317 nm 152

Figure 7.1. IR spectrum for $P(C_6H_4F)_3$ calculated theoretically using Gaussian 09 software ... 162

Figure 7.2. IR spectrum for $P(C_6H_4F)_3$ 163

Figure 7.3. IR spectrum for $AuP(C_6H_4F)_3Cl$ calculated theoretically using Gaussian 09 software 163

Figure 7.4. IR spectrum for $AuP(C_6H_4F)_3Cl$ 164

Figure 7.5. IR spectrum for $Au(P(C_6H_4F)_3)_2Cl$ 164

Figure 7.6. ^1H NMR spectrum of $P(C_6H_4F)_3$ 165

Figure 7.7. ^{1}H NMR spectrum of $AuP(C_6H_4F)_3Cl$ 165

Figure 7.8. ^{1}H NMR spectrum of $Au(P(C_6H_4F)_3)_2Cl$ 166

Figure 7.9. $^{31}P\{^{1}H\}$ NMR spectrum of $P(C_6H_4F)_3$ 166

Figure 7.10. $^{31}P\{^{1}H\}$ NMR spectrum of $AuP(C_6H_4F)_3Cl$ 166

Figure 7.11. $^{31}P\{^{1}H\}$ NMR spectrum of $Au(P(C_6H_4F)_3)_2Cl$ 166

Figure 7.12. ^{1}H NMR spectrum of $AuP(C_6H_4F)_3Cl$ calculated theoretically using Gaussian 09 software 167

Figure 7.13. ^{1}H NMR spectrum of $P(C_6H_4F)_3$ calculated theoretically using Gaussian 09 software 167

Figure 7.14. UV-Vis spectrum of $P(C_6H_4F)_3$ 168

Figure 7.15. UV-Vis spectrum of $AuP(C_6H_4F)_3Cl$ 169

Figure 7.16. UV-Vis spectrum of $Au(P(C_6H_4F)_3)_2Cl$ 169

Figure 7.17. UV-Vis spectrum of $AuP(C_6H_4F)_3Cl$ calculated theoretically using Gaussian 09 software 170

Figure 7.18. UV-Vis spectrum of $P(C_6H_4F)_3$ calculated Theoretically using Gaussian 09 software 170

Figure 7.19. Excitation spectrum of $P(C_6H_4F)_3$ collected at room temperature by monitoring the emission at 430 nm 173

Figure 7.20. Excitation spectrum of $AuP(C_6H_4F)_3Cl$ collected at room temperature by monitoring the emission at 411 nm 174

Figure 7.21. Excitation spectrum of $AuP(C_6H_4F)_3Cl$ collected at room temperature by monitoring the emission at 450 nm 174

Figure 7.22. Excitation spectrum of $Au(P(C_6H_4F)_3)_2Cl$ collected at room temperature by monitoring the emission at 450 nm 175

Figure 7.23. Excitation spectrum of $Au(P(C_6H_4F)_3)_2Cl$ collected at room temperature by monitoring the emission at 467 nm 175

Figure 7.24. Excitation spectrum of $P(C_6H_4F)_3$ collected in liquid nitrogen by monitoring the emission at 412 nm 176

Figure 7.25. Excitation spectrum of $AuP(C_6H_4F)_3Cl$ collected in liquid nitrogen by monitoring the emission at 416 nm 176

Figure 7.26. Excitation spectrum of $AuP(C_6H_4F)_3Cl$ collected in liquid nitrogen by monitoring the emission at 450 nm 177

Figure 7.27. Excitation spectrum of $Au(P(C_6H_4F)_3)_2Cl$ collected in liquid nitrogen by monitoring the emission at 506 nm 177

Figure 7.28. Excitation spectrum of $Au(P(C_6H_4F)_3)_2Cl$ collected in liquid nitrogen by monitoring the emission at 450 nm 178

Figure 7.29. Excitation spectrum of $Au(P(C_6H_4F)_3)_2Cl$ collected in liquid nitrogen by monitoring the emission at 411 nm 178

Figure 7.30. Emission spectrum of $P(C_6H_4F)_3$ collected at room temperature upon excitation at 389 nm 179

Figure 7.31. Emission spectrum of $AuP(C_6H_4F)_3Cl$ collected at room temperature by exciting it at 350 nm 179

Figure 7.32. Emission spectrum of $AuP(C_6H_4F)_3Cl$ collected at room temperature upon excitation at 343 nm 180

Figure 7.33. Emission spectrum of $AuP(C_6H_4F)_3Cl$ collected at room temperature upon excitation at 389 nm 180

Figure 7.34. Emission spectrum of $Au(P(C_6H_4F)_3)_2Cl$ collected at room temperature upon excitation at 350 nm 181

Figure 7.35. Emission spectrum of $Au(P(C_6H_4F)_3)_2Cl$ collected at room temperature upon excitation at 361 nm 181

Figure 7.36. Emission spectrum of $P(C_6H_4F)_3$ collected in liquid nitrogen upon excitation at 360 nm 182

Figure 7.37. Emission spectrum of $AuP(C_6H_4F)_3Cl$ collected in liquid nitrogen upon excitation at 354 nm 182

Figure 7.38. Emission spectrum of $AuP(C_6H_4F)_3Cl$ collected in liquid nitrogen upon excitation at 361 nm 183

Figure 7.39. Emission spectrum of $Au(P(C_6H_4F)_3)_2Cl$ collected in liquid nitrogen upon excitation at 342 nm 183

Figure 7.40. Emission spectrum of $Au(P(C_6H_4F)_3)_2Cl$ collected in liquid nitrogen upon excitation at 389 nm 184

Figure 8.1. Calculated IR spectrum for $P(C_6F_5)_3$ obtained using Gaussian 09 program 193

Figure 8.2. IR spectrum for $P(C_6F_5)_3$ 194

Figure 8.3. Calculated IR spectrum for $AuP(C_6F_5)_3Cl$ obtained using Gaussian 09 program 19494

Figure 8.4. IR spectrum for $AuP(C_6F_5)_3Cl$ 195

Figure 8.5. IR spectrum for $Au(P(C_6F_5)_3)_2Cl$ 195

Figure 8.6. $^{31}P\{^1H\}$ NMR spectrum of $P(C_6F_5)_3$ 196

Figure 8.7. $^{31}P\{^1H\}$ NMR spectrum of $AuP(C_6F_5)_3Cl$ 197

Figure 8.8. $^{31}P\{^{1}H\}$ NMR spectrum of $Au(P(C_6F_5)_3)_2Cl$ 197

Figure 8.9. UV-Vis spectrum of $P(C_6F_5)_3$ 198

Figure 8.10. UV-Vis spectrum of $AuP(C_6F_5)_3Cl$..... 198

Figure 8.11. UV-Vis spectrum of $Au(P(C_6F_5)_3)_2Cl$..... 199

Figure 8.12. Calculated UV-Vis spectrum of $AuP(C_6F_5)_3Cl$ obtained theoretically using Gaussian 09 program 199

Figure 8.13. Calculated UV-Vis spectrum of $P(C_6F_5)_3$ obtained theoretically using Gaussian 09 program 200

Figure 8.14. Excitation spectrum of $P(C_6F_5)_3$ collected at room temperature by monitoring the emission at 450 nm 202

Figure 8.15. Excitation spectrum of $AuP(C_6F_5)_3Cl$ collected at room temperature by monitoring the emission at 412 nm 203

Figure 8.16. Excitation spectrum of $AuP(C_6F_5)_3Cl$ collected at room temperature by monitoring the emission at 450 nm 203

Figure 8.17. Excitation spectrum of $Au(P(C_6F_5)_3)_2Cl$ collected at room temperature by monitoring the emission at 450 nm..... 204

Figure 8.18. Excitation spectrum of $Au(P(C_6F_5)_3)_2Cl$ collected at room temperature by monitoring the emission at 411 nm..... 204

Figure 8.19. Excitation spectrum of $Au(P(C_6F_5)_3)_2Cl$ collected in liquid nitrogen by monitoring the emission at 520 nm 205

Figure 8.20. Emission spectrum of $(P(C_6F_5)_3$ collected at room temperature upon excitation at 388 nm 205

Figure 8.21. Emission spectrum of $AuP(C_6F_5)_3Cl$ collected at room temperature upon excitation at 344 nm..... 206

Figure 8.22. Emission spectrum of $AuP(C_6F_5)_3Cl$ collected at room temperature upon excitation at 349 nm..... 206

Figure 8.23. Emission spectrum of $AuP(C_6F_5)_3Cl$ collected at room temperature upon excitation at 318 nm..... 207

Figure 8.24. Emission spectrum of $Au(P(C_6F_5)_3)_2Cl$ collected at room temperature upon excitation at 344 nm..... 207

Figure 8.25. Emission spectrum of $Au(P(C_6H_4F)_3)_2Cl$ collected at room temperature upon excitation at 296 nm..... 208

Figure 8.26. Emission spectrum of $Au(P(C_6F_5)_3)_2Cl$ collected at room temperature upon excitation at 287 nm..... 208

Figure 8.27. Emission spectrum of $AuP(C_6F_5)_3Cl$ collected in liquid nitrogen upon excitation at 340 nm 209

List of Tables

Table 3.1 Crystal data and Structural refinement parameters for $AuP(C_8H_9)_3Cl$ collected at room temperature 27

Table 3.2 Selected Bond Lengths [Å] for $AuP(C_8H_9)_3Cl$ complex 28

Table 3.3 Selected Bond Angles [°] for $AuP(C_8H_9)_3Cl$ complex 28

Table 3.4 Comparison of selected experimental and theoretical bond angles and lengths using DFT calculations..... 29

Table 3.5 Crystal data and Structural refinement for $AuP(C_8H_9)_3Cl$ collected at Liquid nitrogen temperature 30

Table 3.6 Nuclear site group theoretical analysis for $AuP(C_8H_9)_3Cl$ complex..... 33

Table 3.7 TD-DFT generated ground-state to excited-state MO transitions for **2**..... 41

Table 3.8 Theoretical results showing the contributions of X, Y, and Z transitions of **2**..... 42

Table 3.9 Atomic contributions for the ground state molecular orbitals for compound **2**..... 55

Table 3.10 Atomic Orbital contribution in the ground state for compound **2** 55

Table 4.1 Crystal data and Structural refinement parameters for $AuP(C_8H_9O_2)_3Cl$ collected at room temperature 68

Table 4.2 Selected Bond Lengths [Å] for $AuP(C_8H_9O_2)_3Cl$ complex 69

Table 4.3 Comparison of selected experimental and theoretical bond angles and lengths using DFT calculations 69

Table 4.4 Selected Bond Angles [°] for $AuP(C_8H_9O_2)_3Cl$ complex 70

Table 4.5 Nuclear site group theoretical analysis for $AuP(C_8H_9O_2)_3Cl$.. 73

Table 4.6 TD-DFT generated ground-state to excited-state MO transitions for **6**..... 80

Table 4.7 Theoretical results showing the contributions of X, Y, and Z transitions of **6**..... 81

Table 4.8 Atomic contributions for the ground state molecular orbitals for compound **6**..... 89

Table 4.9 Atomic Orbital contributions in the ground state for compound **6**..... 90

Table 5.1 Nuclear site group theoretical analysis for $AuP(C_7H_7O)_3Cl$ 105

Table 5.2 TD-DFT generated ground-state to excited-state MO transitions for **10**..... 110

Table 5.3 Theoretical results showing the contributions of X, Y, and Z transitions of **10**..... 111

Table 5.4 Atomic contributions for the ground state molecular orbitals for compound **10**..... 120

Table 5.5 Atomic Orbital contribution in the ground state for compound **10** 121

Table 6.1 Crystal data and Structural refinement parameters for $AuP(C_6H_5)_2(C_4H_9)Cl$ 130

Table 6.2 Selected Bond Lengths [Å] for $AuP(C_6H_5)_2(C_4H_9)Cl$ 131

Table 6.3 Selected Bond Angles [°] for $AuP(C_6H_5)_2(C_4H_9)Cl$ 131

Table 6.4 Comparison of selected experimental and theoretical bond angles and lengths using DFT calculations 132

Table 6.5 Nuclear site group theoretical analysis for $AuP(C_6H_5)_2(C_4H_9)Cl$ 135

Table 6.6 TD-DFT generated ground-state to excited-state MO transitions for **14**..... 143

Table 6.7 Theoretical results showing the contributions of X, Y, and Z transitions of **14**..... 144

Table 6.8 Atomic contributions for the ground state molecular orbitals for compound **14**..... 153

Table 6.9 Atomic Orbital contribution in the ground state for compound **14** 153

Table 7.1 TD-DFT generated ground-state to excited-state MO transitions for **18**..... 171

Table 7.2 Theoretical results showing the contributions of X, Y, and Z transitions of **18**..... 172

Table 7.3 Atomic contributions for the ground state molecular orbitals for compound **18**..... 184

Table 7.4 Atomic Orbital contribution in the ground state for compound **18** 185

Table 8.1 Nuclear site group theoretical analysis for $AuP(C_6F_5)_3Cl$ 196

Table 8.2 TD-DFT generated ground-state to excited-state MO transitions for **22**..... 200

Table 8.3 Theoretical results showing the contributions of X, Y, and Z transitions of **22**..... 201

Table 8.4 Atomic contributions for the ground state molecular orbitals for compound **22**..... 209

Table 8.5 Atomic Orbital contribution in the ground state for compound **22** 210

NOMENCLATURE

Au	Gold
EtOH	Ethanol
$HAuCl_4$	Hydrogen tetrachloroaurate
HOMO	Highest occupied molecular orbital
IL	Intraligand
LC	Ligand-centered
LLCT	Ligand-to-ligand charge-transfer
LMCT	Ligand-to-metal charge-transfer
LMMCT	Ligand-to-metal- • • metal charge-transfer
LUMO	Lowest unoccupied molecular orbital
MC	Metal-centred
MLCT	Metal-to-ligand charge-transfer
MMLCT	Metal • • metal-to-ligand charge-transfer
TBDPP	Tert-butyldiphenylphosphine
TDMOPP	Tris(2,6-dimethoxyphenyl)phosphine
TDMPP	Tris(3,5-dimethylphenyl)phosphine
TFFPP	Tris(4-fluorophenyl)phosphine
TFMOPP	Tris(4-methoxyphenyl)phosphine
THF	Tetrahydrofuran
THT	Tetrahydrothiophene
TPFPP	Tris(Pentafluorophenyl)phosphine

Abstract

The structures, and spectroscopic properties of a series of three new monocoordinated, four new bis-, tris-, and tetrakis-phosphine gold(I) complexes are reported. Six different monodentate tertiary phosphine ligands including tris(3,5-dimethylphenyl)phosphine,tris(2,6-dimethoxyphenyl)phosphine, tris(pentafluorophenyl)phosphine, tris(4-methoxyphenyl)phosphine, tert-butyldiphenyl phosphine, and tris(4-fluorophenyl)phosphine are used in this study. Three of the complexes have been studied with single crystal X-ray crystallographic techniques and the structural information was collaborated with Raman, and ^{31}P-NMR studies. The crystal structure of the complexes reveal the geometry and coordination of the ligands to the gold(I) atom as well as to Cl^- within the crystal lattice. Detail luminescence, ^{1}H-NMR, UV-Vis and FTIR spectroscopic studies were also performed. The photo-luminescence of the complexes compared with that of the ligand show ligand centered emission perturbed by the metal coordination. Theoretical DFT studies conducted on these complexes support the experimental studies and the assignment of the electronic transitions. Comparison of the electronic absorption behaviors also show a hyperchromic shift as the number of chromophores added to the gold (I) center increases and the molar extinction coefficient values of the ligands and the complexes determined are in excess of 10^4 M^{-1} cm^{-1}. Nuclear site analysis was used extensively for elucidating the number of IR and Raman bands that are possible for these complexes. A correlation between the structural and the vibrational data was established.

CHAPTER ONE

Introduction

1.1 Luminescence

Luminescence is the emission of light by certain materials when they are excited by some form of energy. It is in contrast to light emitted from incandescent bodies, such as burning wood or coal, molten iron, and wire heated by an electric current [1]. Luminescence light is enhanced at low temperature. Luminescence may be seen in neon and fluorescent lamps; television, radar, and X-ray fluoroscope screens; organic substances such as luminol or the luciferins in fireflies and glowworms; certain pigments used in outdoor advertising; and also natural electrical phenomena such as lightning and the aurora borealis [2]. In all these phenomena, light emission does not result from the material being at a higher temperature, and so luminescence is often called cold light [2]. The practical value of luminescent materials lies in their capacity to transform invisible forms of energy into visible light [3].

Luminescence emission occurs when an appropriate material absorbs energy from a source such as ultraviolet, X-ray radiation, electron beams, chemical reactions, and so on. The energy lifts the energy of the electrons in the atoms of the material into an excited state, and then, because excited states are unstable, the material undergoes another transition, back to its ground state, and the absorbed energy is liberated in the form of either light or heat or both (all discrete energy states, including the ground state of an atom are defined as quantum states) [4]. The excitation involves only the outermost electrons around the nuclei of the atoms. Luminescence efficiency depends on the degree of transformation of excitation energy into light, and there are relatively few materials that have sufficient luminescence efficiency to be of practical value [4].

As mentioned above, luminescence is characterized by electrons undergoing transitions from excited quantum states. The excitation of the luminescent electrons is not accompanied with appreciable movement of the atoms in the material [5]. When hot materials become luminous and radiate light, in a process called incandescence, the atoms of the material go into a high state of agitation [5]. Of course, the atoms of all material vibrate at room temperature, but sufficient to produce radiation in the far infrared region of the spectrum [5]. With increasing temperature the radiation shifts to the visible region. On the other hand, at very high temperatures, as in shock tubes, collisions of atoms can be so violent that electrons dissociate from the atoms and recombine with them, emitting light: in this case, luminescence and incandescence become indistinguishable [5].

Luminescence can occur as a result of many different kinds of excitation, including photo-, electro, chemi-, thermo-, sono-, or triboluminescence [5]. In practice, excitation produce x-rays, cathode rays, or UV emission of a gas discharge. In addition to the type of excitation, two other terms are used to classify luminescent materials which are related to the decay time (τ): fluorescence ($\tau < 10$ ms) and Phosphorescence ($\tau > 0.1$ s). These two are classified under what is called Photoluminescence [5].

1.2 Photoluminescence

Photoluminescence (abbreviated as PL) is light emission from any form of matter after the absorption of photons (electromagnetic radiation). It is one of many forms of luminescence (light emission) and is initiated by photoexcitation (excitation by photons), hence the prefix photo- Following excitation, various relaxation processes typically occur in which photons are re-radiated [6]. Time periods between absorption and emission may vary: ranging from short femtosecond-regime for emission involving free-carrier plasma in inorganic semiconductors up

to milliseconds for phosphorescent processes in molecular systems; and under special circumstances delay of emission may even span to minutes or hours [6]. Observation of photoluminescence at a certain energy can be viewed as indication that excitation populated an excited state associated with this transition energy. While this is generally true in atoms and similar systems, correlations and other more complex phenomena also act as sources for photoluminescence in many-body systems such as semiconductors. A theoretical approach to handle this is given by the semiconductor luminescence equations [6].

Photoluminescence is divided into two categories: fluorescence and phosphorescence. A pair of electrons occupying the same electronic ground state have opposite spins and are said to be in a singlet spin state (Figure 1a). When an analyte absorbs an ultraviolet or visible photon, one of its valence electrons moves from the ground state to an excited state with a conservation of the electron's spin (Figure 1b). Emission of a photon from the singlet excited state to the singlet ground state—or between any two energy levels with the same spin—is called fluorescence. The probability of fluorescence is very high and the average lifetime of an electron in the excited state is only 10^{-5}–10^{-8} s [7]. Fluorescence, therefore, decays rapidly once the source of excitation is removed. In some cases an electron in a singlet excited state is transformed to a triplet excited state (Figure 1c) in which its spin is no longer paired with the ground state. Emission between a triplet excited state and a singlet ground state—or between any two energy levels that differ in their respective spin states–is called phosphorescence. Because the average lifetime for phosphorescence ranges from 10^{-4}–10^{4} s, phosphorescence may continue for some time after removing the excitation source [7].

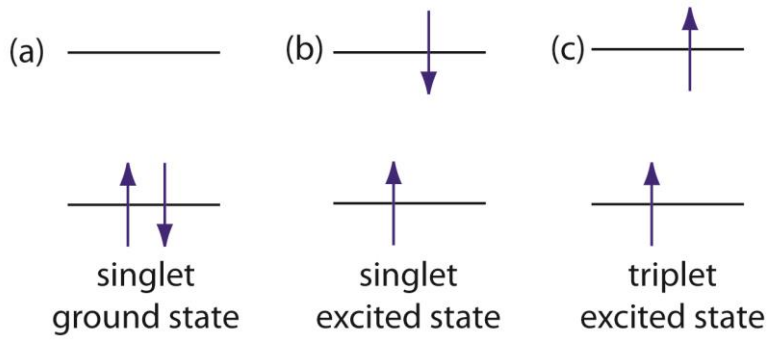

Figure 1. Electron configurations for (a) a singlet ground state; (b) a singlet excited state; and (c) a triplet excited state.

The use of molecular fluorescence for qualitative analysis and semi-quantitative analysis can be traced to the early to mid-1800s, with more accurate quantitative methods appearing in the 1920s. Instrumentation for fluorescence spectroscopy using a filter, or a monochromator for wavelength selection appeared in the 1930s and 1950s respectively. Although the discovery of phosphorescence preceded that of fluorescence by almost 200 years, qualitative and quantitative applications of molecular phosphorescence did not receive much attention until after the development of fluorescence instrumentation [7].

More processes may occur when a substance undergoes internal energy transitions before re-emitting the energy from the absorption event. Electrons change energy states by either resonantly gaining energy from absorption of a photon or losing energy by emitting photons. In chemistry-related disciplines, one often distinguishes between fluorescence and phosphorescence. The prior is typically a fast process, yet some amount of the original energy is dissipated so that re-emitted light photons will have lower energy than did the absorbed excitation photons. The re-emitted photon in this case is said to be red shifted, referring to the reduced energy it carries following this loss (as the Jablonski diagram shows). For phosphorescence, absorbed photons undergo intersystem crossing where they enter into a state

with altered spin multiplicity, usually a triplet state. Once energy from this absorbed electron is transferred in this triplet state, electron transition back to the lower singlet energy states is quantum mechanically forbidden, meaning that it happens much more slowly than other transitions. The result is a slow process of radiative transition back to the singlet state, sometimes lasting minutes or hours. This is the basis for "glow in the dark" substances

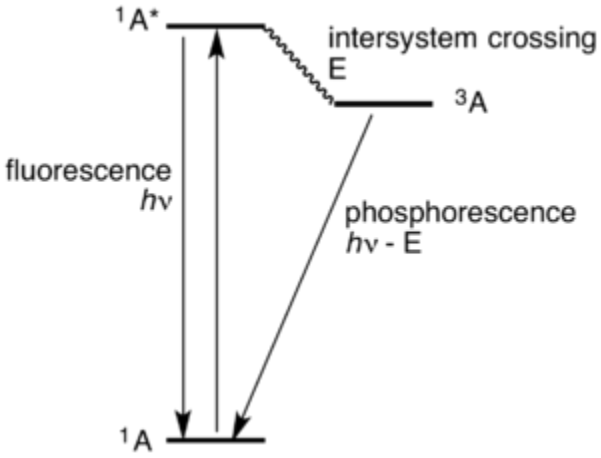

A Jablonski diagram showing the excitation of molecule A to its singlet excited state ($^1A^*$) followed by intersystem crossing to the triplet state (^3A) that relaxes to the ground state by phosphorescence.

To appreciate the origin of fluorescence and phosphorescence we must consider what happens to a molecule following the absorption of a photon. Let's assume that the molecule initially occupies the lowest vibrational energy level of its electronic ground state, which is a singlet state labeled S_0 in Figure 2. Absorption of a photon excites the molecule to one of several vibrational energy levels in the first excited electronic state, S_1, or the second electronic excited state, S_2, both of which are singlet states. Relaxation to the ground state occurs by a number of mechanisms, some involving the emission of photons and others occurring without emitting

photons [8]. These relaxation mechanisms are shown in Figure 2. The most likely relaxation pathway is the one with the shortest lifetime for the excited state.

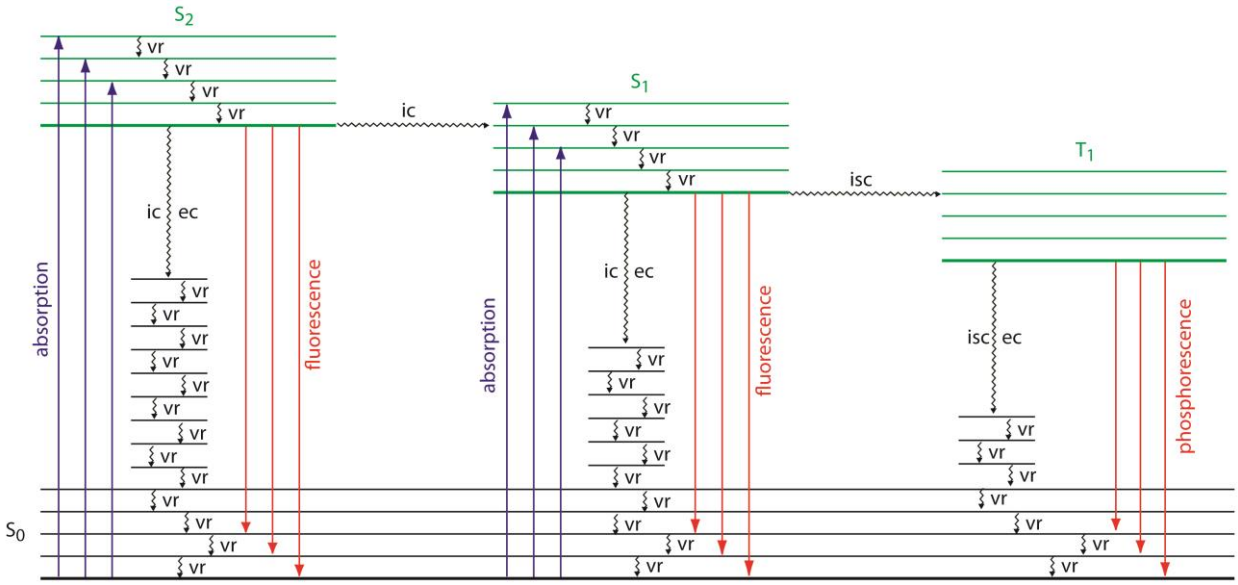

Figure 1.1. Energy level diagram for a molecule showing pathways for the deactivation of an excited state: *vr* is vibrational relaxation; *ic* is internal conversion; *ec* is external conversion; and *isc* is an intersystem crossing.

The lowest vibrational energy for each electronic state is indicated by the thicker line. The electronic ground state is shown in black and the three electronic excited states are shown in green. The absorption, fluorescence, and phosphorescence of photons also are shown. Depending on the localization of the electron density in the excited species, the electronic transition is classified as follows:

a. Charge transfer between complex and the environment

These transition can be classified into charge transfer to solvent (CTTS, electron transfers from the photoexcited complex to the surrounding solvent molecules) and ion-pair charge transfer (IPCT, exchange of an electron between the complex and usually ionic component of its secondary co-ordination sphere). CTTS is favored if there is no low energy ligand acceptor

orbitals and the presence of low-lying unoccupied orbital on the solvent molecules in the first and second coordination sphere of the complexes [8].

b. Metal centered transition

These are transitions between orbitals localized predominantly on the metal center. Such interaction can be divided into ligand field (LF) transition (d-d and f-f transitions in the complexes of transition and transition-f elements, respectively), Rydberg transition (electronic transition between orbitals with different principal quantum numbers) and intervalence charge transfer transition (IVCT, only found in polynuclear bridged complexes and involve transfer of electron form one to the other metal atom). It should be noted that in d^{10} complexes, no LF transition is possible, as the outermost d-orbitals are completely filled [8].

c. Charge transfer between metal and ligand

This involves electronic transition between molecular orbitals of different localization. If the electron is transferred from an orbital localized in metal center to an orbital localized in the ligand canter, it is called metal-to-ligand charge transfer (MLCT). In compounds displaying MLCT the metal center involved is relatively electron rich and the ligand orbital is relatively electron deficient. On the other hand, electron transfer in opposite direction may occur if the metal is relatively electron deficient and the ligand is relatively electron rich, and this is termed as ligand-to- metal charge transfer (LMCT). Besides, a kind of transition known as $\sigma \rightarrow a_{\pi}$ (σ-π^*) transition could also be under this class as the transition involves considerable charge transfer character. This transition involves the transfer of electron initially localized in a ligand-metal σ bond orbital to the π^* orbital of the ligand. Such transition originated

d. Ligand centered transition

These are transitions between orbitals localized primarily on a coordinated ligand of the complex, intraligand, IL. Upon coordination there is only little change about the transition energy, pattern or even band shape as compared with the free ligand, although the lifetime and the quantum yield of the emission may be different. Besides, ligand-to-ligand charge transfer (LLCT) transitions are found to involve the transition of electron from one coordinated ligand to another ligand [8].

1.3 Gold Chemistry

1.3.1 History. Gold was discovered as shining yellow nuggets and is undoubtedly the first metal known to early civilizations. The symbol derives from the Latin word aurum, which is related to the goddess of dawn, Aurora [9]. Early civilizations equated gold with gods and rulers, and gold was sought in their name and dedicated to their glorification. Humans almost intuitively attribute a high value to gold, associating it with power, beauty, and the cultural elite. And since gold is widely distributed all over the globe, it has been perceived in the same way throughout ancient and modern civilizations everywhere. Archeological digs suggest gold was first used in the Middle East where the first known civilizations developed [9]. The largest collection of gold and jewelry in the world included a gold coffin whose quality showed the advanced state of Egyptian craftsmanship and gold working (second millennium BC). The Persian Empire, in what is now Iran, made frequent use of gold in artwork as part of the religion of Zoroastrianism [9]. Gold was first used as money in around 700 BC, when Lydian merchants (western Turkey) produced the first coins [9]. These were simply stamped lumps of a 63% gold and 27% silver mixture known as “electrum.” Nevertheless, gold as a metal has been omnipresent since the dawn of civilization and its chemistry has played a major role in history [9]. Initially, all that was known of its chemistry was its concentration, recovery, and purification. Moreover, compounds,

such as tetrachloroauric acid or salts of the anions $[Au(CN)_2]^-$ or $[Au(CN)_4]^-$, were very important because they were intermediates in the recovery of the metal. The chemistry of gold was merely regarded as an art to recover and convert gold metal into all possible forms of ornamental, monetary, anticorrosive or electrical usage [10]. It is therefore no surprise that the chemistry of gold, which is so clearly dominated by the metallic state, remained undeveloped for so long. The associated development of an old handicraft, with all its secrets, into a field of research based on technology is a good example of how gold chemistry has finally matured into an advanced branch of science with a significant bearing on applications in many fields [10].

1.3.2 Chemical and Physical Properties. Gold is not very hard; a knife can easily scratch pure gold and it is very heavy or even dense for a metallic mineral. Some of the other characteristics of gold are ductility, malleability and sectility, meaning it can be stretched into a wire, pounded into other shapes, and cut into slices [10]. Gold is the most ductile and malleable element on our planet. It is a great metal for jewelry because it never tarnishes. The color and luster of gold are what make this metal so attractive. Gold is found as the free metal and in tellurides [10]. It is widely distributed and almost always associated with pyrite or quartz. It is found in veins and in alluvial deposits. Gold also occurs in seawater in concentrations of 0.1–2 mg ton^{-1}, depending on the location of the sample. In the mass, gold is a yellow-colored metal, although it may be black, ruby, or purple when finely divided [11]. One ounce of gold can be beaten out to 300 ft^2. Gold is a good conductor of electricity and heat. It is not affected by exposure to air or to most reagents. It is inert and a good reflector of infrared radiation. Gold is usually alloyed to increase its strength. Pure gold is measured in troy weight, but when gold is alloyed with other metals the term karat is used to express the amount of gold present [11]. Gold has an electrochemical potential which is the lowest of any metal. This means that gold in any

cationic form will accept electrons from virtually any reducing agent to form metallic gold. It is the most electronegative of all metals, which once again confirms its noble character. Moreover, although the electron affinity for metals is not usually included in textbooks for gold; the process from gold (0) to gold (–1) can be easily accomplished, and it has, in fact, been known since 1930 [11].

1.3.3 Theoretical Considerations. The electronic configuration of gold(0) is $5d^{10}6s^{1}$; for gold(1) it is $5d^{10}6s^{0}$ and for the Au(–1) anion it is $5d^{10}6s^{2}$. These configurations would justify the relative stability of gold(1) compounds, with 10 electrons in a closed set of 5d orbitals, or even, to some extent, the formation of the aurate anion, but they do not allow us to understand the predominance of the metallic form[12]. Post-lanthanide elements contain a large number of protons in their atomic nuclei; therefore, the electrons move in a field of very high nuclear charge, which leads to velocities approaching that of light and, consequently, they have to be treated according to Einstein's theories of relativity[12]. This is particularly true for electrons that are in s orbitals, which have wavefunctions that correspond to a finite electron density at the atomic nucleus, but it is less important for electrons in p or d orbitals [12]. Electrons moving at a speed close to the speed of light cannot be treated in terms of classical physics, but they are assigned a relativistic mass that is larger than the mass of the electron at rest. The effect on the 6s electrons, in the post-lanthanide elements, is that the orbital radius is contracted and the distance of the electron from the nucleus is reduced [12]. There are several physical and chemical consequences of this effect in gold chemistry:

1. The color of gold. Gold has an absorption beginning at 2.4 eV, attributed to a transition from the filled 5d band to the Fermi level (essentially the 6s band). It therefore reflects red and

yellow light and strongly absorbs blue and violet. The analogous absorption for silver, however, lies in the ultraviolet, at around 3.7 eV.

2. A marked reduction in the lengths of covalent bonds involving gold atoms is often found and the covalent radius of gold is smaller than that of silver. The estimated covalent radii for silver and gold are 1.33 and 1.25 Å, respectively, so di-coordinated gold is smaller than silver by about 0.09(1) Å.

3. In gold, more than in silver, both states are now available for bonding. The closed shell $5d^{10}$ is no longer chemically inert and can interact with other elements, that is, with other gold atoms in molecules or clusters. Bonding between two gold(I) centers with equal charge and a closed shell $5d^{10}$ configuration can also be rationalized, and this is a very difficult fact to explain in terms of classical bonding. The metal atoms approach each other to an equilibrium distance of between 2.7 and 3.3 Å. This range includes the distance between gold atoms in gold metal and approaches, or even overlaps with, the range of distances established for the few authentic Au–Au single bonds. Schmidbaur has called this effect aurophillic attraction or aurophilicity.

4. The small difference in energy between the 6s, 6p and 5d orbitals leads to the efficient formation of linear two-coordinate complexes in gold(1). However, silver(1) prefers the formation of three- and four coordinate derivatives.

5. The destabilization of the 5d orbitals allows the easy formation of the oxidation state Au(III) state in gold to be explained. This is almost absent in silver and stabilization of the 6s orbital explains the reason for the possible formation of the Au(–1), oxidation state, which is unknown in silver. Theoretical calculations have played a key role in understanding the origin of these differences and also in the development of gold and silver chemistries [12]. Bonding between closed-shell atoms was successfully traced in several early theoretical investigations by extended

Huckel quantum chemical calculations. Based on the hybridization concept, the nature of the bonding interaction could be qualitatively rationalized in the language of chemists [12].

The introduction of relativistic effects in more advanced calculations has shown that bonding between closed-shell metal atoms or ions may be strongly enhanced by these effects. Since relativistic effects have been known to reach a local maximum for gold in particular, aurophilicity was accepted as a logical consequence of these contributions. In fact, aurophillic bonding is considered as an effect based largely on the electron correlation of closed shell components, somewhat similar to van der Waals interactions but unusually strong. All these studies have consistently shown that calculations will only reproduce the attractive forces between the gold atoms very well if relativistic affects are included [12].

1.3.4 Chemistry. Since the early 1980s, the chemistry of gold has undergone continuous expansion; not only well-established areas of research have developed, but also new innovative approaches have enabled great diversification of the fields of research [13]. The metal and its complexes also have special characteristics that make them suitable for several uses. Gold possesses special characteristic features that make it unique, such as high chemical and thermal stability, mechanical softness, high electrical conductivity, and attractive appearance [13].

All these attributes gave rise to many relevant applications. For example, gold is an essential element for nanoscale electronic devices because it is resistant to oxidation and mechanically robust[13]. The well-known elegant red color in Venetian crystal glass stems from surface Plasmon absorption of blue light by gold nanoparticles a few tens of nm in size. Gold compounds have been used successfully for the treatment of rheumatoid arthritis. Gold is also an outstanding element for use as a heterogeneous catalyst operating at ambient temperature

because it is catalytically active at low temperature (200–350 K compared with Pd and Pt at 400–800 K); in the last few years several uses in homogeneous catalysis have also been reported [14].

The chemistry of gold(I) species is by far the most developed. Many monoclear, dinuclear or, in general, polynuclear derivatives with several types of ligands have been described. It is difficult to say which type of complexes are more stable and important for gold, although those of phosphine or polyphosphine ligands have been studied in depth, as have organometallic gold complexes or species with chalcogenolate or chalcogenide ligands [15]. The chemistry of gold(1) complexes is dominated by linear two-coordinate complexes of the form [AuXL], which, despite being known for a long time, have returned to prominence because they display short intermolecular gold–gold contacts that associate the monomeric units into dimers, oligomers or even uni- and multidimensional polymers [15]. These aurophillic interactions, together with other secondary bonds such as hydrogen bonds, play a role in determining the solid state arrangement of Au(1) complexes.

The tendency of molecules containing an Au---Au interaction to crystallize with more than one molecule in the asymmetric unit ($Z > 1$) has been calculated [16]. This behavior is believed to be related to the size of the differential of the two substituents. If the two ligands have a disparity in size, the $Z > 1$ is favored, whereas the ligands of equivalent size have a tendency to form structures with $Z > 1$. This fact can be easily seen in neutral complexes of the type [AuXL], which have been prepared for a great variety of donor ligands [16]. The neutral ligand is mainly a phosphine, arsine, isocyanide, carbine, ylide, amine, and etc., and the anionic moiety can be a halide, alkyl or aryl, and chalcogenolate [16].

1.3.5 Photochemistry of d^{10} Gold (I) Complexes. Au(I) has an electronic configuration $[Xe]4f^{14}5d^{10}$ and it can form linear, trigonal planar or tetrahedral complexes in which the

hybridization of gold can be considered to be sp(linear), sp^2(trigonal planar) or sp^3(tetrahedral), respectively, using the 6s and one or more of the 6p orbitals of gold in bonding. In some cases, the 5d orbitals of gold are involved in bonding to some extent. Among the three coordination modes, linear complexes are most common as compared with other d^{10} Cu(I) and Ag(I) species [17]. Since Au(I) is regarded as a soft metal, it will bond to the softer end of the ligand, for example. In view of this, it is not surprising that most of the stable Au(I) complexes found are consisting of phosphine ligands. Studies in the photochemistry of Au(I) complexes are advantageous since the electronic configuration of Au(I), as mentioned earlier, consists of completely filled d^{10} configuration. Unlike metal centers with d^1 to d^9 configuration, d-d transitions cannot occur in d^{10} Au(I) complexes [17].

Thus, other types of transition and excited state chemistry could be investigated in Au(I) complexes as ligand field transition. In fact, the luminescent properties of d^{10} metal complexes have attracted much attention recently. As early as in 1970. The investigation of the luminescent properties of Au(I) complexes has been relatively active in the past two decades [18]. For example, $AuCl_2^-$ and $AuBr_2^-$ are found to be luminescent and the lowest energy excited states were interpreted as resulting from metal-localized 5d→6s and 5d→6p transitions, while those of AuI_2^- include also states of the ligand to metal charge transfer (LMCT) type[18]. In contrast the lowest energy excited state for Au(I) complexes with π-acceptors ligands (CN^-, CNR, $P(OMe)_3$) have been assigned as MLCT states. On the other hand, monomeric Au(I) phosphines $[Au(PPh_3)Cl]$ and $[Au(PR_3)_2]^+$ have been reported to exhibit π→π* transition on the phenyl ring. It is shown that the ligand dependence of the lowest energy excited states implies changes in the nature of the highest occupied molecular orbitals (HOMO's) and lowest unoccupied molecular orbitals (LUMO's) in the Au(I) complexes [18].

1.4 Ligands

The term ligand has its origin in coordination chemistry. It denotes a molecule that is able to bind to a metal center in most cases via one or several free electron pairs. Ligands can be described by the number of electron-pair donor atoms as monodentate, bidentate, tridentate etc. ligands[19]. The latter are also called chelating ligands. A typical classification of ligands is according to their electronic properties. They serve either as a σ-donating, σ-donating/π-accepting, or σ,π-donating/π-accepting ligands. A more practical, often encountered approach is the classification of ligands according to their donor atoms, especially when larger molecules and molecules containing heteroatoms are regarded [19]. The choice of the ligand for a metal center can be made from a large variety of ligand types. The donor atom can be changed from hard to soft, as for example in the series NR_3 to BiR_3 [19].

$$NR_3 > PR_3 > AsR_3 > SbR_3 > BiR_3$$

hard soft

Periodic change in ligand hardness

The choice of the right ligand can influence; (1) the solubility of the active species; (2) the shielding and sterical properties of the complex, (3) the electron-density at the metal atom; and (4) the lifetime and turnover-numbers of the complex.

1.4.1 Phosphine Ligands. Phosphines are good ligands for a soft and electron rich d^6 and d^{10} metal centers and form stable complexes [21]. An additional benefit of phosphines as compared with ligands containing nitrogen or oxygen as donor atoms, are the magnetic properties of the ^{31}P nucleus: With its spin of 1/2 and an abundance of 100% it is an extraordinarily good tool for NMR spectroscopy, which offers an easy way for reaction control [20]. Phosphine ligands are usually strong σ-donor ligands and only weak π-acceptors, this effect

can be increased with electron-donating groups in the rest R, while electron with-drawing groups in R favor the π-acceptor backbonding [20].

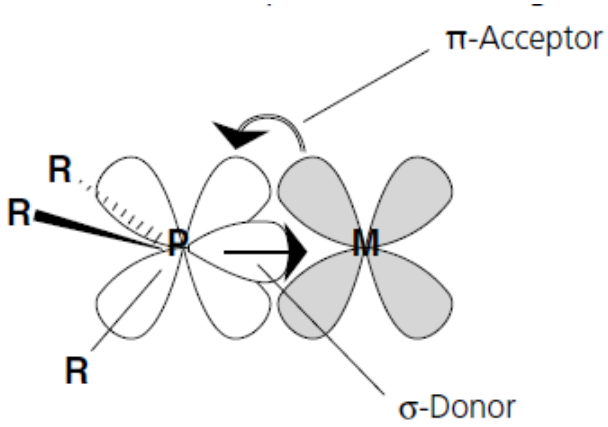

The size and steric demand of the phosphine ligand as approximately described by the cone-angle (θ) of the phosphine. A bulkier ligand (with large cone-angle) tends to have a higher dissociation rate than smaller ligands and electron-rich metal-centers tend to accelerate the "oxidative addition".

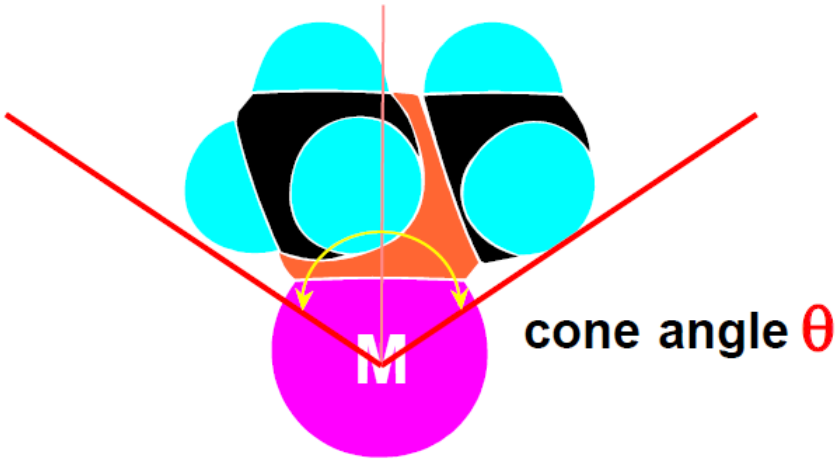

Some typical examples of commonly used phosphine ligands and their properties

Phosphine Ligands	Cone angle	σ-donor	stability
Triphenylphosphine	*145°*	*medium*	*air-stable*
Tricyclohexylphosphine	*170°*	*strong*	*air-sensitive*
Tri-(tert-butyl)phosphine	*182°*	*strong*	*air-sensitive*
Trimesitylphosphine	*212°*	*medium-strong*	*air-stable*
Trimethylphosphine	*118°*	*medium-strong*	*air-sensitive*

The following list indicate the Increasing σ-Donor Ability of selected phosphine ligands. $PMePh_2$ (136°), PMe_2Ph (122°), PMe_3 (118°), PEt_3 (132°) $P(Cy)_3$ (170°) tricyclohexylphosphine, $P(t\text{-}Bu)_3$ (182°). These alkyl phosphines are strong σ-donors; usually colorless liquids, somewhat to very air-sensitive, horrible smelling (unless very high MW and non-volatile). Whereas the following list includes the phosphine ligands with poor σ-Donors, and strong π-accepting ability. Phosphites: $P(OMe)_3$ (107°), $P(OEt)_3$ (110°), $P(OPh)_3$ (128°). Phosphites are relatively poor σ-donors, but can be fairly good π-acceptor ligands (about half as strong as CO). In general the ones with low molecular weight are usually colorless liquids, while the ones with higher MW compounds are white solids, air-stable, albeit moisture sensitive and sometimes sweet smelling [22].

Phosphines have only been characterized as simple $2e^-$ donating, terminal-only ligands. No true μ_x-bridging monophosphines are known (although bridging phosphides, PR_2^-, are very common). Phosphines generally tend to orient trans to one another in order to minimize steric interactions (especially true for bulky PR_3). Chelating bisphosphine ligands are used to enforce cisoidal coordination geometries when needed [23]. The basicity of the donor atom is another convenient way to tune the properties of a ligand. In the series of the phosphines starting from

P^tBu_3 and going to PPh_3 the donor atom and the denticity do not change, and the steric bulk remains about the same, but the donor properties of the ligands vary strongly [24]. Finally, the properties of the substituents allow the tuning of the steric bulk of a phosphine ligand. In the series PMe_3, PEt_3, P^iPr_3, P^tBu_3 the points mentioned above remain the same, but the cone angle of the ligands increases strongly[25].

The aim of this research is to be able to coordinate various phosphine containing ligands especially the tertiary based ones to a gold(I) center. Available literature data shows that monodentate phosphine based ligands can be coordinated to the gold(I) center. However, literature on the coordination of more than two monodentate phosphine ligands to the gold (I) center is scarece in particular. We explored the coordination of several monodentate phosphine ligands to the gold(I) center, and studied their structural and luminescent properties. This approach is thought to contribute to the understanding of electronic and structural effects in complexation reactions and coordination chemistry of gold(I) complexes. Various spectroscopic measurement techniques including Raman, FT-IR, NMR, X-ray were used to elucidate these complexes and their luminescent properties monitored.

CHAPTER TWO

Experimental Methods

2.1 Physical measurements and instrumentations

2.1.1 NMR Spectroscopic Measurements. ^{1}H NMR spectra with chemical shifts relative to tetramethylsilane (Me_4Si) in deuterated chloroform ($CDCl_3$) were recorded on a Varian 300-411149 Fourier-transform NMR spectrometer (300 MHz). $^{31}P\{^{1}H\}$ NMR spectra with chemical shifts relative to 0.0485M Triphenylphosphate in deuterated chloroform ($CDCl_3$) were recorded on the 300 MHz Bruker 300 and 300 MHz Varian NMR 300-411149 FT-NMR spectrometer.

2.1.2 FT-IR Spectroscopic Measurements. All infrared spectra were obtained as potassium bromide (KBr) disc, prepared by compressing the ground mixture of sample and KBr powder, on a Shimadzu IR-PRESTIGE-21 Fourier transform infrared spectrophotometer ($4000-300\ cm^{-1}$).

2.1.3 Raman Spectroscopic Measurements. Raman data were collected using the Horiba XploRA Raman Confocal Microscope System. Raman spectroscopy techniques are used to observe vibrational, rotational, and other low-frequency modes in a system. One thing that Raman systems rely on is inelastic scattering of the monochromatic light. The monochromatic light usually comes from the laser in the near infrared, near UV or visible range. The laser light interacts with phonons and molecular vibrations resulting in the energy of the laser photons being shifted. The shift that occurs gives information about the vibrational modes.

2.1.4 Ultraviolet and Visible (UV-Vis) Spectroscopic Measurements. All the UV-vis spectra data were collected on a Shimaddzu UV-2401 PC UV-Vis Recording Spectrometer.

2.1.5 Photoluminescence Spectroscopic Measurements. Excitation and emission spectra obtained at room temperature and with liquid nitrogen filled in the cold-finger Dewar flask were recorded on a Photon Technology International (PTI) spectrometer model QM-7/SE, and equipped with a Hamamatsu R928P photomultiplier tube with corning filters. It uses a LPS-220B power supply unit, a Brytebox and MD-5020 motor drive. The instrument uses Ushio - 75Xe xenon arc lamp, and a model 101M f/4 0.2-meter Czerny Turner with a 4nm/mm bandpass Monochromator. The instrument also uses the model 814 analog/photo-counting Photomultiplier detector. The instrument operation, data collection, and handling were all controlled using the advanced FeliX32 software. All samples for the luminescent studies were loaded on a borosilicate capillary tubes and was sealed from the atmosphere using a micro touch.

2.1.6 X-ray Crystallography Studies. X-ray data were collected using a Bruker AXS SMART X2S system based diffractometer equipped with a CCD 485 Breeze detector and a Ricor K535 power supply unit. A suitable crystal was chosen and mounted on a pin using a micromount needle from Bruker Corporation using Paratone-N oil purchased from Hampton Research. The diffraction data for the determination of the crystal structures were collected on CD-R using the Bruker CCD 485 Breeze detector for cell refinement, and data reduction with Apex, X-SHELL and Mercury software. The structures were solved using the Apex, XSHEL and Mercury software program by direct methods. The XSHELL program(s) was used to refine the structures, while molecular graphics were done using the APEX2.

2.1.7 Group Theoretical analysis (Nuclear Site Group Analysis). Nuclear site group analysis provides a procedure for determining symmetry characteristics of crystals. This method is simply a generalization of a molecular site group analysis in that a site symmetry is carried out

on every atom in the unit cell. By determining the site symmetry of each atom in this way, a set of tables may be constructed to allow symmetry and selection rule determination.

2.1.8 Computational Studies. All of the theoretical calculations for the various ligands and their complexes were completed using the GAUSSIAN ' 09 software package. Geometry optimizations and vibration frequency calculations were performed with the Becke three-parameter hybrid functional using the Perdew‐Wang correlation functional (B3PW91) level of density functional theory (DFT). The 6‐311 G(d, p) basis set was utilized for C, P, Cl, and H. The LANL2DZ basis set was used in conjunction with two f-type polarization functions and p-type functions for the $5s^2$ $5p^6$ $5d^{10}$ $6s^1$ valence electrons of gold, and one d-type polarization function for phosphorus. The predicted absorption spectra of the optimized structures were accomplished by time-dependent density functional theory (TD-DFT) without consideration of any solvent effect. Molecular orbitals iso-density diagrams (iso-values: 0.02 atomic units) of molecular orbitals were created using the GaussView 5 software (Gaussian Inc.)

2.2 Chemical Reagents

All glassware were oven-dried prior to use. The chemicals used for the synthesis, recrystallization and all the standards used for the characterization were purchased from Sigma Aldrich. The chemicals include: tetrahydrothiophene, hydrogen tetrachloroaurate, hexanes, tetrahydrofuran, dichloromethane, tris(pentaflouorophenyl)phosphine, tris(4-fluorophenyl) phosphine, tris(2,6-dimethoxyphenyl)phosphine, tris(3,5-dimethylphenyl)phosphine, tris(4-methoxyphenyl) phosphine, tert-butyl diphenyl phosphine

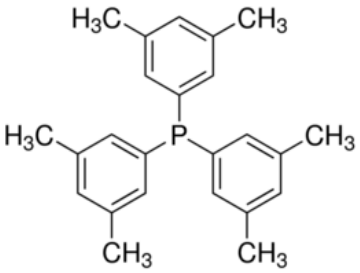

Tris(3,5-dimethylphenyl)phosphine

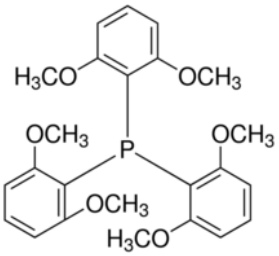

Tris(2,6-dimethoxyphenyl)phosphine

Tris(pentaflouorophenyl)phosphine

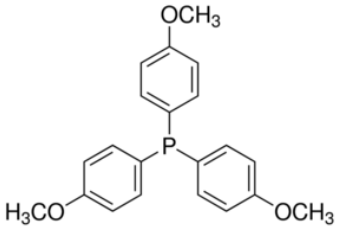

Tris(4-methoxyphenyl) phosphine

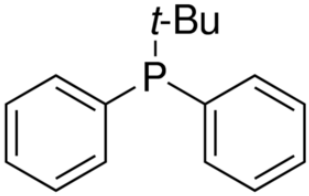

tert-butyl diphenyl phosphine

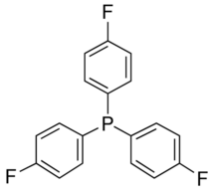

tris(4-fluorophenyl)phosphine

2.3 Reagent Preparation

Chloro-tetrahydrothiophene gold(I) is prepared according to literature without further purification. tetrahydrofuran (THF) solvent is purified by distillation. Dichloromethane (CH_2Cl_2), tris(pentaflouorophenyl)phosphine, tris(4-flourophenyl)phosphine, tris(2,6 dimethoxyphenyl) phosphine, tris(3,5dimethylphenyl)phosphine, tris(4-methoxyphenyl) phosphine, tert-butyl diphenyl phosphine were used without further purification.

2.4 Syntheses

All of the synthetic procedures were conducted using a schlenk technique.

Synthesis of chloro (tetrahydrothiophene) gold (I), AuCl(THT) (**1**). A 200-mL flask fitted with a teflon-coated magnetic stirring bar was charged with a solution of hydrogen tetrachloroaurate(III) ($H[AuCl_4]\cdot 4H_2O$, 1.6g , 3.9 mmol) in a mixture of 3 mL of water and 13 mL of ethanol. Drop wise addition of tetrahydrothiophene (0.72 mL, 8.16 mmol) gives rise to the formation of a bulky yellow precipitate of $AuCl_3(SC_4H_8)$, which is transformed into the white solid of $AuCl(SC_4H_8)$ while the addition is continued. The mixture is stirred for 15 min at room temperature and the white precipitate is filtered, washed with two 5-mL portions, of ethanol and vacuum dried. Yield 1.20 g (96.4%).

CHAPTER THREE

Synthesis and Characterization of mono-, bis-, tris-, and tetrakis-{tris(3, 5-dimethylphenyl)phosphine} gold(I) complexes

3.1 Syntheses

3.1.1 Tris(3,5-dimethylphenyl)phosphine gold (I) chloride (2). Tris(3,5-dimethylphenyl)phosphine (0.0200 g, 0.058 mmol) was added to a solution of $(C_4H_8S)AuCl$ (0.0134 g, 0.058 mmol) in tetrahydrofuran (20 mL) at −80 ˚C and the reaction stirred for 2 hours. The solvent was removed by purging nitrogen gas into the solution, until all the solvent dried up. The residue was then recrystallized from CH_2Cl_2/n-hexane mixture for days. Partial evaporation of the solvent provided quality crystals.

3.1.2 Bis{Tris(3,5-dimethylphenyl)phosphine} gold (I) chloride (3). Tris(3,5-dimethylphenyl)phosphine (0.0400 g, 0.116 mmol) was added to a solution of $(C_4H_8S)AuCl$ (0.0134 g, 0.058 mmol) in tetrahydrofuran (20 mL) at −80 ˚C and the reaction stirred for 2 hours. The solvent was removed by purging nitrogen gas into the solution, until all the solvent dried up. The residue was then recrystallized from CH_2Cl_2/n-hexane mixture for days. Partial evaporation of the solvent provided quality crystals.

3.1.3 Tris{Tris(3,5-dimethylphenyl)phosphine} gold (I) chloride (4). Tris(3,5-dimethylphenyl)phosphine (0.0600 g, 0.174 mmol) was added to a solution of $(C_4H_8S)AuCl$ (0.0134 g, 0.058 mmol) in tetrahydrofuran (20 mL) at −80 ˚C and the reaction stirred for 2 hours. The solvent was removed by purging nitrogen gas into the solution, until all the solvent dried up. The residue was then recrystallized from CH_2Cl_2/n-hexane mixture for several days. Partial evaporation of the solvent provided quality crystals.

3.1.4 Tetrakis-{Tris(3,5-dimethylphenyl)phosphine} gold (I) chloride (5). Tris(3,5-dimethylphenyl)phosphine (0.0800 g, 0.232 mmol) was added to a solution of $(C_4H_8S)AuCl$ (0.0134 g, 0.058 mmol) in tetrahydrofuran (20 mL) at −80 ˚C and the reaction stirred for 2 hours. The solvent was removed by purging nitrogen gas into the solution, until all the solvent dried up. The residue was then recrystallized from CH_2Cl_2/n-hexane mixture for days. Partial evaporation of the solvent provided quality crystals.

3.2 Results

3.2.1 X-ray Crystallography. Diffraction data were collected on x-ray quality crystals. The structure of the monocoordinated TDMPP gold (I) complex, $AuP(C_8H_9)_3Cl$, is shown in Figure 3.1, and the structural data along with selected bond lengths and angles collected at room and liquid nitrogen temperatures are listed in Tables 3.1, 3.2, 3.3, 3.4 and 3.5.

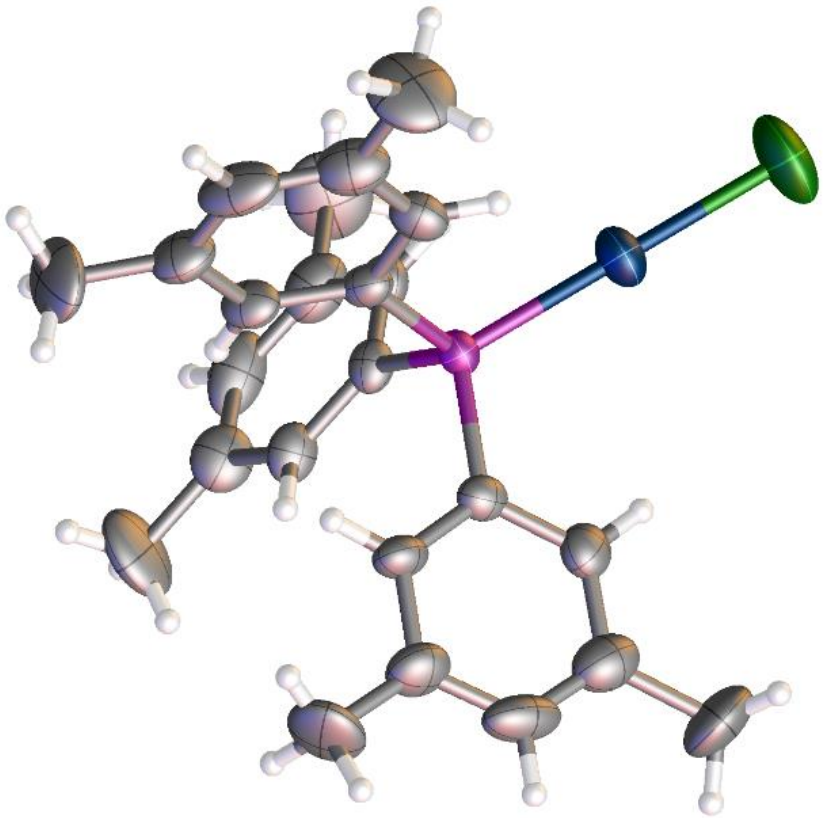

Figure 3.1. Thermal ellipsoid diagram of the $AuP(C_8H_9)_3Cl$ complex.

Table 3.1

Crystal data and Structural refinement parameters for $AuP(C_8H_9)_3Cl$ collected at room temperature

Empirical formula	$C_{24}H_{27}$ Au Cl P
Formula weight	578.84
Temperature	293 K
Wavelength	0.71073 Å
Crystal system	Trigonal
Space group	P3
Unit cell dimensions	a = 14.5452 (4) Å c = 9.69817 (19) Å
Volume	1776.90 (7) $Å^3$
Z	3
Density (calculated)	1.623 mg cm^{-3}
Absorption coefficient	6.40 mm^{-1}
$F_{(000)}$	846
Crystal size	0.35 × 0.13 × 0.12 mm
Theta range for data collection	θ = 2.7–24.7°
Index ranges	-17<h<16, -17<k<17, -11<l<11
Reflections collected	10741
Independent reflections	4226 [R(int) = 0.035]
Completeness to theta = 25.1°	99.9%
Absorption correction	Multi-scan
Max. and min. transmission	1.000 and 0.5222
Refinement method	Full-matrix least-squares on F^2
Data / restraints / parameters	4226 / 1 / 250
Goodness-of-fit on F^2	1.05
Final R indices [I>2sigma(I)]	R1 = 0.034, wR2 = 0.067
Absolute structure parameter	−0.013 (9)
Large diff. peak and hole	0.40 e $Å^{-3}$ and −0.96 e $Å^{-3}$

Table 3.2

Selected Bond Lengths [Å] for $AuP(C_8H_9)_3Cl$ complex

Bond	Bond Length [Å]
Au(1)—P(1)	2.230 (4)
Au(1)—Cl(1)	2.299 (6)
Au(2)—Cl(2)	2.281 (5)
Au(2)—P(2)	2.238 (5)
Cl(3)—Au(3)	2.286 (6)
Au(3)—P(3)	2.219 (5)
P(1)—C(1)	1.817 (7)
P(3)—C(17)	1.825 (7)
P(2)—C(9)	1.824 (7)

Table 3.3

Selected Bond Angles [°] for $AuP(C_8H_9)_3Cl$ complex

Measured Bond	Bond Angles [°]
P(1)—Au(1)—Cl(1)	180.0 (4)
Cl(2)—Au(2)—P(2)	180.0 (2)
P(3)—Au(3)—Cl(3)	180.0 (4)
C(6)—C(1)—P(1)	118.6 (5)
C(2)—C(1)—P(1)	122.0 (2)
C(1)—P(1)—Au(1)	113.2 (2)
C(17)—P(3)—Au(3)	113.8 (7)
C(9)—P(2)—Au(2)	112.9 (3)

Table 3.4

Comparison of selected experimental and theoretical bond angles and lengths using DFT calculations

EXPERIMENTAL BOND LENGTH [Å]		CALCULATED BOND LENGTH [Å]
Au(1)—P(1)	2.230	2.390
Au(1)—Cl(1)	2.299	2.332
P(1)—C(1)	1.817	1.806
EXPERIMENTAL BOND ANGLE [°]		CALCULATED BOND ANGLE [°]
P(1)—Au(1)—Cl(1)	180.0	180.0
C(1)—P(1)—Au(1)	113.2	112.8
C(17)—P(1)—C(9)	109.3	108.5

Table 3.5

Crystal data and structural refinement for $AuP(C_8H_9)_3Cl$ collected at Liquid nitrogen temperature

Empirical formula	$C_{24}H_{27}$ Au Cl P
Formula weight	578.84
Temperature	180 K
Wavelength	0.71073 Å
Crystal system	Trigonal
Space group	P3
Unit cell dimensions	a = 14.3751 (14) Å c = 9.6636 (9) Å
Volume	1729.4 (3) $Å^3$
Z	3
Density (calculated)	1.667 Mg cm^{-3}
Absorption coefficient	6.57 mm^{-1}
$F_{(000)}$	846
Crystal size	0.35 × 0.13 × 0.12 mm
Theta range for data collection	θ = 3.3–28.0°
Index ranges	-17<h<16, -14<k<17, -11<l<11
Reflections collected	5659
Independent reflections	3457 [R(int) = 0.048]
Completeness to theta = 25.3°	99.9%
Absorption correction	Multi-scan
Max. and min. transmission	1.000 and 0.490
Refinement method	Full-matrix least-squares on F^2
Data / restraints / parameters	3457 / 1 / 250
Goodness-of-fit on F^2	1.0
Final R indices [I>2sigma(I)]	R1 = 0.038, wR2 = 0.080
Absolute structure parameter	−0.005 (13)
Large diff. peak and hole	0.58 e $Å^{-3}$ and −1.03 e $Å^{-3}$

3.2.2 Infrared Spectroscopy. All infrared spectra were obtained as potassium bromide (KBr) disc, prepared by compressing the ground mixture of sample and KBr powder, on a Shimadzu IR-PRESTIGE-21 Fourier transform infrared spectrophotometer (4000−300 cm^{-1}). Figure 3.2, 3.3, 3.4, 3.5 and 3.6 show comparison of the experimental and theoretically calculated IR spectra of the mono-, di-, tri- and tetracoordinated TDMPP gold (I) complexes.

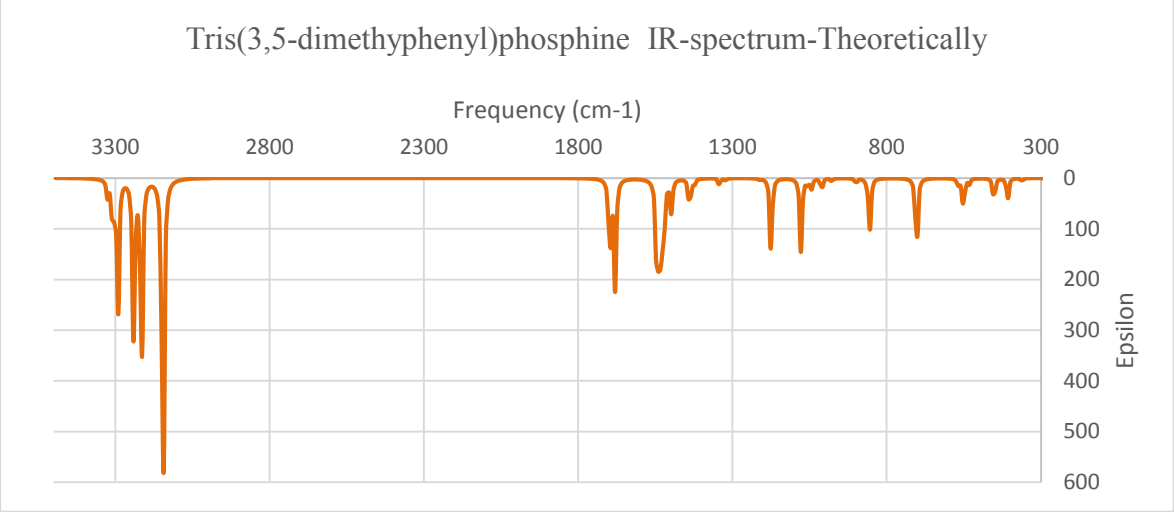

Figure 3.2. IR spectrum for $P(C_8H_9)_3$ calculated theoretically using Gaussian 09.

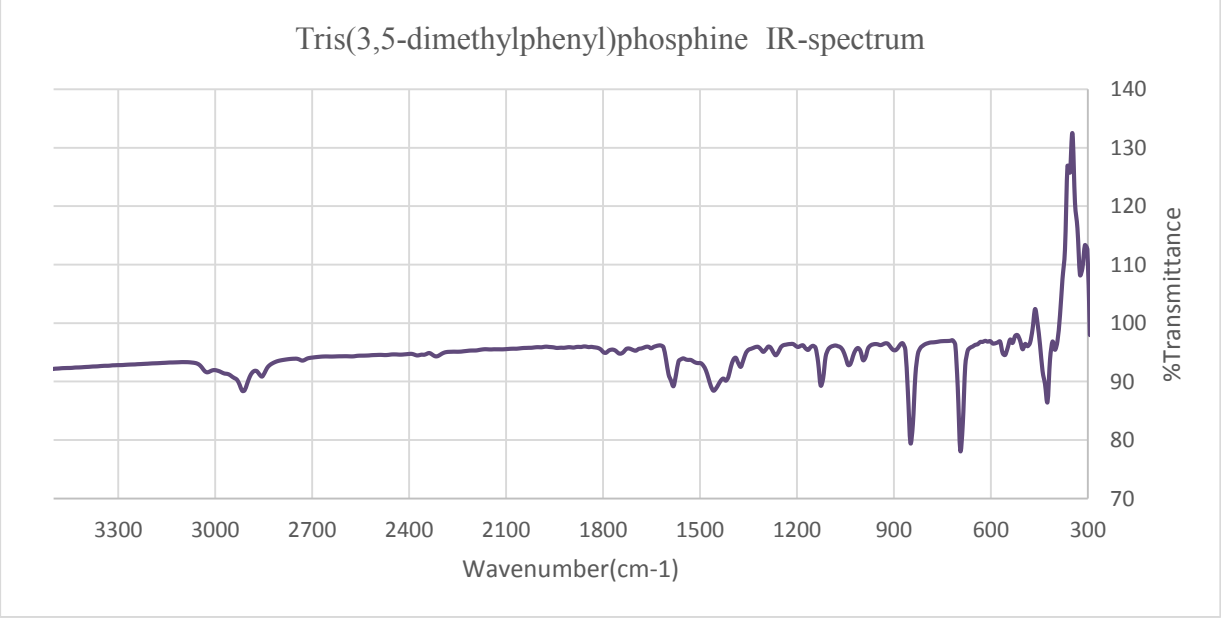

Figure 3.3. IR spectrum for $P(C_8H_9)_3$.

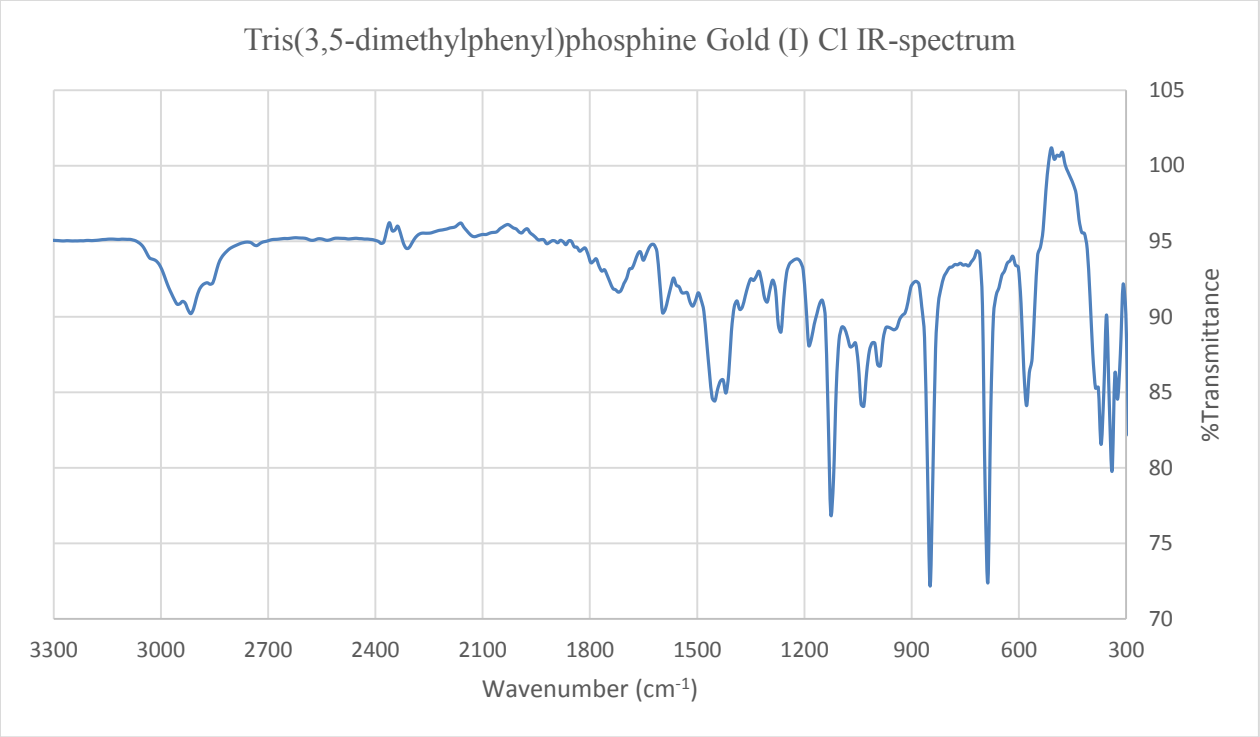

Figure 3.4. IR spectrum for $AuP(C_8H_9)_3Cl$.

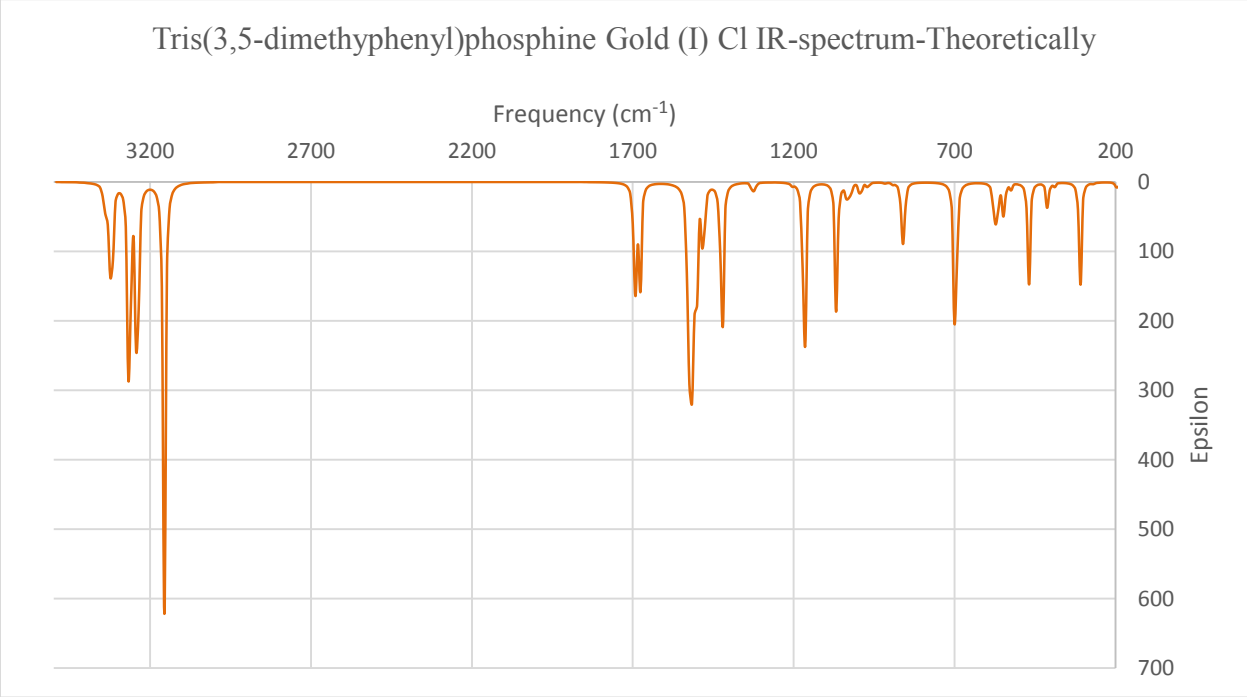

Figure 3.5. IR spectrum for $AuP(C_8H_9)_3Cl$ calculated theoretically using Gaussian 09.

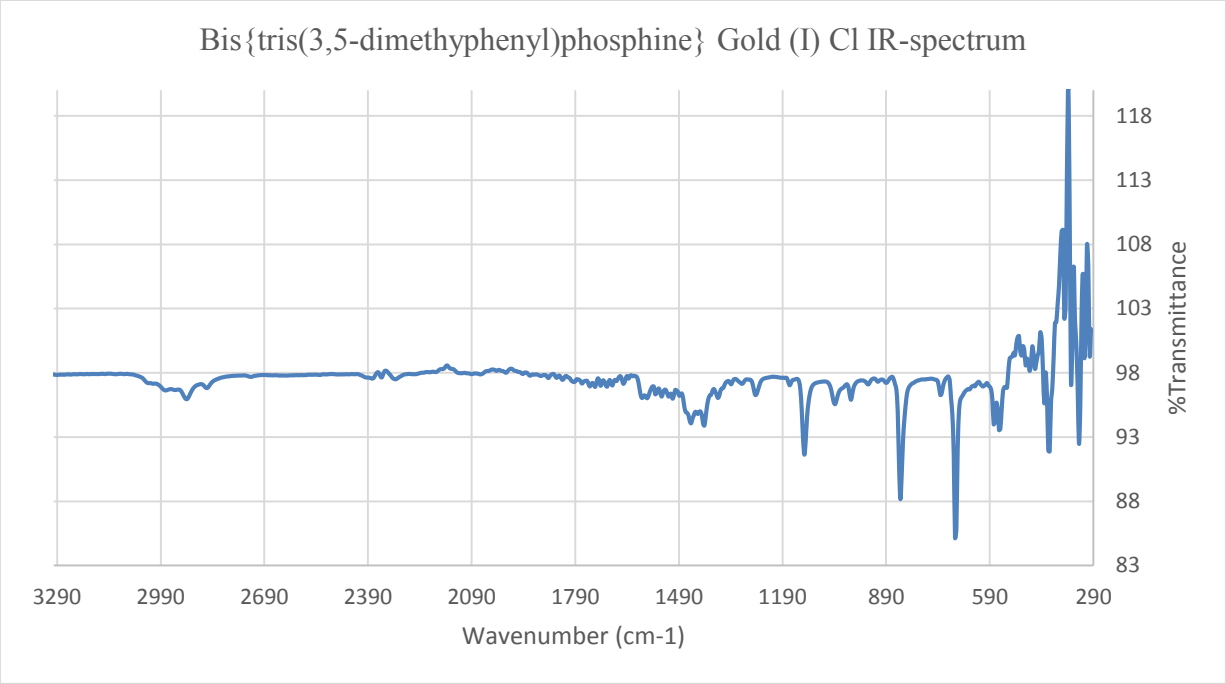

Figure 3.6. IR spectrum for $Au(P(C_8H_9)_3)_2Cl$.

Table 3.6

Nuclear site group theoretical analysis for $AuP(C_8H_9)_3Cl$ complex

NUCLEAR SITE GROUP THEORETICAL ANALYSIS ($C_{24}H_{27}$ Au Cl P)					
ATOMS	Au	P	Cl	C_a	C_b
SITES (16A)	C_1	C_1	C_1	C_1	C_3
VIBRATIONAL (16B)	3A + 3E	3A + 3E	3A + 3E	3A + 3E	A + E
TOTAL CONTRIBUTION = 13A + 13E					
ACOUSTIC MODES (16E) = A + E					
OPTICAL MODES = 12A + 12E					
IR ACTIVE (16E) = 12A + 12E					
RAMAN ACTIVE (16E) = 12A + 12E					

3.2.3 Nuclear Magnetic Resonance. The ^{1}H NMR spectral data for the monocoordinated TDMPP gold complex is shown in Figure 3.8. The spectrum shows peaks at 2.3 (18H), 7.1 (6H), 7.3 (3H) ppm. The spectrum of the dicoordinated TDMPP gold (I) complex is shown in Figures 3.9. The spectrum of this complex displays peaks at 2.2 (18H), 7.1 (3H), 7.0 (6H) ppm. The ^{1}H NMR spectral data for the free ligand TDMPP is shown in Figure 3.7 with peaks at 2.2(18H), 7.0(6H), 7.2 (3H)ppm. The $^{31}P\{^{1}H\}$ NMR spectral data for the ligand, **2** and **3** is found in Figures 3.10, 3.11 and 3.12 showing peaks at 33, 45.8 and 60.0ppm respectively. Theoretically calculated proton NMR using Gaussian 09 is also shown in Figures 3.13 and 3.14.

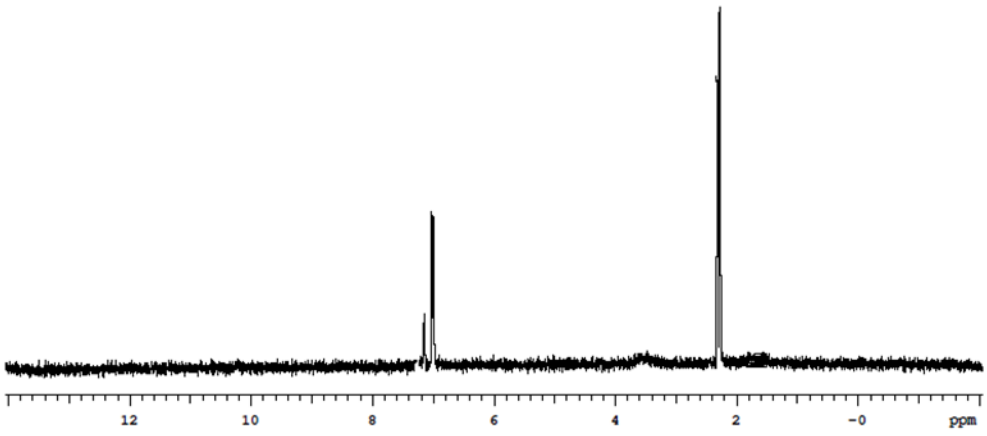

Figure 3.7. ^{1}H NMR spectrum of $P(C_8H_9)_3$.

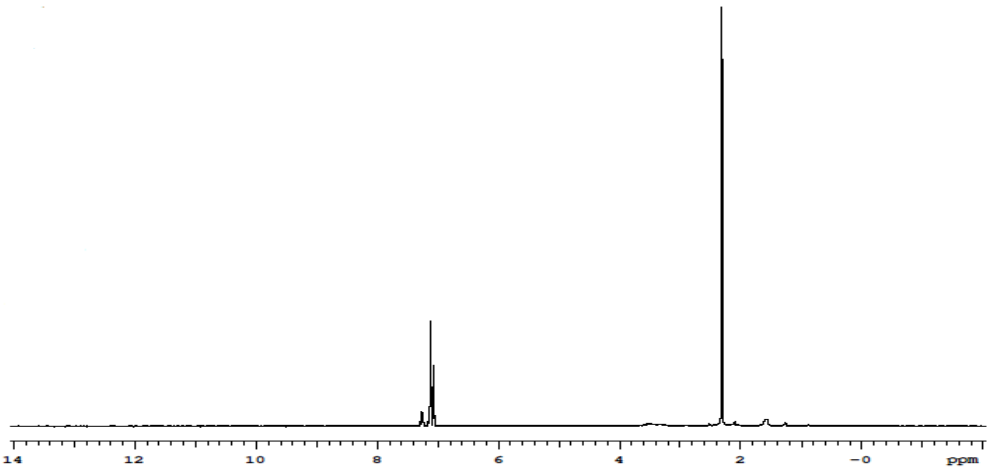

Figure 3.8. ^{1}H NMR spectrum of $AuP(C_8H_9)_3Cl$.

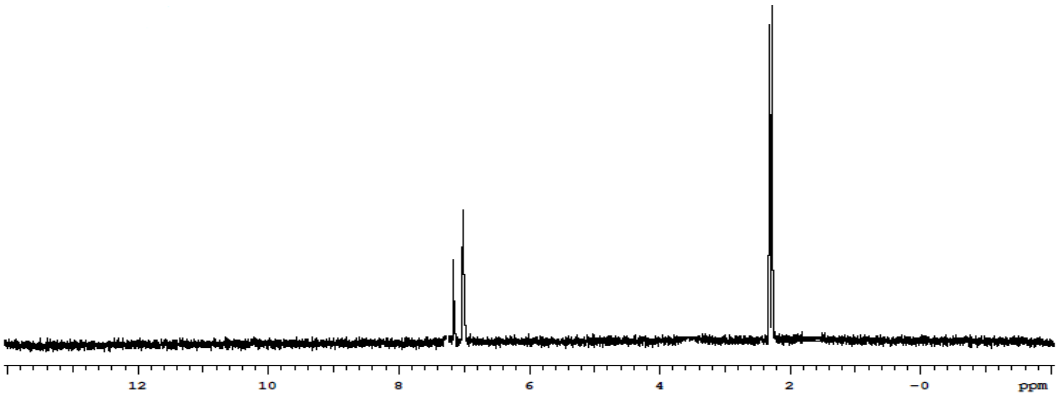

Figure 3.9. ^{1}H NMR spectrum of $Au(P(C_8H_9)_3)_2Cl$.

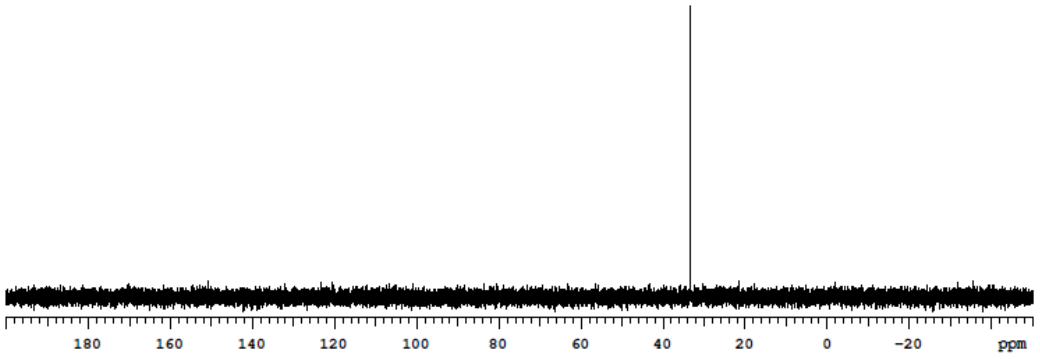

Figure 3.10. $^{31}P\{^{1}H\}$ NMR spectrum of $P(C_8H_9)_3$.

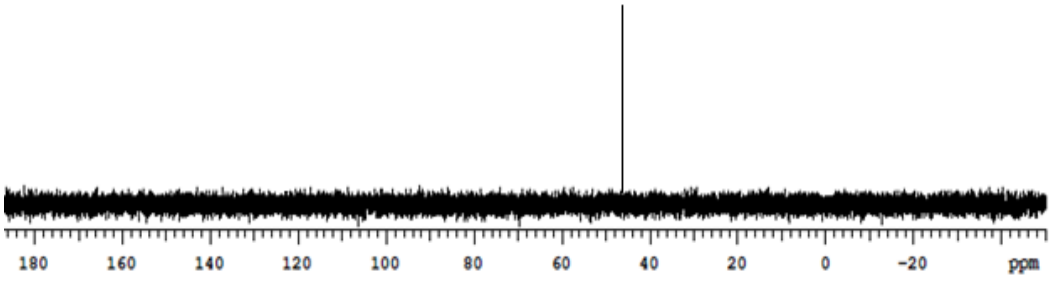

Figure 3.11. $^{31}P\{^{1}H\}$ NMR spectrum of $AuP(C_8H_9)_3Cl$.

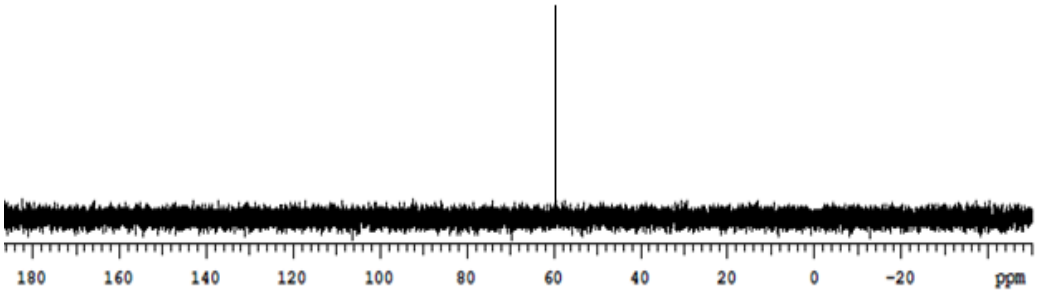

Figure 3.12. $^{31}P\{^{1}H\}$ NMR spectrum of $Au(P(C_8H_9)_3)_2Cl$.

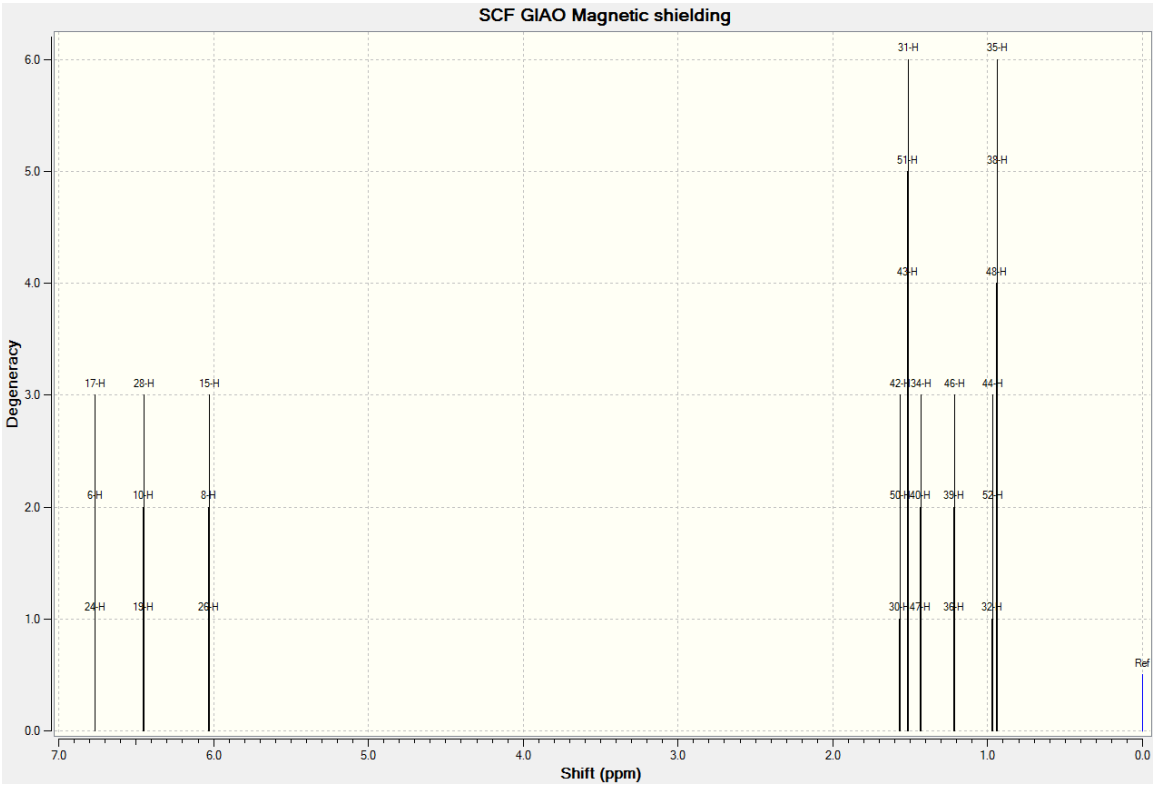

Figure 3.13. ^{1}H NMR spectrum of $P(C_8H_9)_3$ obtained from theoretical calculation using Gaussian 09 program.

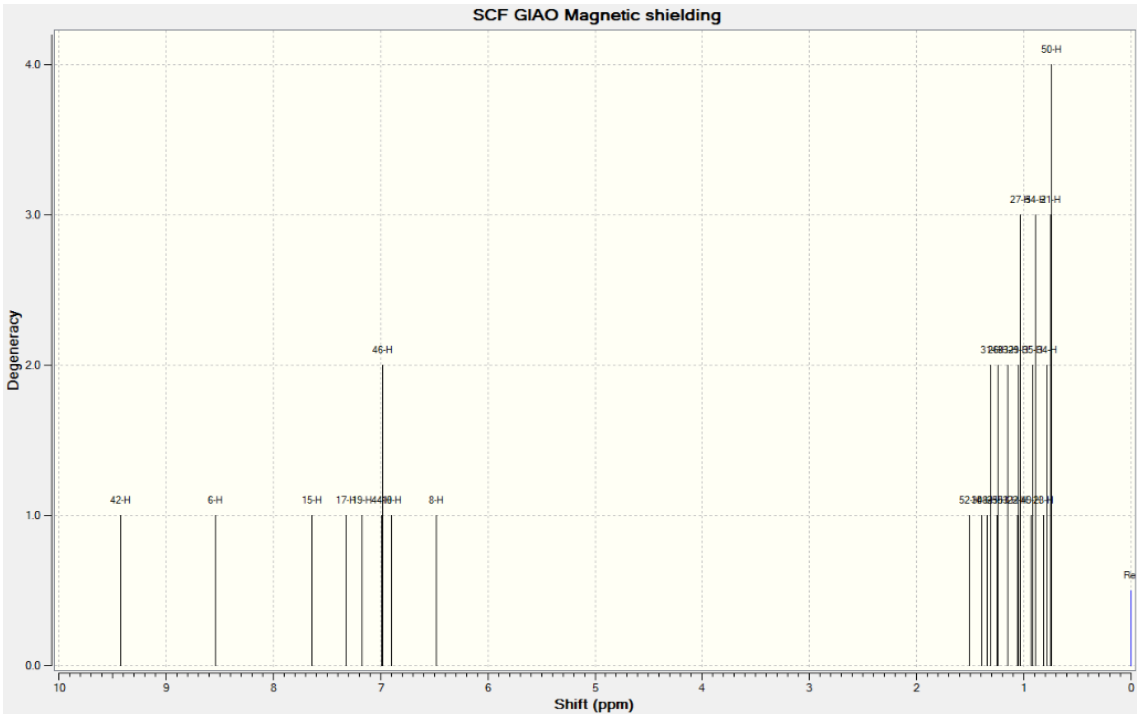

Figure 3.14. ^{1}H NMR spectrum of $AuP(C_8H_9)_3Cl$ obtained from theoretical calculation using Gaussian 09 program.

3.2.4 UV-Vis Spectroscopy. All of the samples used for the UV-vis (absorption) experiment, were dissolved in spectroscopic grade acetonitrile (CH_3CN). The TDMPP ligand has a broad absorption band shown in Figure 3.15 that maximizes around 250 nm with a calculated molar absorptivity of 6.13 x 10^4 $M^{-1}cm^{-1}$. The absorption spectrum of **2** is shown in Figure 3.16. A broad absorption profile maximizes at about 250 nm with a calculated molar absorptivity value of 9.15 x 10^4 $M^{-1}cm^{-1}$. In Figure 3.17 is shown the absorption profile for **3** which has a band maximum of about 250 nm with a calculated molar absorptivity of 1.51 x 10^5 $M^{-1}cm^{-1}$. The theoretically calculated spectrum using the DFT method, provides the spectrum shown in Figures 3.18 and 3.19 with a broad absorption spectrum at 250 nm and 260 for **2** and the TDMPP ligand, respectively.

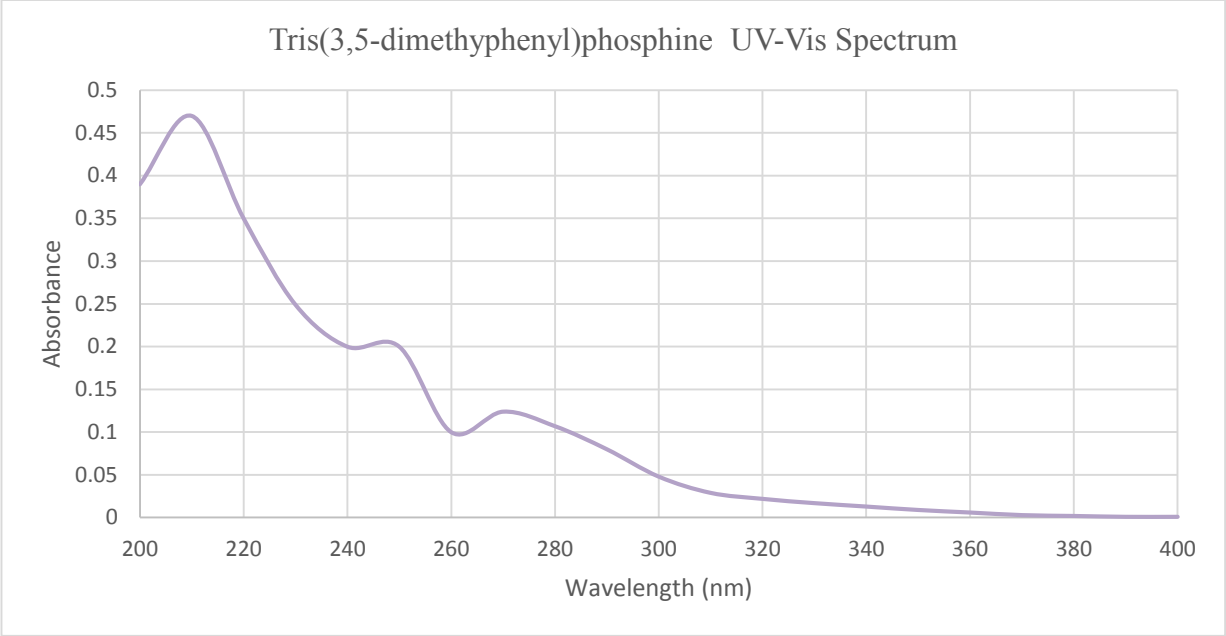

Figure 3.15. UV-vis spectrum of $P(C_8H_9)_3$.

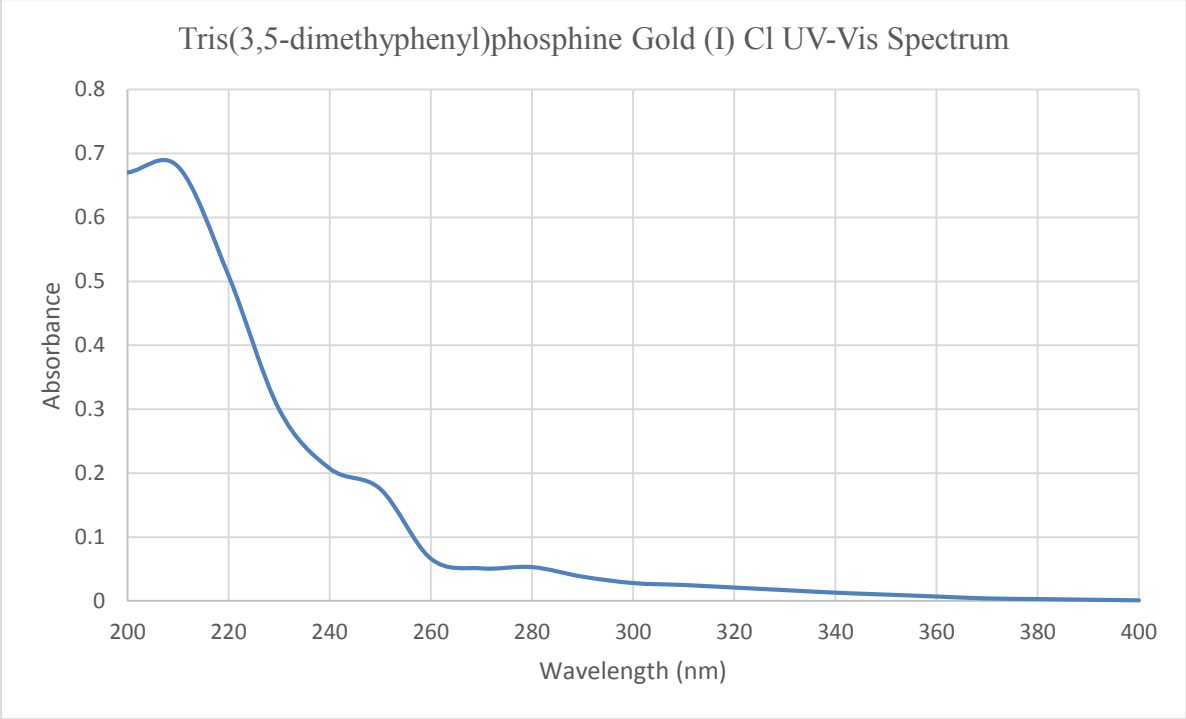

Figure 3.16. UV-vis spectrum of $AuP(C_8H_9)_3Cl$.

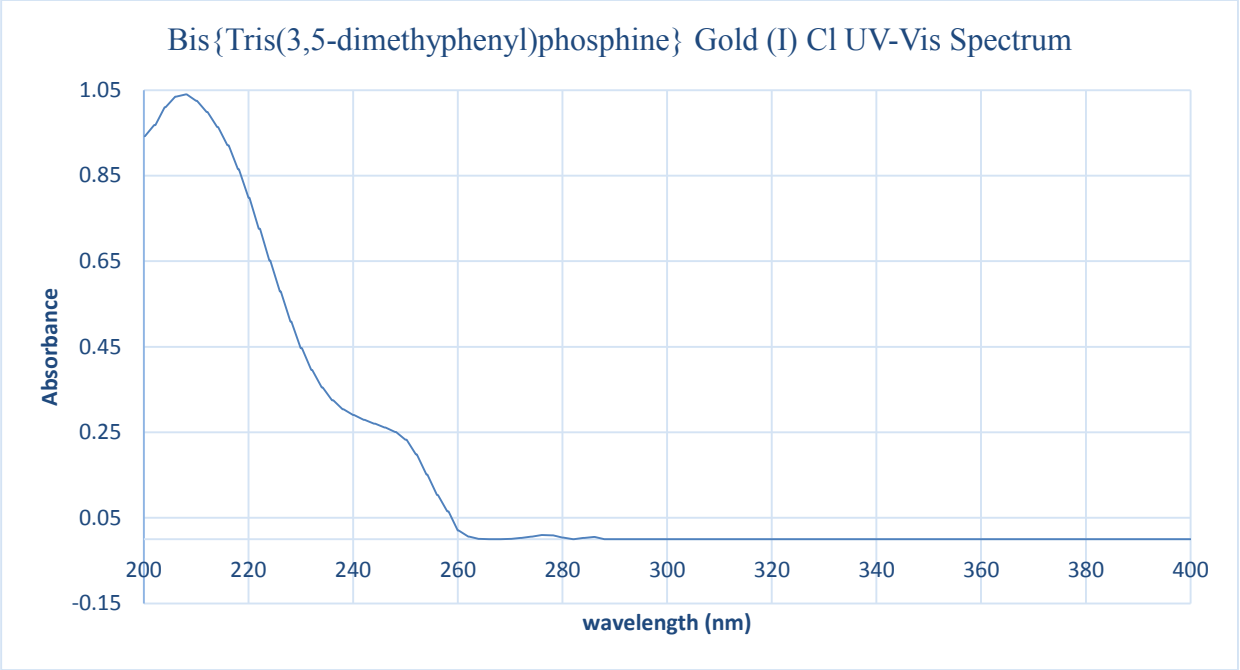

Figure 3.17. UV-Vis spectrum of $Au(P(C_8H_9)_3)_2Cl$.

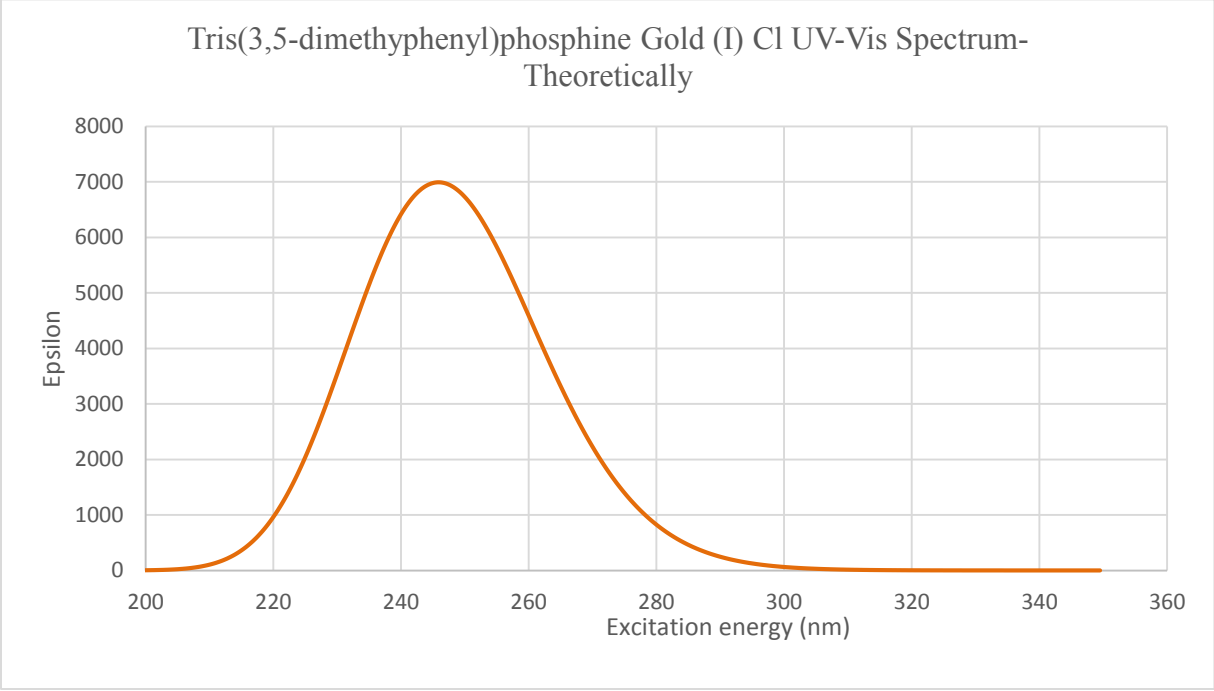

Figure 3.18. Calculated UV-Vis spectrum of $AuP(C_8H_9)_3Cl$ using Gaussian 09 program.

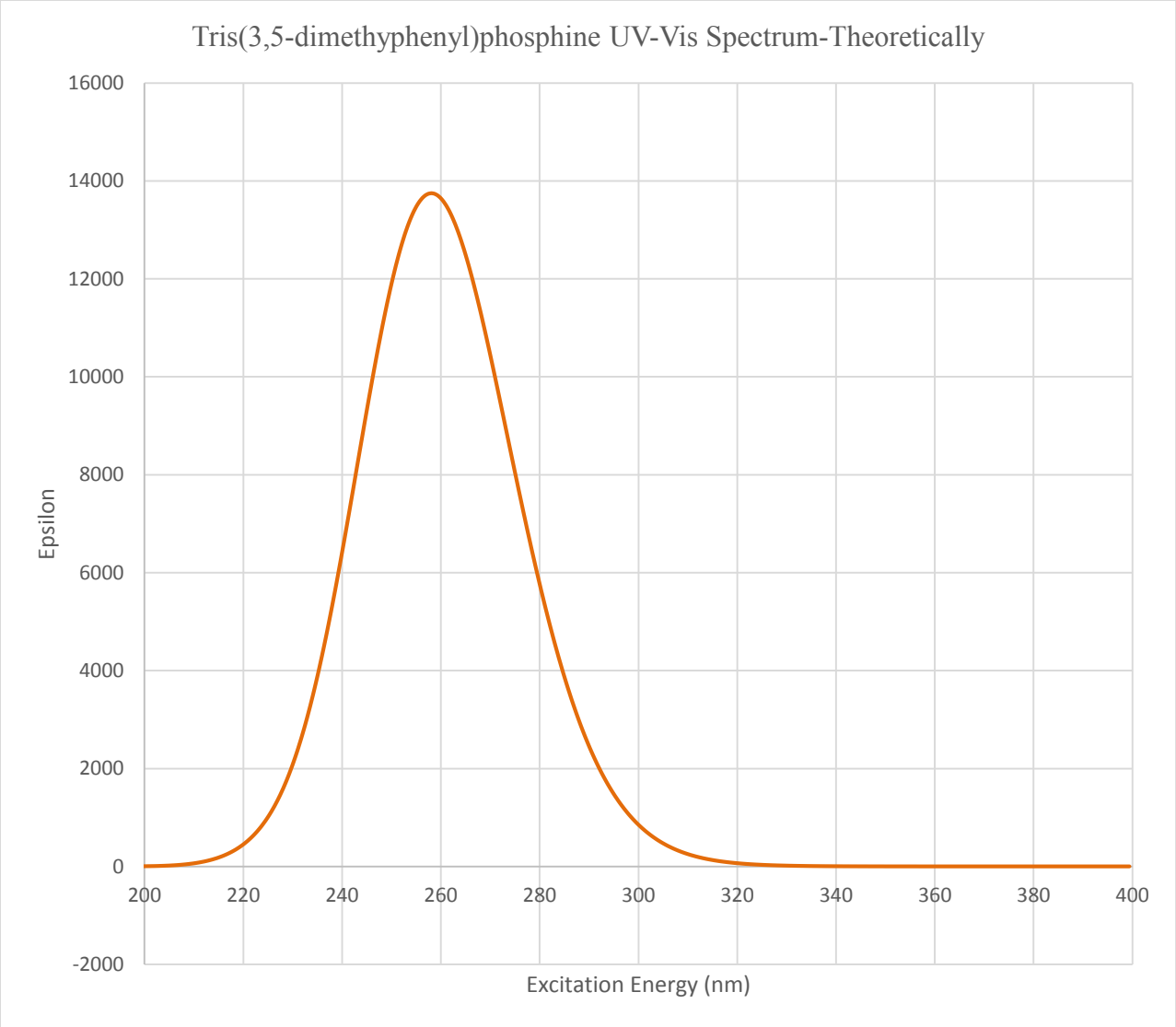

Figure 3.19. Calculated UV-Vis spectrum of $P(C_8H_9)_3$ using Gaussian 09 program.

Table 3.7

TD-DFT generated ground-state to excited-state MO transitions for ***2***

TRANSITIONS	CORRESPONDING ORBITALS	% CONTRIBUTION
X	93 → 102	17.39
	100 → 102	82.61
Y	97 → 105	8.25
	99 → 104	10.45
	101 → 102	38.46
	100 → 103	10.61
	101 → 103	10.83
	101 → 104	13.46
	101 → 107	7.94
Z	96 → 105	8.25
	99 → 102	38.43
	99 → 103	10.56
	100 → 104	10.54
	101 → 103	13.46
	101 → 104	10.83
	101 → 106	7.92

Table 3.8

Theoretical results showing the contributions of X, Y, and Z transitions of ***2***

Excitation	λcalc. (nm)	%Contribution to the transition		Transition Energy (cm^{-1})	λexp. (nm)
X	250.51				250
Major contribution:					
	100→ 102	82.61		39,920	
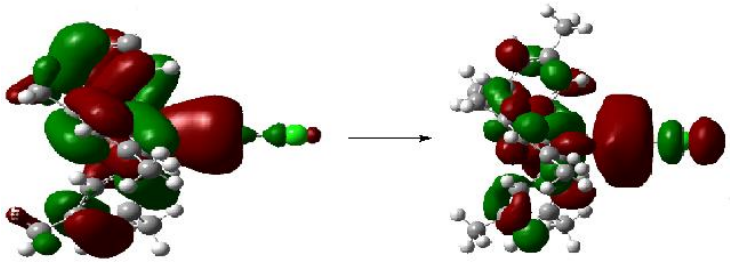					
Y	247.40				
Major contribution:					
	101→ 102	38.46		40,421	
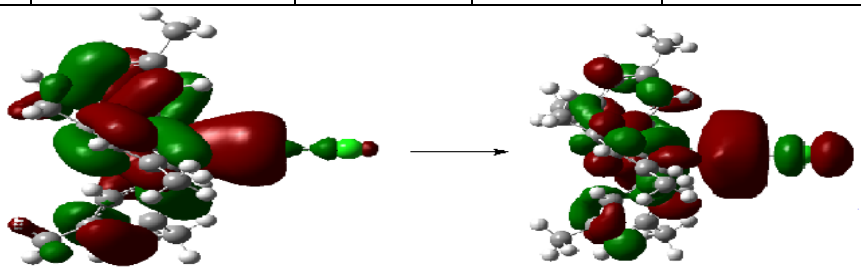					
Z	247.38				
Major contribution:					
	99 → 102	38.43		40,424	
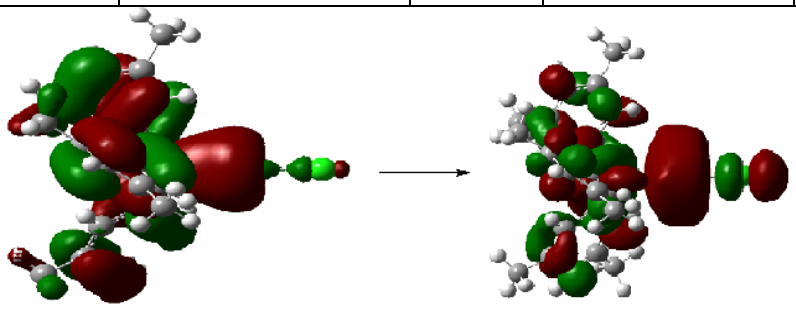					

3.2.5 Luminescence. The excitation spectra of the TDMPP ligand collected at room temperature are shown in Figures 3.20 to 3.22. The excitation spectra for the $AuP(C_8H_9)_3Cl$ at room temperature are shown in Figures 3.23, 3.24, 3.25 and 3.26 covering the spectral region from 297 – 534 nm, 280 - 436 nm, 283 - 507 nm, and 291 - 522 nm. All of the spectra were collected by monitoring the emission band of 554, 473, 527 and 542 nm, respectively. The spectrum shows vibronic components at 337, 387, 457, 467,507 nm monitored at 554 nm; 295, 357, 390, 403 nm monitored at 473; 323, 443 nm monitored at 527; and 336, 391, 461 monitored at an emission of 542.

The excitation spectrum collected in liquid nitrogen temperature is shown in Figures 3.27, 3.28, 3.29 and 3.30 covering the spectral region of 280 - 440 nm, 280 - 417 nm, 280 -451 nm, 280 -492 nm when monitored at an emission band of 450, 437, 471 and 512, respectively. The spectrum monitored at 450 nm shows vibronic components at 287, 330, 385 nm, while the one monitored at 471 consists of vibronic coupling at 325, 340, 380 nm. monitored at 437; 325, 340, 380 nm monitored; and 325, 340, 380, 435 nm monitored at an emission of 512. The emission spectrum for the ligand collected at room temperature is shown in Figures 3.31, 3.32, 3.33 and 3.34. The emission spectrum for both room and liquid nitrogen temperatures for **2** can be found in Figure 3.35, 3.36, 3.37, 3.38 and 3.39, 3.40, 3.41 respectively.

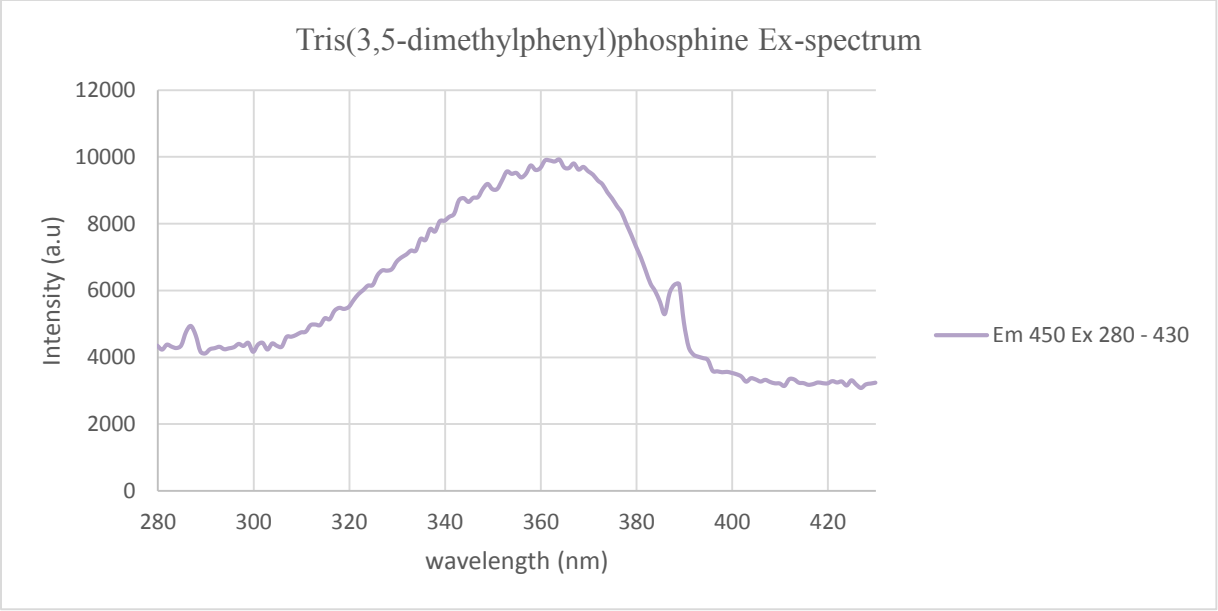

Figure 3.20. Excitation spectrum of TDMPP ligand collected at room temperature by monitoring the emission at 450 nm.

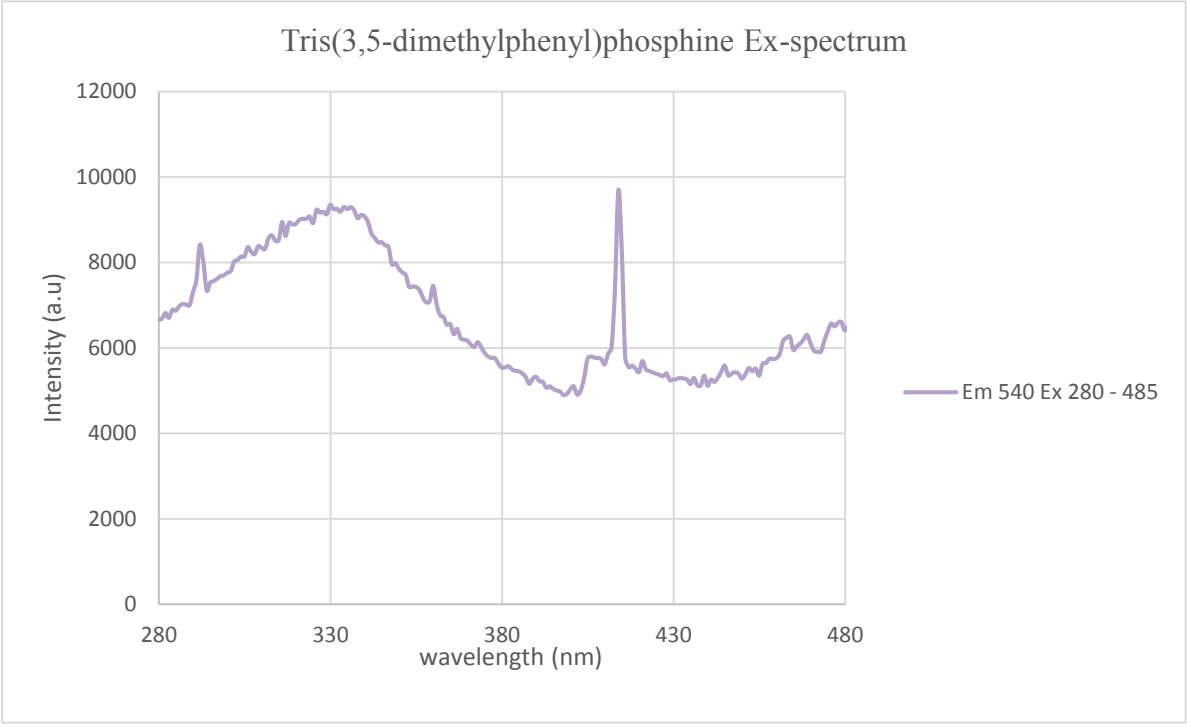

Figure 3.21. Excitation spectrum of TDMPP ligand collected at room temperature by monitoring the emission at 540 nm.

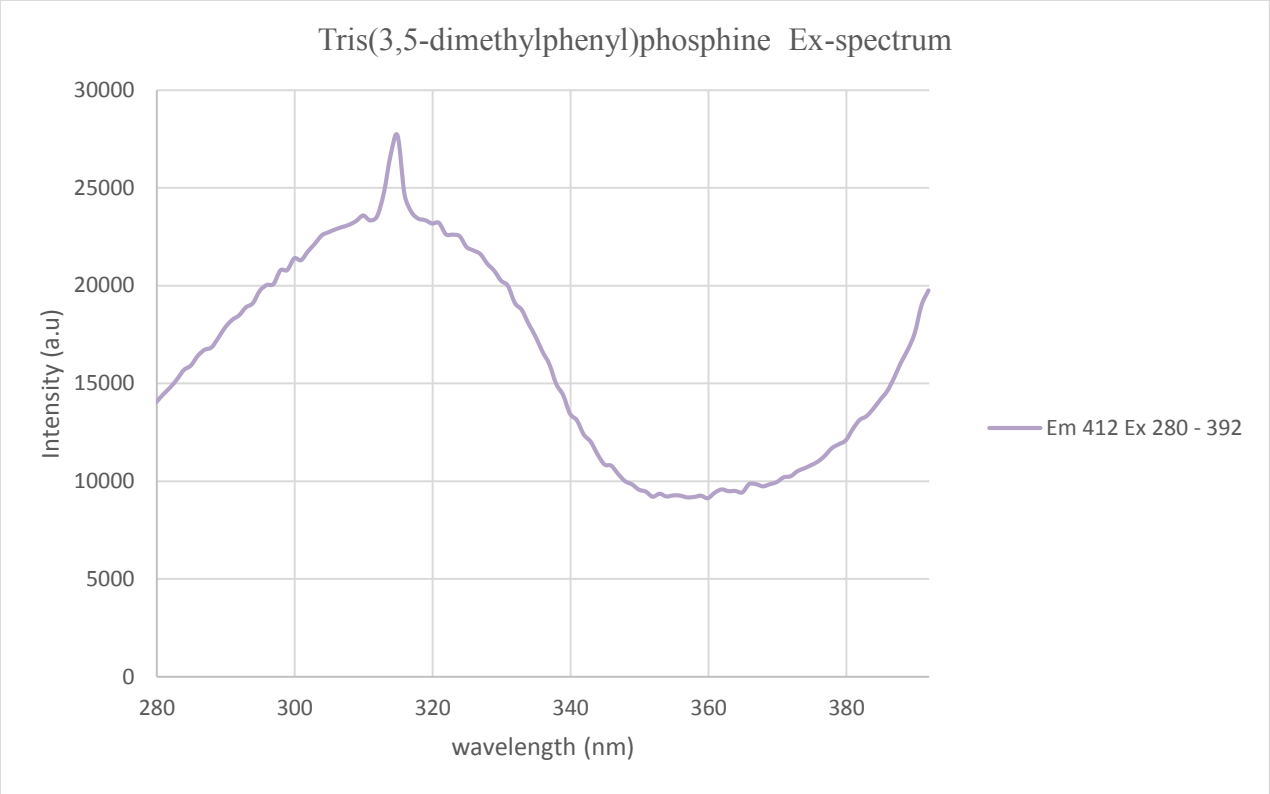

Figure 3.22. Excitation spectrum of TDMPP ligand collected at room temperature by monitoring the emission at 412 nm.

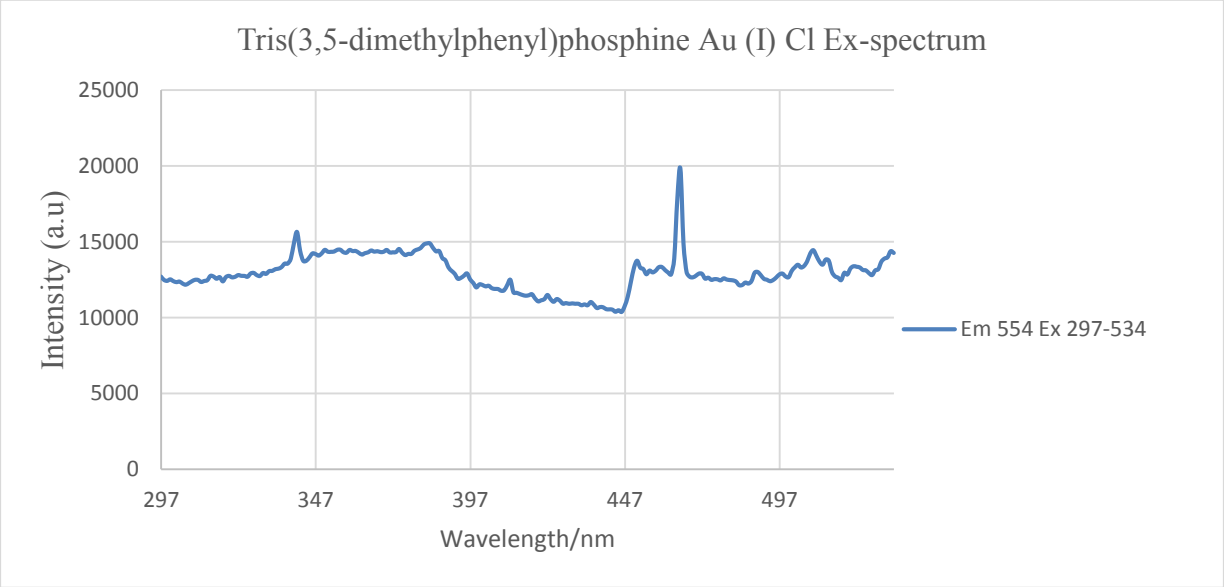

Figure 3.23. Excitation spectrum of $AuP(C_8H_9)_3Cl$ collected at room temperature by monitoring the emission at 554 nm.

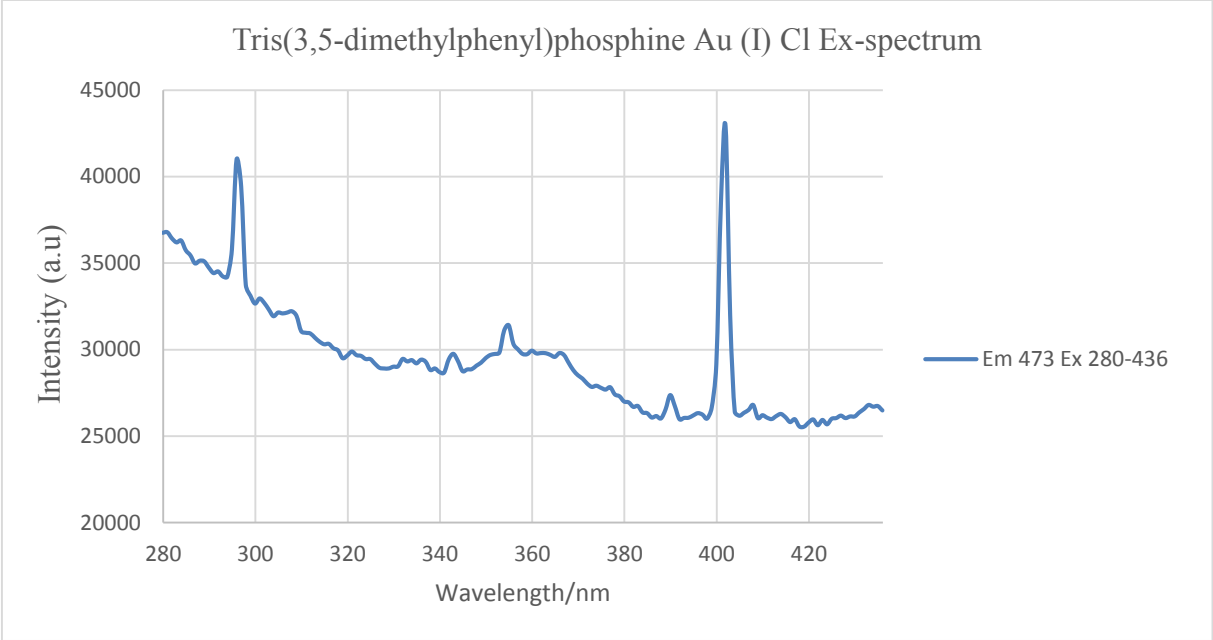

Figure 3.24. Excitation spectrum of $AuP(C_8H_9)_3Cl$ collected at room temperature by monitoring the emission at 473 nm.

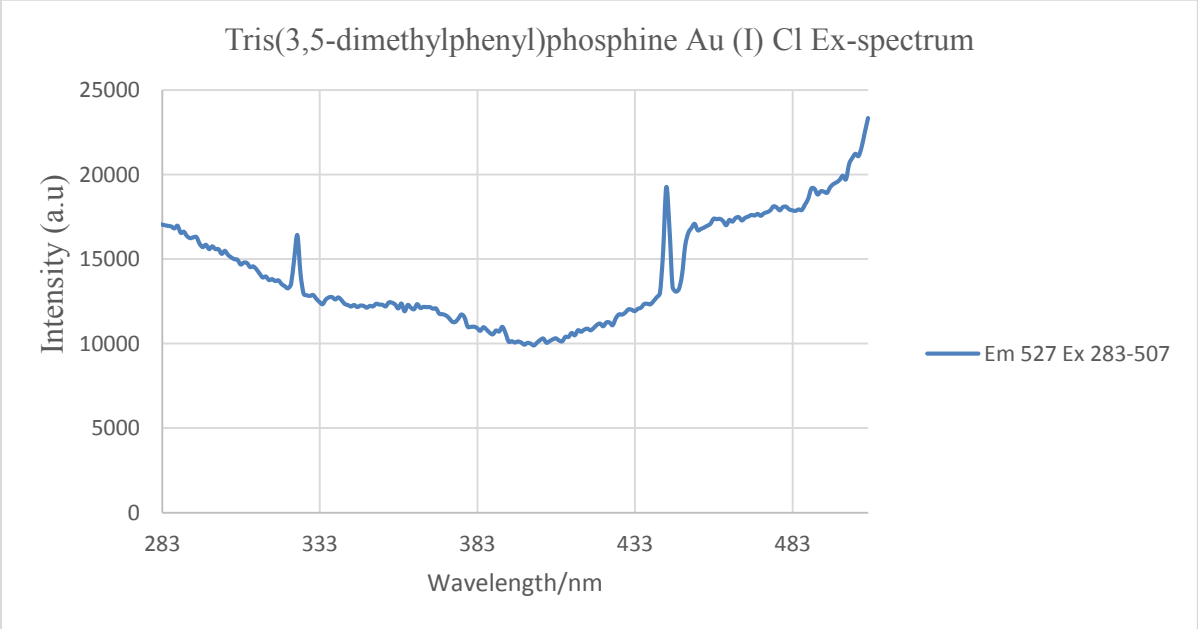

Figure 3.25. Excitation spectrum of $AuP(C_8H_9)_3Cl$ collected at room temperature by monitoring the emission at 527 nm.

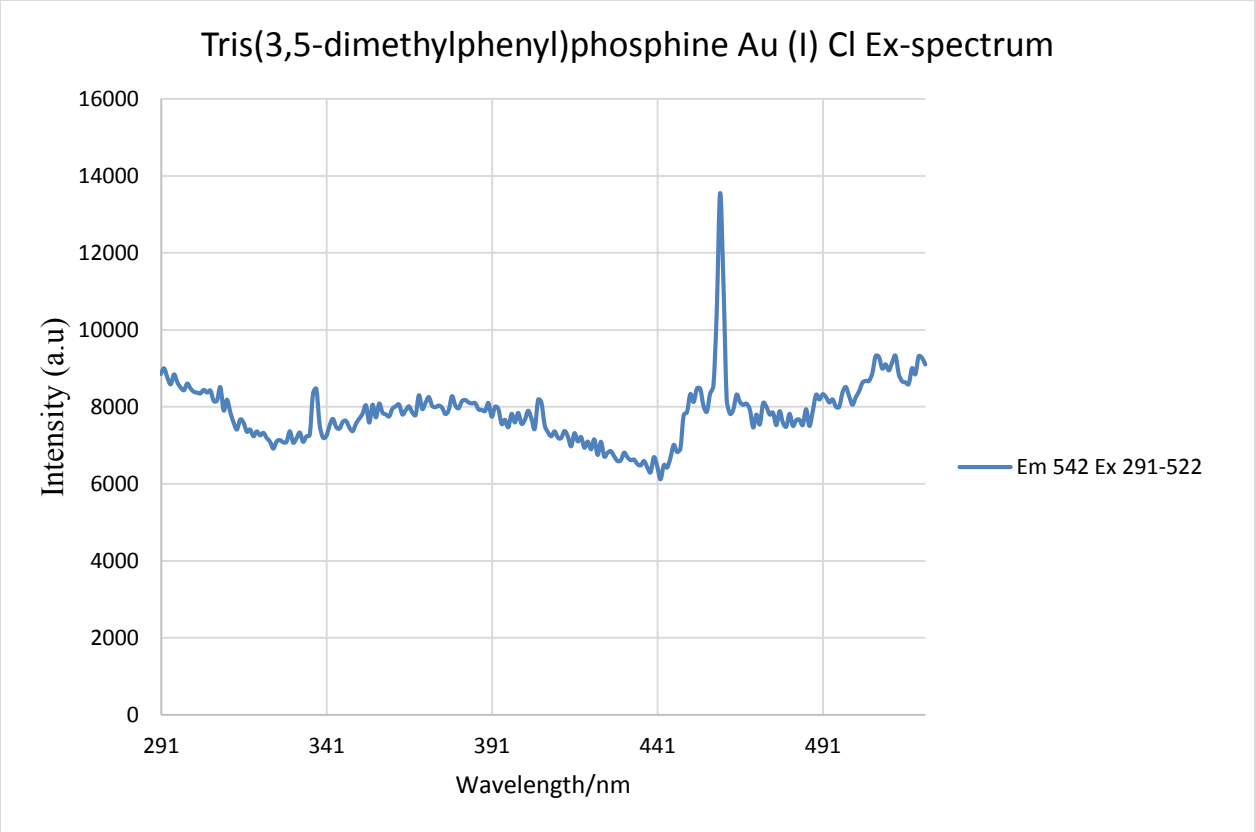

Figure 3.26. Excitation spectrum of $AuP(C_8H_9)_3Cl$ collected at room temperature by monitoring the emission at 542 nm.

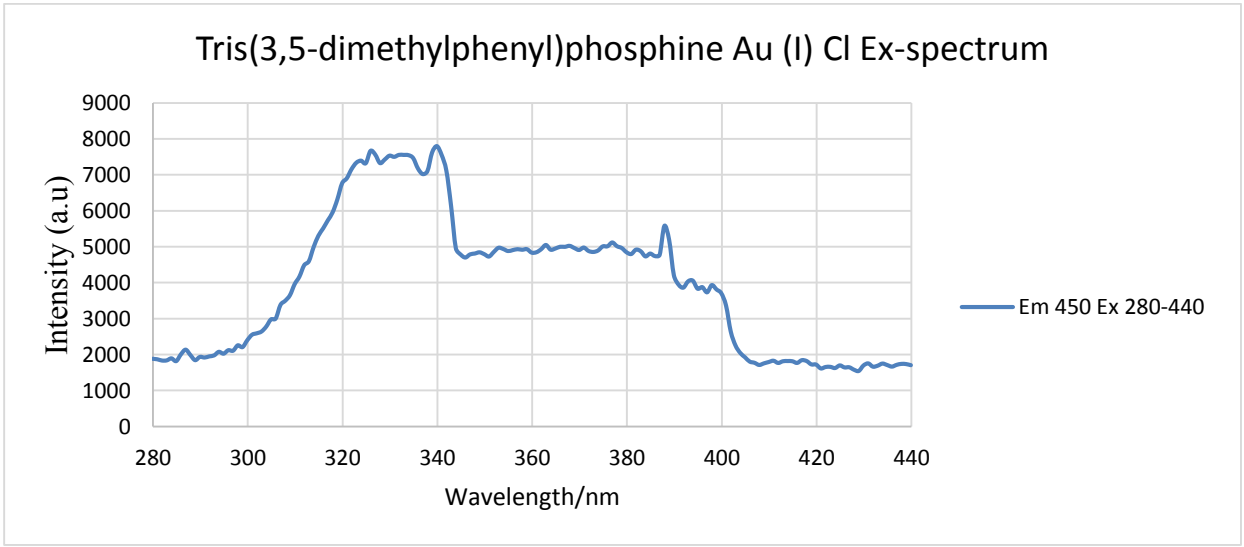

Figure 3.27. Excitation spectrum of $AuP(C_8H_9)_3Cl$ collected in liquid nitrogen by monitoring the emission at 450 nm.

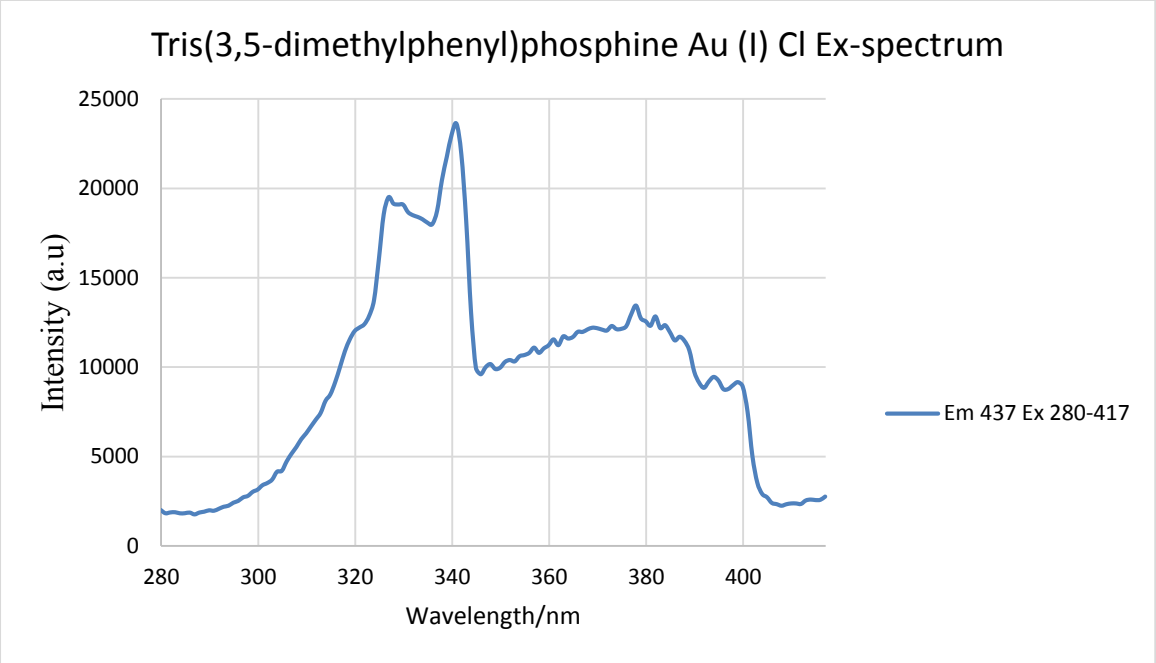

Figure 3.28. Excitation spectrum of $AuP(C_8H_9)_3Cl$ collected at liquid nitrogen temperature by monitoring the emission at 437 nm.

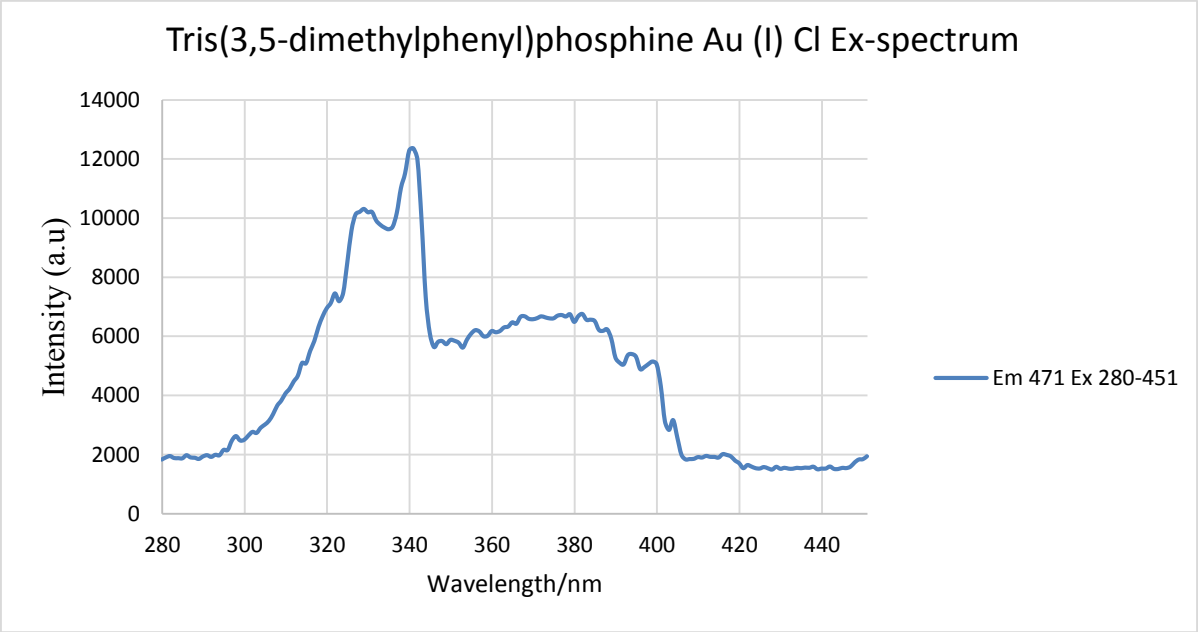

Figure 3.29. Excitation spectrum of $AuP(C_8H_9)_3Cl$ collected in liquid nitrogen by monitoring the emission at 471 nm.

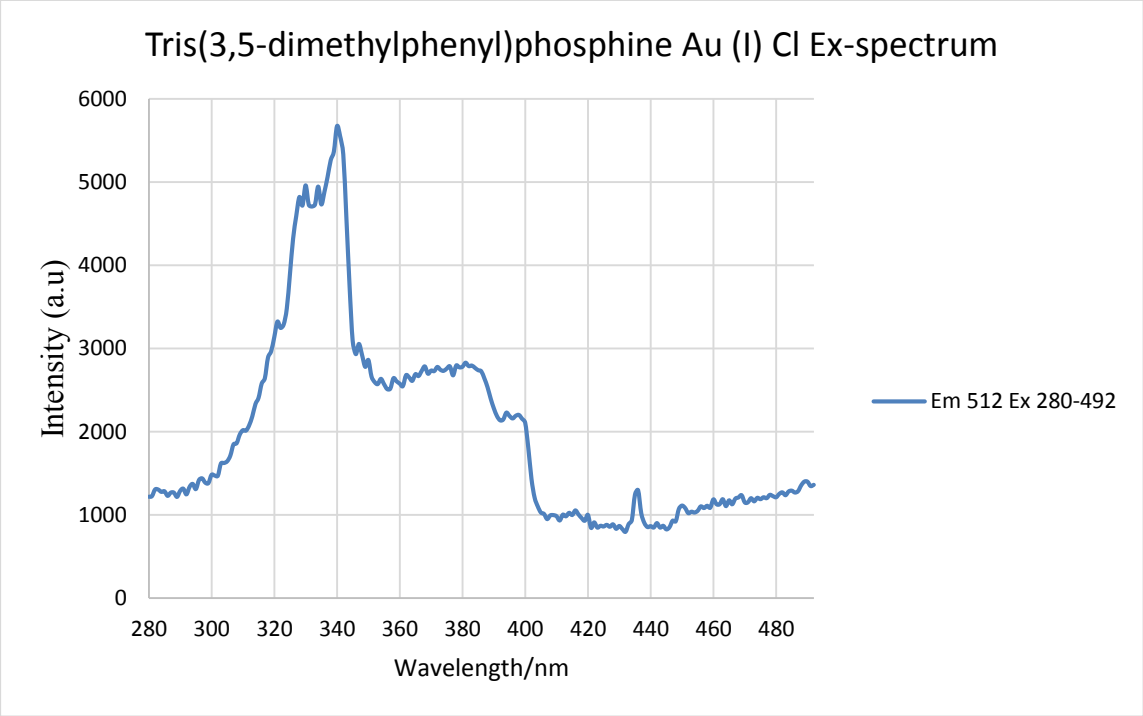

Figure 3.30. Excitation spectrum of $AuP(C_8H_9)_3Cl$ collected at liquid nitrogen temperature by monitoring the emission at 512 nm.

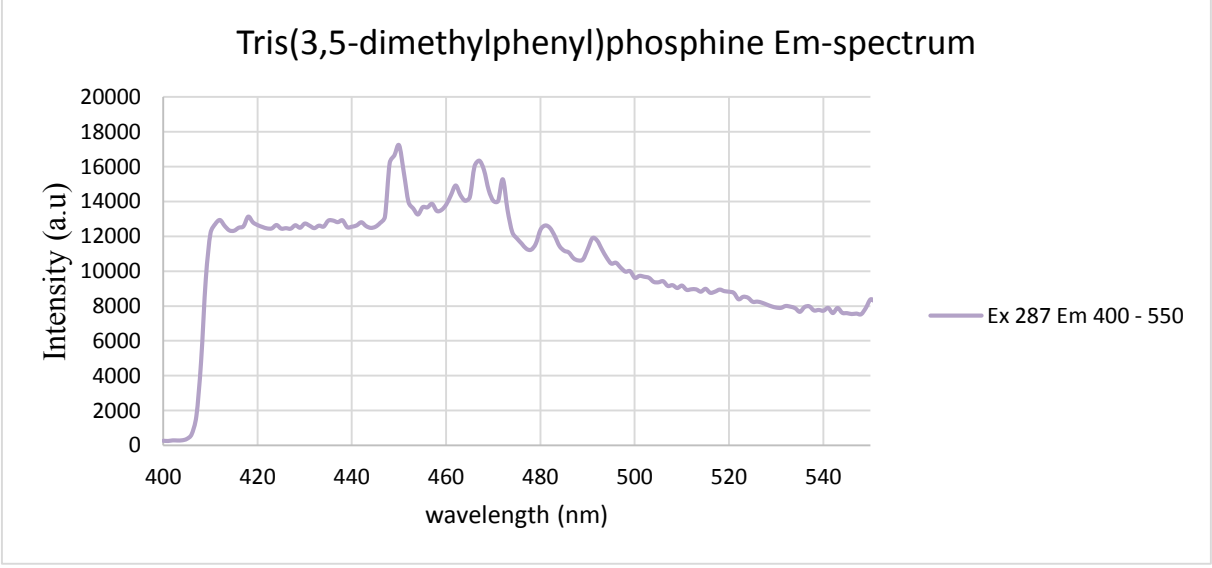

Figure 3.31. Emission spectrum of TDMPP ligand collected at room temperature upon excitation at 287 nm.

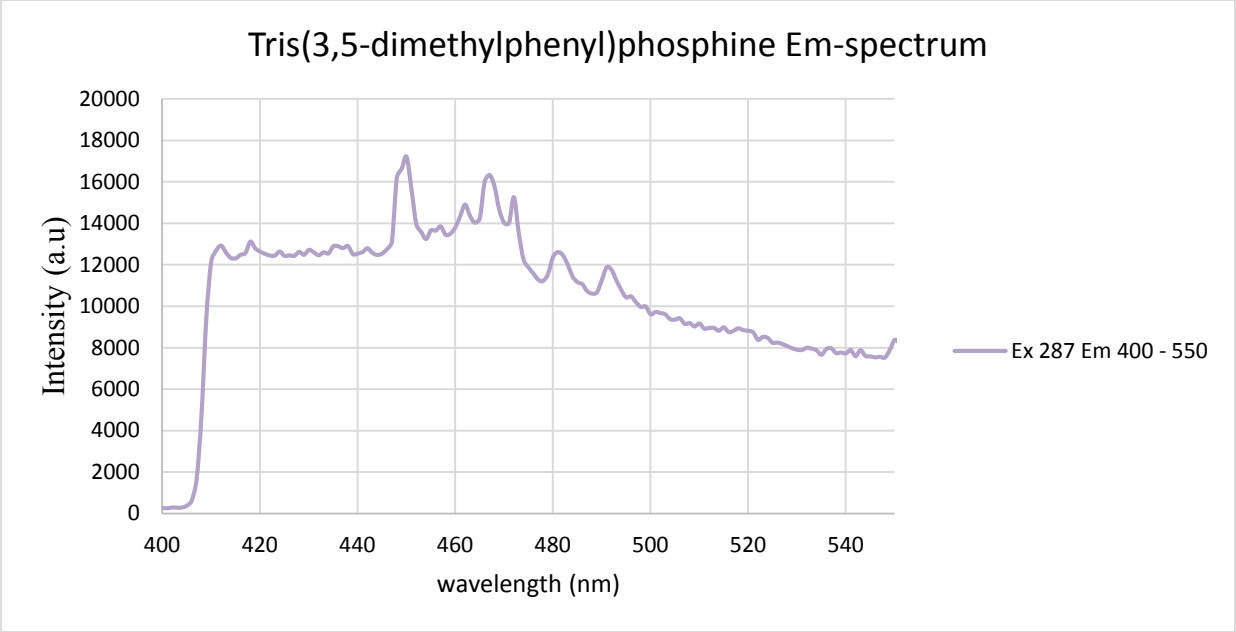

Figure 3.32. Emission spectrum of TDMPP ligand collected at room temperature upon excitation at 287 nm.

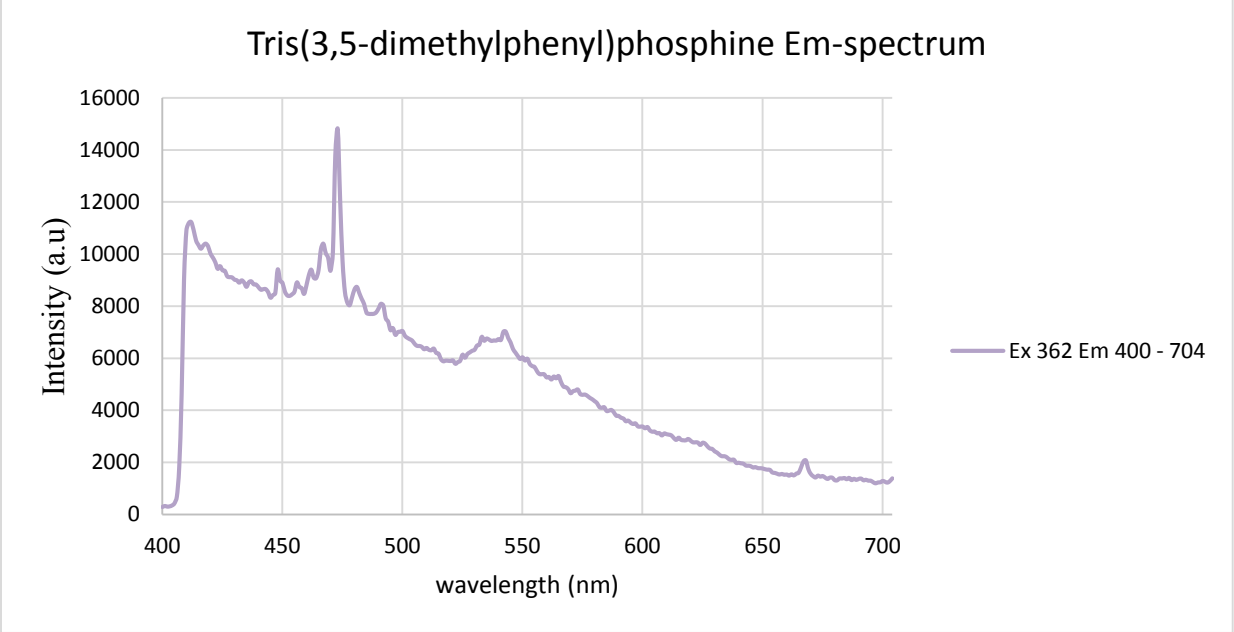

Figure 3.33. Emission spectrum of TDMPP ligand collected at room temperature upon excitation at 362 nm.

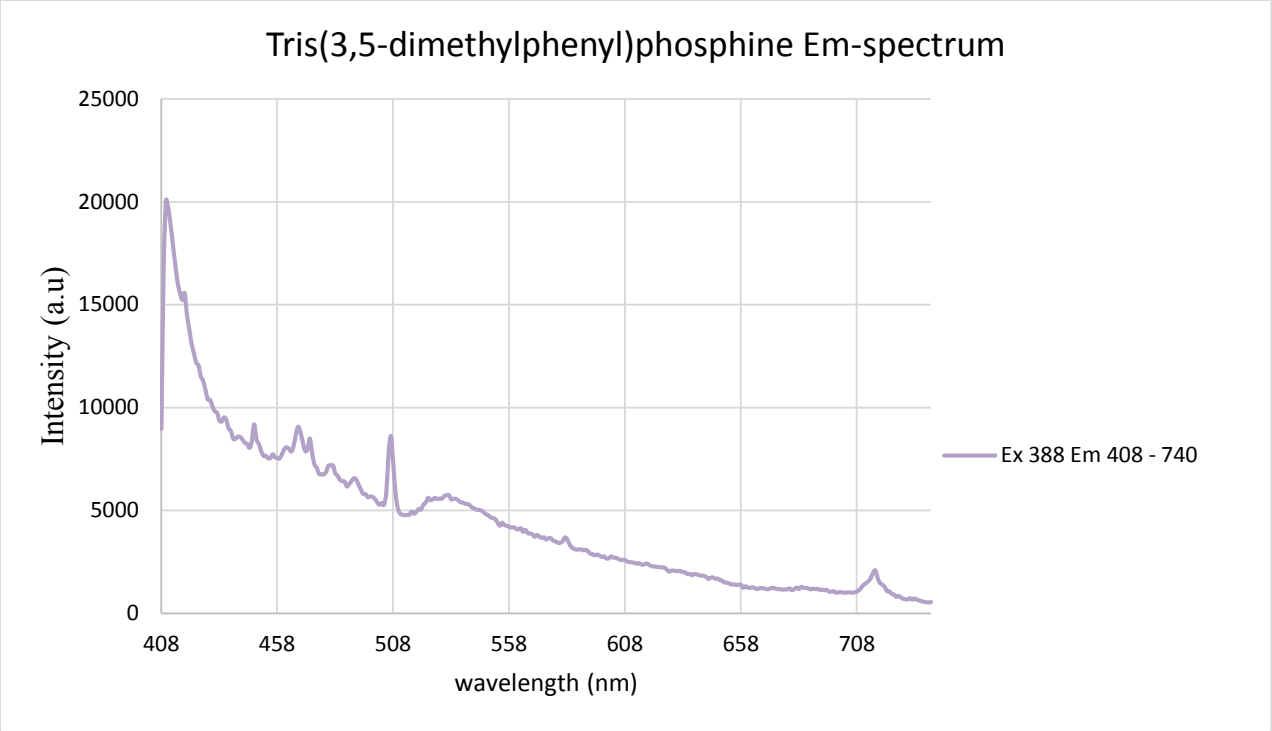

Figure 3.34. Emission spectrum of TDMPP ligand collected at room temperature upon excitation at 388 nm.

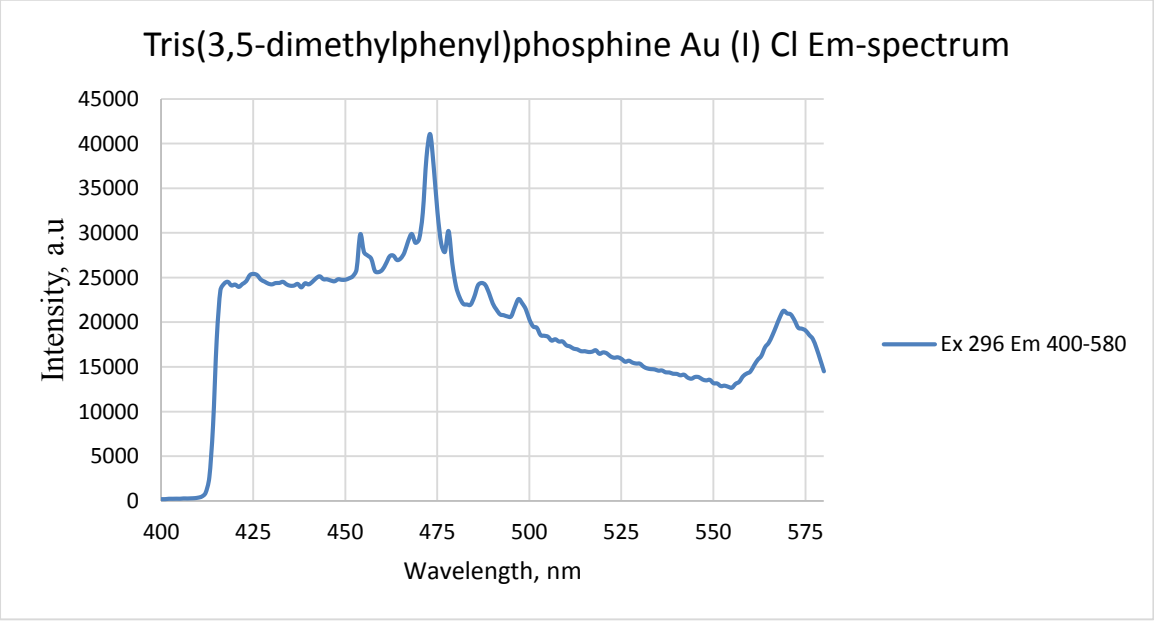

Figure 3.35. Emission spectrum of $AuP(C_8H_9)_3Cl$ collected at room temperature upon excitation at 296 nm.

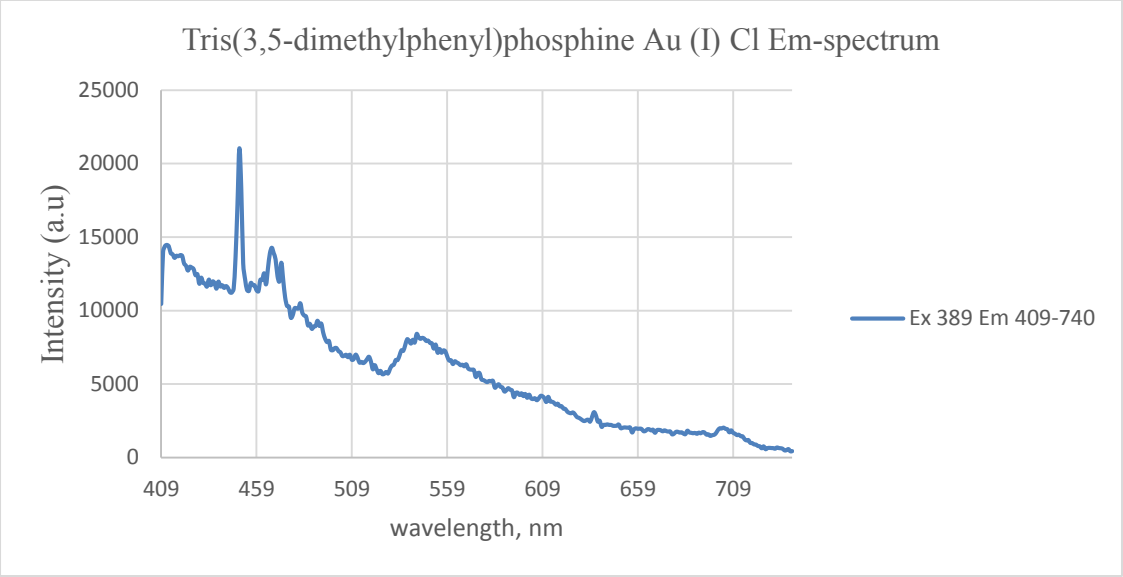

Figure 3.36. Emission spectrum of $AuP(C_8H_9)_3Cl$ collected at room temperature upon excitation at 389 nm.

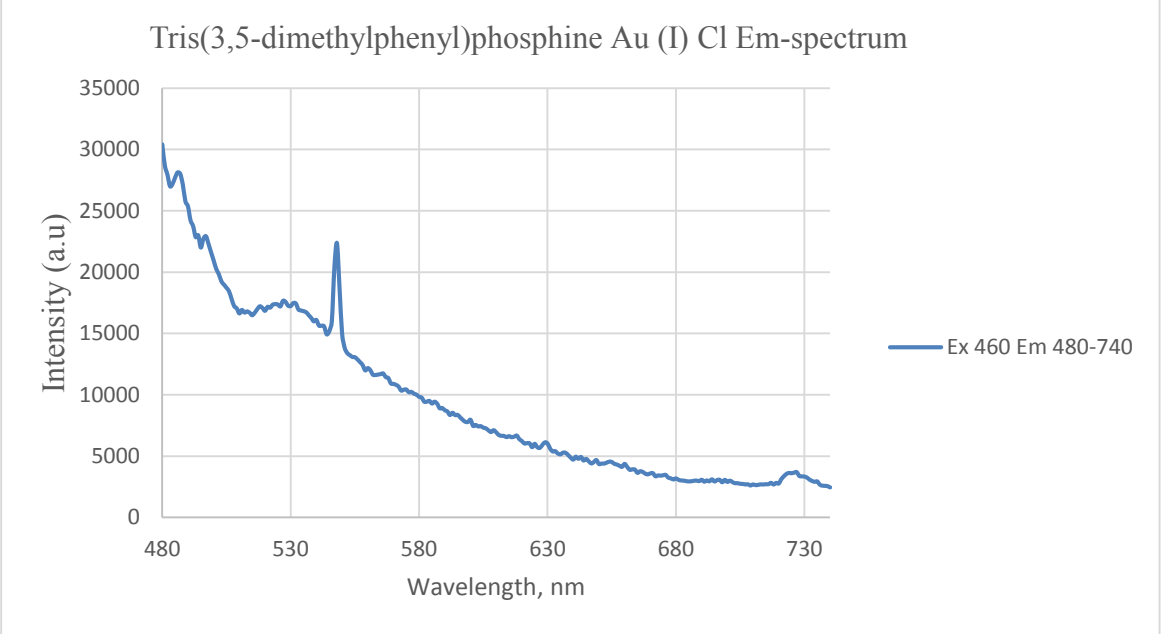

Figure 3.37. Emission spectrum of $AuP(C_8H_9)_3Cl$ collected at room temperature upon excitation at 460 nm.

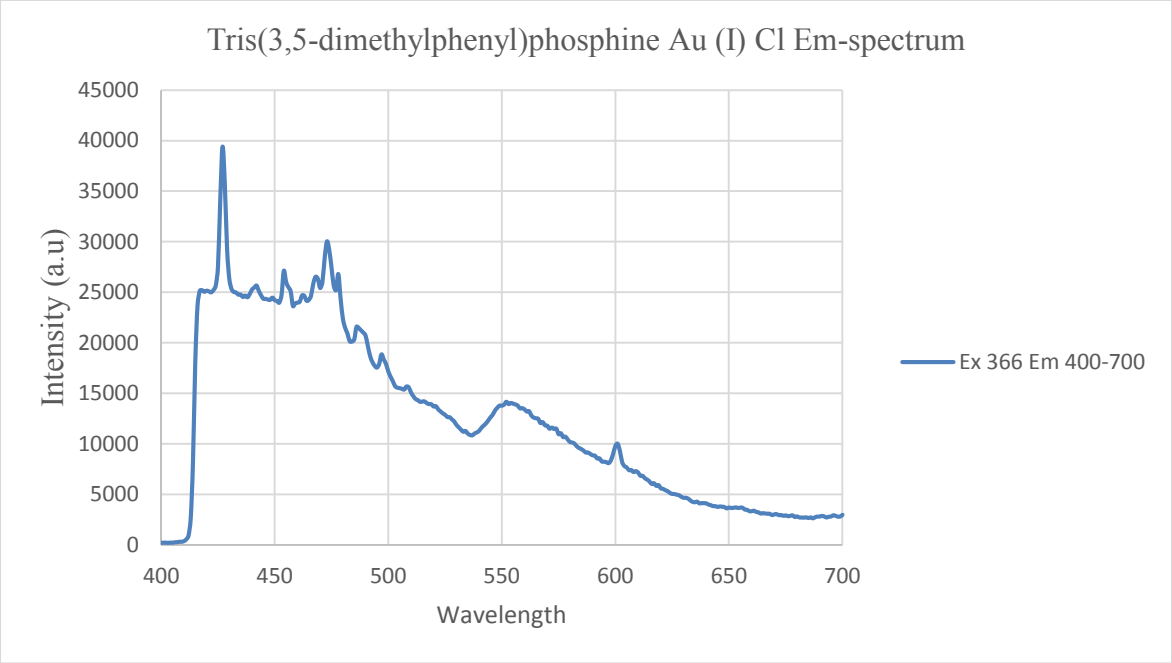

Figure 3.38. Emission spectrum of $AuP(C_8H_9)_3Cl$ collected at room temperature upon excitation at 366 nm.

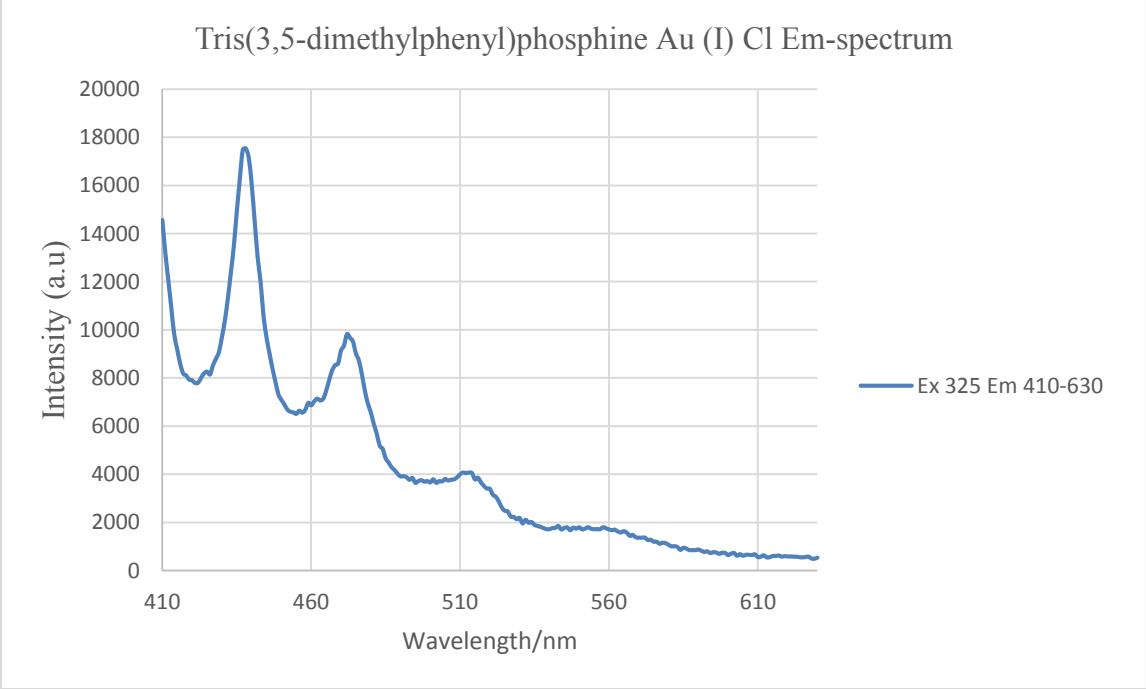

Figure 3.39. Emission spectrum of $AuP(C_8H_9)_3Cl$ collected in liquid nitrogen upon excitation at 325 nm.

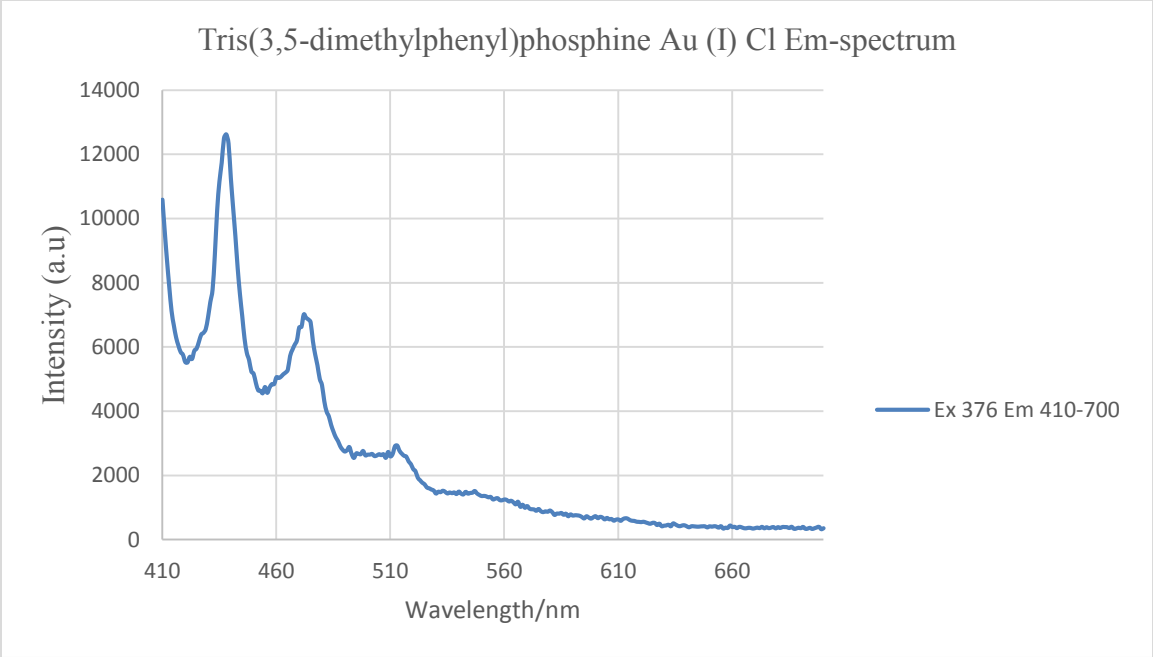

Figure 3.40. Emission spectrum of $AuP(C_8H_9)_3Cl$ collected in liquid nitrogen upon excitation at 376 nm.

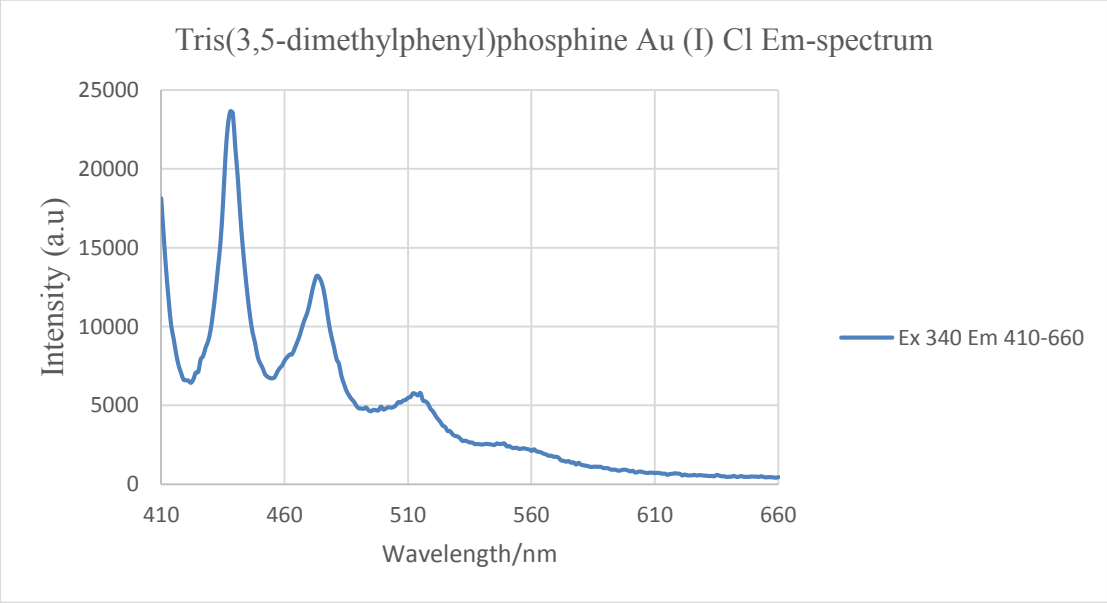

Figure 3.41. Emission spectrum of $AuP(C_8H_9)_3Cl$ collected in liquid nitrogen by exciting it at 340 nm.

Table 3.9

*Atomic contributions for the ground state molecular orbitals for compound **2***

ATOMIC CONTRIBUTIONS (%)				
Orbitals	Au	Ligand	P	C
104	7.02	92.98	9.42	83.56
103	14.74	85.26	7.40	77.86
102	9.75	90.25	8.81	81.44
HOMO-LUMO GAP				
101	28.75	71.25	21.31	49.94
100	12.20	87.80	2.05	94.75
99	12.70	87.30	1.91	85.39

Table 3.10

*Atomic orbital contributions in the ground state for compound **2***

ATOMIC ORBITAL CONTRIBUTIONS (%)				
Orbitals	Au	Ligand	P	C
104	4.88s, 2.14d	8.64s, 25.07px, 42.75py, 16.52pz	4.18px, 4.04py 1.20pz	8.64s, 20.89px 38.71py, 15.32pz
103	7.63s, 1.24px 2.68py, 3.19pz	13.23s, 8.55px 17.17py, 46.31pz	2.05s, 5.35pz	11.18s, 8.55px 17.17py, 40.96pz
102	3.01s, 2.50px 2.85py, 1.39pz	11.78s, 14.46px 27.86py, 36.15pz	1.39s, 2.25px 5.17py	10.39s, 12.21px 22.69py, 36.15pz
HOMO-LUMO GAP				
101	16.83s, 5.69pz 6.23d	5.55s, 1.95px 14.57py, 63.31pz	2.06s, 1.95px 6.82pz	3.49s, 14.57py 56.49pz
100	6.34s, 5.86d	25.76py, 62.04pz	2.05pz	25.76py, 68.99pz
99	1.11s, 11.59d	42.16py, 45.14pz	1.91py	40.25py, 45.14pz

3.2.6 Raman Spectroscopy. The Raman spectra were collected by placing the crystals and the ligands on a microscope slide and analyzed using the Horiba XploRA Raman Confocal Microscope System. Figures 3.42, 3.43, 3.44 and 3.45 show comparison of experimental and theoretical Raman spectra for the mono-, di-, tri- and tetracoordinated TDMPP gold complexes.

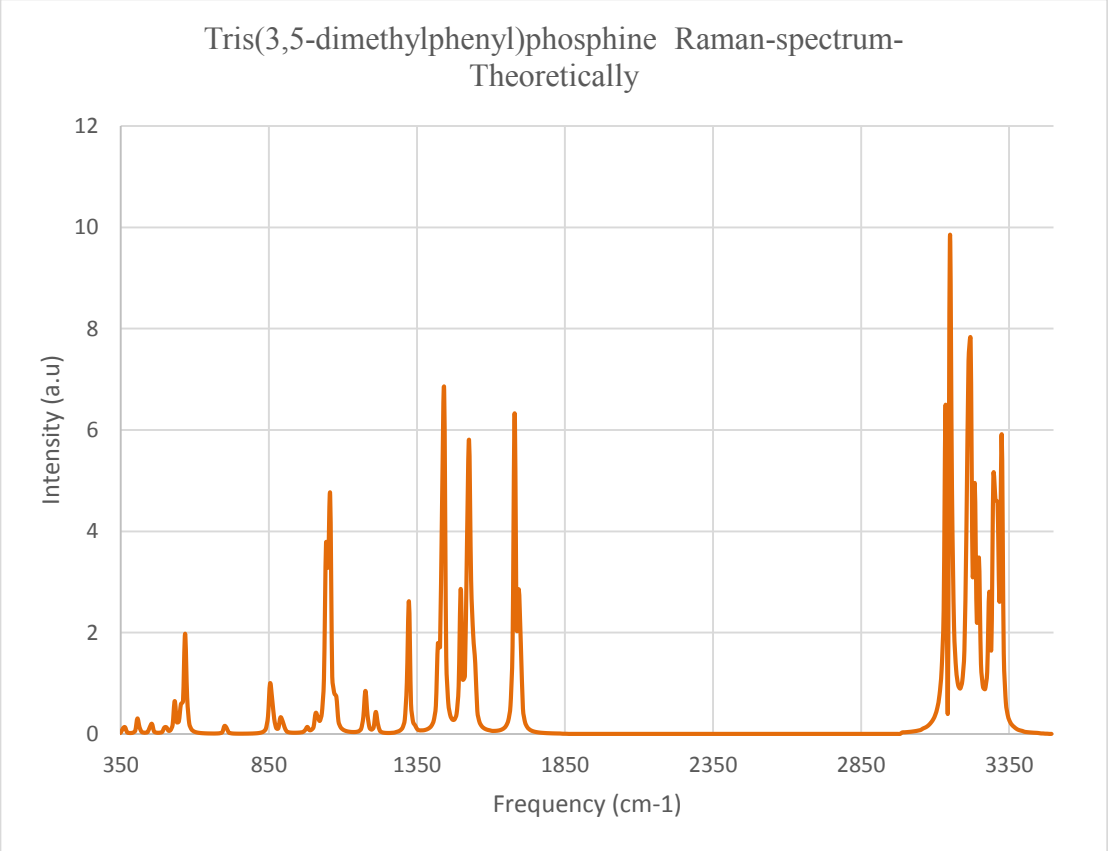

Figure 3.42. Raman spectrum for $P(C_8H_9)_3$ obtained from the theoretical calculation using Gaussian 09 program.

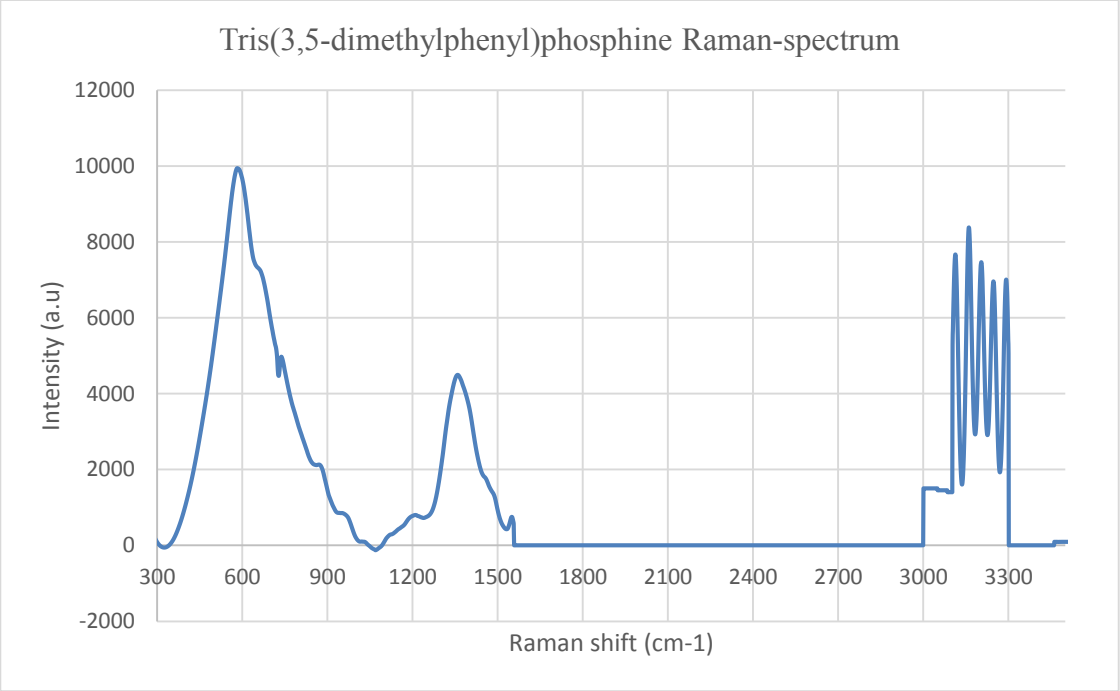

Figure 3.43. Experimentally collected Raman spectrum for $P(C_8H_9)_3$ system.

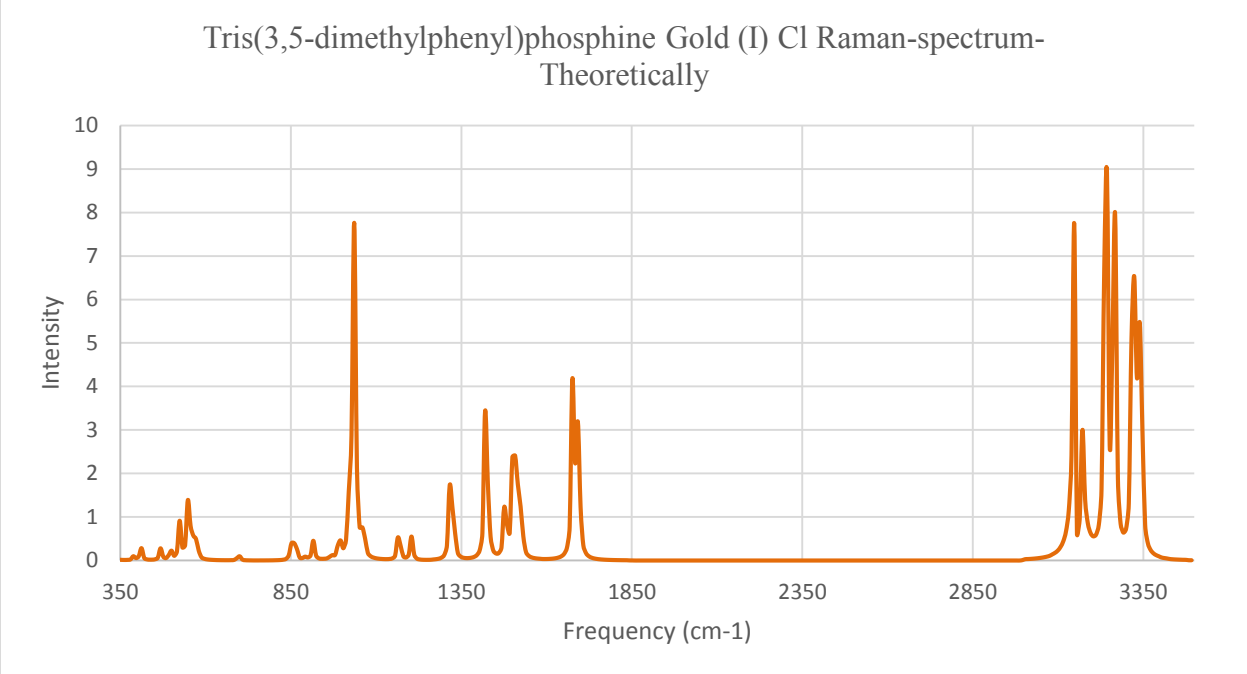

Figure 3.44. Raman spectrum for $AuP(C_8H_9)_3Cl$ obtained from theoretical calculation using the Gaussian 09 program.

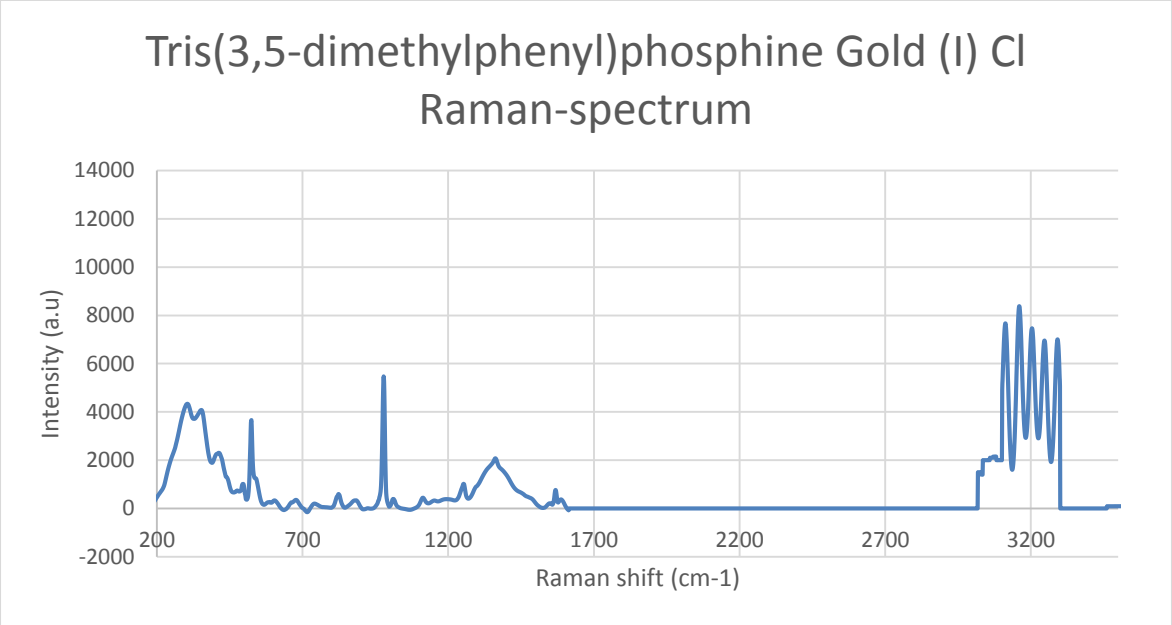

Figure 3.45. Experimentally collected Raman spectrum for $AuP(C_8H_9)_3Cl$ system.

3.3 Discussion

3.3.1 X-ray Crystallography. The X-ray crystal structure shows all the atoms and how they are bonded to one another. The P(1)—Au(1)—Cl(1) bond angle has a linear geometry with a bond angle of 179.6° for the monocoordinated TDMPP gold complex, $AuP(C_8H_9)_3Cl$ (**2**). The respective bond angle is in conformity with the linearity expected for sp hybridization found in Au(I) complexes. The Au(1)—P(1) and Au(1)—Cl(1) bond distances for $AuP(C_8H_9)_3Cl$ are shown in Tables 3.2 are 2.318 (8) and 2.346 (10). The Au(1)—P(1) and Au(1)—Cl(1) bond lengths of **2** show no significant differences in values with previous data on gold phosphine complexes. The X-ray data also show the lack of intermolecular Au‑Au aggregate formation. The weak aurophilic interactions are prevented due to steric factors as a result of the large cone angle of the TDMPP ligand.

3.3.2 Infrared Spectroscopy (Vibrational Studies). The IR-spectrum of **2** is shown in Figure 3.4. The spectrum has twenty four (24) distinct bands. Characteristic bands appear at 3032

cm^{-1} for the aromatic C–H stretching of the phenyl ring, 2908 and 2847 cm^{-1} for the asymmetric and symmetric aliphatic C–H (CH_3) stretching, 1597 cm^{-1} and 1450 cm^{-1} pair for C=C phenyl ring stretching, 1126 cm^{-1} for the P–Ar stretching, 849 cm^{-1} for the aromatic C–H bending. The Au-P and the Au-Cl stretchings are observed at 360 cm^{-1} and 330 cm^{-1}, respectively. The presence of the Au-P peak at 360 cm^{-1} which is absent in the spectrum of the ligand shown at Figure 3.2 is an indication that the TDMPP ligand has been successfully coordinated to the gold (I) center. Nuclear site group theoretical analysis for **2** also predicts twenty four (24) IR-active modes. From Table 3.1, compound **2** has a space group P3 with Z = 3. The modes for this unit cell can be found by consulting table 16A [26]. The unit cell content includes 72 C-atoms, 3 Au-atoms, 3 Cl-atoms and 3 P-atoms. Hence inspection of table 16A indicates that the Au, Cl, P, the unique aliphatic substituents carbons (C_a) should all occupy the C_1 sites. The remaining aromatic carbons (C_b) must lie on C_3 sites, in one folds repetitively. Table 16B[26], the vibrational modes of **2** are A + E for the aromatic C-atoms, 3A + 3E for each nucleus on the C_1 sites. The total contribution from C, P, Au and Cl is 13A + 13E. From table 16E, the acoustic modes are A + E and the optical modes are 12A + 12E. The distribution of the optical modes shows that Twenty four (24) (12A + 12E) modes are expected to be IR-active from the selection rules. Comparison of these predictions with the observed and calculated spectra show that twenty four distinct frequencies are observed for **2**. Hence the experimental and theoretical prediction match very well.

3.3.3 Nuclear Magnetic Resonance. The ^1H NMR spectrum of **2** shown at figure 3.8 showed splitting at chemical shift at δ = 7.1 (m, 6H, Ar–H), δ = 7.3 (m, 3H, Ar–H), and δ = 2.3 (s, 18H, CH_3). The peak intensities of the proton environments correspond to the number of H-atoms in the respective vicinities or environments. Comparison of the ^1H NMR spectral data

between **2** and its free ligand (TDMPP) indicates a slight downfield shifting. Peaks for TDMPP ligand found in figure 3.7 show splitting at δ = 7.0 (m, 6H, Ar–H), δ = 7.2 (m, 3H, Ar–H), and δ = 2.2 (s, 18H, CH_3). The slight difference in the position of the peaks between **2** and its ligand is an indication that the ligand has successfully coordinated to the gold center. The $^{31}P\{^1H\}$ NMR spectral data for the TDMPP ligand, the **2** and **3** are shown in Figures 3.10, 3.11 and 3.12. A strong sharp peak is observed at 32.5 45.8, and 60.0 ppm, respectively. Upon an increased coordination of the ligand to the gold center shows a concomitant downfield shift of the ^{31}P nmr value. This trend is a result of the weakening of the Au-P bond and consequently de-shielding of the electrons causing the peak to shift to a larger chemical shift value (downfield). The overall trend appears consistent for gold phosphine complexes where the mono substituted systems usually show smaller chemical shift values than the di, tri substituted complexes [32]. For example, the mono, tris, and tetrakis substituted (TFP)nAuCl compounds have ^{31}P NMR coordination chemical shift (ccs) of 48.4, 66.1, 63.1 respectively [32]. Also, the mono, di, tris, and tetrakis substituted (TPA)nAuCl compounds have ^{31}P NMR values of -51.4, -36.1, -56.1, and -58.0 ppm respectively [27-31]. The increase in the chemical shift value on going from the TDMPP, to the **2** and **3** is consistent with the general trend that chemical shift values increase as the coordination number increases. The trend of downfield shifting is also an indication that the ligand has successfully been coordinated to the gold (I) center.

3.3.4 UV-Vis Spectroscopy. The absorption spectral data for the TDMPP ligand, $AuP(C_8H_9)_3Cl$ and $Au(P(C_8H_9)_3)_2Cl$ reveal similarities in their high-energy broad UV absorption profiles. The absorbance maximum for the free TDMPP ligand shown at Figure 3.13 is observed at 250 nm with a smaller less intense band at 270 nm with low energy tail extending all the way

to 400 nm. Similarly, all of the TDMPP‑gold(I) complexes also show similar higher energy band maxima near 250 nm . Based on the spectral similarities between the ligand and the complexes as well as the molar absorptivity values of 6.13 x 10^4 $M^{-1}cm^{-1}$, 9.15 x 10^4 $M^{-1}cm^{-1}$ and 1.51 x 10^5 $M^{-1}cm^{-1}$ for the TDMPP, $AuP(C_8H_9)_3Cl$ and $Au(P(C_8H_9)_3)_2Cl$ respectively, the 250 nm band is assignable to a $\pi\rightarrow\pi^*$ intraligand transition, which is as result of the presence of double bond in the aromatic phenyl ring. The transition is slightly affected by the coordination with the Au metal. The weaker band at 270 nm which is present in the ligand is absent in the absorption spectra of the complexes **2** and **3** at Figure 3.14 and 3.15 respectively, indicating that the transition is affected by coordination with the metal. This band is assignable to an $n\rightarrow\pi^*$ transition and its absence in the absorption spectrum of **2** and **3** is indicative of participation of the lone pair electrons in the bonding scheme of the TDMPP ligand. The higher molar extinction coefficient value of the ligand and the complexes is an indication that the electronic transitions involved as a result of the absorption are statistically probable (said to be 'allowed') due to the fact that their molar extinction **ε** values are in excess of 10 000. It is also interesting to note that the TDMPP ligand, the **2** and the **3** complexes absorbs at similar energies but with the extinction coefficients of **3** about twice more intense than that of **2** and in turn about twice that of the TDMPP ligand . The enhancement of the extinction coefficient in **3** relative to **2** and relative to TDMPP is understandable in view of the presence of two more identical chromophores absorbing at the same region.

3.3.5 Luminescence. The gold(I) complexes and the TDMPP ligand luminescent when excited under UV radiation. The emission spectra of the complexes both at room temperature and in liquid nitrogen have very similar profiles indicating a similar origin for the electronic transitions. The emission spectra of the TDMPP ligand at room temperature shown at Figure

3.31 to 3.34 is characterize by a sharp band and maximizes around 450 nm. The gold complex (2) shown at Figure 3.35 to 3.38 also maximizes around 475 nm. The shift to the longer wavelength (red shift) from 450 nm of the TDMPP to 475 nm of $AuP(C_8H_9)_3Cl$ is due to the fact that at the excited states, the $\pi \rightarrow \pi^*$ transitions of the TDMPP is more polar than their ground states and as a result, a greater charge separation is observed in the excited state. The coordination of the TDMPP to the gold (I) center causes a dipole–dipole interaction which reduces the energy of the excited state more than the ground state, hence making the $AuP(C_8H_9)_3Cl$ to emit at a longer wavelength. This emission at a longer wavelength by $AuP(C_8H_9)_3Cl$ compare to the ligand is also an indication that the ligand has successfully been coordinated to the gold (I) center. Similar emission bands for **2** in liquid nitrogen were observed at 450 nm and 475 nm (Figure 3.39 – 3.41) showing fine vibronic structures arising from the v(C=C) stretch of the phenyl ring of the ligand. Vibrational progressions with spacing of 1598-1682 cm^{-1} were also observed in complex **2** in liquid nitrogen, typical of the v(C=C) vibrational mode of the phenyl group. The excitation spectrum of the TDMPP ligand and that of **2** at room temperature and in liquid nitrogen are shown in Figure 3.20-22 for TDMPP and Figure 3.23-29 for **2** consists of a well-defined broad bands with an average spacing of 1163-1350 cm^{-1}. This spacing is assignable to an electronic transition coupled with vibronic component corresponding to v(C=C) symmetric stretching mode within the phenyl ring. With reference to the previous luminescence studies on tertiary phosphine gold(I) complexes the emission bands at 475 nm in complexes **2** tentatively assigned as derived from excited states of P−> Au ligand-to-metal charge transfer (LMCT) origin. This suggests that the ligand centered transition is responsible for the photoluminescence in **2**.

3.3.6 Raman Spectroscopy. The Raman-spectrum of **2** at Figure 3.45 has Twenty four (24) distinct peaks. It showed the appearance characteristic bands at 3117 cm^{-1} for υ(C−H) stretching of the phenyl ring, 1574cm^{-1} for the asymmetric δ(CH_3) stretching, 1580 cm^{-1} for υ(CC) aromatic ring chain vibrations, 1339 cm-1 for δ (CH_3) symmetric stretching, 1100 cm^{-1} for the P–Ar stretching, 360 cm-1 for the Au-P stretching, 315 cm-1 for the Au-Cl. Group Theoretical Analysis (Nuclear site group analysis) for **2** also predicts Eighteen (18) Raman-active modes. Table 3.6 summarizes the group theoretical analysis for 2. The presence of the Au-P peak at 360 cm^{-1} which is absent in the spectrum of the ligand shown at Figure 3.43 is an indication that the TDMPP ligand has been successfully coordinated to the gold (I) center.

3.3.7 Computational Studies

3.3.7.1 Structural Comparison. The X-ray crystallographic structure of **2** were compared to theoretical calculations using the GAUSSIAN '09 software package. Shown in Table 3.4 are selected bond angles and bond distances of 2. Although slightly longer, longer and shorter, the calculated bond distances for Au(1)—Cl(1), Au(1)—P(1) and P(1)—C(1) respectively using the LANL2DZ basis set are in good agreement with the experimental X-ray crystal structures data as given in Table 3.2. The experimental bond distances of 2.299 (10) [Å], 2.230 (8) [Å] and 1.817 (3) [Å] for **2** changes by 0.033 [Å], 0.16[Å] and 0.011 [Å] from the calculated bond distances of (2.332[Å]), (2.390 [Å]) and (1.806[Å]) for Au(1)—Cl(1), Au(1)—P(1) and P(1)—C(1) respectively. Similarly the theoretical bond angles of 180.0 [°], 112.8 [°] and 108.5[°] for P(1)—Au(1)—Cl(1), C(1)—P(1)—Au(1) and C(17)—P(1)—C(9) respectively for **2**, are in agreement with the experimental bond angles of 180.0[°] for P(1)—Au(1)—Cl(1), 113.2[°] for C(1)—P(1)—Au(1) and 109.3[°] for C(17)—P(1)—C(9).

3.3.7.2 Spectroscopic Comparison. The theoretical calculated IR spectrum of 2 using Gaussian 09 shown at Figure 3.5 also predicts Twenty four (22) distinct bands with a slight shift in the position of some of the individual peaks, but on a whole both the calculated and the experimental spectrum of both the ligand and the complex shows similar IR-spectrum. The theoretical ^{1}H NMR of for both the ligand and the gold complex shown on Figure 3.13 and Figure 3.14 also showed similar splitting patterns and chemical shift values as that of the experimental ones.

3.3.7.3 Electronic Comparison

3.3.7.3.1 Luminescence. The result of the population analysis for **2** is shown in Table 3.9 and 3.10 for the percentage atomic and atomic orbital contributions respectively for the metal and the TDMPP ligand, as well as individual atomic participation for the selected highest three occupied molecular orbitals and lowest three unoccupied molecular orbitals. The second highest occupied molecular orbital (SHOMO), HOMO-100 has the largest contribution from the ligand at 96.8% and the metal at 3.2% followed by the third highest occupied molecular orbital (THOMO), HOMO-99 at 87.30% and 12.70% contributions, respectively. The contribution of the gold atom in the HOMO-100 orbital derives from 5s and 5dxz atomic orbitals at 1.84% and 1.36% contributions, respectively. The atomic contribution of the TDMPP ligand is comprised of Phosphorus and Carbon with percentage contributions of 25.76py, 71.04pz orbitals. However, the gold contribution of the THOMO comes also from 1.11% of the 5s and 11.59% of the 5dxz atomic orbitals with the remaining contribution from the 5py and 5pz orbitals of the phosphorus and Carbon atoms of the TDMPP ligand. The table also shows the first three lowest unoccupied molecular orbital (LUMOs) contributions, which are mainly ligand centered contributions. The orbital description as ligand based and partial metal based transitions is thus substantiated to

support the observations surrounding the luminescent behavior of **2** and hence the assignment of π→π* transition is in a proper order.

3.3.7.3.2 UV-Vis. The HOMO‑LUMO gap calculated value by the TD-DFT method was 39920 cm^{-1} corresponding to 250.51 nm. The theoretical calculated spectrum for **2** obtained using TDDFT with the LANL2DZ basis set to identify the orbital(s) contributing to the observed absorption is shown at Figure 3.16. The TD-DFT generated ground-state to excited-transitions is shown on Table 3.7 which summarizes the orbital that took part most in the transitions X, Y, and Z. From Table 3.7, transition X supports an assignment of the SHOMO-100→LUMO-102, a π→π* type transition. This confirms why the n→π* is not present in the experimental UV-Vis spectrum of **2**. The transition Y and Z has transitions from the HOMO-101→LUMO-102 and the third HOMO-99→LUMO-102 respectively. Table 3.8 summarizes the various transitions pictorially of the theoretically generated ground-state to excited-state transitions for X, Y and Z. These calculated spectrum values are in good agreement with the experimental UV-Vis spectrum of 2, since both the experimental and calculated spectrum shows a strong absorption maximum around 250 nm.

CHAPTER FOUR

Synthesis and Characterization of mono-, bis-, tris-, and tetrakis-{tris(2, 6-dimethoxyphenyl)phosphine} gold(I) complexes

4.1 Syntheses

4.1.1 Tris(2,6-dimethoxyphenyl)phosphine gold (I) chloride (6). Tris(2,6-dimethoxyphenyl)phosphine (0.0200g, 0.045 mmol) was added to a solution of $(C_4H_8S)AuCl$ (0.0105 g, 0.045 mmol) in tetrahydrofuran (20 ml) at −80 °C and the reaction stirred for 2 hours. The solvent was removed by purging nitrogen gas into the solution, until all the solvent dried up. The residue was then recrystallized from CH_2Cl_2/n-hexane mixture for days. Partial evaporation of the solvent provided quality crystals.

4.1.2 Bis{Tris(2,6-dimethoxyphenyl)phosphine} gold (I) chloride (7). Tris(2,6-dimethoxyphenyl)phosphine (0.0400g, 0.09 mmol) was added to a solution of $(C_4H_8S)AuCl$ (0.0105 g, 0.045 mmol) in tetrahydrofuran (20 ml) at −80 °C and the reaction stirred for 2 hours. The solvent was removed by purging nitrogen gas into the solution, until all the solvent dried up. The residue was then recrystallized from CH_2Cl_2/n-hexane mixture for days. Partial evaporation of the solvent provided quality crystals.

4.1.3 Tris{tris(2,6-dimethoxyphenyl)phosphine} gold (I) chloride (8). Tris(2,6-dimethoxyphenyl)phosphine (0.0600g, 0.135 mmol) was added to a solution of $(C_4H_8S)AuCl$ (0.0105 g, 0.045 mmol) in tetrahydrofuran (20 ml) at −80 °C and the reaction stirred for 2 hours. The solvent was removed by purging nitrogen gas into the solution, until all the solvent dried up. The residue was then recrystallized from CH_2Cl_2/n-hexane mixture for days. Partial evaporation of the solvent provided quality crystals.

4.1.4 Tetrakis{Tris(2,6-dimethoxyphenyl)phosphine} gold (I) chloride (9).Tris(2,6-dimethoxyphenyl)phosphine (0.0400g, 0.09 mmol) was added to a solution of $(C_4H_8S)AuCl$ (0.0105 g, 0.045 mmol) in tetrahydrofuran (20 ml) at −80 °C and the reaction stirred for 2 hours. The solvent was removed by purging nitrogen gas into the solution, until all the solvent dried up. The residue was then recrystallized from CH_2Cl_2/n-hexane mixture for days. Partial evaporation of the solvent provided quality crystals.

4.2 Results

4.2.1 X-ray Crystallography. Diffraction data were collected on x-ray quality crystals. The structure of the monocoordinated TDMOPP gold (I) complex, $AuP(C_8H_9O_2)_3Cl$ is shown in Figure 4.1 The structural data and selected bond lengths and angles are listed in Tables 4.1, 4.2, 4.3 and 4.4.

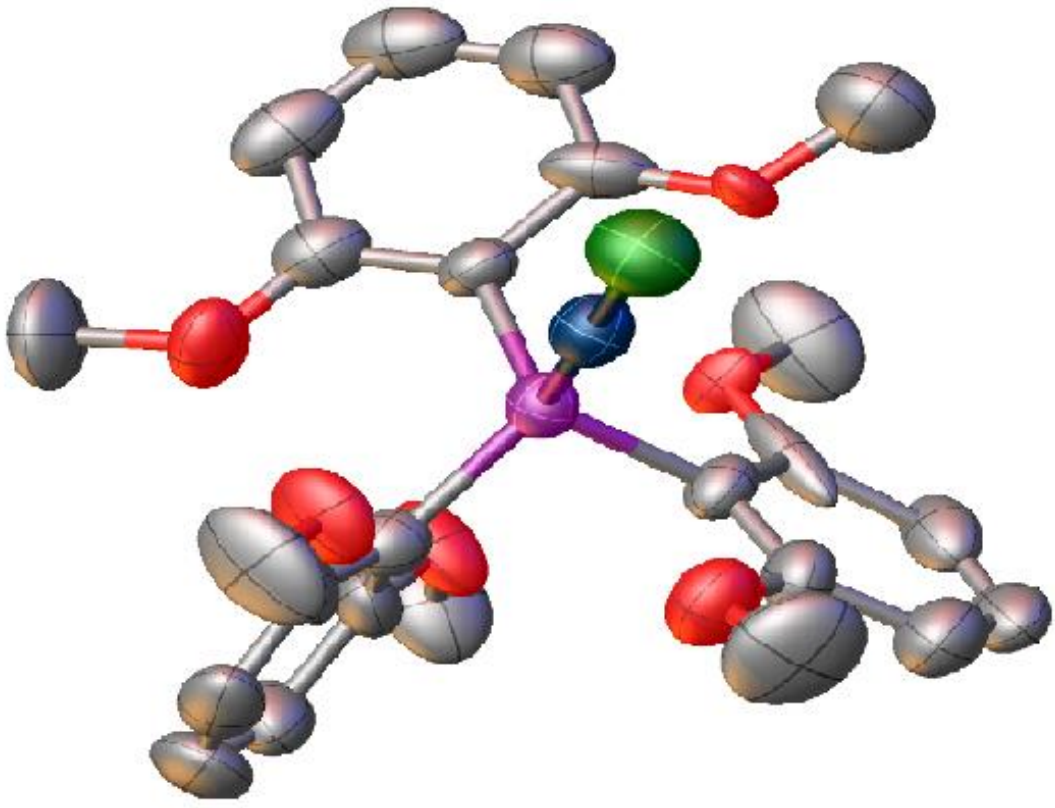

Figure 4.1. Thermal ellipsoid diagram of the $AuP(C_8H_9O_2)_3Cl$ complex.

Table 2.1

Crystal data and Structural refinement parameters for $AuP(C_8H_9O_2)_3Cl$ complex

Empirical formula	$C_{24}H_{27}AuClO_6P$	
Formula weight	674.84	
Temperature	293K	
Wavelength	0.71073 Å	
Crystal system	Triclinic	
Space group	P-1	
Unit cell dimensions	a = 10.9905 (4) Å	α = 107.799 (3)°
	b = 15.0909 (5) Å	β = 91.139 (3)°
	c = 16.3661 (6) Å	γ = 93.812 (3)°
Volume	2576.48 (15)Å^3	
Z	4	
Density (calculated)	1.740 Mg cm^{-3}	
Absorption coefficient	5.91 mm^{-1}	
$F_{(000)}$	1320	
Crystal size	0.35 × 0.31 × 0.14 mm	
Theta range for data collection	2.8 to 27.0°	
Index ranges	-13<h<13, -17<k<18, -19<l<19	
Reflections collected	36841	
Independent reflections	9253 [R(int) = 0.049]	
Completeness to theta = 25.2°	99.9%	
Absorption correction	Analytical	
Max. and min. transmission	0.554, 0.178	
Refinement method	Full-matrix least-squares on F^2	
Data / restraints / parameters	9253 / 0 / 607	
Goodness-of-fit on F^2	1.07	
Final R indices [I>2sigma(I)]	R1 = 0.044, wR2 = 0.128	
Large diff. peak and hole	1.77 e Å^{-3} and −2.58 e Å^{-3}	

Table 4.2

Selected Bond Lengths [Å] for $AuP(C_8H_9O_2)_3Cl$ complex

Measured Bond	Bond Length [Å]
Au(1)—P(1)	2.244 (2)
Au(1)—Cl(1)	2.299 (2)
Au(2)—P(2)	2.253 (3)
Au(2)—Cl(2)	2.294 (3)
P(1)—C(1)	1.825 (8)
P(1)—C(17)	1.841 (2)
P(2)—C(41)	1.833 (9)
P(2)—C(33)	1.836 (9)
P(2)—C(25)	1.822 (9)
O(1)—C(2)	1.345 (12)

Table 4.3

Comparison of experimental and calculated theoretical bond angles and length using DFT calculations

EXPERIMENTAL BOND LENGTH [Å]		CALCULATED BOND LENGTH [Å]
Au(1)—P(1)	2.244	2.389
Au(1)—Cl(1)	2.299	2.331
P(1)—C(1)	1.825	1.809
EXPERIMENTAL BOND ANGLE [°]		CALCULATED BOND ANGLE [°]
P(1)—Au(1)—Cl(1)	177.3	180.0
C(1)—P(1)—Au(1)	112.1	110.1
C(17)—P(1)—C(9)	111.0	108.9

Table 4.4

Selected Bond Angles [°] for $AuP(C_8H_9O_2)_3Cl$ complex

Measured Bond	Bond Angles [°]
P(1)—Au(1)—Cl(1)	177.28 (8)
P(2)—Au(2)—Cl(2)	179.84 (11)
C(1)—P(1)—C(9)	102.9 (9)
C(9)—P(1)—C(17)	111.0 (4)
C(1)—P(1)—C(17)	111.6 (4)
C(9)—P(1)—Au(1)	115.1 (3)
C(1)—P(1)—Au(1)	112.1 (3)
C(17)—P(1)—Au(1)	104.3 (3)
C(41)—P(2)—C(33)	100.7 (4)
C(25)—P(2)—C(41)	110.4 (4)
C(25)—P(2)—C(33)	111.3 (4)
C(41)—P(2)—Au(2)	110.1 (3)
C(33)—P(2)—Au(2)	115.4 (3)
C(25)—P(2)—Au(2)	116.9 (6)

4.2.2 Infrared Spectroscopy. All infrared spectra were obtained as potassium bromide (KBr) disc, prepared by compressing the ground mixture of sample and KBr powder, on a Shimadzu IR-PRESTIGE-21 Fourier transform infrared spectrophotometer (4000−300 cm^{-1}). Figures 4.2, 4.3, 4.4, 4.5 and 4.6 show both experimental and theoretical IR spectra of the TDMOPP ligand, the mono-, di-, tri- and tetra-coordinated TDMOPP gold (I) complexes.

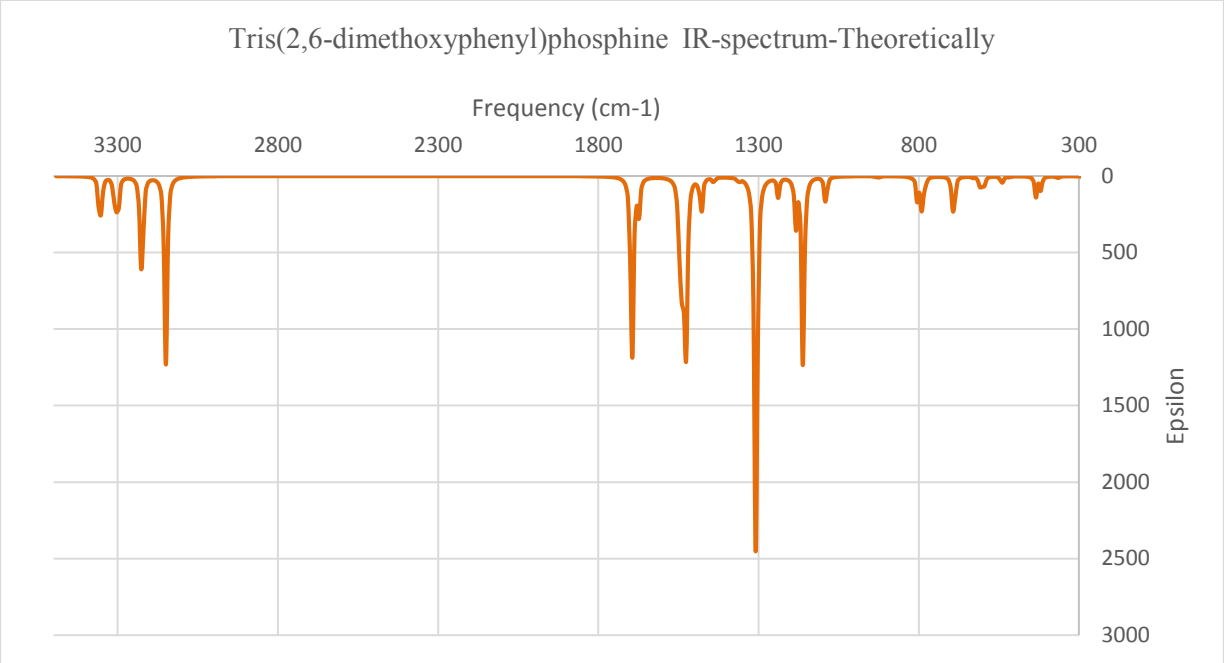

Figure 4.2. IR spectrum for $P(C_8H_9O_2)_3$ calculated theoretically using Gaussian 09 software.

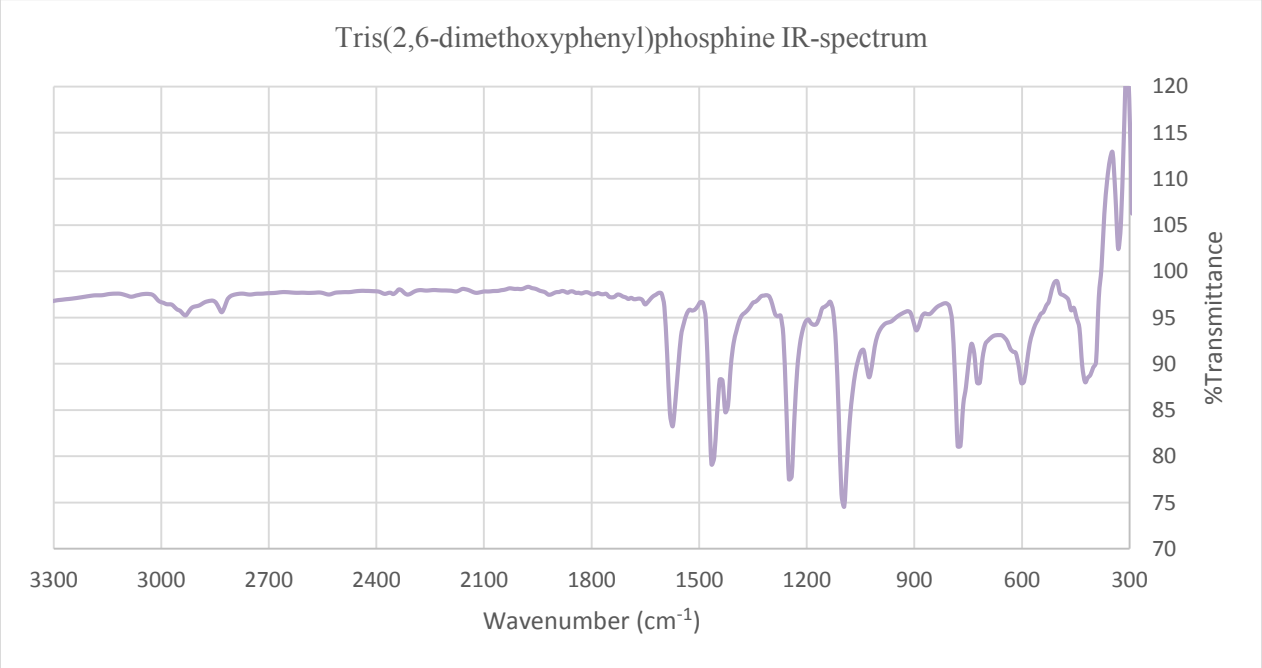

Figure 4.3. IR spectrum for $P(C_8H_9O_2)_3$.

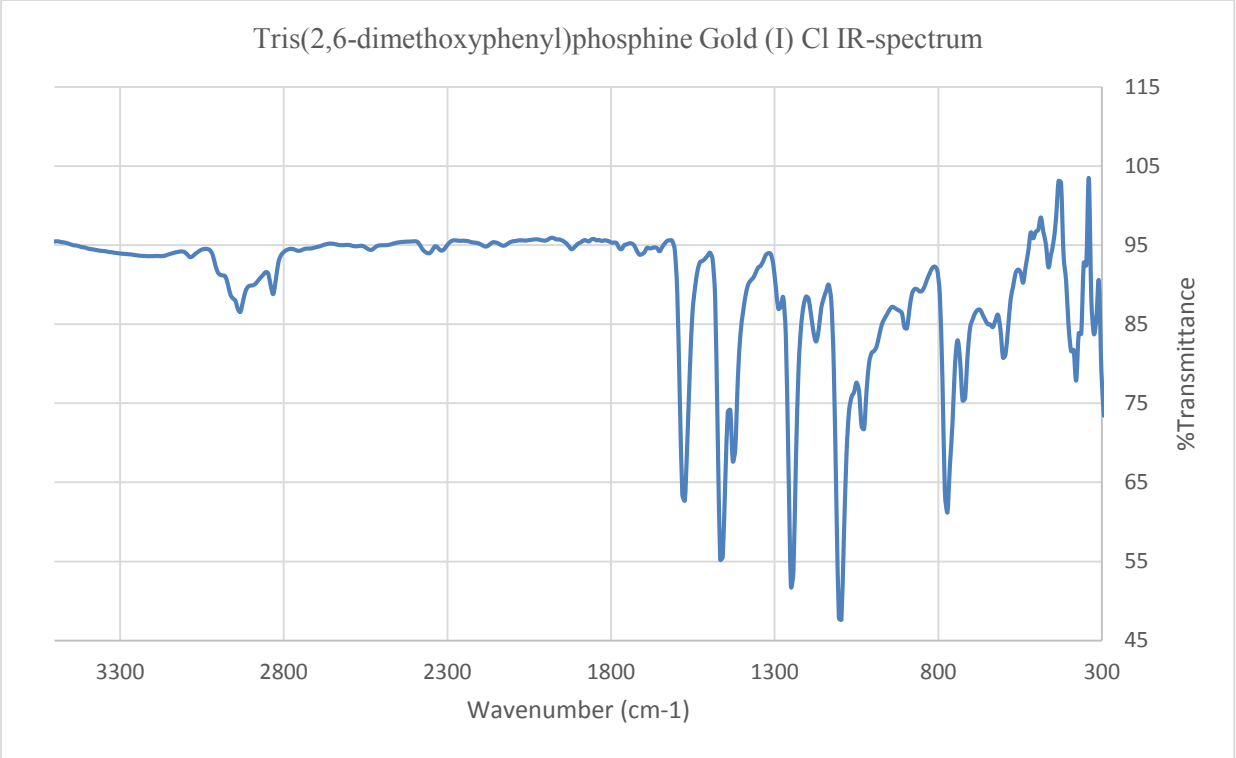

Figure 4.4. IR spectrum for $AuP(C_8H_9O_2)_3Cl$.

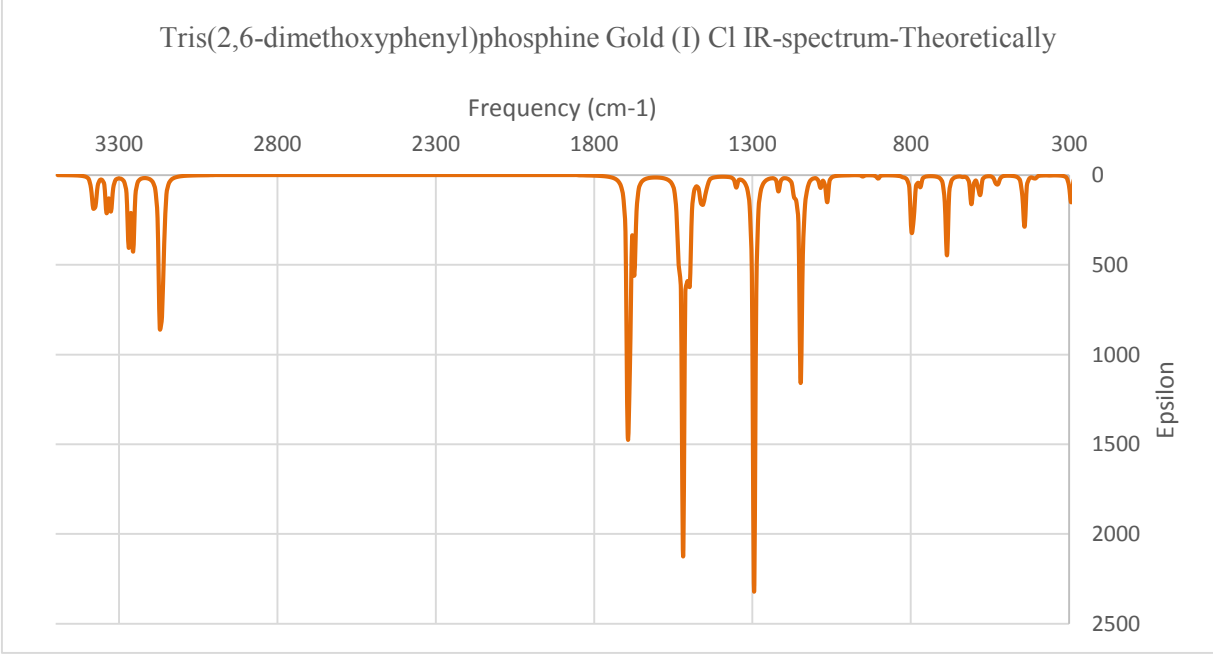

Figure 4.5. IR spectrum for $AuP(C_8H_9O_2)_3Cl$ calculated theoretically using Gaussian 09 software.

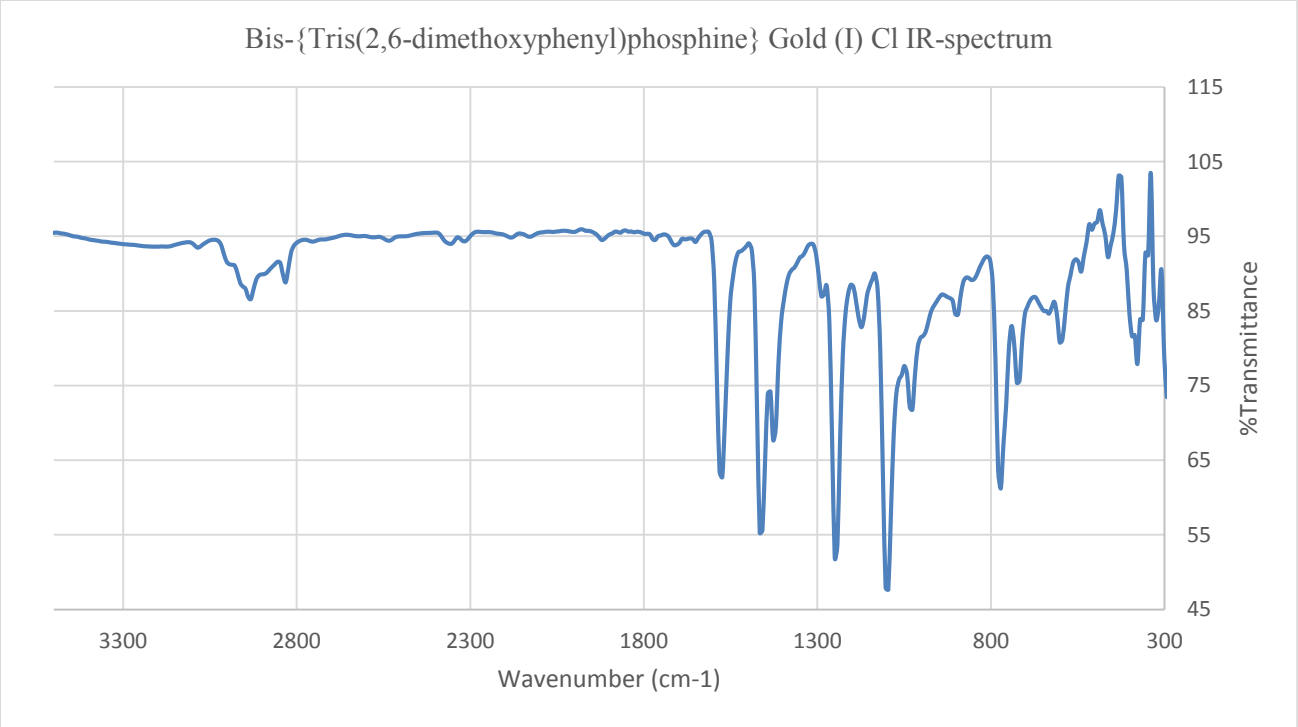

Figure 4.6. IR spectrum for $Au(P(C_8H_9O_2)_3)_2Cl$.

Table 4.5

Nuclear site group theoretical analysis for $AuP(C_8H_9O_2)_3Cl$

GROUP THEORETICAL ANALYSIS (NUCLEAR SITE ANALYSIS)					
MODES	Au	Cl	P	C	O
SITES (5A)	C_1	C_1	C_1	Ci	C_2
VIBRATIONAL(5B)	$3A_g + 3A_u + 3B_g + 3B_u$	$3A_g + 3A_u + 3B_g + 3B_u$	$3A_g + 3A_u + 3B_g + 3B_u$	$3A_u + 3B_u$	$A_g + A_u + 2B_g + 2B_u$
TOTAL CONTRIBUTION = $10A_g + 13A_u + 11B_g + 14B_u$					
ACOUSTIC MODES (5E) = $A_u + B_u$					
OPTICAL MODES = $10A_g + 12A_u + 11B_g + 13B_u$					
IR ACTIVE (5E) = $12A_u + 13B_u$					
RAMAN ACTIVE (5E) = $10A_g + 11B_g$					

4.2.3 Nuclear Magnetic Resonance. The ^{1}H NMR spectral data for the monocoordinated TDMOPP gold complex was found in Figure 4.8 showing peaks at 3.4 (18H), 7.2 (6H) 6.4 (3H) ppm and that of the dicoordinated TDMOPP gold (I) complex was found in Figure 4.9 showing peaks at 3.5 (18H), 6.5 (3H), 7.3 (6H) ppm. The ^{1}H NMR spectral data for the free ligand TDMOPP was found in Figure 4.7 showing peaks at 3.3 (18H), 7.2 (6H), 6.3 (3H) ppm. The $^{31}P\{^{1}H\}$ NMR spectral data for the ligand, **2** and **3** was found in Figure 4.10, 4.11 and 4.12 showing peaks at -33.0, -2.6 and -20.0 ppm respectively. Theoretically calculated proton NMR using Gaussian 09 is also shown at Figure 4.13 and 4.14.

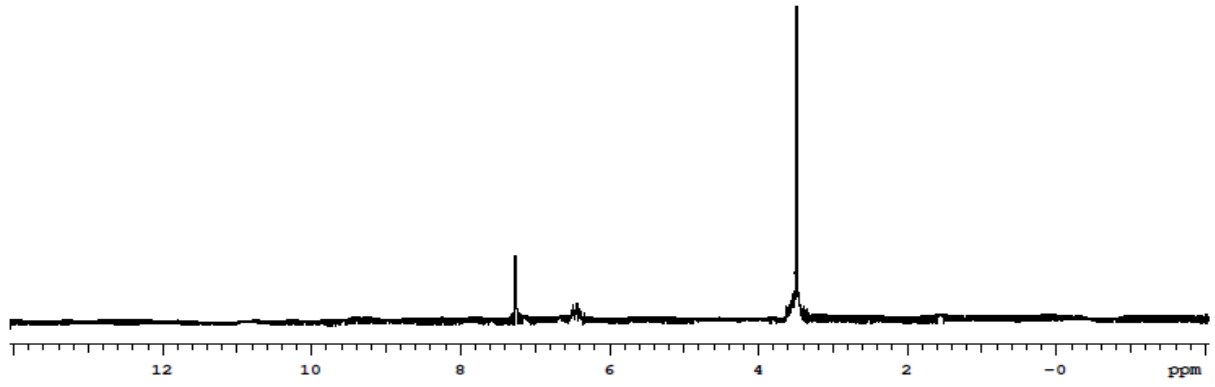

Figure 4.7. ^{1}H NMR spectrum of $P(C_8H_9O_2)_3$.

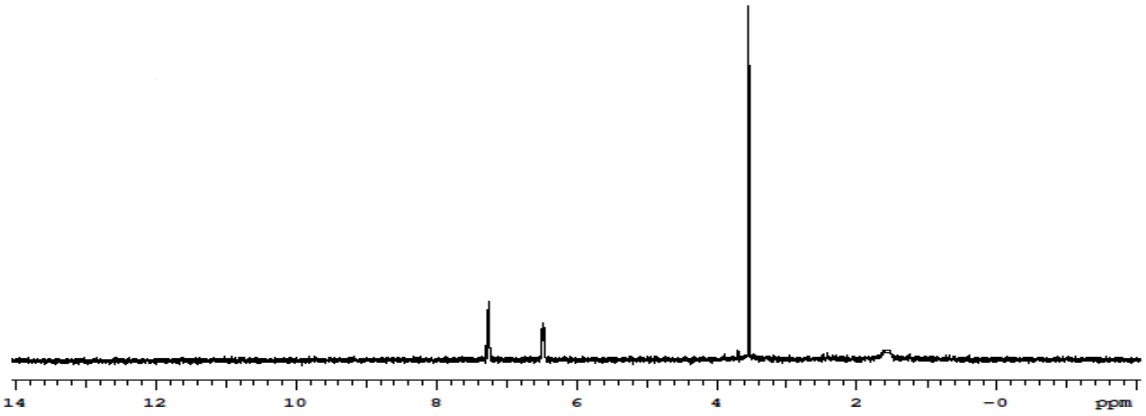

Figure 4.8. ^{1}H NMR spectrum of $AuP(C_8H_9O_2)_3Cl$.

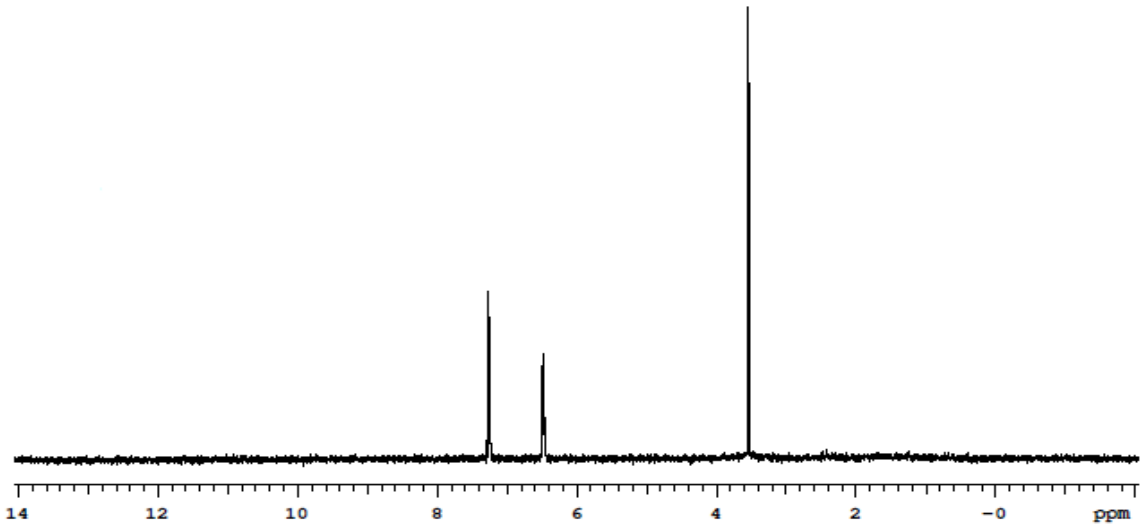

Figure 4.9. ^{1}H NMR spectrum of $Au(P(C_8H_9O_2)_3)_2Cl$.

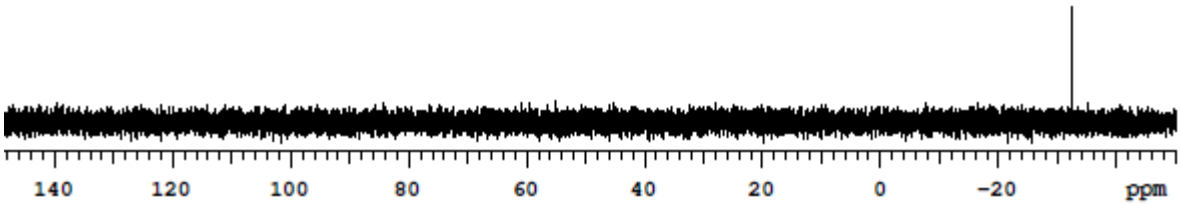

Figure 4.10. $^{31}P\{^{1}H\}$ NMR spectrum of $P(C_8H_9O_2)_3$.

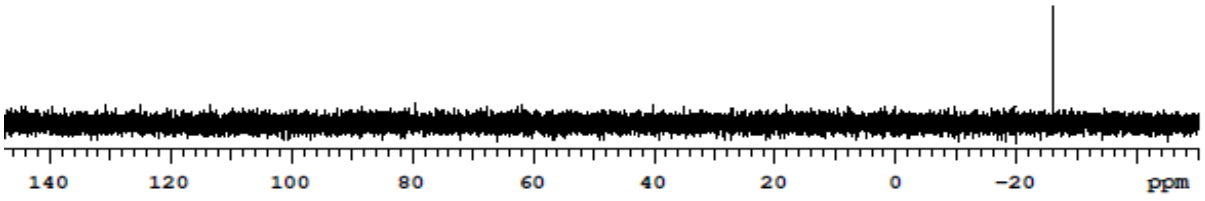

Figure 4.11. $^{31}P\{^{1}H\}$ NMR spectrum of $AuP(C_8H_9O_2)_3Cl$.

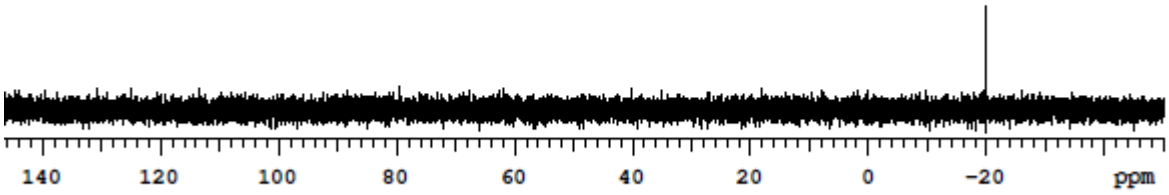

Figure 4.12. $^{31}P\{^{1}H\}$ NMR spectrum of $AuP((C_8H_9O_2)_3)_2Cl$.

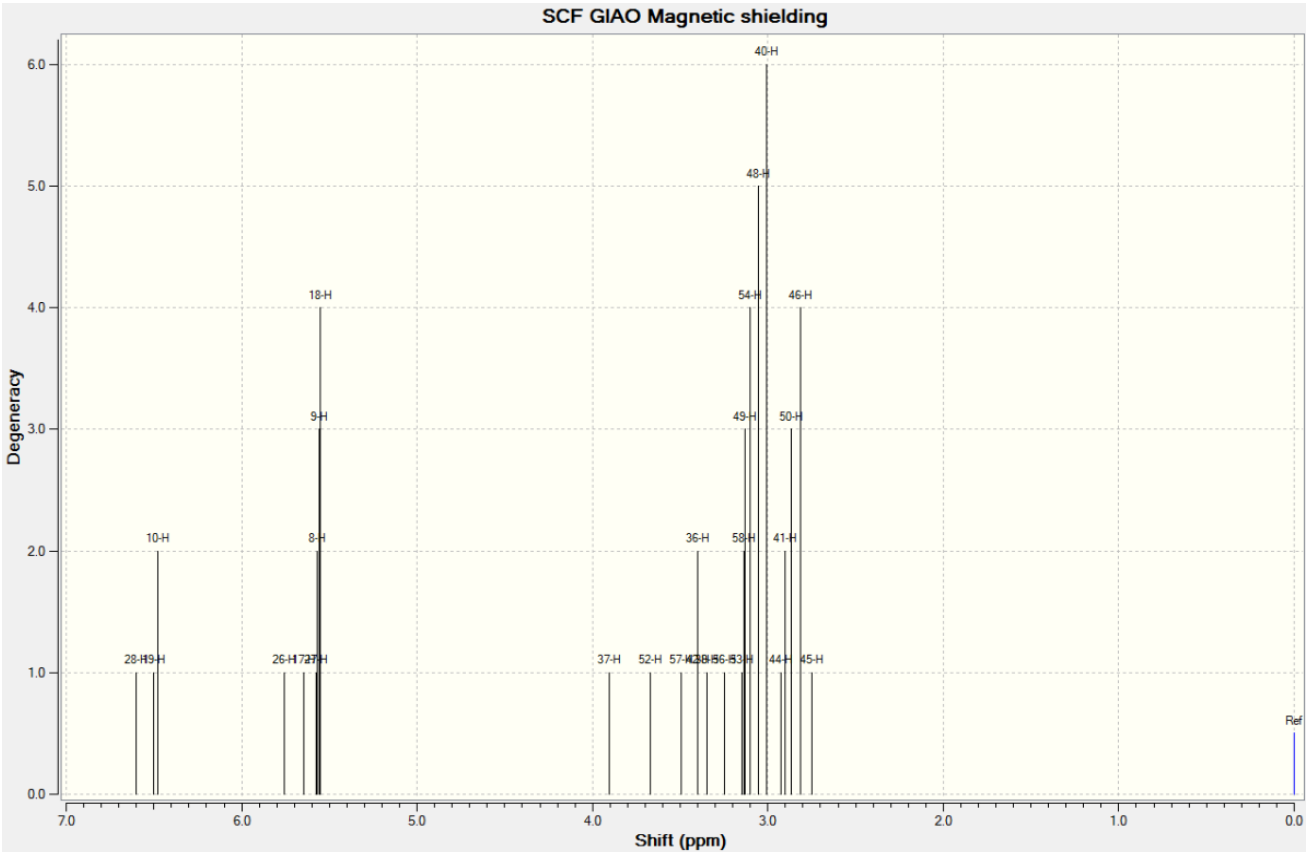

Figure 4.13. ^{1}H NMR spectrum of $P(C_8H_9O_2)_3$ calculated theoretically using Gaussian 09 software.

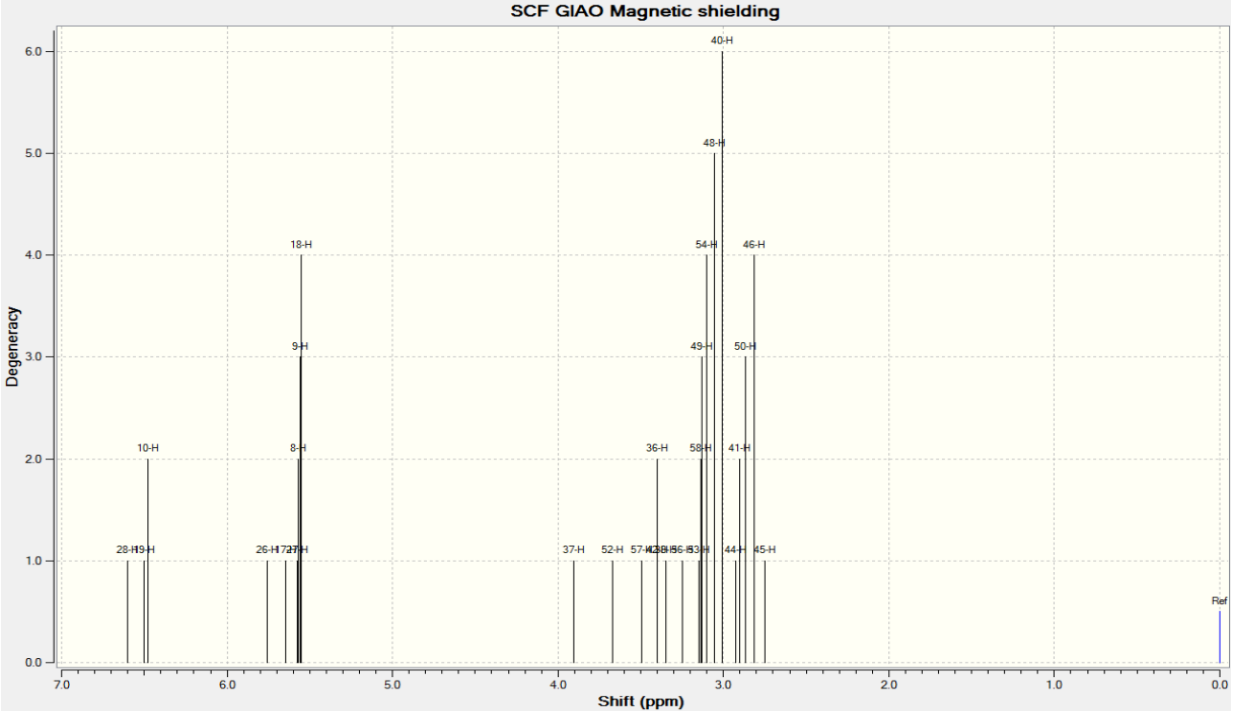

Figure 4.14. ^{1}H NMR spectrum of $AuP(C_8H_9O_2)_3Cl$ calculated theoretically using Gaussian 09 software.

4.2.4 UV-Vis Spectroscopy. All of the samples used for the ultraviolet visible (absorption) experiment, were dissolved in spectroscopic grade acetonitrile (CH_3CN). The TDMOPP ligand has a broad absorption spectrum shown in Figure 4.15 that maximizes around 250 nm with a calculated molar absorptivity of 6.30 x 10^4 $M^{-1}cm^{-1}$. The absorption spectrum of **6** shown in Figure 4.16 has a broad absorption profile maximizes at about 250 nm with a calculated molar absorptivity of 9.51 x 10^4 $M^{-1}cm^{-1}$. In Figure 4.17 is shown the absorption profile for compound **7** which has a band maximum of about 250 nm with a calculated molar absorptivity of 1.68 x 10^5 $M^{-1}cm^{-1}$. The theoretical spectrum using DFT calculations, as shown in Figure 4.18 and 4.19 for both **6** and the free ligand respectively has a broad absorption band at 270 nm.

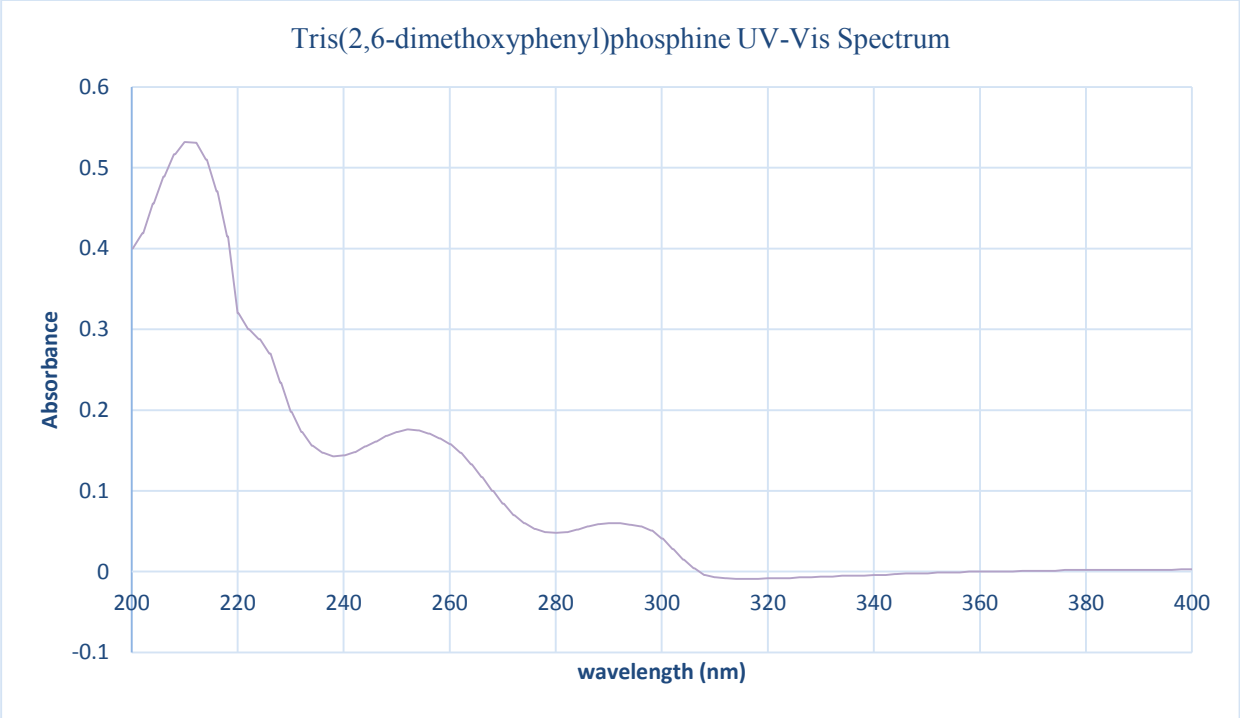

Figure 4.15. UV-Vis spectrum of $P(C_8H_9O_2)_3$.

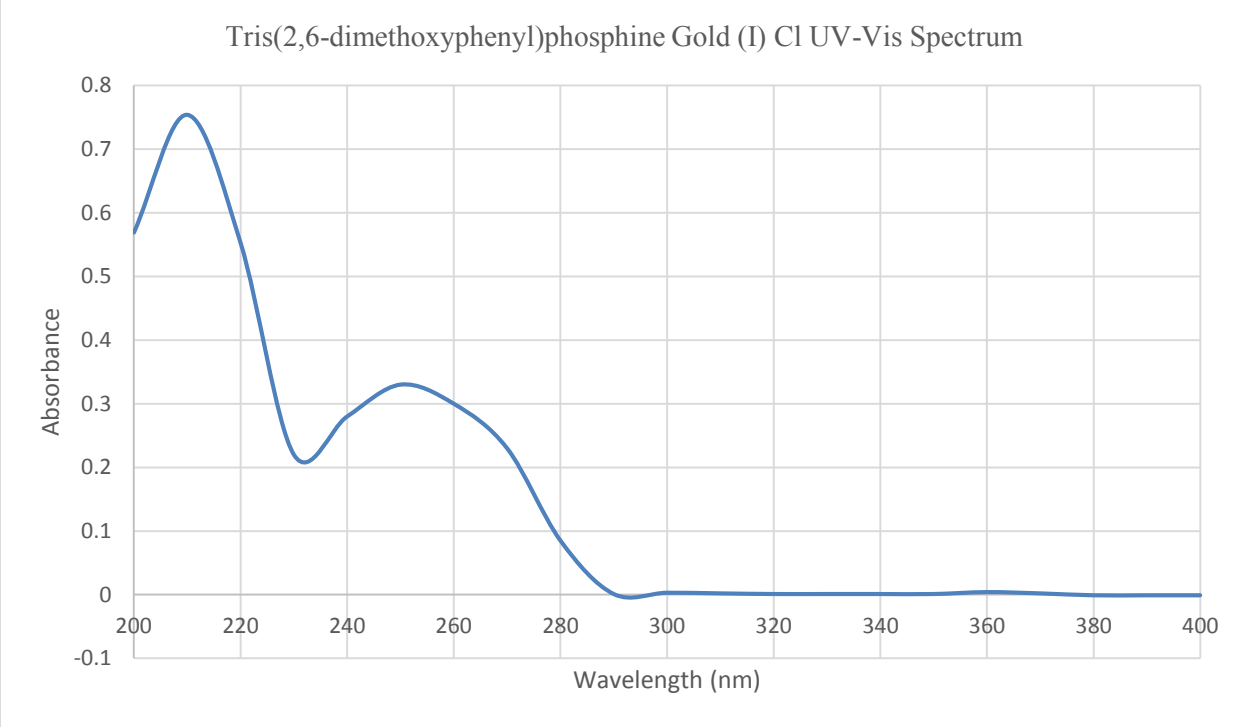

Figure 4.16. UV-Vis spectrum of $AuP(C_8H_9O_2)_3Cl$.

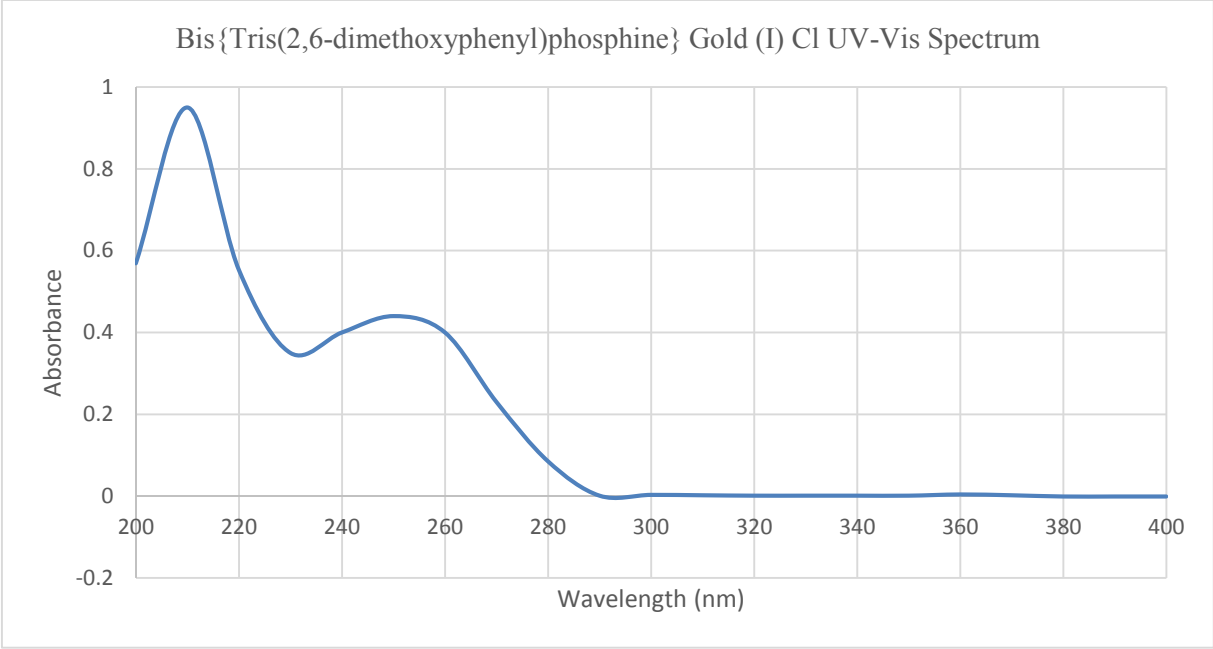

Figure 4.17. UV-Vis spectrum of $AuP((C_8H_9O_2)_3)_2Cl$.

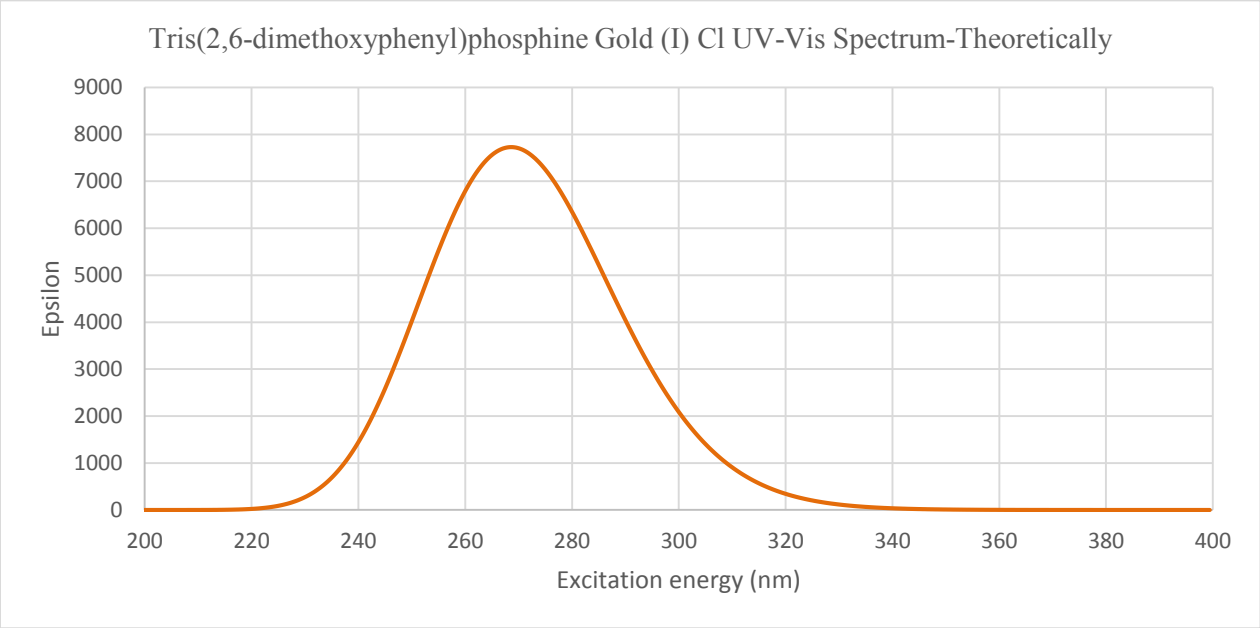

Figure 4.18. UV-Vis spectrum of $AuP(C_8H_9O_2)_3Cl$ calculated theoretically using Gaussian 09 software.

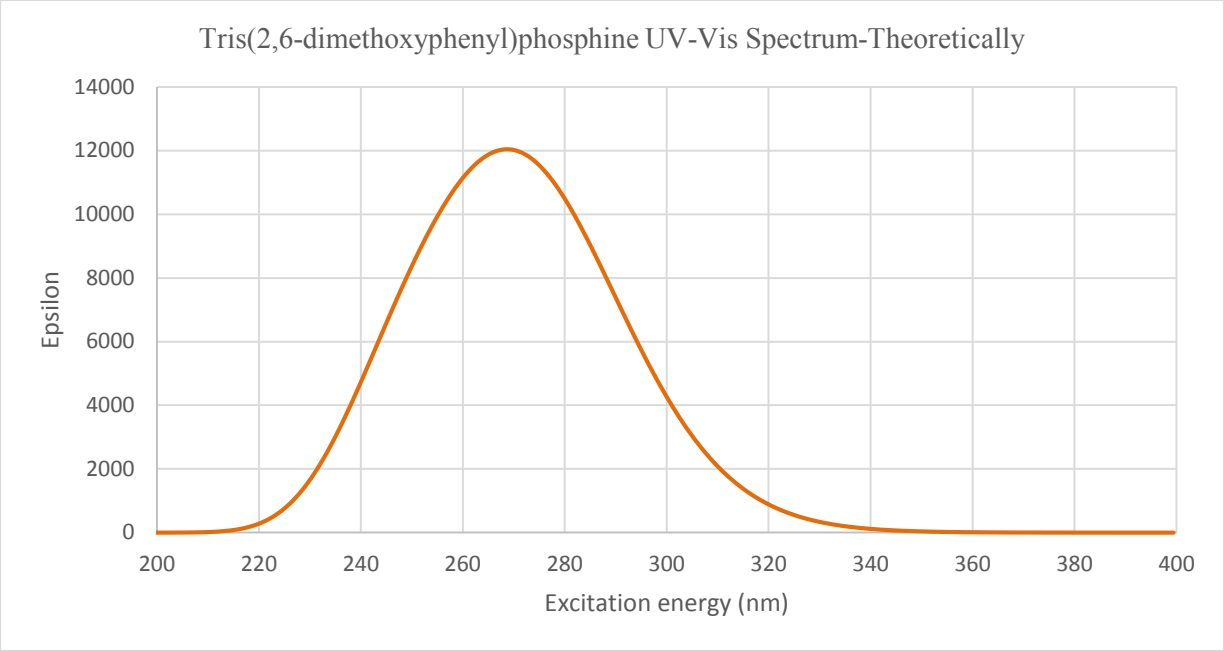

Figure 4.19. UV-Vis spectrum of $P(C_8H_9O_2)_3$ calculated theoretically using Gaussian 09 software.

Table 4.6

TD-DFT generated ground-state to excited-state MO transitions

TRANSITIONS	CORRESPONDING ORBITALS	% CONTRIBUTION
X	124 → 128	74.26
	124 → 132	25.74
Y	121 → 127	10.46
	122 → 126	10.17
	123 → 126	54.27
	124 → 126	12.59
	125 → 127	12.51
Z	121 → 126	10.03
	122 → 127	10.27
	123 → 127	54.45
	124 → 127	12.53
	125 → 126	12.71

Table 4.7

Theoretical results showing the contributions of X, Y, and Z transitions of ***6***

Excitation	λcalc. (nm)	%Contribution to the transition		Transition Energy (cm^{-1})	λexp. (nm)
X	274.54				250
Major contribution:					
	124→ 128	74.26		36,426	
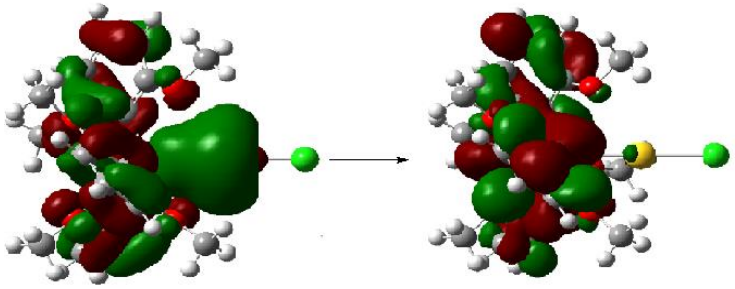					
Y	266.12				
Major contribution:					
	123 → 126	54.27		37,577	
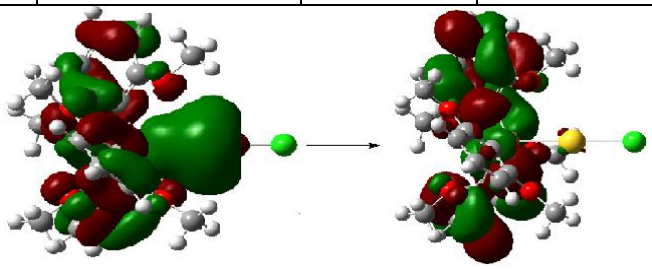					
Z	266.11				
Major contribution:					
	123 → 127	54.45		37,579	
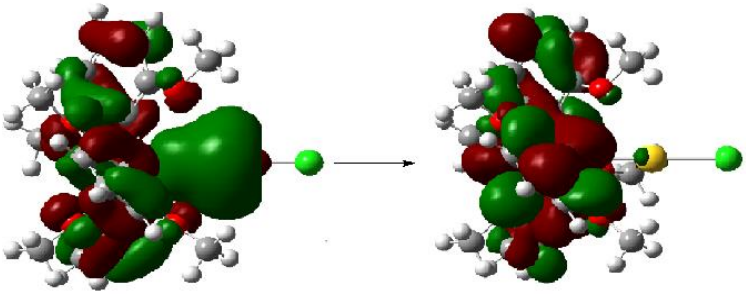					

4.2.5 Luminescence. The excitation spectra of the TDMOPP ligand collected at room temperature are shown in Figures 4.20 - 4.21. The excitation spectra for the $AuP(C_8H_9O_2)_3Cl$ complex collected at room temperature are shown in Figures 4.22, 4.23 and 4.24 covering the spectral region of 295 - 530 nm, 280 - 453 nm, 280 - 500 nm, 295 - 530 nm and monitored at emission bands of 550, 473 and 527, respectively. The spectra monitored at 550 nm exhibit vibronic bands at 335, 365, 460 nm, while the spectra monitored at 527 exhibit vibronic bands at325, 445, 390 nm. Similarly, the spectrum monitored at 473 nm also exhibit vibronic bands centering at 295, 355, 400 nm.

The excitation spectrum collected at liquid nitrogen temperature is shown in Figure 4.25 covering the spectral region of 280 - 430 and monitored at an emission band of 450. The spectrum shows vibronic components at 341, 380, and 385 nm. The emission spectra of the ligand collected at room temperature is shown in Figures 4.26 and 4.27. The emission spectra for both room and liquid nitrogen temperatures for **6** are shown in Figures 4.28, 4.29, 4.30, 4.31 and 4.32, 4.33.

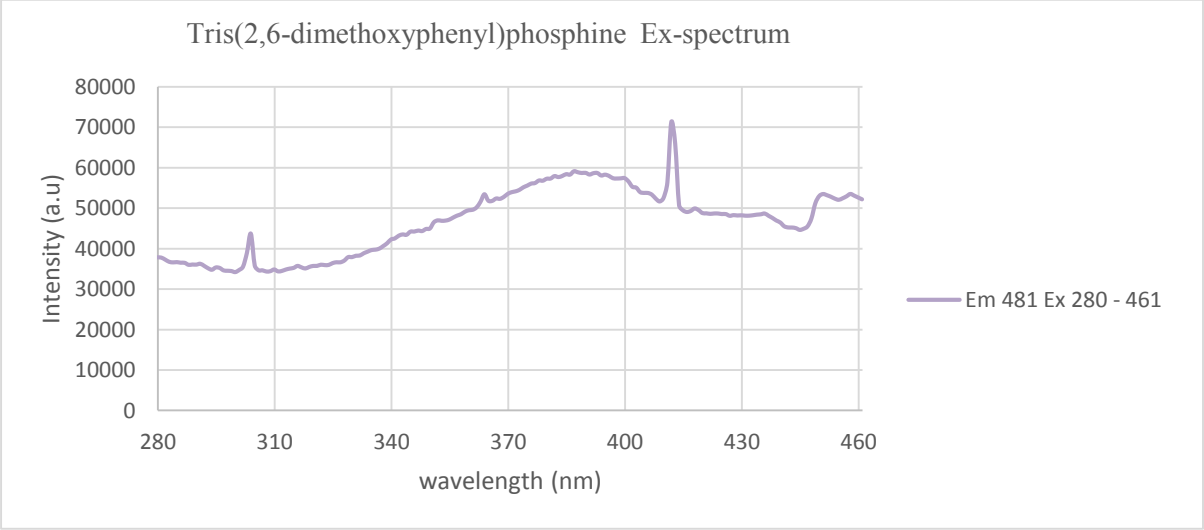

Figure 4.20. Excitation spectrum of TDMOPP ligand collected at room temperature by monitoring the emission at 481 nm.

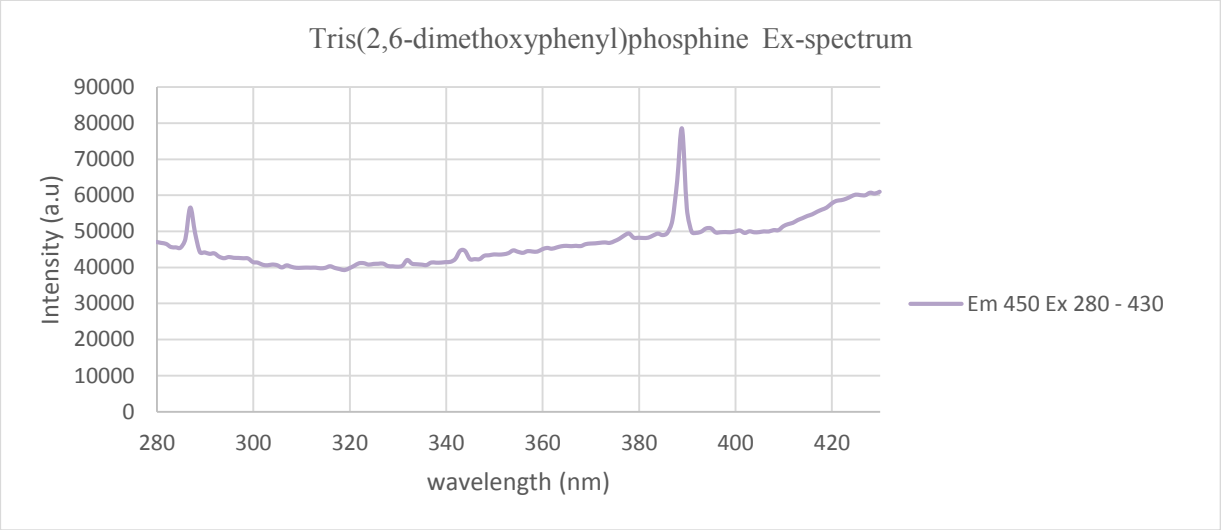

Figure 4.21. Excitation spectrum of TDMOPP ligand collected at room temperature by monitoring the emission at 450 nm.

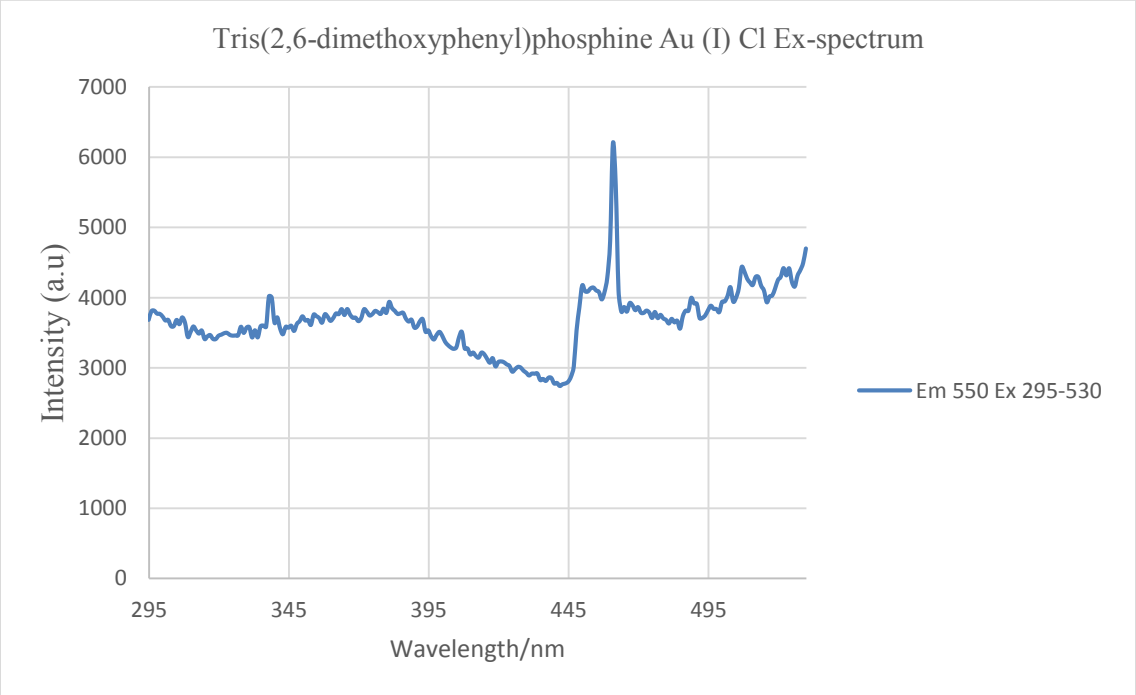

Figure 4.22. Excitation spectrum of $AuP(C_8H_9O_2)_3Cl$ collected at room temperature by monitoring the emission at 550 nm.

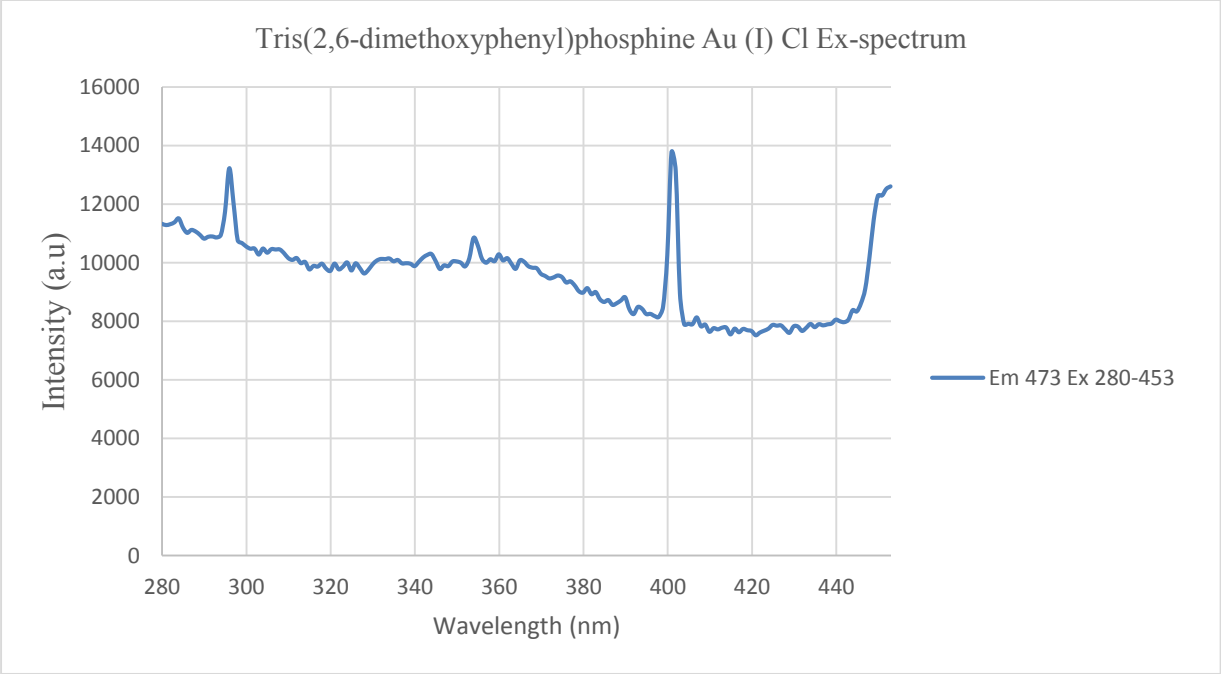

Figure 4.23. Excitation spectrum of $AuP(C_8H_9O_2)_3Cl$ collected at room temperature by monitoring the emission at 473 nm.

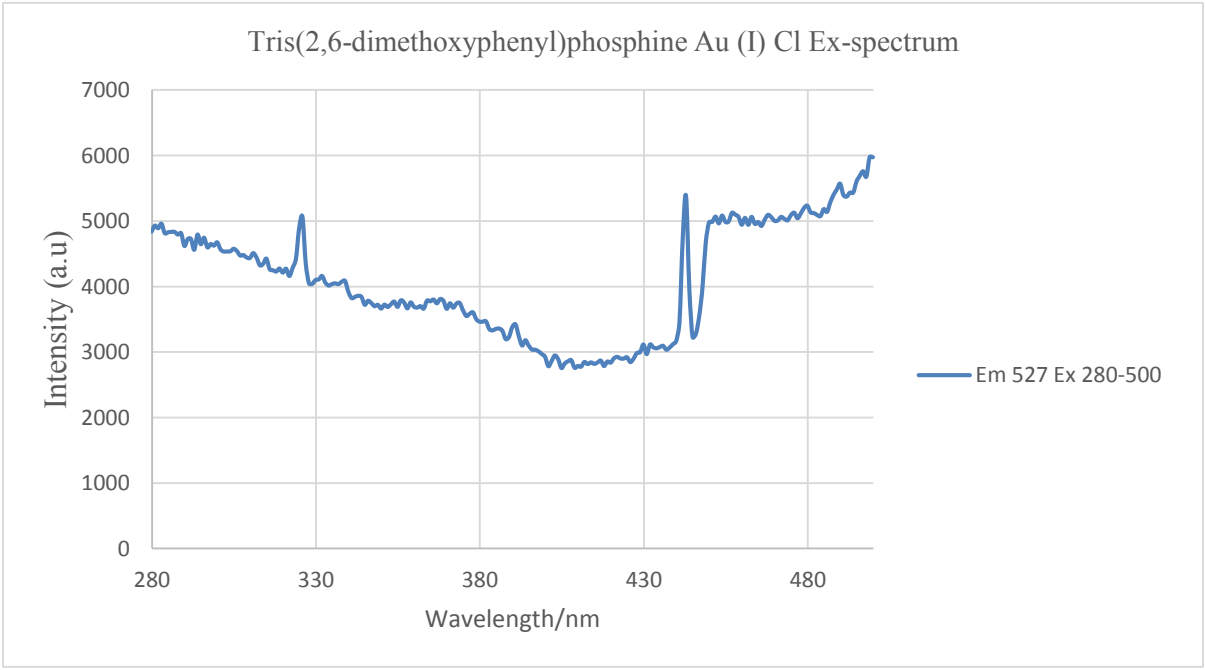

Figure 4.24. Excitation spectrum of $AuP(C_8H_9O_2)_3Cl$ collected at room temperature by monitoring the emission at 527 nm.

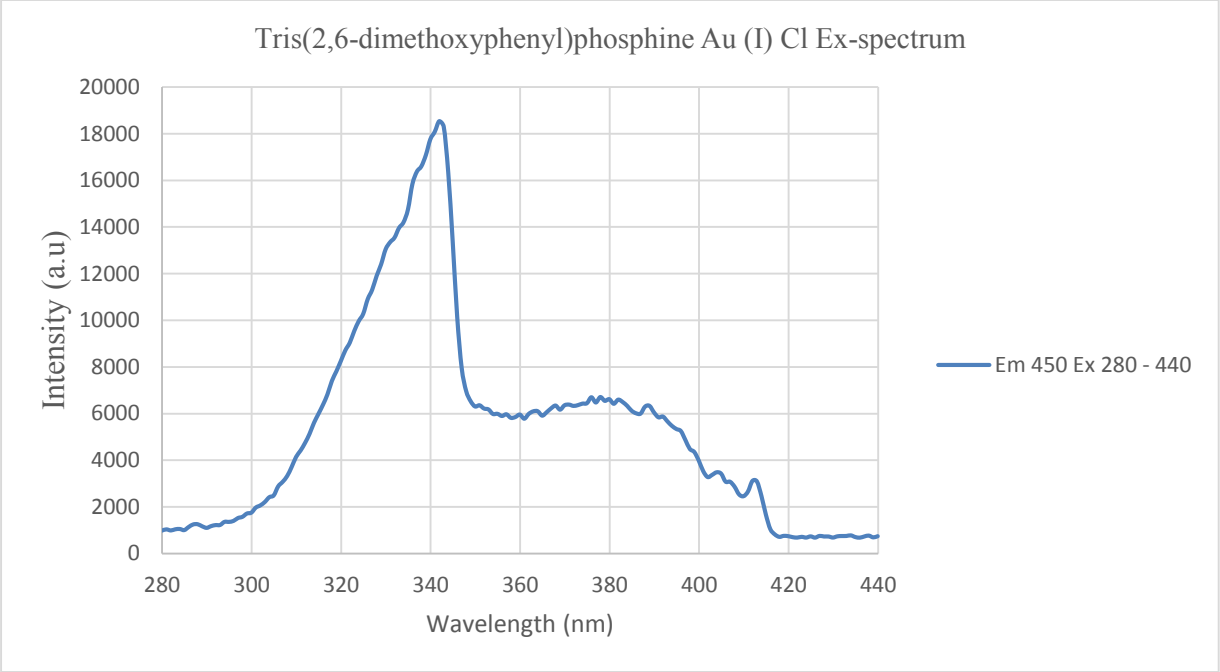

Figure 4.25. Excitation spectrum of $AuP(C_8H_9O_2)_3Cl$ collected in liquid nitrogen by monitoring the emission at 450 nm.

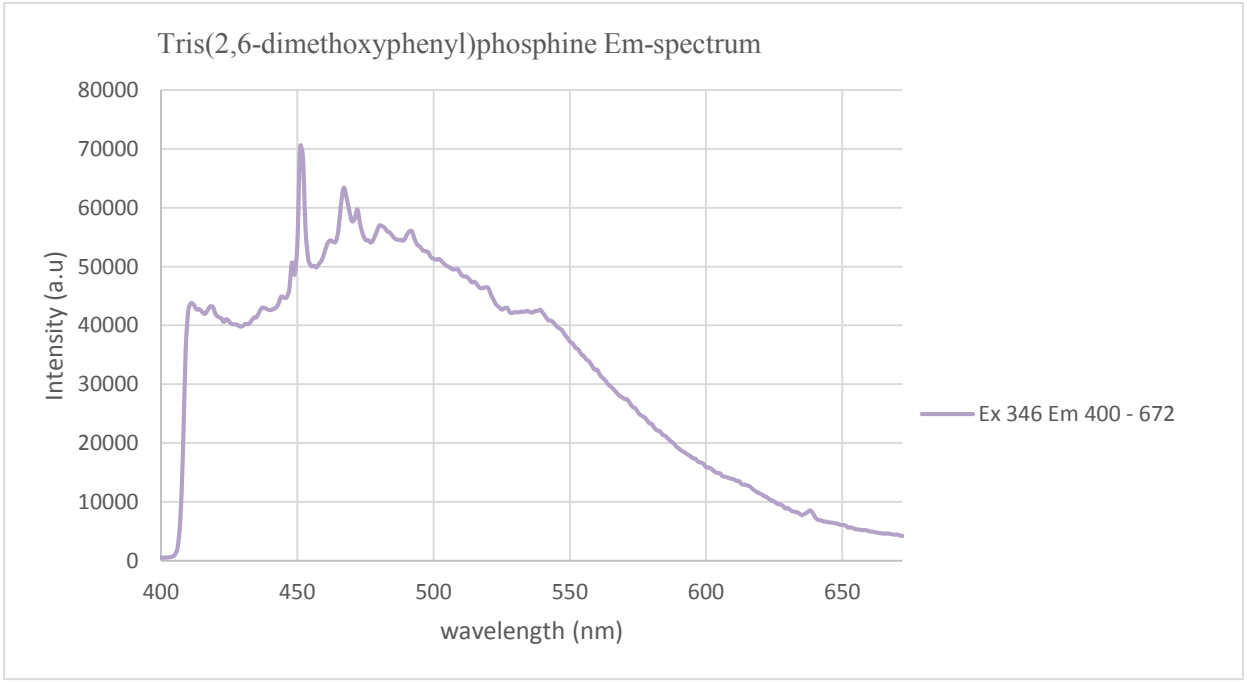

Figure 4.26. Emission spectrum of TDMPP ligand collected at room temperature by exciting it at 346 nm.

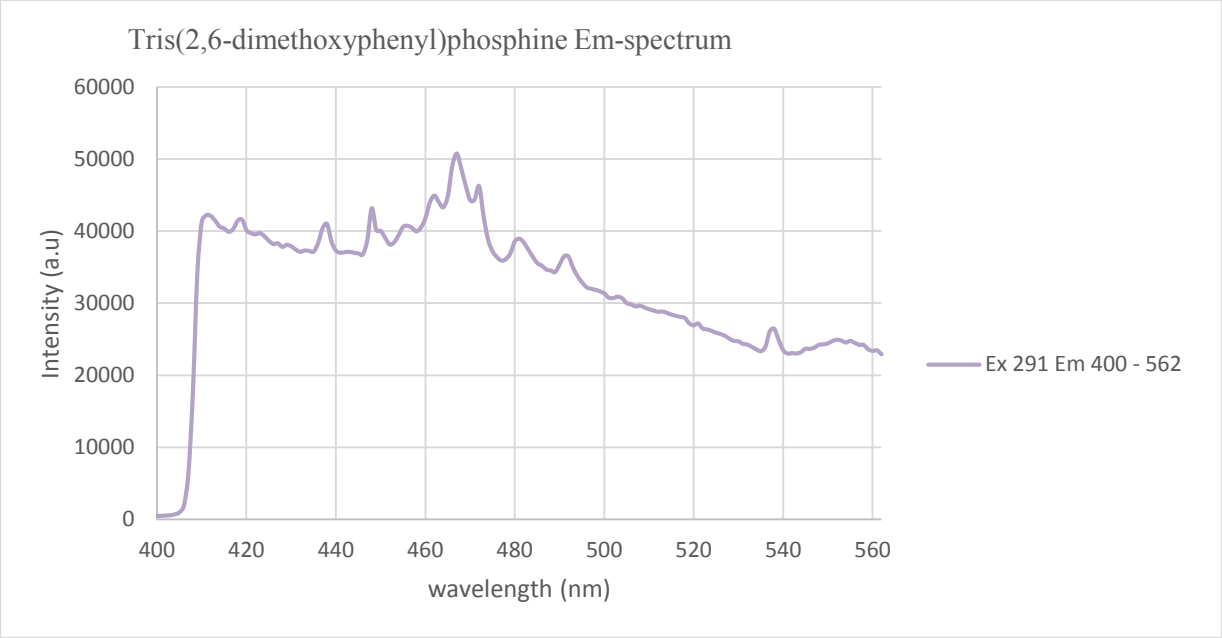

Figure 4.27. Emission spectrum of TDMPP ligand collected at room temperature by exciting it at 291 nm.

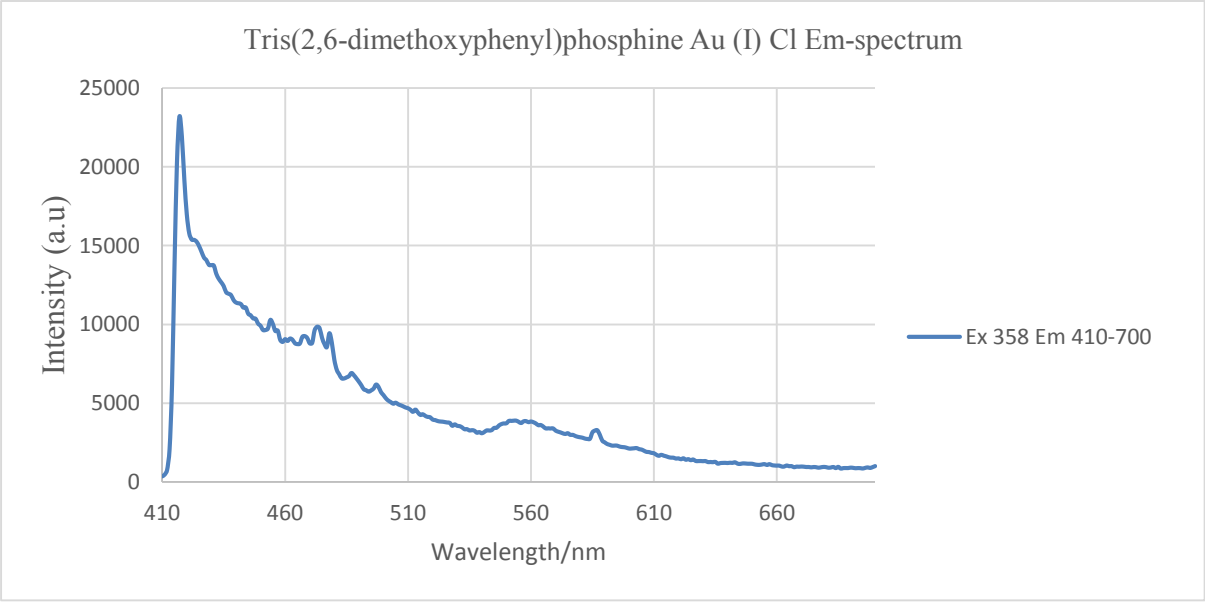

Figure 4.28. Emission spectrum of $AuP(C_8H_9O_2)_3Cl$ collected at room temperature upon excitation with the 358 nm wavelength.

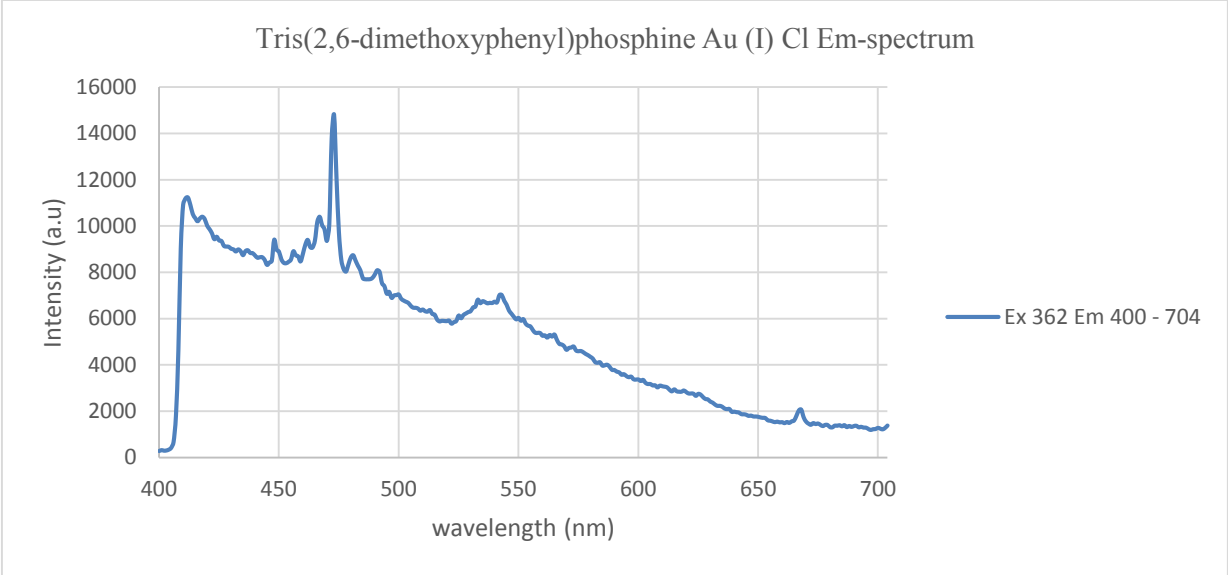

Figure 4.29. Emission spectrum of $AuP(C_8H_9O_2)_3Cl$ collected at room temperature by exciting it at 362 nm.

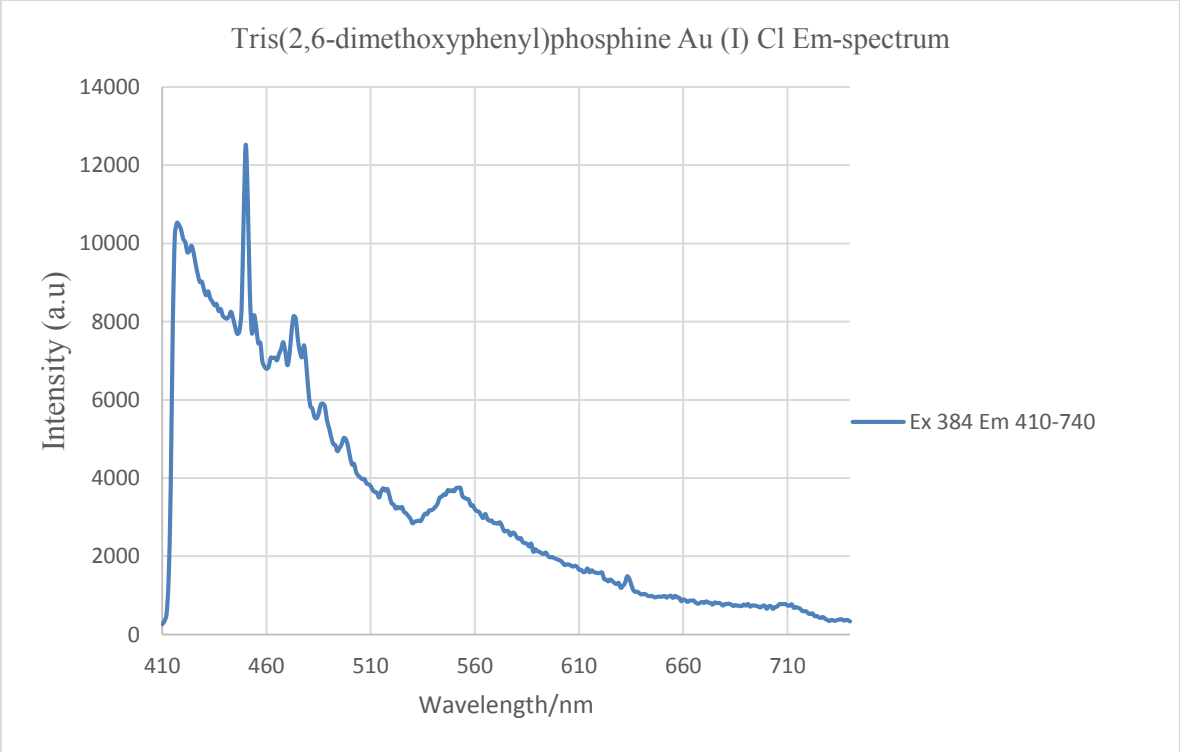

Figure 4.30. Emission spectrum of $AuP(C_8H_9O_2)_3Cl$ collected at room temperature upon excitation with the 384 nm wavelength.

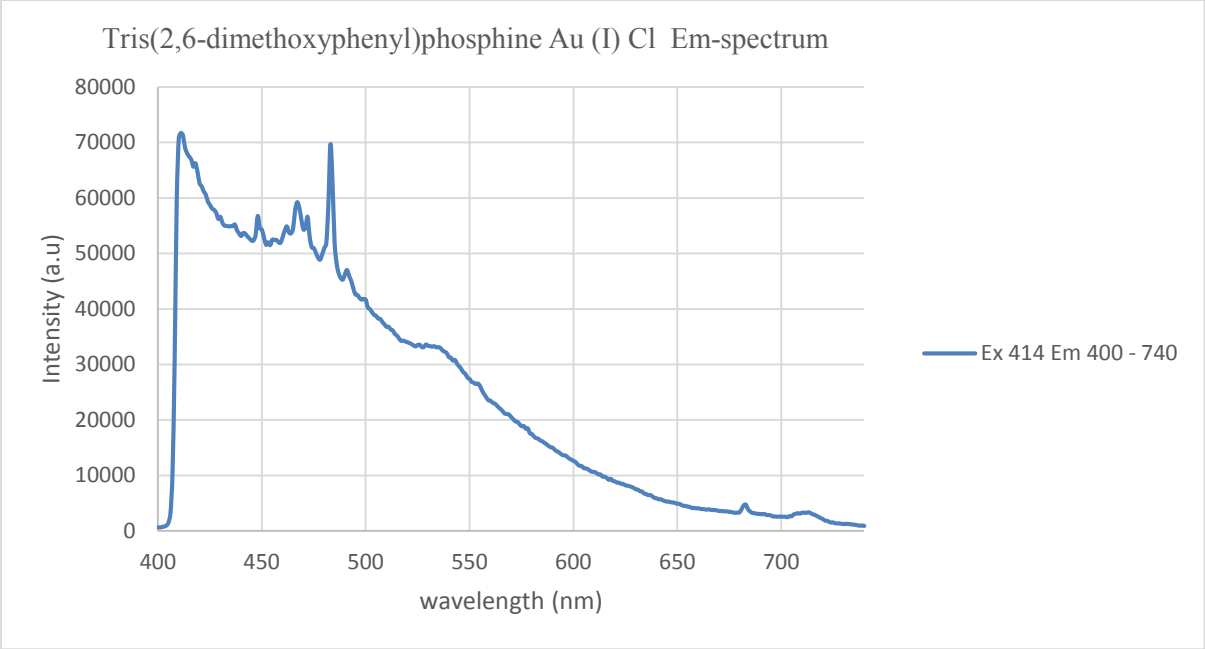

Figure 4.31. Emission spectrum of $AuP(C_8H_9O_2)_3Cl$ collected at room temperature upon excitation with the 384 nm wavelength.

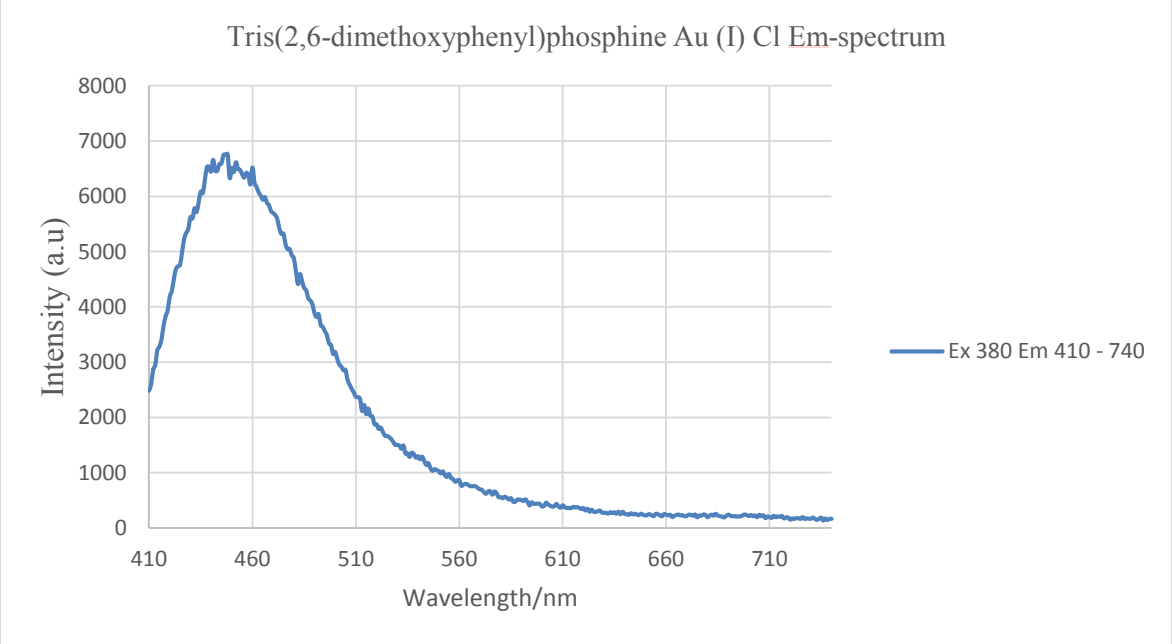

Figure 4.32. Emission spectrum of $AuP(C_8H_9O_2)_3Cl$ collected in liquid nitrogen upon excitation with the 384 nm wavelength.

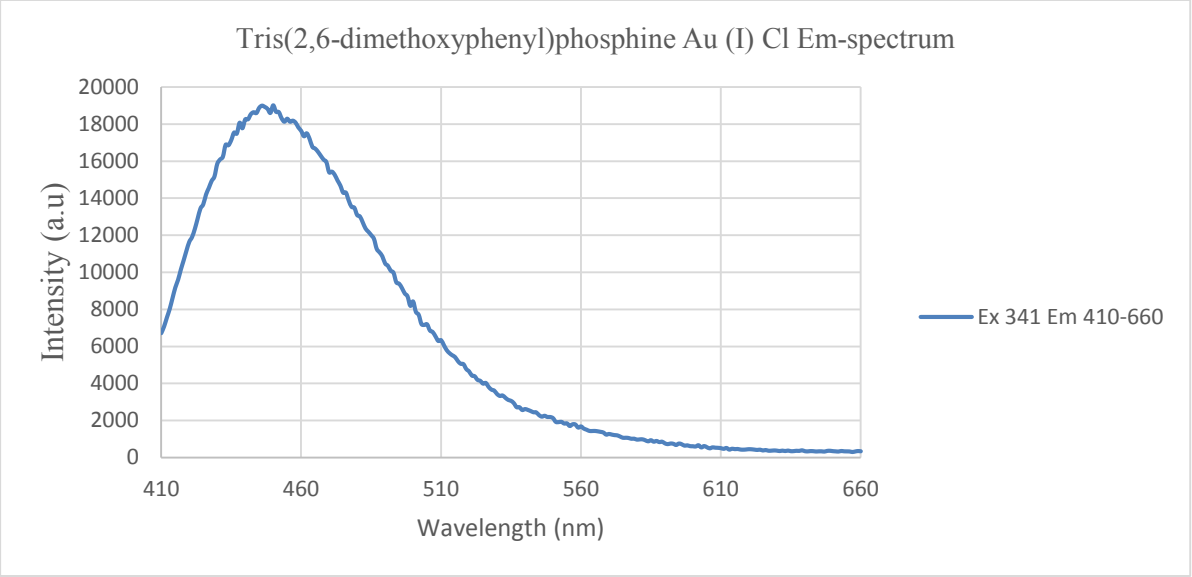

Figure 4.33. Emission spectrum of $AuP(C_8H_9O_2)_3Cl$ collected in liquid nitrogen upon excitation with the 384 nm wavelength.

Table 4.8

Atomic contributions for the ground state molecular orbitals of compound ***6****.*

ATOMIC CONTRIBUTIONS (%)					
Orbitals	Au	Ligand	P	O	C
128	14.20	85.80	4.64	5.42	75.86
127	3.07	96.93	5.68	4.29	86.96
126	3.06	96.94	5.67	4.74	86.53
HOMO-LUMO GAP					
125	14.07	85.93	9.94	14.02	61.97
124	1.22	98.78	1.72	27.18	69.88
123	1.88	98.12		25.98	72.14

Table 4.9

*Atomic orbital contributions in the ground state for compound **6***

ATOMIC ORBITAL CONTRIBUTIONS (%)					
Orbitals	Au	Ligand	P	O	C
128	7.35s, 5.76px 1.09d	13.87s, 36.11px, 18.53py, 17.29pz	1.96s, 2.69px	2.69py, 2.63pz	11.94s, 33.42px 15.84py, 14.66pz
127	1.02py, 2.05pz	8.10s, 35.56px 35.44py, 17.83pz	2.87py, 2.81pz	1.32px, 2.97py	8.10s, 34.24px 29.06py, 15.02pz
126	2.03py, 1.03pz	7.79s, 37.00px 19.78py, 32.37pz	2.81py, 2.86pz	2.39px, 2.35pz	7.79s, 34.61px 16.97py, 27.16pz
HOMO-LUMO GAP					
125	8.04s, 6.03d	2.27s, 42.92px 18.63py, 22.11pz	2.27s, 3.10px 4.57pz	6.52px, 4.88py 2.62pz	33.30px, 9.18py 19.49pz
124	1.22px	47.90px, 29.47py 21.41pz	1.72px	11.49px, 8.99py 6.70pz	34.69px, 20.48py 14.71pz
123	1.88d	50.82px, 10.74py 36.56pz		13.46px, 2.20py 10.32pz	37.36px, 8.54py 26.24pz

4.2.6 Raman Spectroscopy. The Raman spectra were collected by placing the crystals and the ligands on a microscope slide and analyzed using the Horiba XploRA Raman confocal microscope system. Figure 4.34, 4.35, 4.36 and 4.37 shows both experimental and theoretical Raman spectra for the mono-, di-, tri- and tetra-coordinated TDMOPP gold (I) complexes.

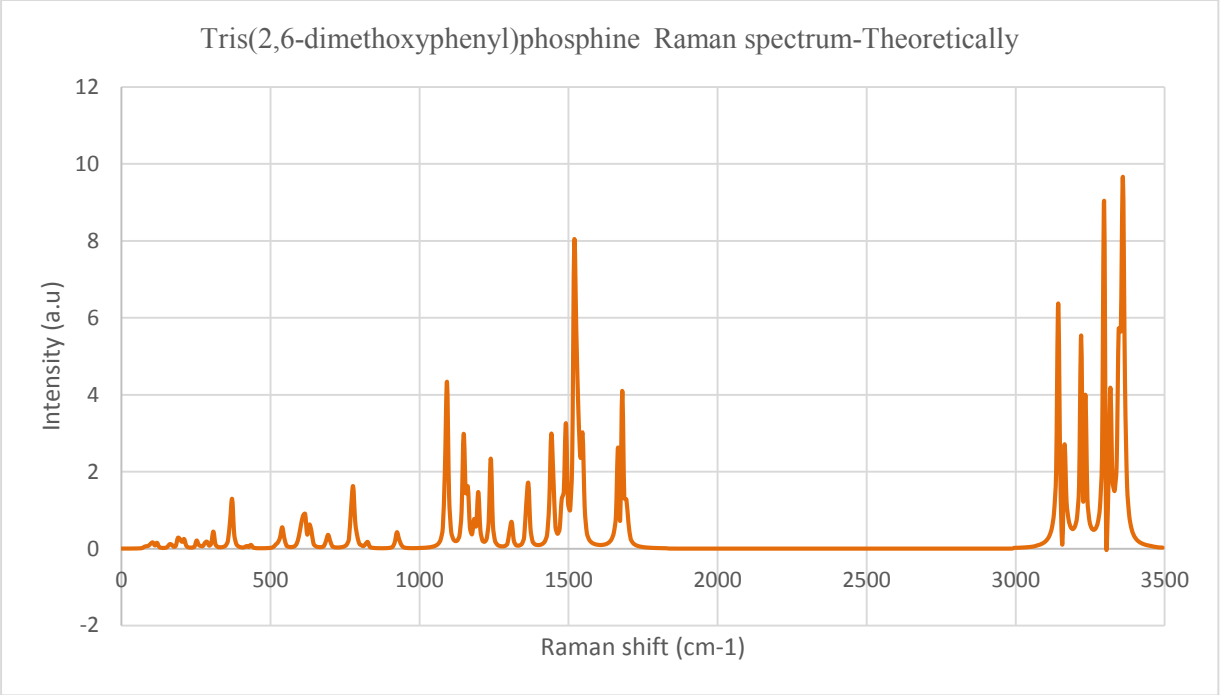

Figure 4.34. Raman spectrum for $P(C_8H_9O_2)_3$ obtained from the theoretical calculation using the Gaussian 09 software program.

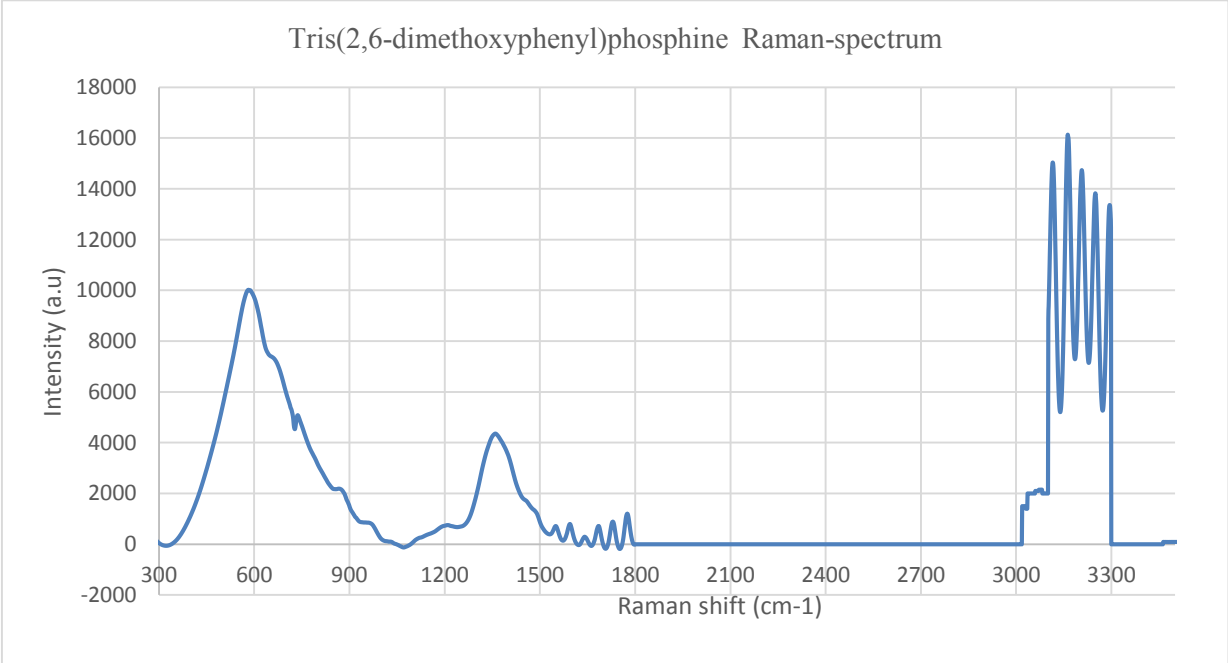

Figure 4.35. Raman spectrum for $P(C_8H_9O_2)_3$.

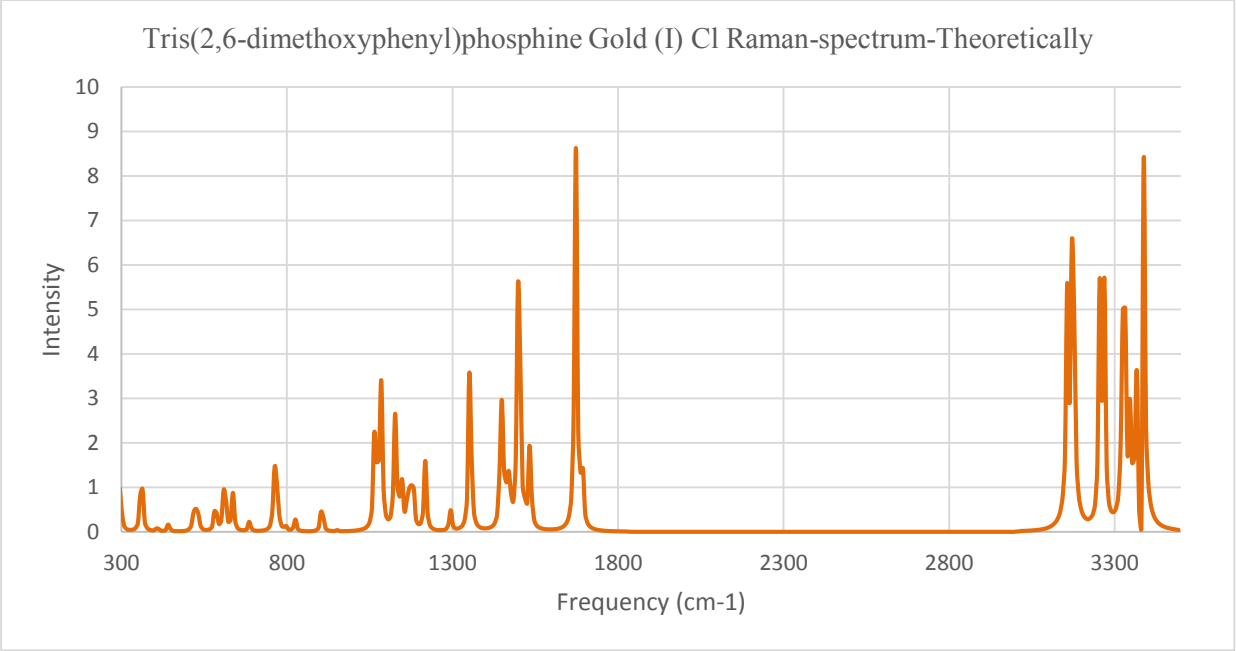

Figure 4.36. Raman spectrum for $AuP(C_8H_9O_2)_3Cl$ obtained from the theoretical calculation using the Gaussian 09 software program.

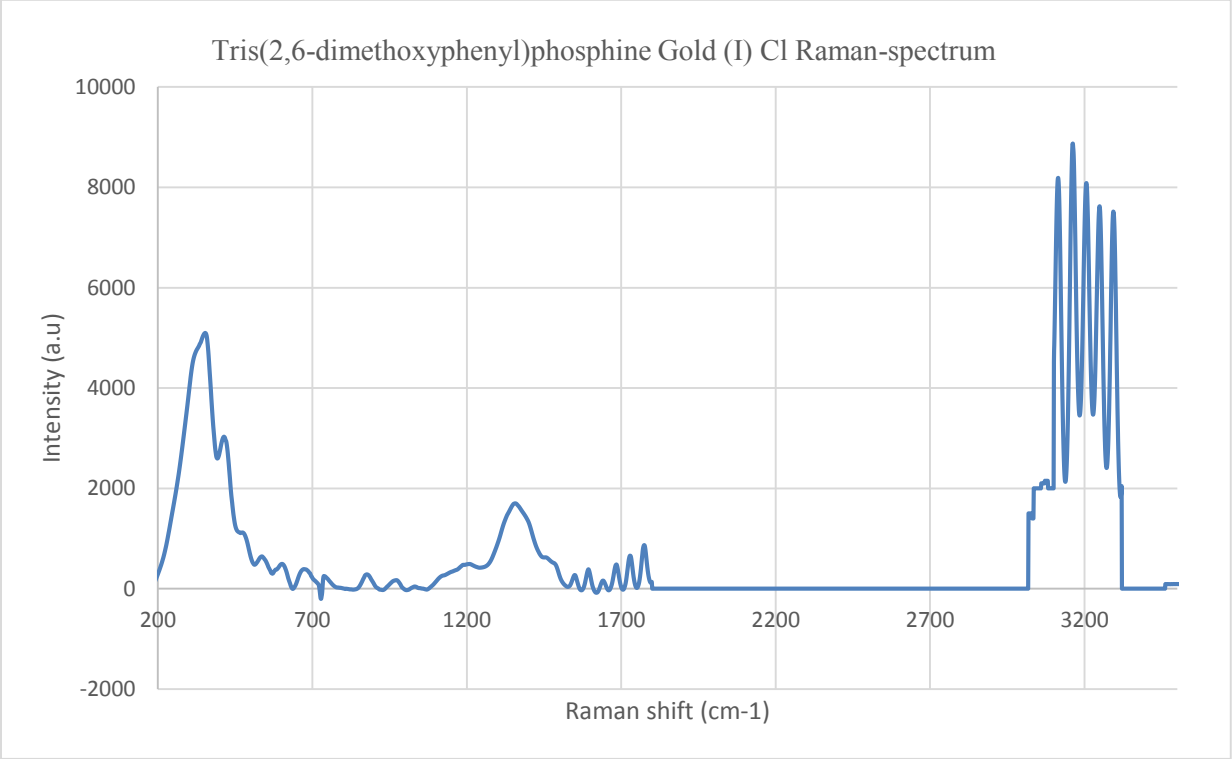

Figure 4.37. Raman spectrum for $AuP(C_8H_9O_2)_3Cl$.

4.3 Discussion

4.3.1 X-ray Crystallography. The X-ray crystal structures show a clear distinction between the various atoms and their connectivities. The P(1)—Au(1)—Cl(1) bond angle has a linear geometry with a bond angle of 177.0° for the monocoordinated TDMOPP gold complex, $AuP(C_8H_9O_2)_3Cl$ (**6**). The respective bond angle is in conformity with the linearity expected for sp hybridization found in Au(I) complexes. The Au(1)—P(1) and Au(1)—Cl(1) bond distances in $AuP(C_8H_9O_2)_3Cl$ shown on Table 4.2 are 2.243 (8) and 2.299 (10). There is no significant differences in values between the Au(1)—P(1) and Au(1)—Cl(1) bond lengths of **6** when compared to previous data on gold phosphine complexes. The X-ray data also show the lack of intermolecular Au‑Au aggregate formation. The weak aurophilic interactions are prevented due to steric factors as a result of the large cone angle of the TDMOPP ligand.

4.3.2 Infrared Spectroscopy (Vibrational Studies). The IR-spectrum of **6** at Figure 4.4 has twenty six (26) distinct bands. It shows a weak aromatic C–H stretching of the phenyl ring at 3001 cm^{-1}, the asymmetric and symmetric aliphatic C–H (CH_3) stretching at 2931 cm^{-1} and 2831 cm^{-1}, the C=C phenyl ring stretching pair at 1574 cm^{-1} and 1462 cm^{-1}, the aromatic C–O stretching at 1246 cm^{-1}, the aliphatic C–O stretching at 1165 cm^{-1}, the P–Ar stretching at 1103 cm^{-1}, the aromatic C–H bending at 895 cm^{-1}, the P–C stretching at 775 cm^{-1}, the Au-P stretching at 360 cm^{-1}, and the Au-Cl stretching at 330 cm^{-1}. The presence of the Au-P peak at 360 cm^{-1} which is absent in the spectrum of the ligand shown at Figure 4.3 is an indication that the TDMOPP ligand has been successfully coordinated to the gold (I) center. Nuclear site group theoretical analysis for **6** predicts twenty six (26) IR-active modes. From table 4.1, compound **6** has a space group of P-1 with Z = 4. With Z = 4, it means **6** contains four formula units per unit cell. The modes for this unit cell can be found by

consulting table 2A of Rousseau, et al. method [26]. The unit cell content of 96 C- atoms, 24 O-toms, 4 Au-atoms, 4 Cl-atoms and 4-P atoms, can be assigned, by inspection of table 2A, as 4 unique C-atoms and 2 unique O-atoms. Three of the unique C-atoms, one of the oxygen atoms along with an Au, Cl and P-atoms occupy C_1 sites, while the remaining O and C-atoms the must lie on the C_1 sites in one fold repetitively. From table 5B, the vibrational modes of compound **6** are $3A_u$ for the remaining O and C-atom, $3A_g + 3A_u$ for each nucleus on the C_1 sites. The total contribution from C, O, P, Au and Cl is, therefore, $21A_g + 27A_u$. From table 2E of Rousseau, et al. method [26] , the acoustic mode is A_u and the optical modes are $21A_g + 26A_u$. The distribution of the optical modes show that twenty six ($26A_u$) modes are expected to be IR-active from the selection rule. Comparison of these predictions with the observed and calculated spectra shows the presence of all twenty six distinct frequencies.

4.3.3 Nuclear Magnetic Resonance. The ^{1}H NMR spectrum of **6** shown at figure 4.8 showed splitting at chemical shift at δ = 7.2 (m, 6H, Ar–H), δ = 6.4 (m, 3H, Ar–H), and δ = 3.4 (s, 18H, CH_3). The peak intensities of the proton environments correspond to the number of H-atoms in the respective vicinities or environments. Comparison of the ^{1}H NMR spectral data between **6** and the free ligand (TDMOPP) shows a slight downfield shifting. Peaks for TDMOPP ligand found in figure 4.7 show splitting at δ = 7.2 (m, 6H, Ar–H), δ = 6.3 (m, 3H, Ar–H), and δ = 3.3 (s, 18H, CH_3). The slight difference in the position of the peaks between **6** and its ligand is an indication that the ligand has successfully coordinated to the gold center. The $^{31}P\{^1H\}$ NMR spectral data for the TDMOPP ligand, compounds **6** and **7** are shown at Figures 4.10, 4.11 and 4.12. Strong sharp peaks are observed at -33.0, -26.0 and -20.0 ppm respectively. With the coordination of the mono, di, tris, and tetrakis to the gold(I) chloride center the trend of downfield shifting is seen. As discussed previously for the other phosphine

ligands weakening of the gold-phosphine bond and consequently de-shielding causes the downfield shift of the peak.. The overall trend appears consistent for gold phosphine complexes where the mono substituted systems usually show smaller chemical shift values than the di, tri substituted complexes. For example, the mono, tris, and tetrakis substituted $(TFP)_nAuCl$ compounds have ^{31}P NMR coordination chemical shift (ccs) of 48.4, 66.1, 63.1, respectively [32]. Also, the mono, di, tris, and tetrakis substituted $(TPA)_nAuCl$ compounds have ^{31}P NMR values of -51.4, -36.1, -56.1, and -58.0 ppm respectively [27-31]. The increase in the chemical shift value on going from the TDMOPP, to the **6** and to the **7** is consistent with the general trend that chemical shift values increases as the coordination number increases. The trend of downfield shifting is also an indication that the ligand has successfully been coordinated to the gold (I) center.

4.3.4 UV-Vis Spectroscopy. The absorption spectral data for the TDMPP ligand, $AuP(C_8H_9O_2)_3Cl$ and $AuP((C_8H_9O_2)_3)_2Cl$ reveal similarities in their high-energy broad UV absorption profiles. The absorbance maximum for the free TDMOPP ligand shown at Figure 4.15 is observed at 250 nm with a smaller less intense band at 290 nm with low energy tail extending all the way to 400 nm. Similarly, both the mono and the dicoordinated TDMOPP-gold(I) complexes also show similar higher energy band maxima near 250 nm . Based on the spectral similarities between the ligand and the complexes as well as the molar absorptivity values of 6.30×10^4 $M^{-1}cm^{-1}$, 9.51×10^4 $M^{-1}cm^{-1}$ and 1.68×10^5 $M^{-1}cm^{-1}$ for the TDMOPP, $AuP(C_8H_9O_2)_3Cl$ and $AuP((C_8H_9O_2)_3)_2Cl$ respectively, the 250 nm band is assignable to a $\pi \rightarrow \pi^*$ intraligand transition, which is as result of the presence of double bond in the aromatic phenyl ring. The transition is slightly affected by the coordination with the Au metal. The weaker band at 290 nm which is present in the ligand is absent in the absorption spectra of the complexes **6**

and **7** at Figure 4.16 and 4.17 respectively, indicating that the transition is affected by coordination with the metal. This band is assignable to an n→π* transition and its absence in the absorption spectrum of **6** and **7** is indicative of participation of the lone pair electrons in the bonding scheme of the TDMOPP ligand. The higher molar extinction coefficient value of the ligand and the complexes is an indication that the electronic transitions involved as a result of the absorption are statistically probable (said to be 'allowed') due to the fact that their molar extinction **ε** values are in excess of 10 000. It is also interesting to note that the TDMOPP ligand, the **6** and the **7** complexes absorbs at similar energies but with the extinction coefficients of **7** about twice more intense than that of **6** and in turn about twice that of the TDMOPP ligand . The enhancement of the extinction coefficient in **7** relative to **6** and relative to TDMOPP is understandable in view of the presence of two more identical chromophores absorbing at the same region.

4.3.5 Luminescence. The gold(I) complexes and the TDMOPP ligand luminescent when excited under UV radiation. The emission spectra of the complexes both at room temperature and in liquid nitrogen have very similar profiles indicating a similar origin for the electronic transitions. The emission spectra of the TDMOPP ligand at room temperature shown at Figure 4.26 and 4.27 is characterize by a sharp band and maximizes around 452 nm. The gold complex (**6**) shown at Figure 4.28 to 4.31 also maximizes around 478 nm. The shift to the longer wavelength (red shift) from 452 nm of the TDMOPP to 478 nm of $AuP(C_8H_9O_2)_3Cl$ is due to the fact that at the excited states, the π→π* transitions of the TDMOPP is more polar than their ground states and as a result, a greater charge separation is observed in the excited state. The coordination of the TDMOPP to the gold (I) center causes a dipole–dipole interaction which reduces the energy of the excited state more than the ground state, hence making the

$AuP(C_8H_9O_2)_3Cl$ to emit at a longer wavelength. This emission at a longer wavelength by $AuP(C_8H_9O_2)_3Cl$ compare to the ligand is also an indication that the ligand has successfully been coordinated to the gold (I) center. Similar emission bands for **6** in liquid nitrogen were observed at 454 nm (Figure 4.32 – 4.33) showing fine vibronic structures arising from the ν(C=C) stretch of the phenyl ring of the ligand. Vibrational progressions with spacings of 1350 cm^{-1} were also observed in complex **6** in liquid nitrogen, typical of the ν(C=C) vibrational mode of the phenyl group. The excitation spectrum of the TDMOPP ligand and that of **6** at room temperature and in liquid nitrogen shown at Figure 4.20-21 for TDMOPP and Figures 4.22-24 for **6** consists of a well-defined broad band with an average spacing of 1300-1350 cm^{-1}. This spacing is assignable to an electronic transition coupled with vibronic component corresponding to ν(C=C) symmetric stretching mode within the phenyl ring. With reference to the previous luminescence studies on tertiary phosphine gold(I) complexes the emission bands at 478 nm in complexes **6** tentatively assigned as derived from excited states of P–> Au ligand-to-metal charge transfer (LMCT) origin. This suggests that the ligand centered transition is responsible for the photoluminescence in **6**.

4.3.6 Raman Spectroscopy. The Raman-spectrum of **6** at Figure 4.37 has twenty one (21) distinct peaks. It showed the appearance characteristic bands at 3117 cm^{-1} for υ(C–H) stretching of the phenyl ring, 2970 cm-1 for (O-CH3) stretch, 1574cm^{-1} for the asymmetric δ(CH_3) stretching, 1580 cm^{-1} for υ(CC) aromatic ring chain vibrations, 1339 cm-1 for δ (CH_3) symmetric stretching, 1100 cm^{-1} for the P–Ar stretching, 850 cm-1 for υ(C-O-C) symmetric stretching, 360 cm^{-1} for the Au-P stretching, 315 cm-1 for the Au-Cl. Group Theoretical Analysis (Nuclear site group analysis) for **6** also predicts twenty one (21) Raman-active modes. Table 4.5 summarizes the group theoretical analysis for 6. The presence of the Au-P peak at 360

cm^{-1} which is absent in the spectrum of the ligand shown at Figure 4.35 is an indication that the TDMOPP ligand has been successfully coordinated to the gold (I) center.

4.3.7 Computational Studies

4.3.7.1 Structural Comparison. The X-ray crystallographic structure of **6** were compared to theoretical calculations using the GAUSSIAN ‘09 software package. Shown in Table 4.3 are selected bond angles and bond distances of **6**. Although slightly shorter, the calculated bond distances for Au(1)—Cl(1) and Au(1)—P(1) respectively using the LANL2DZ basis set are in good agreement with the experimental X-ray crystal structures data as given in Table 4.2. The experimental bond distances of 2.299(10) [Å] and 2.244(8) [Å] for **6** changes by 0.032 [Å] and 0.145[Å] from the calculated bond distances of (2.331[Å]) and (2.389[Å]) for Au(1)—Cl(1) and Au(1)—P(1) respectively. Similarly the theoretical bond angles of 180.0 °, 110.1°and 108.9[°] for P(1)—Au(1)—Cl(1), C(1)—P(1)—Au(1) and C(17)—P(1)—C(9) respectively for **6**, are in agreement with the experimental bond angles of 177.0[°] for P(1)—Au(1)—Cl(1), 112.1[°] for C(1)—P(1)—Au(1) and 111.0[°] for C(17)—P(1)—C(9).

4.3.7.2 Spectroscopic Comparison. The theoretical calculated IR spectrum of **6** using Gaussian 09 shown in Figure 4.5 also predicts twenty five (25) distinct bands with a slight shift in the position of some of the individual peaks, but on a whole both the calculated and the experimental spectra of both the ligand and the complex shows similar IR-spectra. The theoretical ^{1}H NMR spectrum for both the ligand and the gold complex shown on Figures 4.13 and 4.14 also show similar splitting patterns and chemical shift values as that of the experimental ones.

4.3.7.3 Electronic Comparison

4.3.7.3.1 Luminescence. The result of the population analysis for **6** is shown in Table 4.8 and 4.9 for the percentage atomic and atomic orbital contributions respectively for the metal

and the TDMOPP ligand, as well as individual atomic participation for the selected highest three occupied molecular orbitals and lowest three unoccupied molecular orbitals. The second highest occupied molecular orbital (SHOMO), HOMO-124 has the largest contribution from the ligand at 98.28% and the metal at 1.72% followed by the third highest occupied molecular orbital (THOMO), HOMO-123 at 98.12% and 1.88% contributions, respectively. The contribution of the gold atom in the HOMO-124 orbital derives from 5px atomic orbitals at 1.72% contributions. The atomic contribution of the TDMOPP ligand is comprised of Phosphorus, Oxygen and Carbon with percentage contributions of 47.90px, 29.47py and 21.41pz orbitals. However, the gold contribution of the THOMO comes from 1.88% of the 5dxz atomic orbitals with the remaining contribution from the 5px, 5py and 5pz orbitals of the phosphorus, Oxygen and Carbon atoms of the TDMOPP ligand. The table also shows the first three lowest unoccupied molecular orbital (LUMOs) contributions, which are mainly ligand centered contributions. The orbital description as ligand based and partial metal based transitions is thus substantiated to support the observations surrounding the luminescent behavior of **6** and hence the assignment of $\pi \rightarrow \pi^*$ transition is in a proper order.

4.3.7.3.2 UV-Vis. The HOMO‑LUMO gap calculated value by the TD-DFT method was 36,426 cm^{-1} corresponding to 274.54 nm. The theoretical calculated spectrum for **6** obtained using TDDFT with the LANL2DZ basis set to identify the orbital(s) contributing to the observed absorption is shown at Figure 4.18. The TD-DFT generated ground-state to excited-transitions is shown on Table 4.6 which summarizes the orbital that took part most in the transitions X, Y, and Z. From Table 4.6, transition X supports an assignment of the SHOMO-124→LUMO-128, a $\pi \rightarrow \pi^*$ type transition. This confirms why the $n \rightarrow \pi^*$ is not present in the experimental UV-Vis spectrum of **6**. The transition Y and Z has transitions both from the third HOMO-123→LUMO-

126 and to the LUMO-127 respectively. Table 4.7 summarizes the various transitions pictorially of the theoretically generated ground-state to excited-state transitions for X, Y and Z. These calculated spectrum values are in good agreement with the experimental UV-Vis spectrum with a slight red shifting of about 24 nm.

CHAPTER FIVE

Synthesis and Characterization of mono-, bis-, tris-, and tetrakis-{tris(4-methoxyphenyl)phosphine} gold(I) complexes

5.1. Syntheses

5.1.1 Tris(4-methoxyphenyl)phosphine gold (I) chloride (10). Tris(4-methoxyphenyl)phosphine (0.0200 g, 0.057 mmol) was added to a solution of $(C_4H_8S)AuCl$ (0.0132 g, 0.057 mmol) in tetrahydrofuran (20 ml) at −80 ˚C and the reaction stirred for 2 hours. The solvent was removed by purging nitrogen gas into the solution, until all the solvent dried up. The residue was then recrystallized from CH_2Cl_2/n-hexane mixture for several days. Partial evaporation of the solvent provided quality crystals.

5.1.2 Bis{tris(4-methoxyphenyl)phosphine} gold (I) chloride (11). Tris(4-methoxyphenyl)phosphine (0.0400 g, 0.114 mmol) was added to a solution of $(C_4H_8S)AuCl$ (0.0132 g, 0.057 mmol) in tetrahydrofuran (20 ml) at −80 ˚C and the reaction stirred for 2 hours. The solvent was removed by purging nitrogen gas into the solution, until all the solvent dried up. The residue was then recrystallized from CH_2Cl_2/n-hexane mixture for days. Partial evaporation of the solvent provided quality crystals.

5.1.3 Tris{Tris(4-methoxyphenyl)phosphine} gold (I) chloride (12). Tris(4-methoxyphenyl)phosphine (0.0600 g, 0.171 mmol) was added to a solution of $(C_4H_8S)AuCl$ (0.0132 g, 0.057 mmol) in tetrahydrofuran (20 ml) at −80 ˚C and the reaction stirred for 2 hours. The solvent was removed by purging nitrogen gas into the solution, until all the solvent dried up. The residue was then recrystallized from CH_2Cl_2/n-hexane mixture for several days. Partial evaporation of the solvent provided quality crystals.

5.1.4 Tetrakis{tris(4-methoxyphenyl)phosphine} gold (I) chloride (13). Tris(4-methoxyphenyl)phosphine (0.0400 g, 0.228 mmol) was added to a solution of $(C_4H_8S)AuCl$ (0.0132 g, 0.057 mmol) in tetrahydrofuran (20 ml) at −80 ˚C and the reaction stirred for 2 hours. The solvent was removed by purging nitrogen gas into the solution, until all the solvent dried up. The residue was then recrystallized from CH_2Cl_2/n-hexane mixture for days. Partial evaporation of the solvent provided quality crystals.

5.2 Results

5.2.1 X-ray Crystallography. Diffraction data were collected on x-ray quality crystals. The structure of the monocoordinated TFMOPP gold (I) complex, $AuP(C_7H_7O)_3Cl$, has already been published by Soo Yei Ho and Edward R. T. Tiekink[33]. However, the di-, tri and the tetra-coordinated complexes have been synthesized and studied in this research.

5.2.2 Infrared Spectroscopy. All infrared spectra were obtained as potassium bromide (KBr) disc, prepared by compressing the ground mixture of sample and KBr powder, on a Shimadzu IR-PRESTIGE-21 Fourier transform infrared spectrophotometer (4000−300 cm^{-1}). Figure 5.1, 5.2, 5.3 and 5.4 shows both experimental and theoretical IR spectrum of the mono-, di-, tri- and tetracoordinated TFMOPP gold (I) complexes.

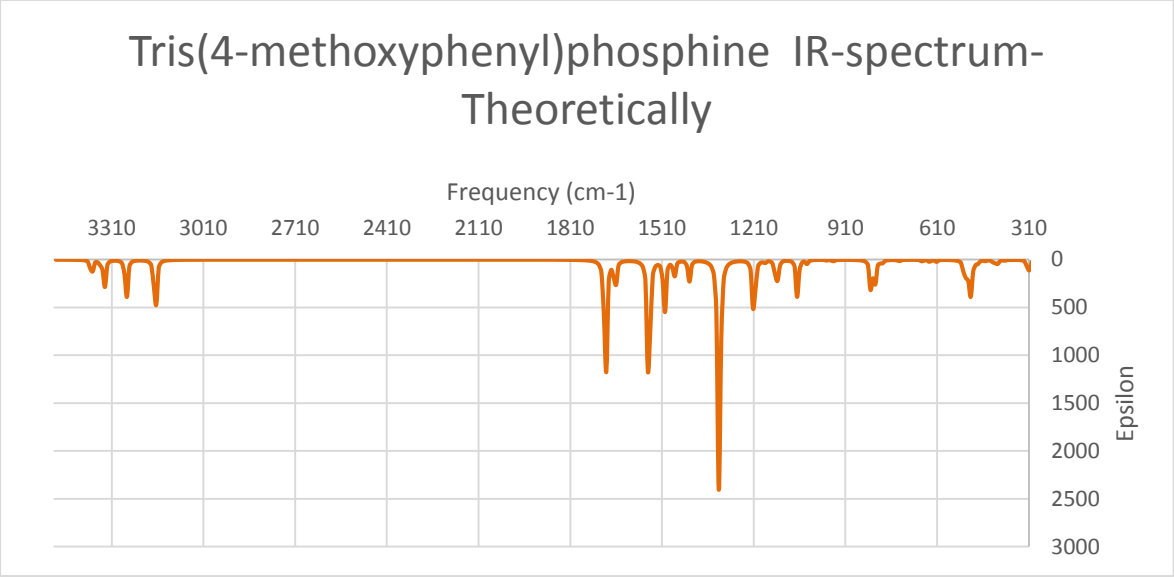

Figure 5.1. Theoretically calculated IR spectrum for $P(C_7H_7O)_3$ measured using Gaussian 09 software.

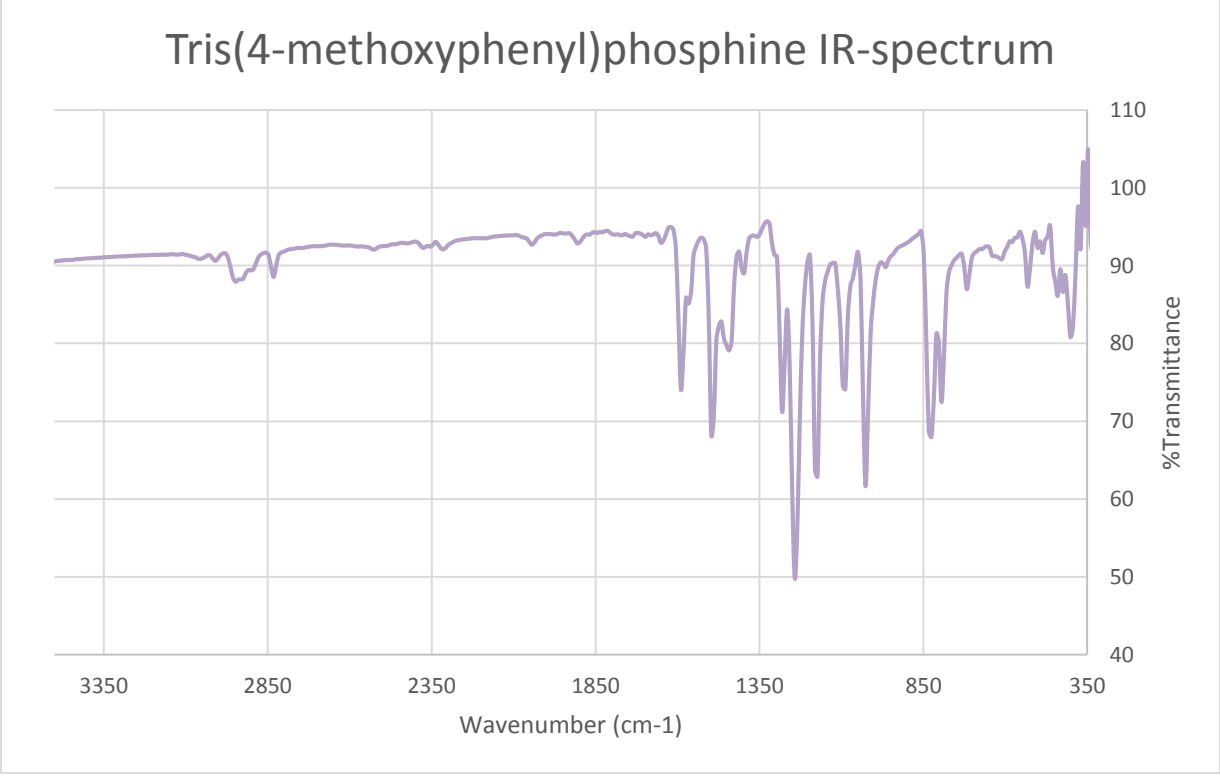

Figure 5.2. IR spectrum for $P(C_7H_7O)_3$.

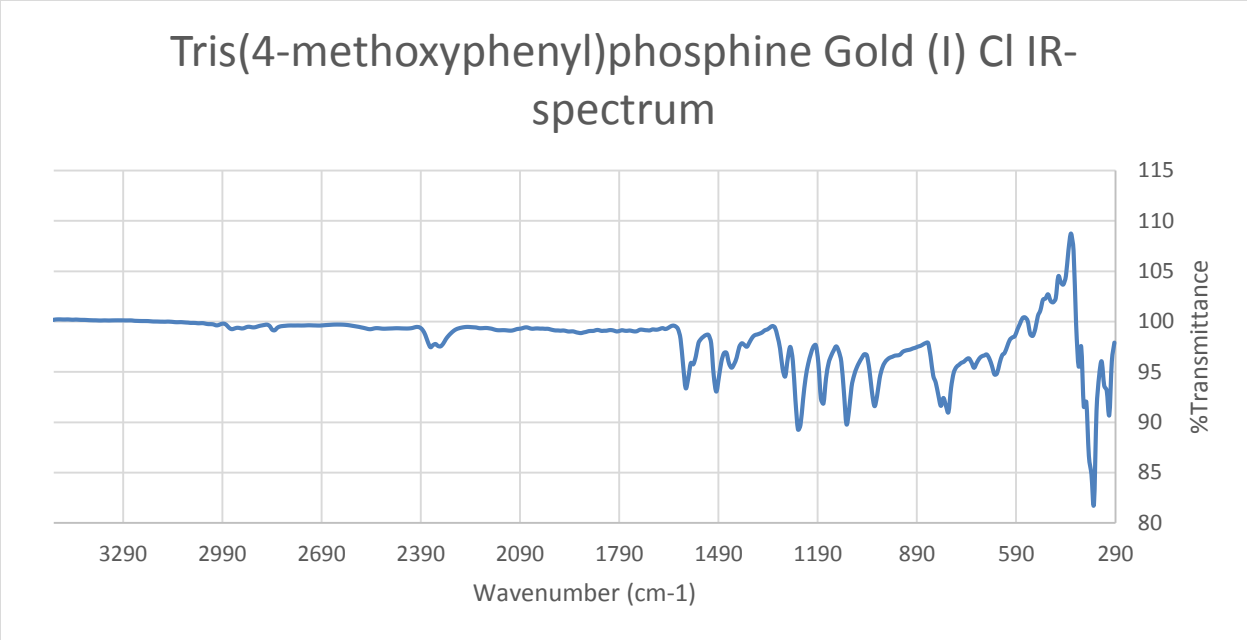

Figure 5.3. IR spectrum for $AuP(C_7H_7O)_3Cl$.

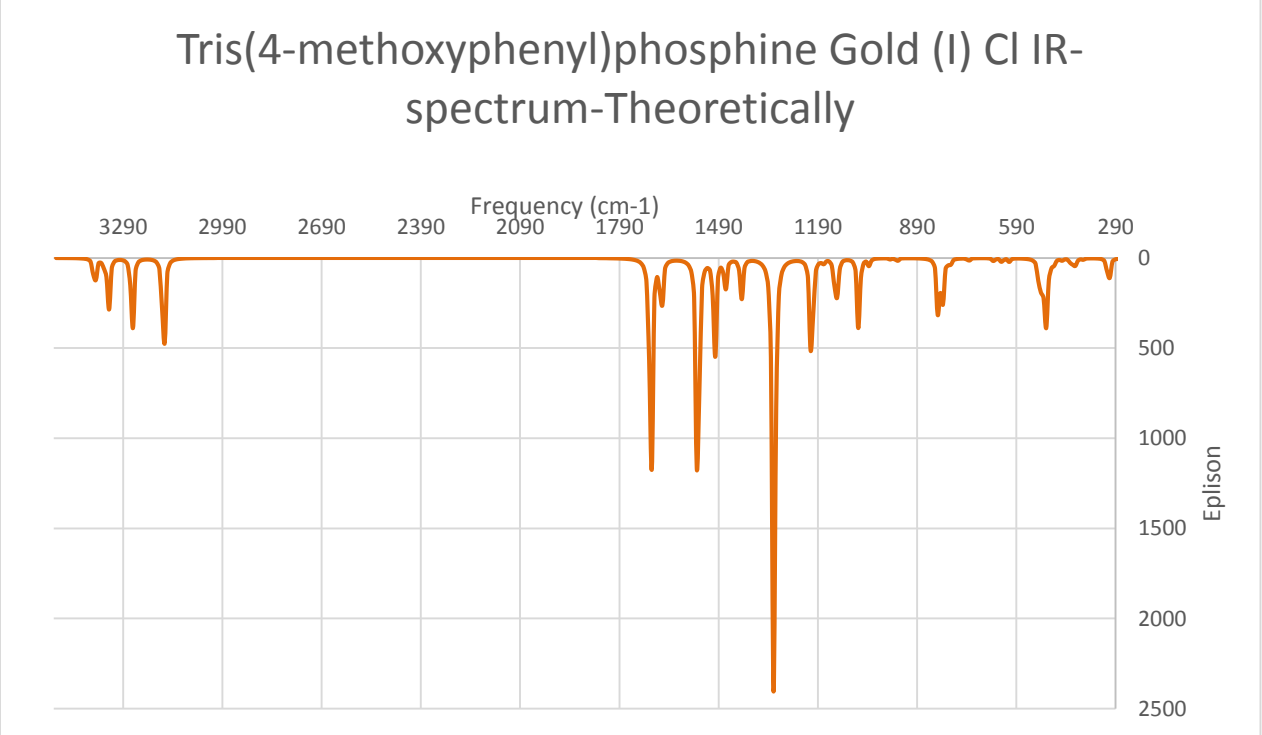

Figure 5.4. Theoretically calculated IR spectrum for $AuP(C_7H_7O)_3Cl$ using Gaussian 09 program.

Table 5.1

Nuclear site group theoretical analysis for $AuP(C_7H_7O)_3Cl$

NUCLEAR SITE GROUP ANALYSIS FOR $[AuP(C_7H_7O)_3Cl]$					
ATOMS	Au	P	Cl	O	C
SITES (5A)	C_1	C_1	C_1	C_2	C_i
VIBRATIONAL (5B)	$3A_g + 3A_u + 3B_g + 3B_u$	$3A_g + 3A_u + 3B_g + 3B_u$	$3A_g + 3A_u + 3B_g + 3B_u$	$A_g + A_u + 2B_g + 2B_u$	$3A_u + 3B_u$
TOTAL CONTRIBUTION = $10A_g + 13A_u + 11B_g + 14B_u$					
ACOUSTIC MODES (5E) = $A_u + B_u$					
OPTICAL MODES = $10A_g + 12A_u + 11B_g + 13B_u$					
IR ACTIVE (5E) = $12A_u + 13B_u$					
RAMAN ACTIVE (5E) = $10A_g + 11B_g$					

5.2.3 Nuclear Magnetic Resonance. The ^1H NMR spectral data for the monocoordinated TFMOPP gold complex is shown in Figure 5.6. Strong peaks are observed at 3.8 (9H), 6.9 (6H) 7.5 (6H) ppm. The 1H NMR spectral data for the free ligand, TFMOPP, is also given in Figure 5.5 showing peaks at 3.8(9H), 6.8 (6H), 7.4 (6H) ppm. The $^{31}P\{1H\}$ NMR spectral data for the ligand, and compound 10 is given in Figures 5.7, and 5.8 showing peaks at 31.0, and 40.0 ppm, respectively. Theoretically calculated proton NMR using Gaussian 09 is also shown in Figures 5.9 and 5.10.

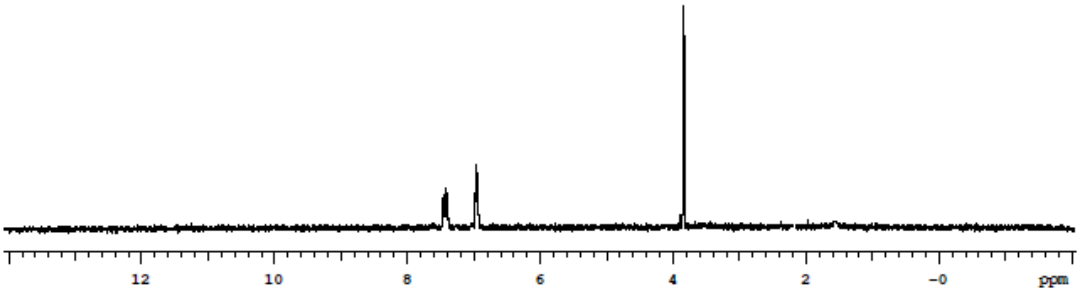

Figure 5.5. ^{1}H NMR spectrum of $P(C_7H_7O)_3$.

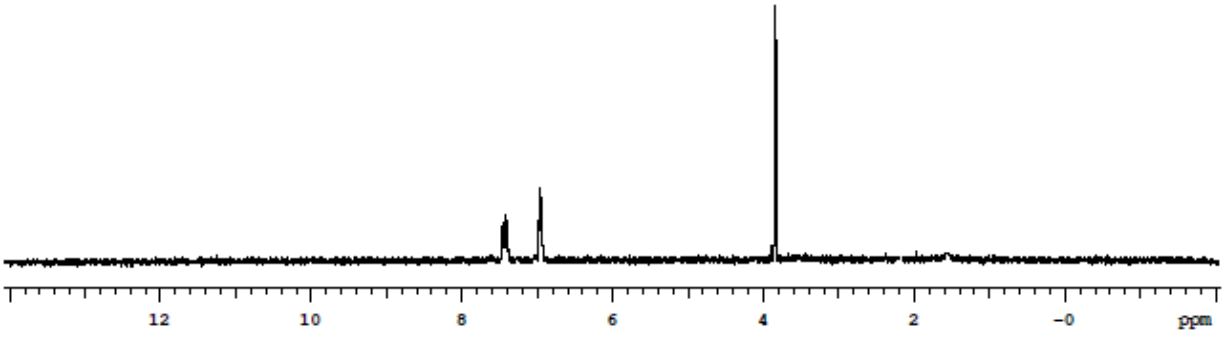

Figure 5.6. ^{1}H NMR spectrum of $AuP(C_7H_7O)_3Cl$.

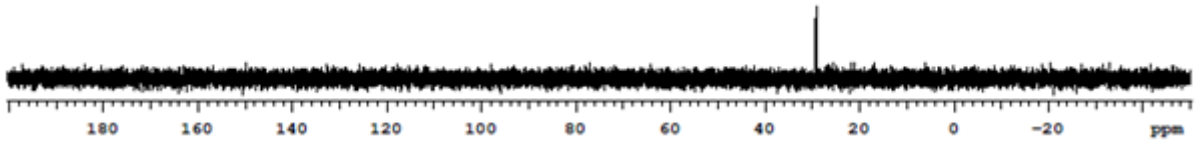

Figure 5.7. $^{31}P\{^{1}H\}$ NMR spectrum of $P(C_7H_7O)_3$.

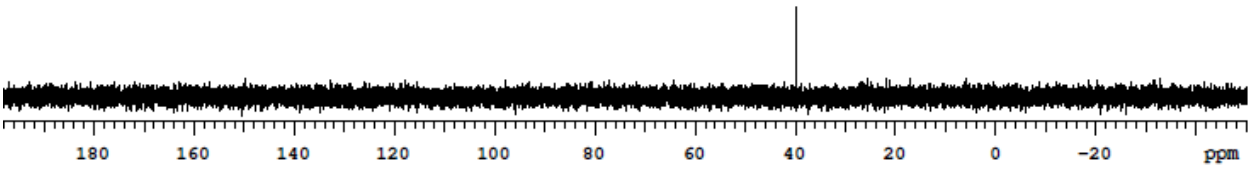

Figure 5.8. $^{31}P\{^{1}H\}$ NMR spectrum of $AuP(C_7H_7O)_3Cl$.

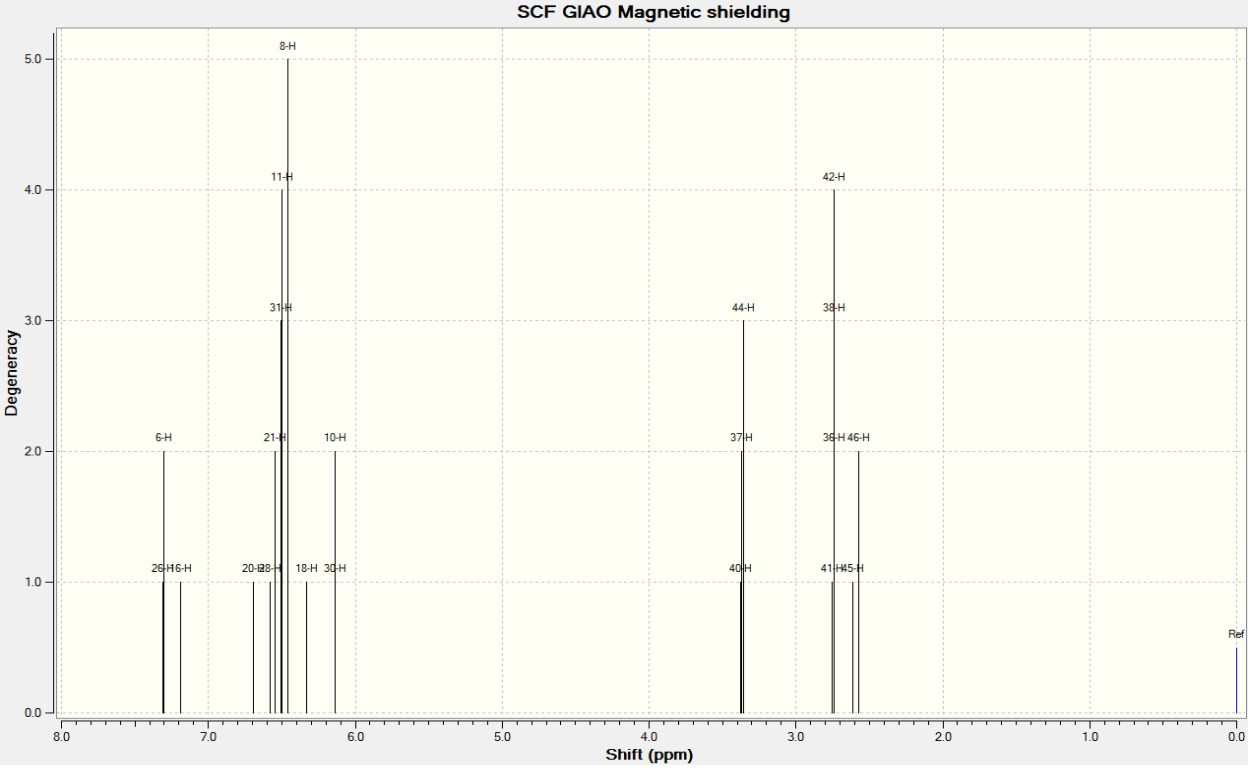

Figure 5.9. ^{1}H NMR spectrum of $P(C_7H_7O)_3$ calculated theoretically using Gaussian 09 software.

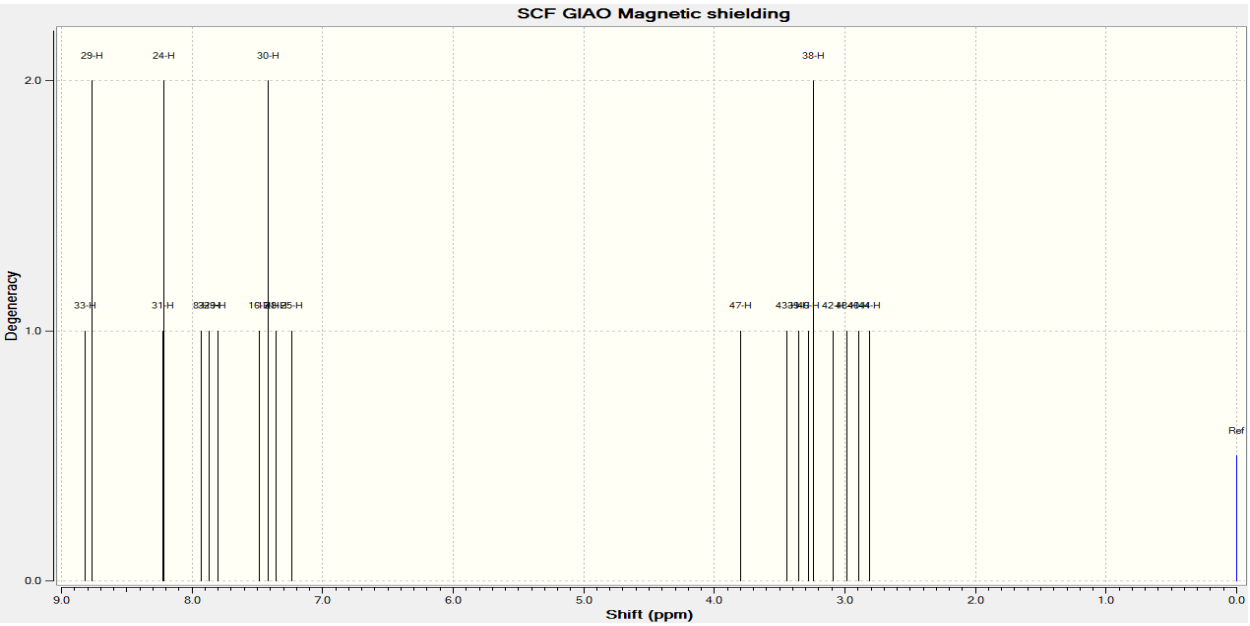

Figure 5.10. ^{1}H NMR spectrum of $AuP(C_7H_7O)_3Cl$ calculated theoretically using Gaussian 09 software.

5.2.4 UV-Vis Spectroscopy. All of the samples used for the ultraviolet visible (absorption) experiment, were dissolved in spectroscopic grade acetonitrile (CH_3CN). The TFMOPP ligand has a broad absorption spectrum shown at Figure 5.11 that maximizes around 250 nm with a calculated molar absorptivity of 5.81 x 10^4 $M^{-1}cm^{-1}$. The absorption spectrum of **10** shown at Figure 5.12 has a broad absorption profile maximizes at about 250 nm with a calculated molar absorptivity of 8.89 x 10^4 $M^{-1}cm^{-1}$. The theoretical spectrum using DFT calculations, shows a spectrum in Figure 5.13 and 5.14 with a broad absorption bands at 260 nm and 250 for the ligand and **10,** respectively.

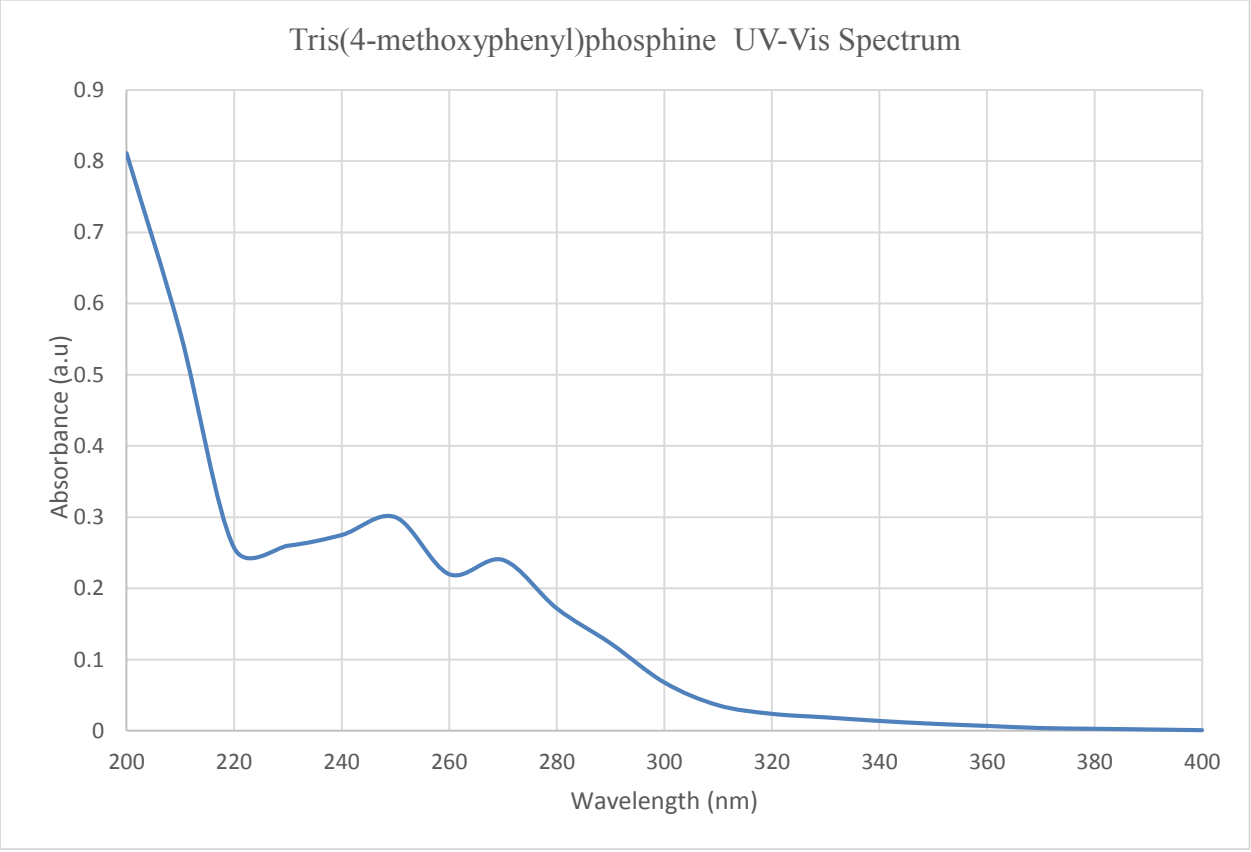

Figure 5.11. UV-Vis spectrum of $P(C_7H_7O)_3$.

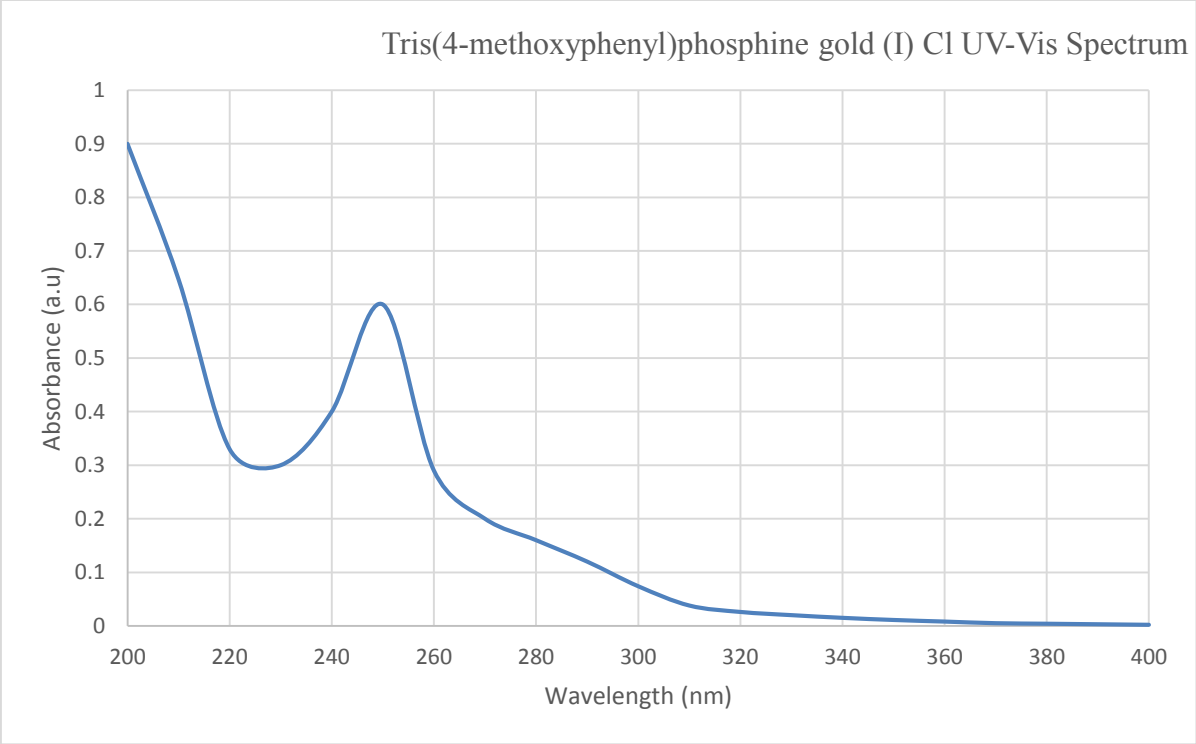

Figure 5.12. UV-Vis spectrum of $AuP(C_7H_7O)_3Cl$.

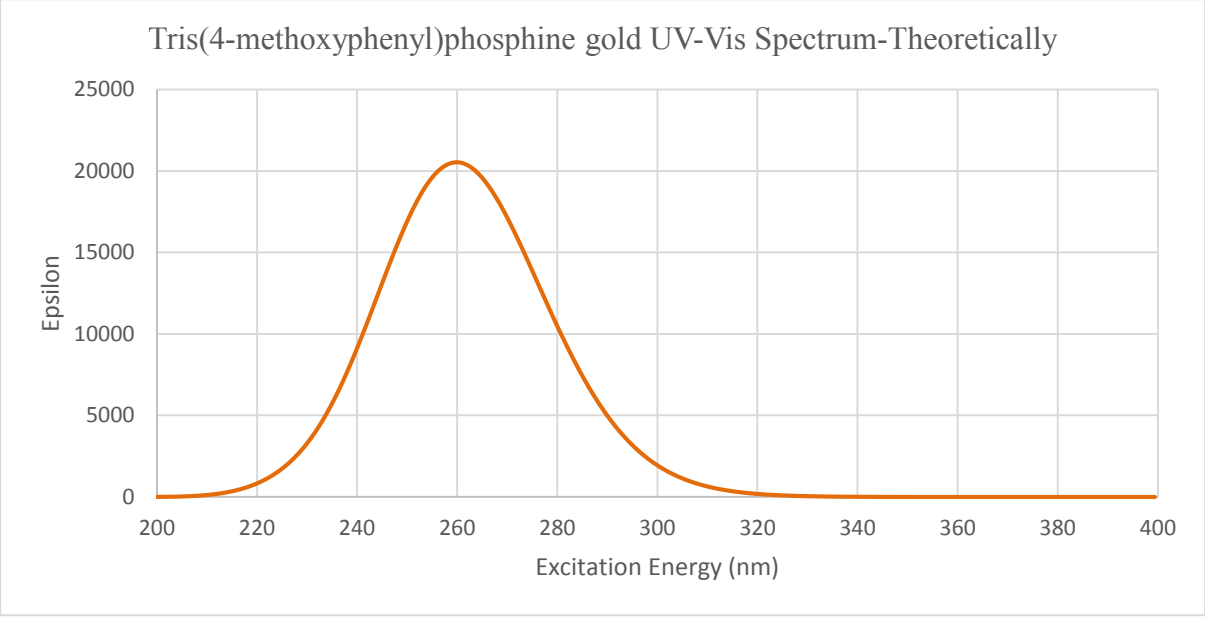

Figure 5.13. UV-Vis spectrum of $P(C_7H_7O)_3$ calculated theoretically using Gaussian 09 program.

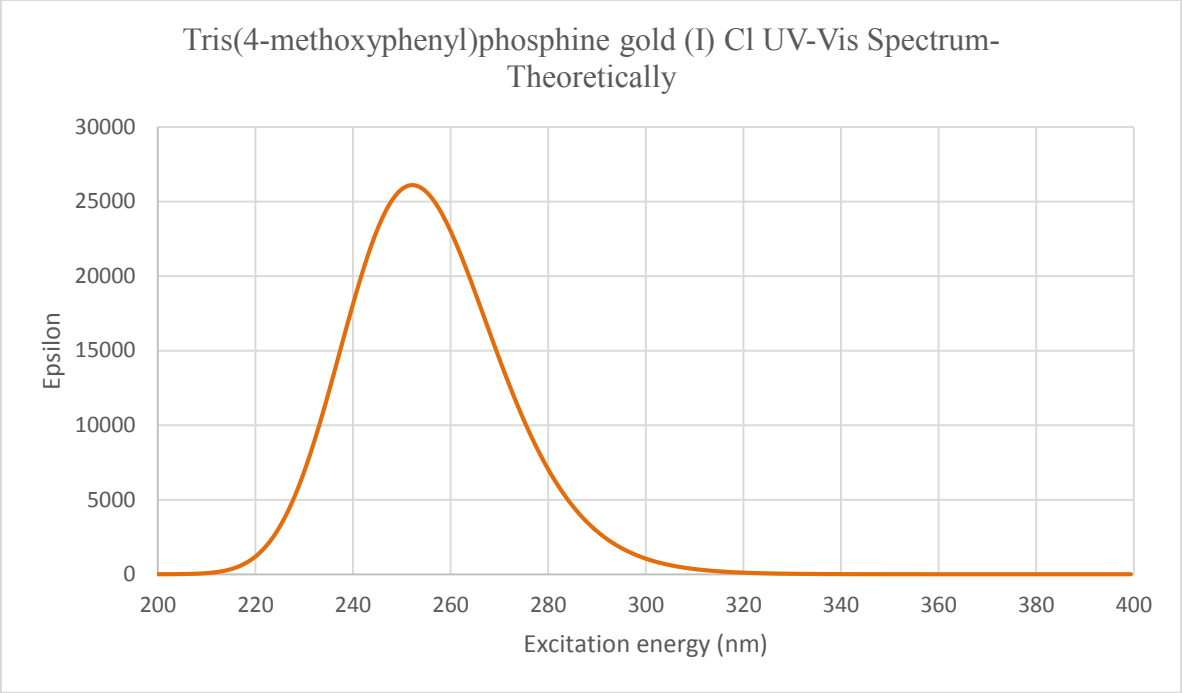

Figure 5.14. Calculated UV-Vis spectrum of $AuP(C_7H_7O)_3Cl$ obtained using Gaussian 09.

Table 5.2

TD-DFT generated ground-state to excited-state MO transitions

TRANSITIONS	CORRESPONDING ORBITALS	% CONTRIBUTION
X	100 → 102	100.00
Y	100→ 102	40.43
	101 → 103	9.57
	101 → 104	40.67
	101 → 107	9.33
Z	99 → 102	27.96
	101→ 103	45.77
	101→ 104	8.79
	101→ 105	8.56
	101→ 106	8.92

Table 5.3

*Theoretical results showing the contributions of X, Y, and Z transitions of **10***

Excitation	λcalc. (nm)	%Contribution to the transition		Transition Energy (cm^{-1})	λexp. (nm)
X	270.00				250
Major contribution:					
	100→ 102	100.00		37,038	
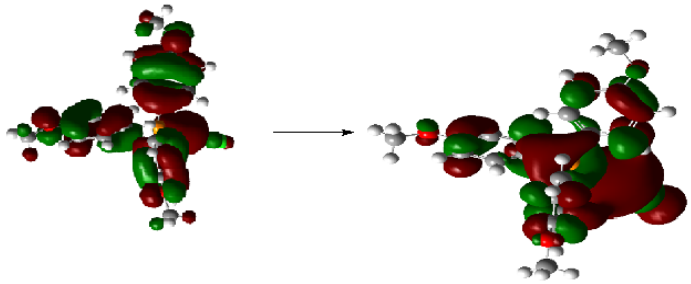					
Y	255.59				
Major contribution:					
	101→ 104	40.67		39,126	
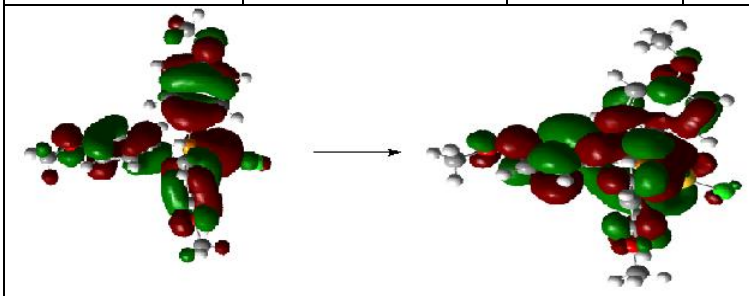					
Z	254.99				
Major contribution:					
	101 → 103	45.77		39,218	
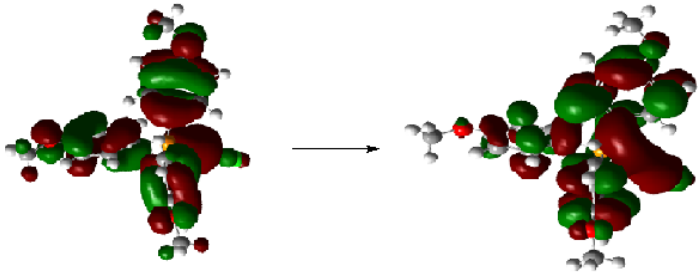					

5.2.5 Luminescence. The excitation spectrum of the TFMOPP ligand is shown in Figure 5.15 at room temperature, while the spectra for the $AuP(C7H7O)_3Cl$ complex at room temperature are given in Figures 5.16, 5.17, 5.18 and 5.19 covering the spectral regions from 280 -472 nm, 280- 460 nm, 280 - 447 nm, 280 - 460 nm, and monitored at the emission band of 492, 480, 467 and 450 nm, respectively. The spectra exhibited splittings around 362, 397 nm. The excitation spectrum collected in liquid nitrogen is shown in Figures 5.20, 5.21 and 5.22 covering the various spectral region as shown in the figures. For the spectrum monitored at 450 nm clear vibronic components are observed at 340, 350 and 362 nm. The emission spectrum for the ligand collected at room temperature is shown in Figure 4.23. The emission spectrum for both room and liquid nitrogen temperature is shown in Figures 5.24, 5.25, 5.26, and 5.27, 5.28, 5.29, 5.30.

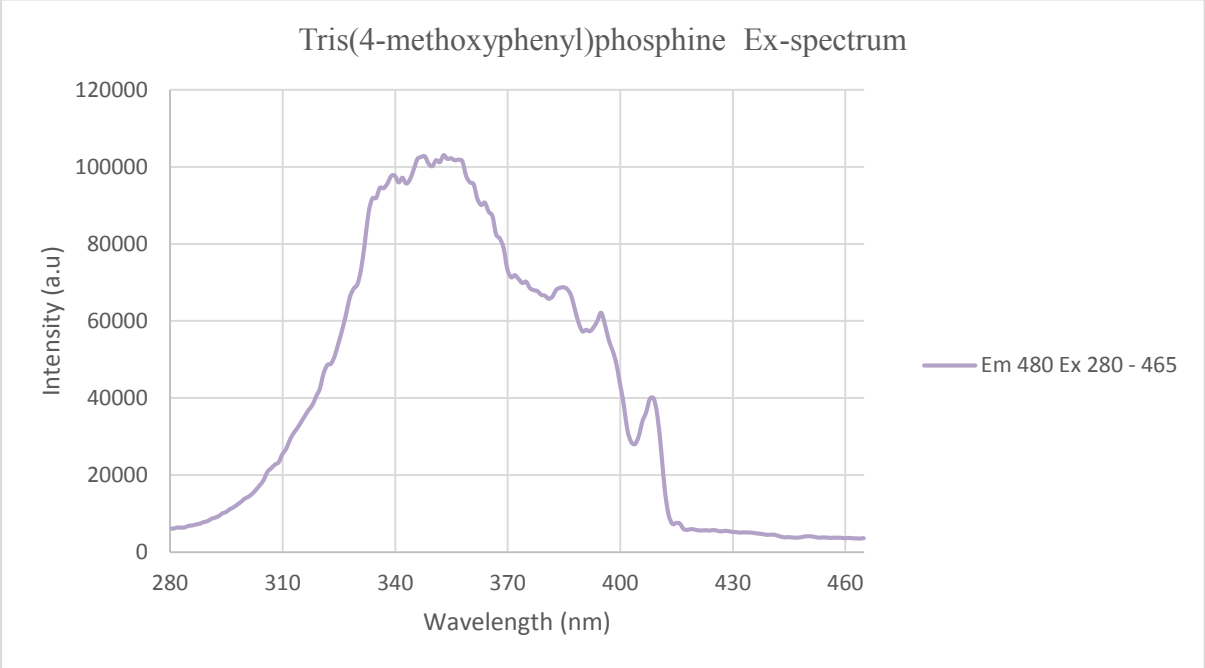

Figure 5.15. Excitation spectrum of $P(C_7H_7O)_3$ collected at room temperature by monitoring the emission at 480 nm.

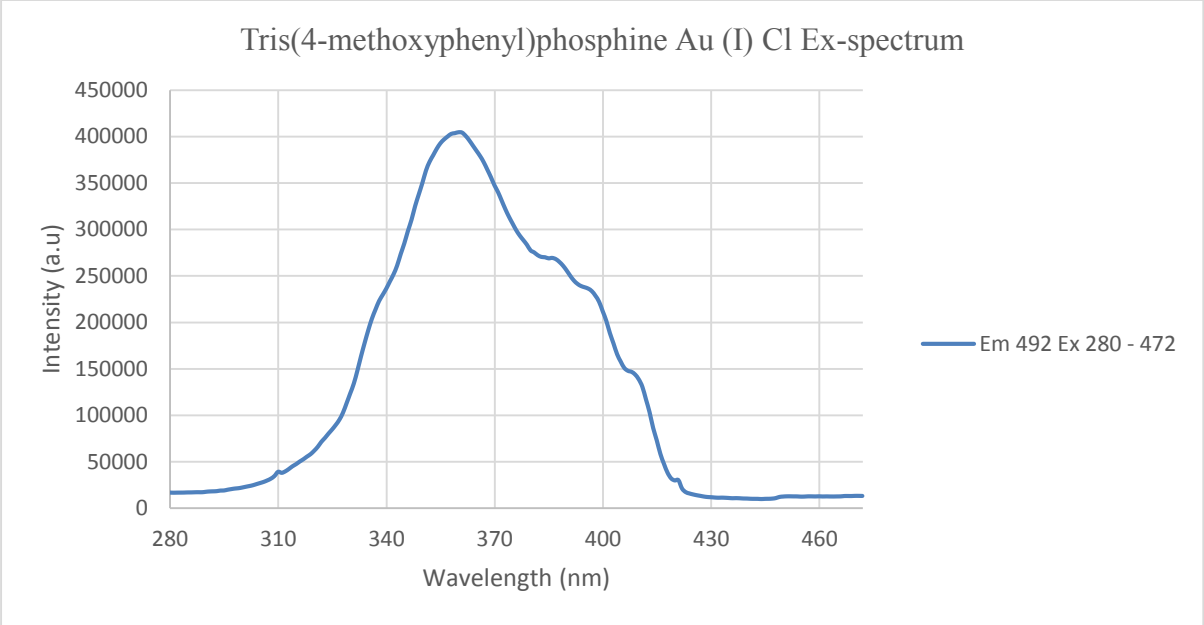

Figure 5.16. Excitation spectrum of $AuP(C_7H_7O)_3Cl$ collected at room temperature by monitoring the emission at 492 nm.

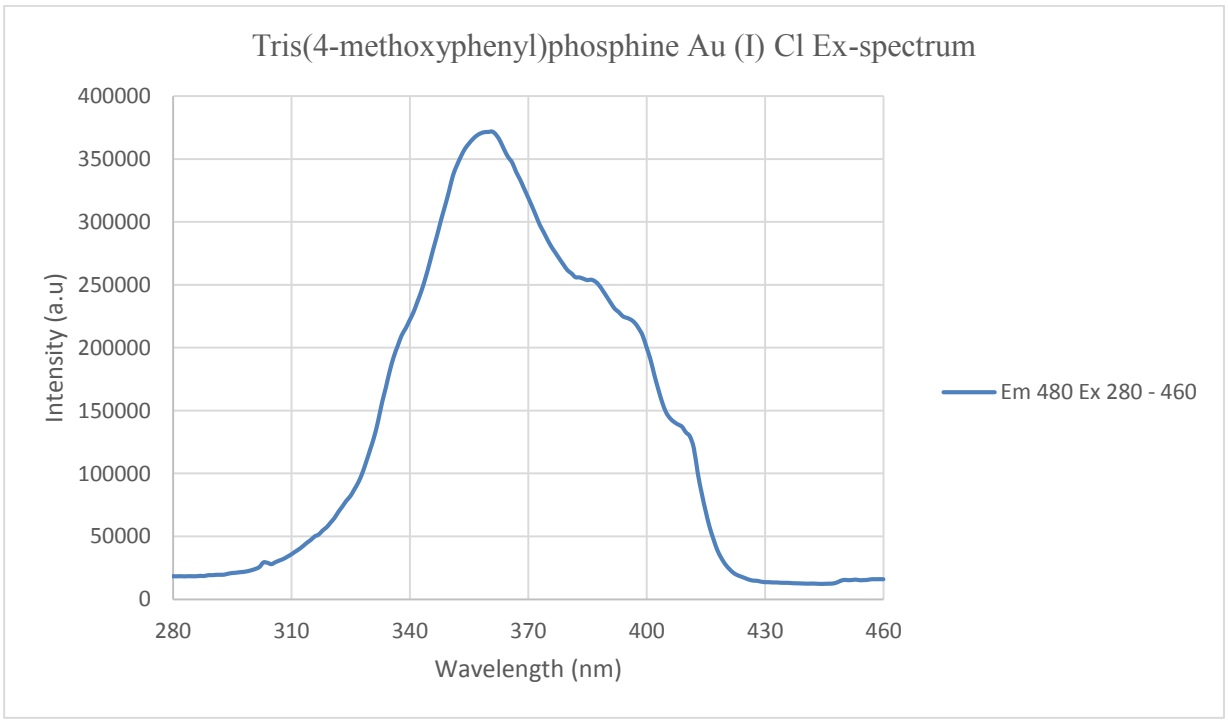

Figure 5.17. Excitation spectrum of $AuP(C_7H_7O)_3Cl$ collected at room temperature by monitoring the emission at 480 nm.

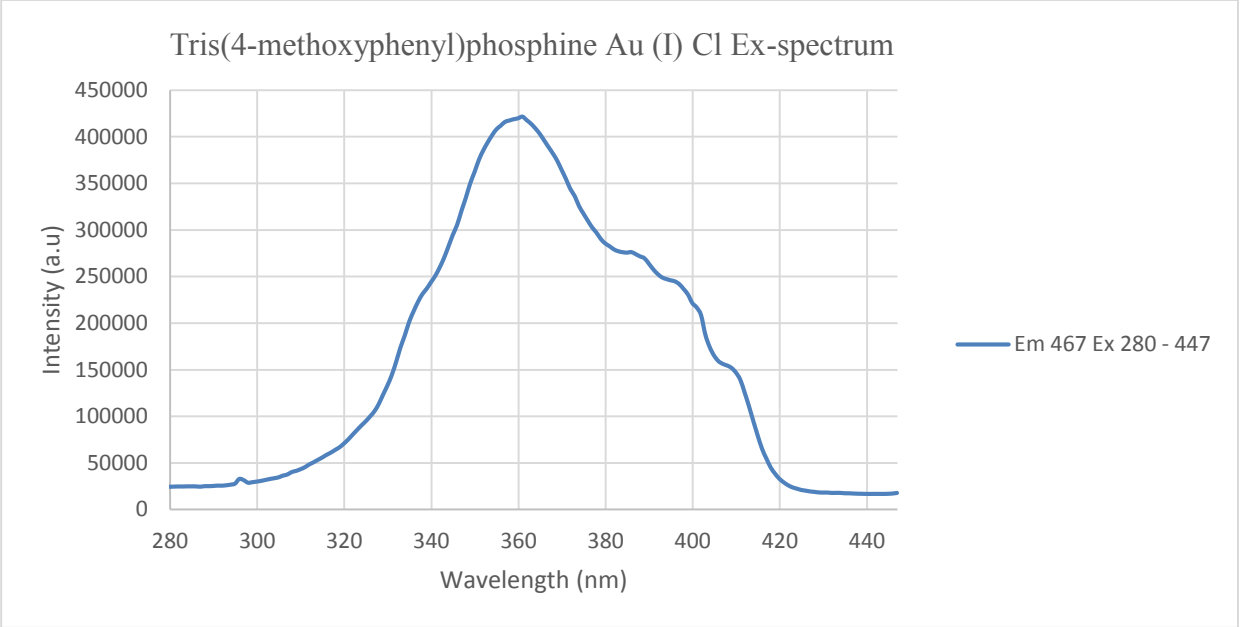

Figure 5.18. Excitation spectrum of $AuP(C_7H_7O)_3Cl$ collected at room temperature by monitoring the emission at 467 nm.

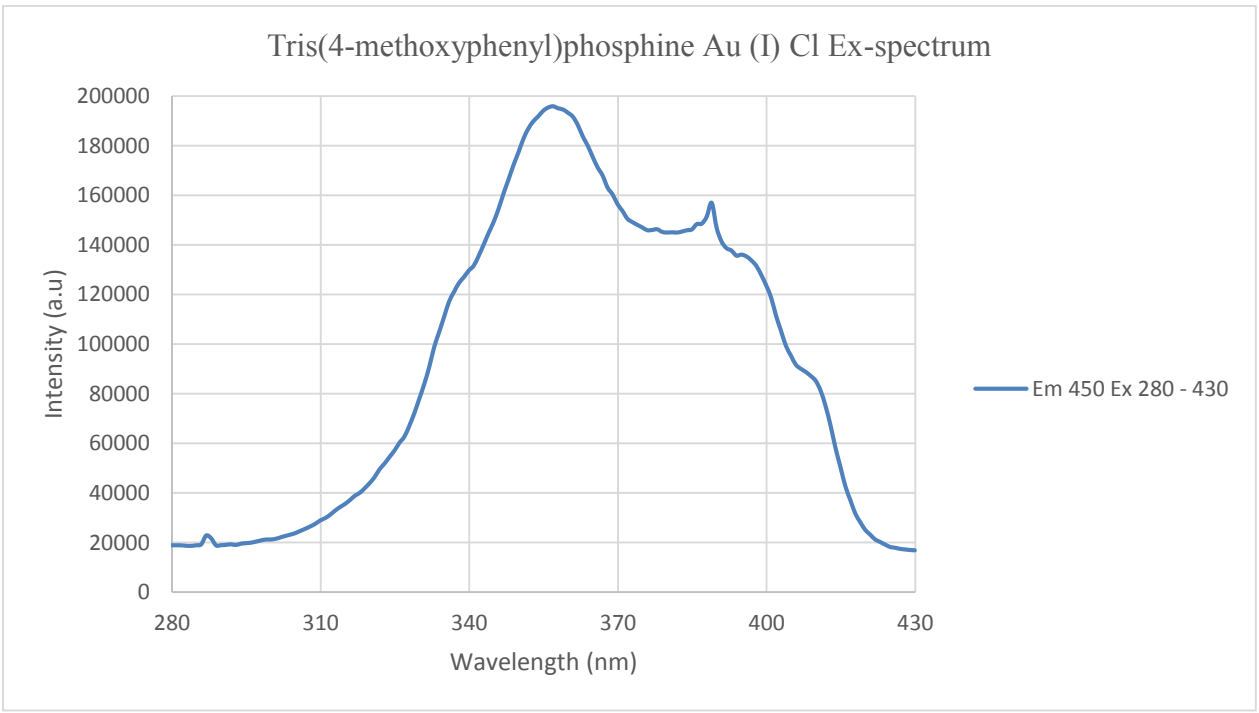

Figure 5.19. Excitation spectrum of $AuP(C_7H_7O)_3Cl$ collected at room temperature by monitoring the emission at 450 nm.

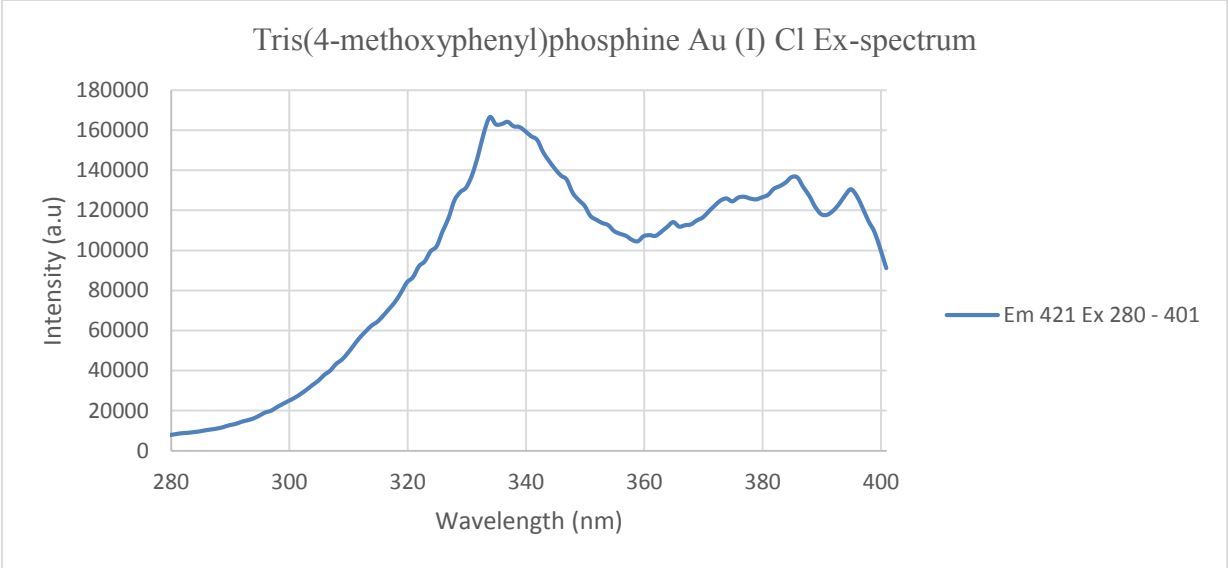

Figure 5.20. Excitation spectrum of $AuP(C_7H_7O)_3Cl$ collected in liquid nitrogen by monitoring the emission at 421 nm.

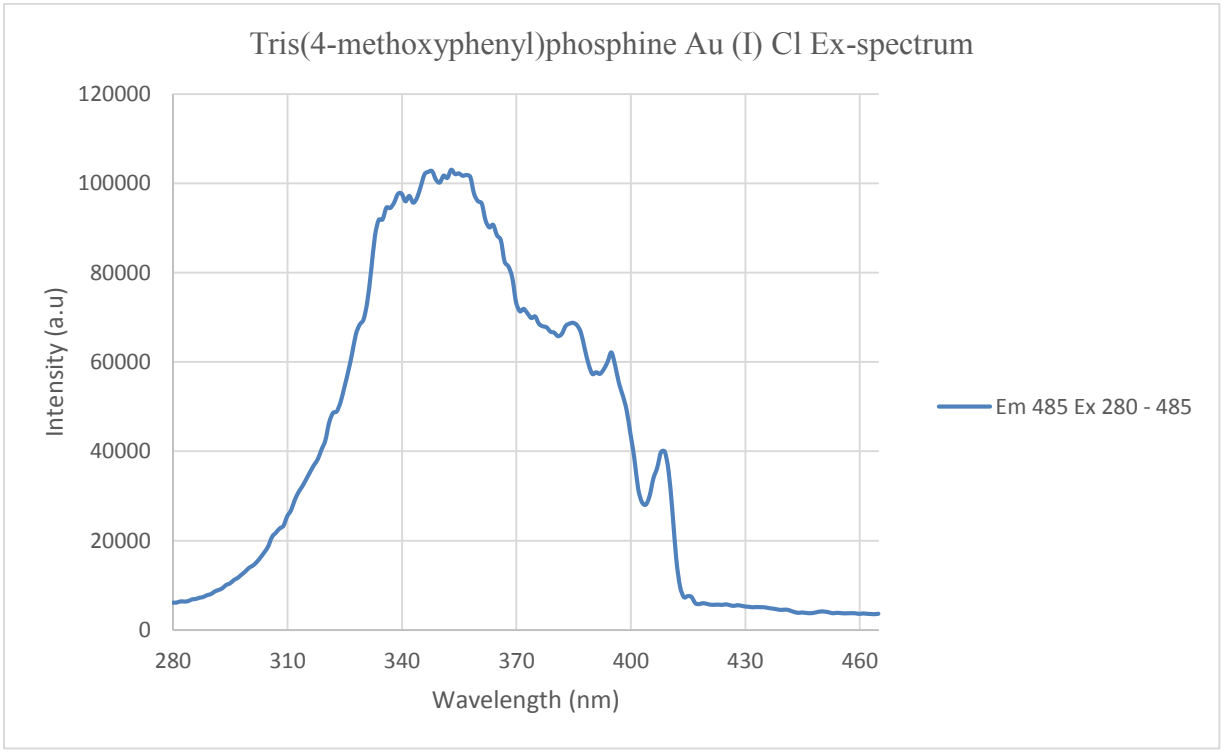

Figure 5.21. Excitation spectrum of $AuP(C_7H_7O)_3Cl$ collected in liquid nitrogen by monitoring the emission at 485 nm.

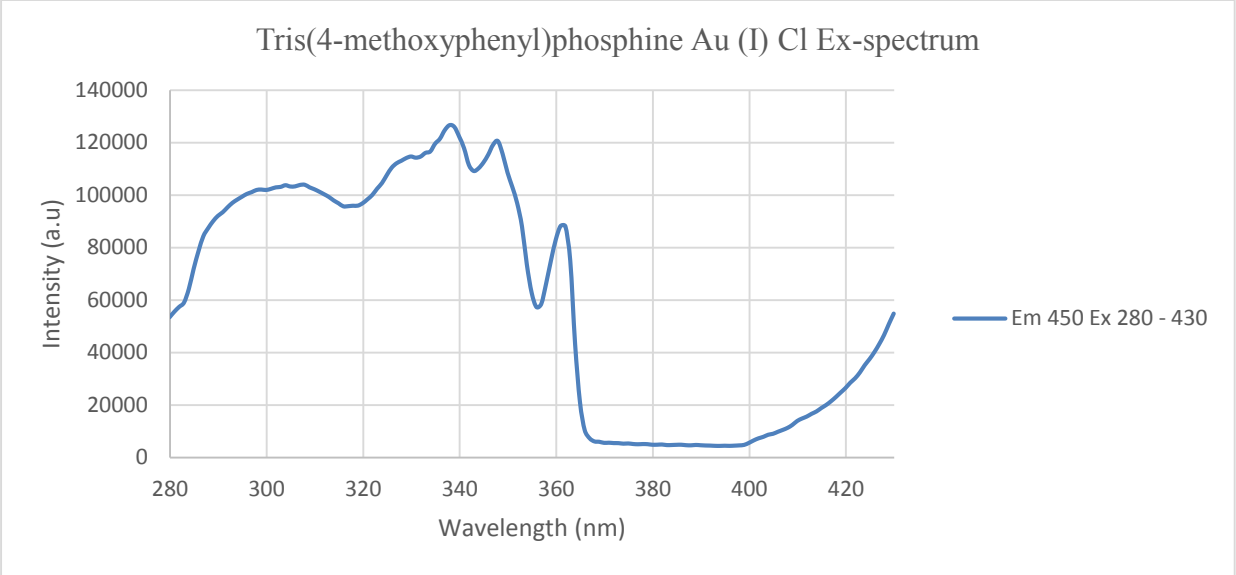

Figure 5.22. Excitation spectrum of $AuP(C_7H_7O)_3Cl$ collected in liquid nitrogen by monitoring the emission at 450 nm.

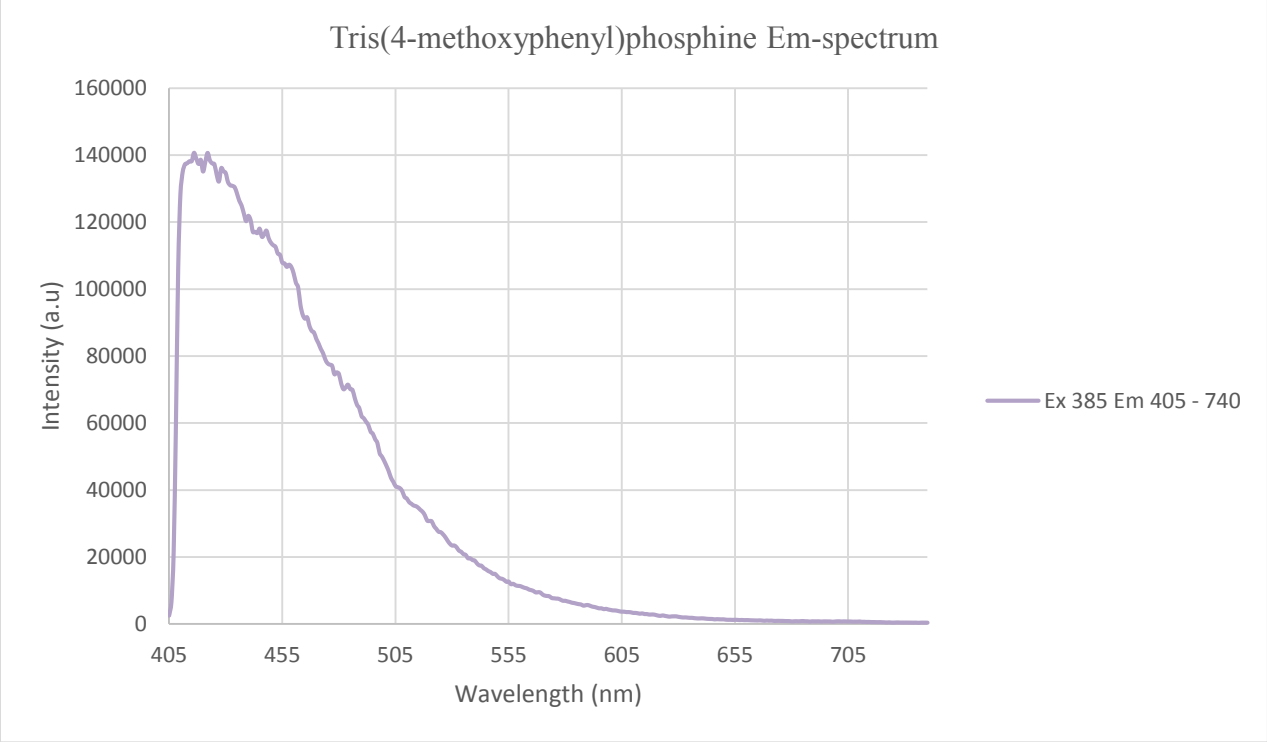

Figure 5.23. Emission spectrum of $P(C_7H_7O)_3$ collected at room temperature upon excitation at 385 nm.

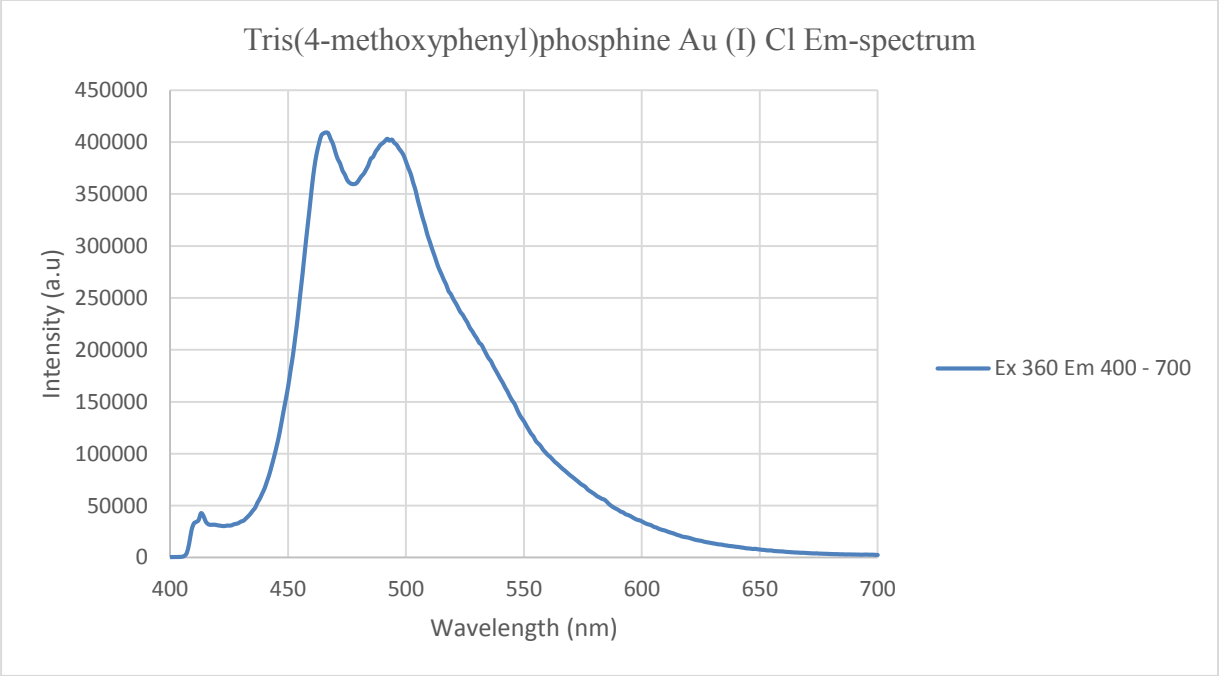

Figure 5.24. Emission spectrum of $AuP(C_7H_7O)_3Cl$ collected at room temperature upon excitation at 360 nm.

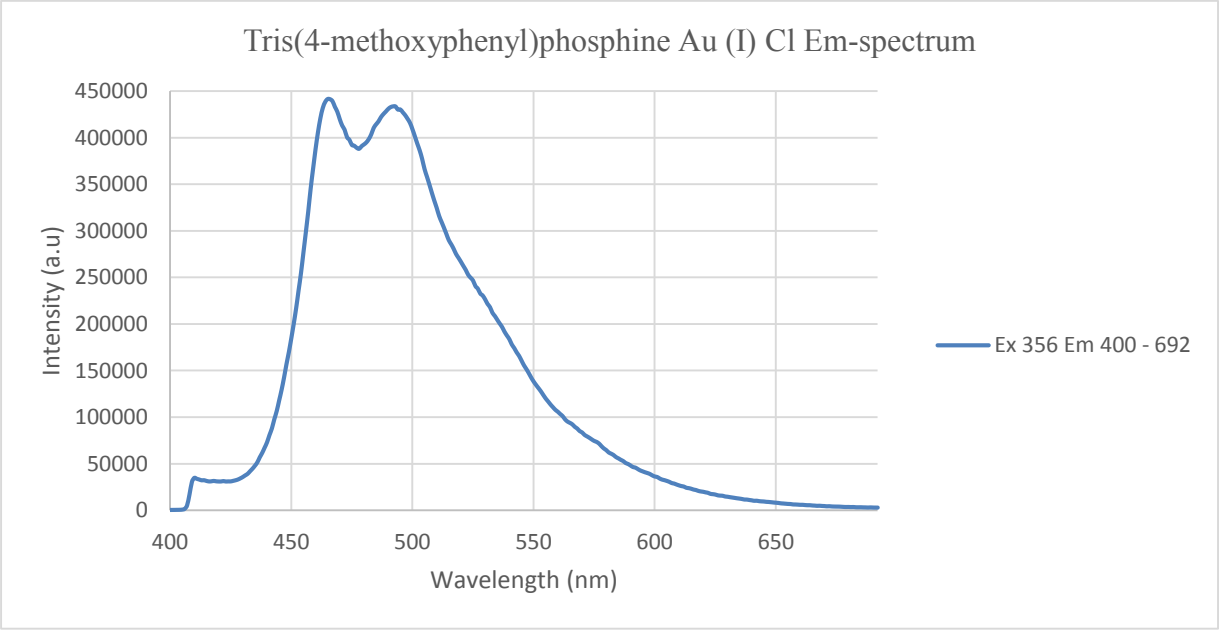

Figure 5.25. Emission spectrum of $AuP(C_7H_7O)_3Cl$ collected at room temperature upon excitation at 356 nm.

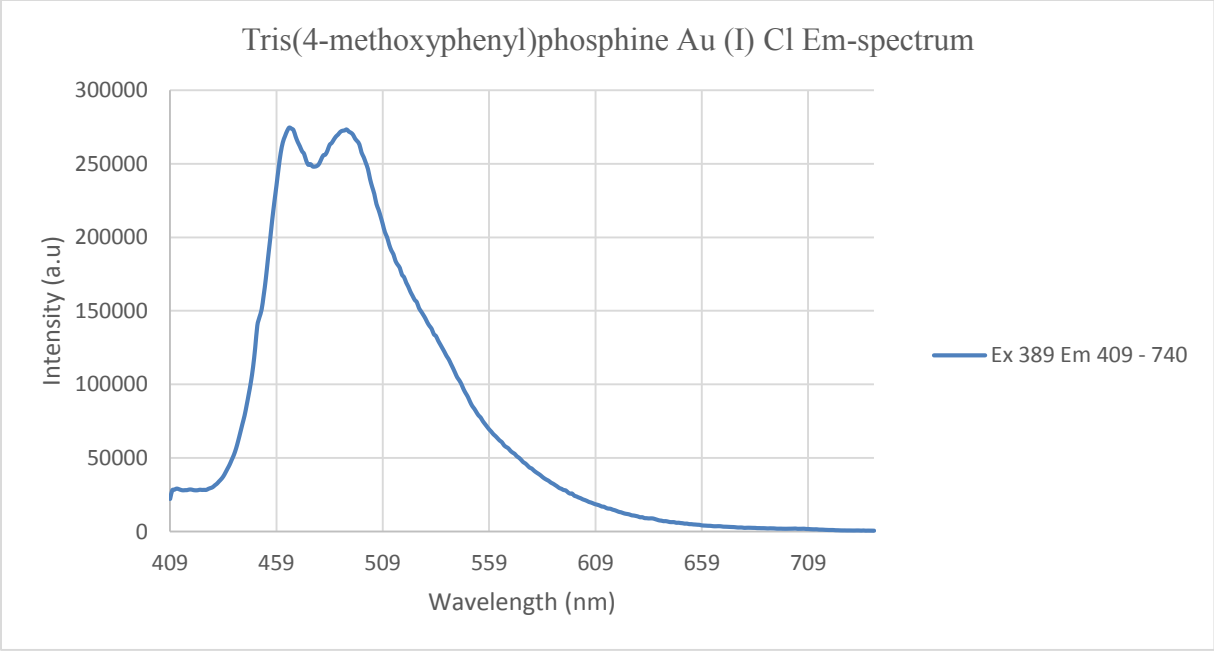

Figure 5.26. Emission spectrum of $AuP(C_7H_7O)_3Cl$ collected at room temperature upon excitation at 389 nm.

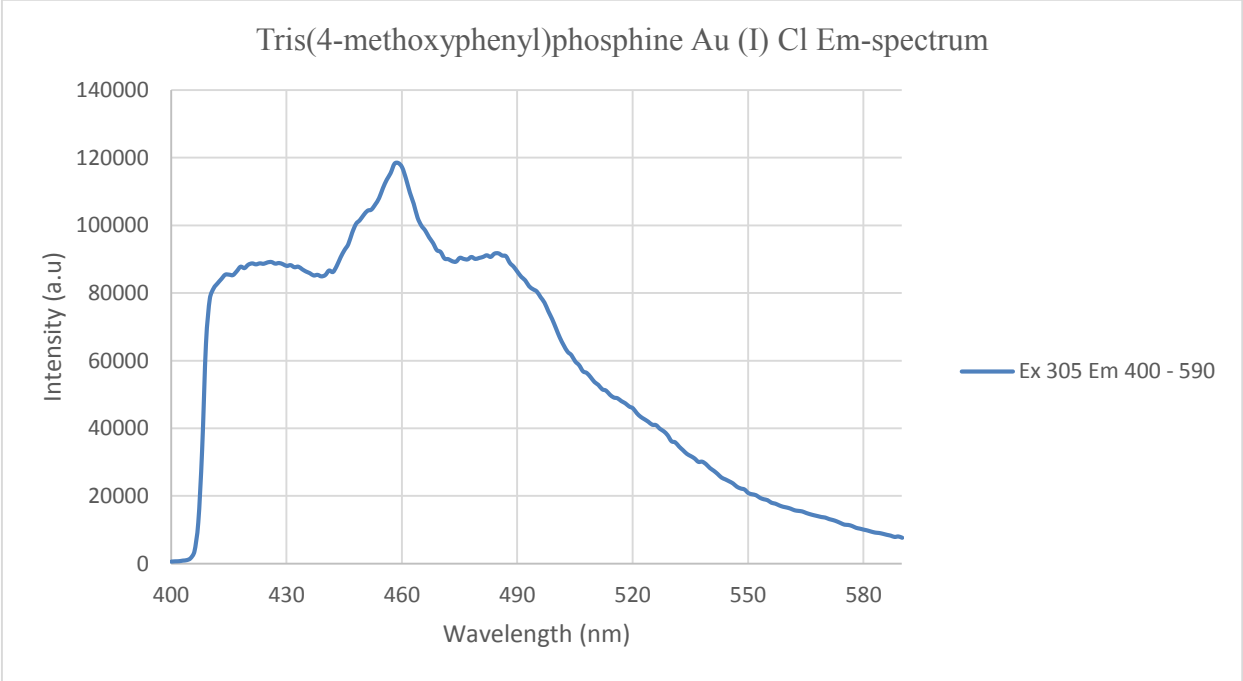

Figure 5.27. Emission spectrum of $AuP(C_7H_7O)_3Cl$ collected in liquid nitrogen upon excitation at 305 nm.

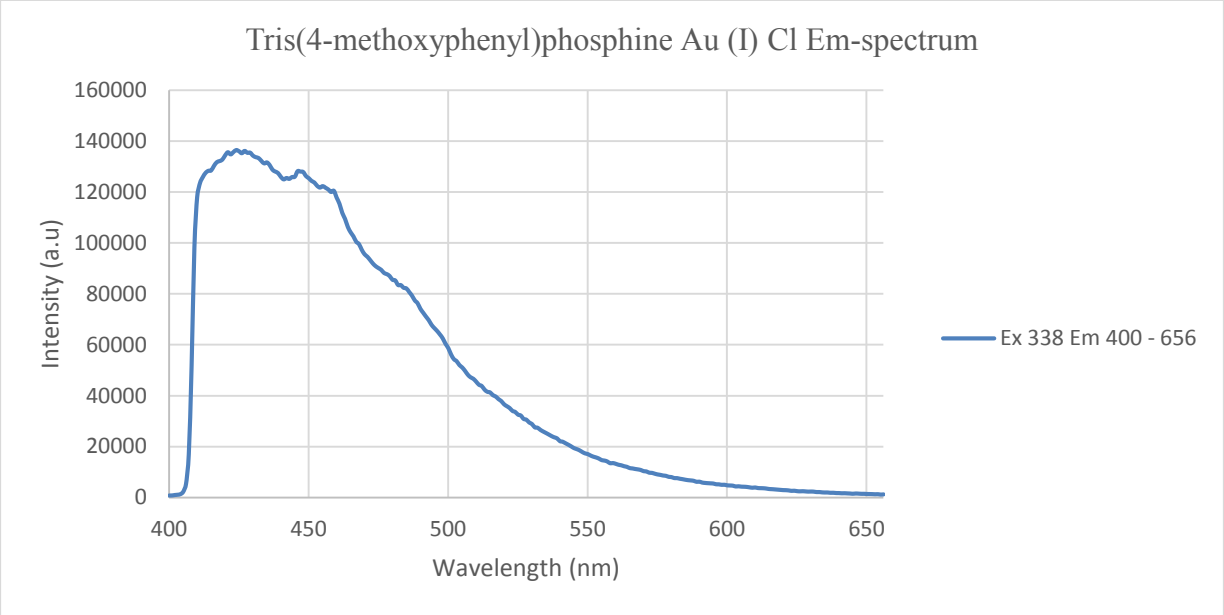

Figure 5.28. Emission spectrum of $AuP(C_7H_7O)_3Cl$ collected in liquid nitrogen upon excitation at 338 nm.

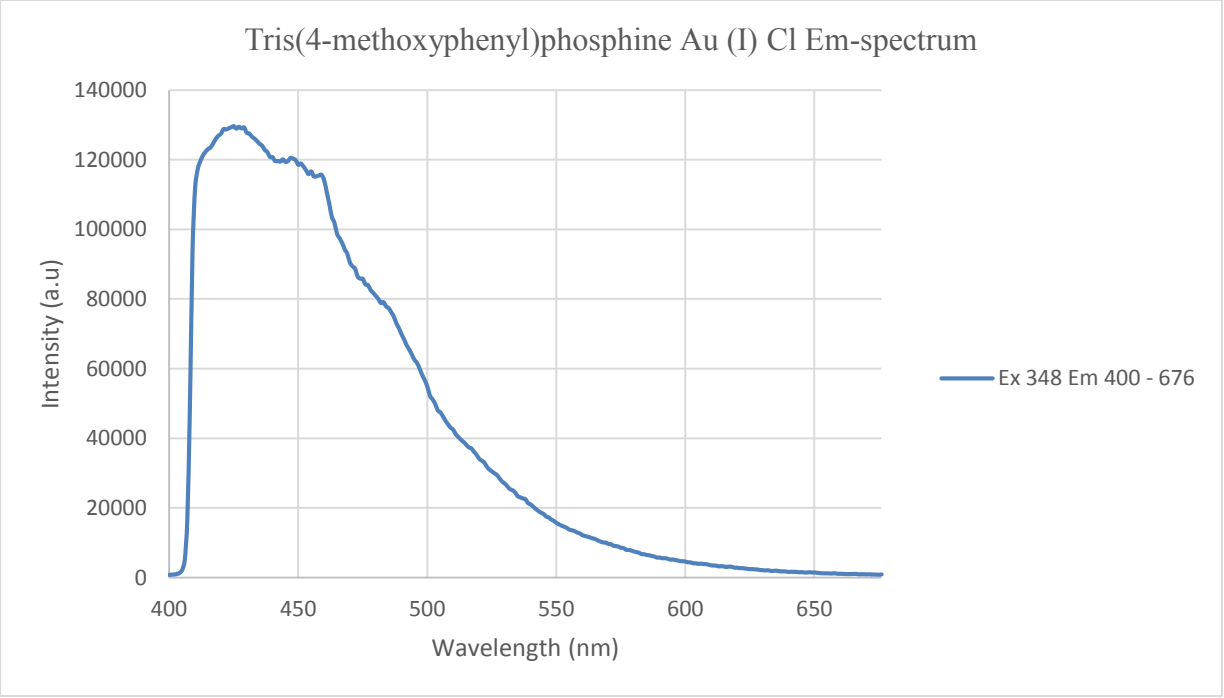

Figure 5.29. Emission spectrum of $AuP(C_7H_7O)_3Cl$ collected in liquid nitrogen upon excitation at 348 nm.

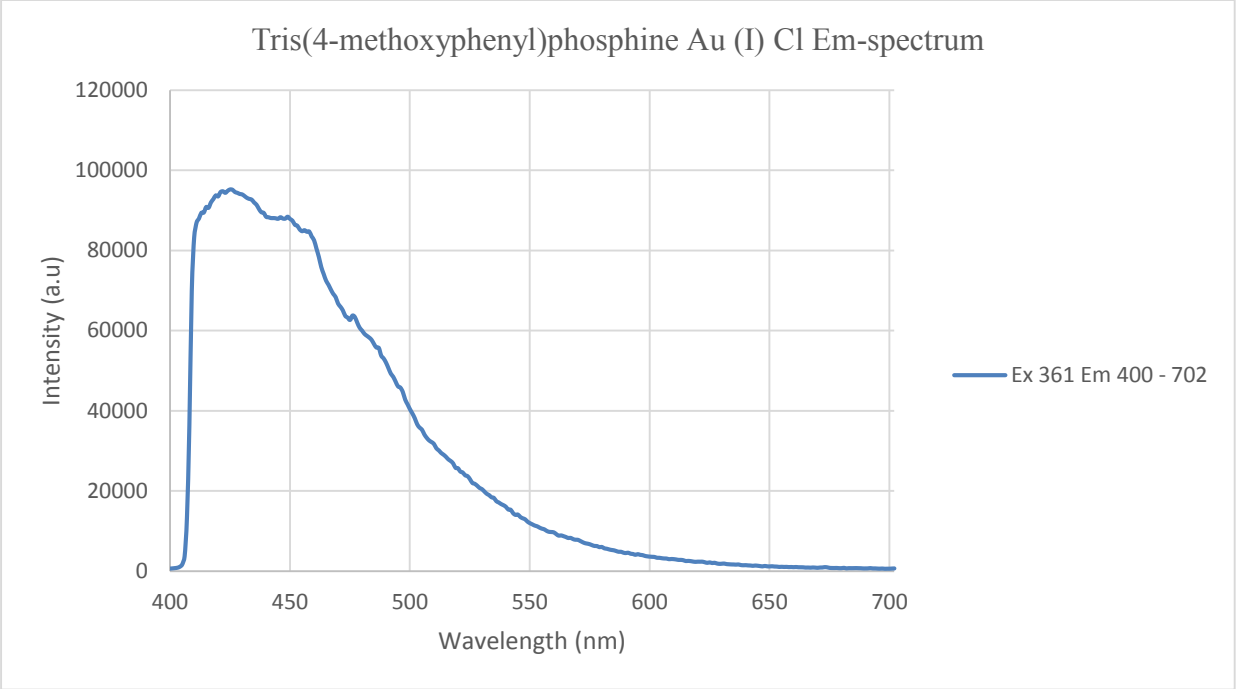

Figure 5.30. Emission spectrum of $AuP(C_7H_7O)_3Cl$ collected in liquid nitrogen upon excitation at 361 nm.

Table 5.4

Atomic contribution for the ground state molecular orbitals for compound ***10***

ATOMIC CONTRIBUTIONS (%)					
Orbitals	Au	Ligand	P	O	C
104	13.77	86.23	7.29	1.01	77.93
103	19.84	80.16	13.72	2.05	64.39
102	15.46	84.54	7.15	1.41	75.98
HOMO-LUMO GAP					
101	7.03	92.97	9.68	10.79	72.50
100	4.83	95.17	2.06	17.51	75.60
99	8.08	91.92	2.33	15.59	74.00

Table 5.5

*Atomic Orbital contribution in the ground state for compound **10***

ATOMIC ORBITAL CONTRIBUTIONS (%)					
Orbitals	Au	Ligand	P	O	C
104	2.33s, 4.43px 2.80py, 4.21pz	12.22s, 26.88px, 26.88py, 20.23pz	1.20s, 1.87px 24.17py, 17.71pz	1.01pz	11.04s, 25.01px 24.17py, 17.71pz
103	7.22px, 5.20py 7.42pz	23.81s, 7.79px 31.81py, 16.75pz	3.98s, 1.58px 3.48py, 4.68pz	2.05py	19.83s, 6.21px 26.28py, 12.07pz
102	2.74s, 6.11px 5.11py, 1.5d	10.38s, 28.22px 22.96py, 22.98pz	1.21s, 4.67px 1.27pz	1.41px,	9.17s, 22.14px 22.96py, 21.71pz
HOMO-LUMO GAP					
101	5.14s, 1.89d	3.22s, 16.89px 35.50py, 37.36pz	3.22s, 2.95py 3.51pz	2.81px, 2.36py 5.62pz	14.08px, 30.19py 28.23pz
100	4.83d	3.05s, 40.37px 3.25py, 48.50pz	2.06px	7.38px, 10.13pz	3.05s, 30.93px 3.25py, 38.37pz
99	8.08d	3.51s, 26.82px 55.09py, 6.50pz	2.33py	5.12px, 7.84py 2.63pz	3.51s, 21.70px 44.92py, 3.87pz

5.3 Discussion

5.3.1 Infrared Spectroscopy (Vibrational Studies). The IR-spectrum of **10** at Figure 5.3 has Twenty five (25) distinct bands. It shows a weak aromatic C–H stretching of the phenyl ring at 3001 cm^{-1}, the asymmetric and symmetric aliphatic C–H (CH_3) stretching at 2931 cm^{-1} and 2831 cm^{-1}, the C=C phenyl ring stretching pair at 1574 cm^{-1} and 1462 cm^{-1}, the aromatic C–O stretching at 1246 cm^{-1}, the aliphatic C–O stretching at 1165 cm^{-1}, the P–Ar stretching at 1103 cm^{-1}, the aromatic C–H bending at 895 cm^{-1}, the P–C stretching at 775 cm^{-1}, the Au-P stretching at 360 cm^{-1} and the Au-Cl stretching at 330 cm^{-1}. Group Theoretical Analysis (Nuclear site group

analysis) for **10** also predicts Twenty five (25) IR-active modes. From the x-ray data of [33], **10** has a space group C_2/c with Z = 8. With Z = 8, it means **10** contains eight formula units per unit cell. The modes for this unit cell can be found by consulting table 5A [26]. Since there are 168 C-atoms, 24 O-toms, 8 Au-atoms, 8 Cl-atoms and 4 P-atoms, it is immediately seen by inspection of table 5A [26], that the 168 C-atoms must lie on the C_i sites, in four folds repetitively, the 24 O-atoms must lie on the C_2 sites also in four folds repetitively and the remaining (Au, P, Cl) must occupy the C_1 sites each. From table 5B [26], the vibrational modes of **10** are $3A_u + 3B_u$ for the C-atom, $A_g + A_u + 2B_g + 2B_u$ for the O-atom, and $3A_g + 3A_u + 3B_g + 3B_u$ for each nucleus on the C_1 sites. The total contribution from C, O, P, Au and Cl is $10A_g + 13A_u + 11B_g + 14B_u$. From table 5E [26], the acoustic mode is $A_u + B_u$ and the optical modes are $10A_g + 12A_u + 11B_g + 13B_u$. The distribution of the optical modes shows that Twenty five (25) ($12A_u + 13B_u$) modes are expected to be IR-active from the selection rule. Comparison of these predictions with the observed calculated spectra shows that Twenty five distinct frequencies are observed.

5.3.2 Nuclear Magnetic Resonance. The ^{1}H NMR spectrum of **10** shown at figure 5.6 showed splitting at chemical shift at δ = 6.9 (m, 6H, Ar–H), δ = 7.5 (m, 6H, Ar–H), and δ = 3.8 (s, 9H, CH_3). The peak intensities of the proton environments corresponds to the number of H-atoms in the respective vicinities. Comparison of the ^{1}H NMR spectral data between **10** and its free ligand (TFMOPP) shows a slight shifting downfield. Peaks for TFMOPP ligand found on figure 5.5 showed splitting at δ = 6.8 (m, 6H, Ar–H), δ = 7.4 (m, 6H, Ar–H), and δ = 3.8 (s, 9H, CH_3). The slight difference in the position of the peaks between **2** and its ligand is an indication that the ligand has successfully coordinated to the gold center. The ^{31}P{^{1}H} NMR spectral data for the TFMOPP ligand, and the **10** shown at Figure 5.7 and 5.8 showed a strong sharp peak at 31.0 ppm, and 40.0ppm respectively. With the coordination of the mono TFMOPP to the gold(I)

chloride center the trend of downfield shifting is seen. This is as a result of the weakening of the carbon-phosphine bond and consequently de-shielding the electrons and causing the peak to shift to a larger chemical shift value (downfield). The overall trend appears consistent for gold phosphine complexes where the mono substituted systems usually show smaller chemical shift values than the di, tri substituted complexes. For example, the mono, tris, and tetrakis substituted $(TFP)_nAuCl$ compounds have ^{31}P NMR coordination chemical shift (ccs) of 48.4, 66.1, 63.1 respectively [32]. Also, the mono, di, tris, and tetrakis substituted $(TPA)_nAuCl$ compounds have ^{31}P NMR values of -51.4, -36.1, -56.1, and -58.0 ppm respectively [27-31]. The increase in the chemical shift value on going from the TFMOPP, to **10** is consistent with the general trend that chemical shift values increases as the coordination number increases. The trend of downfield shifting is also an indication that the ligand has successfully been coordinated to the gold (I) center.

5.3.3 UV-Vis Spectroscopy. The absorption spectral data for the TFMOPP ligand and $AuP(C_7H_7O)_3Cl$ reveal similarities in their high-energy broad UV absorption profiles. The absorbance maximum for the free TFMOPP ligand shown at Figure 5.11 is observed at 250 nm with a smaller less intense band at 270 nm with low energy tail extending all the way to 400 nm. Similarly, the monocoordinated TFMOPP‑gold(I) complexes also show similar higher energy band maxima near 250 nm . Based on the spectral similarities between the ligand and the complexes as well as the molar absorptivity values of 5.81 x 10^4 $M^{-1}cm^{-1}$ and 8.89 x 10^4 $M^{-1}cm^{-1}$ for the TFMOPP, and $AuP(C_7H_7O)_3Cl$ respectively, the 250 nm band is assignable to a $\pi \rightarrow \pi^*$ intraligand transition, which is as result of the presence of double bond in the aromatic phenyl ring. The transition is slightly affected by the coordination with the Au metal. The weaker band at 270 nm which is present in the ligand is absent in the absorption spectra of **10** at Figure 5.12, indicating that the transition is affected by coordination with the metal. This band is assignable to

an n→π* transition and its absence in the absorption spectrum of **10** is indicative of participation of the lone pair electrons in the bonding scheme of the TFMOPP ligand. The higher molar extinction coefficient value of the ligand and the complexes is an indication that the electronic transitions involved as a result of the absorption are statistically probable (said to be 'allowed') due to the fact that their molar extinction **ε** values are in excess of 10 000. It is also interesting to note that the TFMOPP ligand, and the **10** complexes absorbs at similar energies but with the extinction coefficients of **10** about twice more intense than that of the TFMOPP ligand . The enhancement of the extinction coefficient in **10** relative to TFMOPP is understandable in view of the presence of the gold (I) chloride attached to the TFMOPP ligand

5.3.4 Luminescence. The gold(I) complexes and the TFMOPP ligand luminescent when excited under UV radiation. The emission spectra of the complexes both at room temperature and in liquid nitrogen have very similar profiles indicating a similar origin for the electronic transitions. The emission spectra of the TFMOPP ligand at room temperature shown at Figure 5.23 is characterize by a sharp band and maximizes around 420 nm. The emission spectra of the gold complex (**10**) shown at Figure 5.24 to 5.26 was observed at 467 nm and 495 nm showing fine vibronic structures arising from the v(C=C) stretch of the phenyl ring of the ligand, with vibrational progressions with spacings of 1211 cm^{-1} . The shift to the longer wavelength (bathochromic shift) from 420 nm of the TFMOPP to 475 nm of $AuP(C_7H_7O)_3Cl$ is due to the fact that at the excited states, the π→π* transitions of the TFMOPP is more polar than their ground states and as a result, a greater charge separation is observed in the excited state. The coordination of the TFMOPP to the gold (I) center causes a dipole–dipole interaction which reduces the energy of the excited state more than the ground state, hence making the $AuP(C_8H_9)_3Cl$ to emit at a longer wavelength. This emission at a longer wavelength by

$AuP(C_8H_9)_3Cl$ compare to the ligand is also an indication that the ligand has successfully been coordinated to the gold (I) center. Similar emission bands for **10** in liquid nitrogen were observed at 428 nm and 450 nm (Figure 5.27 – 5.30) showing fine vibronic structures arising from the v(C=C) stretch of the phenyl ring of the ligand. Vibrational progressions with spacings of 1142 cm^{-1} were also observed in complex **10** in liquid nitrogen, typical of the v(C=C) vibrational mode of the phenyl group.

The excitation spectrum of the TDMPP ligand and that of **10** at room temperature and in liquid nitrogen shown at Figure 5.15 for TDMPP and Figure 5.16-19 for **10** consists of a well-defined broad band with an average spacing of 1300 cm^{-1}. This spacing is assignable to an electronic transition coupled with vibronic component corresponding to v(C=C) symmetric stretching mode within the phenyl ring. With reference to the previous luminescence studies on tertiary phosphine gold(I) complexes the emission bands at 467 and 495 nm in complexes **10** tentatively assigned as derived from excited states of P–> Au ligand-to-metal charge transfer (LMCT) origin. This suggests that the ligand centered transition is responsible for the photoluminescence in **10**.

5.3.5 Computational Studies

5.3.5.1 Spectroscopic Comparison. The theoretical calculated IR spectrum of **2** using Gaussian 09 shown at Figure 5.4 also predicts Twenty two (22) distinct bands with a slight shift in the position of some of the individual peaks, but on a whole both the calculated and the experimental spectrum of both the ligand and the complex shows similar IR-spectrum. The theoretical ^1H NMR of for both the ligand and the gold complex shown on Figure 5.9 and Figure 5.10 also showed similar splitting patterns and chemical shift values as that of the experimental ones.

5.3.5.2 Electronic Comparison

5.3.5.2.1 Luminescence. The result of the population analysis for **10** is shown in Table 5.4 and 5.5 for the percentage atomic and atomic orbital contributions respectively for the metal and the TFMOPP ligand, as well as individual atomic participation for the selected highest three occupied molecular orbitals and lowest three unoccupied molecular orbitals. The second highest occupied molecular orbital (SHOMO), HOMO-100 has the largest contribution from the ligand at 95.17% and the metal at 4.83% followed by the highest occupied molecular orbital, HOMO-101 at 92.97% and 7.03% contributions, respectively. The contribution of the gold atom in the HOMO-100 orbital derives from 5dxz atomic orbitals at 4.83% contributions. The atomic contribution of the TFMOPP ligand is comprised of Phosphorus, Oxygen and Carbon with percentage contributions of 3.05s, 40.37px, 3.25py and 48.50pz orbitals. However, the gold contribution of the HOMO comes also from 5.14% of the 5s and 1.89% of the 5dxz atomic orbitals with the remaining contribution from the 5py and 5pz orbitals of the phosphorus, Oxygen and Carbon atoms of the TFMOPP ligand. The table also shows the first three lowest unoccupied molecular orbital (LUMOs) contributions, which are mainly ligand centered contributions. The orbital description as ligand based and partial metal based transitions is thus substantiated to support the observations surrounding the luminescent behavior of **10** and hence the assignment of $\pi \rightarrow \pi^*$ transition is in a proper order.

5.3.5.2.2 UV-Vis. The HOMO‑LUMO gap calculated value by the TD-DFT method was 37,038 cm^{-1} corresponding to 270.00 nm. The theoretical calculated spectrum for **10** obtained using TDDFT with the LANL2DZ basis set to identify the orbital(s) contributing to the observed absorption is shown at Figure 5.13. The TD-DFT generated ground-state to excited-transitions is shown on Table 5.2 which summarizes the orbital that took part most in the transitions X, Y, and

Z. From Table 5.2, transition X supports an assignment of the SHOMO-100→LUMO-102, a π→π* type transition. This confirms why the n→π* is not present in the experimental UV-Vis spectrum of **10**. The transition Y and Z has transitions from the HOMO-101→LUMO-104 and HOMO-101→LUMO-103 respectively. Table 5.3 summarizes the various transitions pictorially of the theoretically generated ground-state to excited-state transitions for X, Y and Z. These calculated spectrum values are in good agreement with the experimental UV-Vis spectrum of **10**, with a slight red shifting of about 20 nm which are within the absorption range of aromatic derivatives.

CHAPTER SIX

Synthesis and Characterization of mono-, bis-, tris-, and tetrakis-{tert-butyldiphenyl)phosphine} gold(I) complexes

6.1 Syntheses

6.1.1 Tert-butyldiphenylphosphine gold (I) chloride (14). Tert-butyldiphenylphosphine (0.0200 g, 0.08 mmol) was added to a solution of $(C_4H_8S)AuCl$ (0.0264 g, 0.08 mmol) in tetrahydrofuran (20 ml) at −80 ˚C and the reaction stirred for 2 hours. The solvent was removed by purging nitrogen gas into the solution, until all the solvent dried up. The residue was then recrystallized from CH_2Cl_2/n-hexane mixture for five days. Partial evaporation of the solvent provided quality crystals.

6.1.2 Bis{Tert-butyldiphenylphosphine} gold (I) chloride (15). Tert-butyldiphenylphosphine (0.0400 g, 0.16 mmol) was added to a solution of $(C_4H_8S)AuCl$ (0.0264 g, 0.08 mmol) in tetrahydrofuran (20 ml) at −80 ˚C and the reaction stirred for 2 hours. The solvent was removed by purging nitrogen gas into the solution, until all the solvent dried up. The residue was then recrystallized from CH_2Cl_2/n-hexane mixture for days. Partial evaporation of the solvent provided quality crystals.

6.1.3 Tris-{Tert-butyldiphenylphosphine} gold (I) chloride (16). Tert-butyldiphenylphosphine (0.0600 g, 0.24 mmol) was added to a solution of $(C_4H_8S)AuCl$ (0.0264 g, 0.08 mmol) in tetrahydrofuran (20 ml) at −80 ˚C and the reaction stirred for 3 hours. The solvent was removed by purging nitrogen gas into the solution, until all the solvent dried up. The residue was then recrystallized from CH_2Cl_2/n-hexane mixture for six days. Partial evaporation of the solvent provided quality crystals.

6.1.4 Tetrakis{tert-butyldiphenylphosphine} gold (I) chloride (17). Tert-butyldiphenylphosphine (0.0800 g, 0.32 mmol) was added to a solution of $(C_4H_8S)AuCl$ (0.0264 g, 0.08 mmol) in tetrahydrofuran (20 ml) at −80 ˚C and the reaction stirred for 3 hours. The solvent was removed by purging nitrogen gas into the solution, until all the solvent dried up. The residue was then recrystallized from CH_2Cl_2/n-hexane mixture for six days. Partial evaporation of the solvent provided quality crystals.

6.2 Results

6.2.1 X-ray Crystallography. Diffraction-quality crystal structure for $AuP(C_6H_5)_2(C_4H_9)Cl$, of the monocoordinated TBDPP gold (I) complex is shown in Figure 6.1, and the crystal structure determination data and selected bond lengths and angles are listed in Tables 6.2.1.1, 6.2.1.2 and 6.2.1.3 respectively.

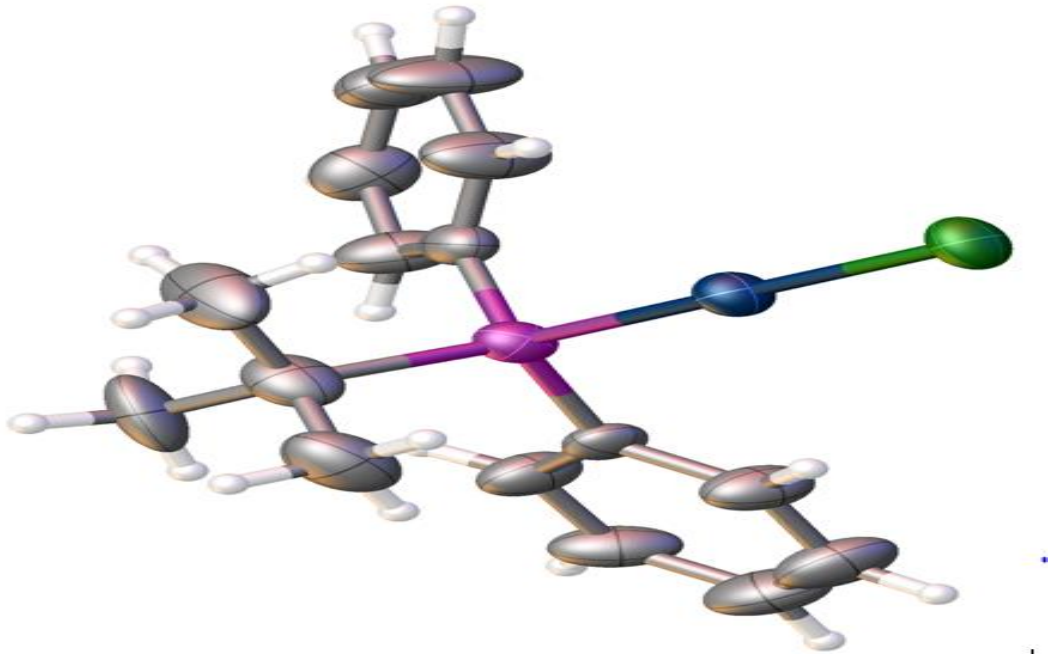

Figure 6.1. Thermal ellipsoid diagram of $AuP(C_6H_5)_2(C_4H_9)Cl$.

Table 6.1

Crystal data and Structural refinement parameters for $AuP(C_6H_5)_2(C_4H_9)Cl$

Empirical formula	$C_{16}H_{19}$ Au Cl P
Formula weight	474.70
Temperature	293K
Wavelength	0.71073 Å
Crystal system	Monoclinic
Space group	$P2_1/n$
Unit cell dimensions	a = 11.2738 (3) Å β = 91.917 (3)°
	b = 12.5351 (4) Å
	c = 11.6461 (4) Å
Volume	1644.89 (9) $Å^3$
Z	4
Density (calculated)	1.971 Mg cm^{-3}
Absorption coefficient	9.19 mm^{-1}
$F_{(000)}$	904
Crystal size	0.38 × 0.15 × 0.14 mm
Theta range for data collection	3.5 to 27.1°
Index ranges	-13<h<13, -15<k<15, -14<l<14
Reflections collected	12101
Independent reflections	3013 [R(int) = 0.029]
Completeness to theta = 25.4°	99.9%
Absorption correction	Multi scan
Max. and min. transmission	1.000, 0.348
Refinement method	Full-matrix least-squares on F^2
Data / restraints / parameters	3013 / 0 / 175
Goodness-of-fit on F^2	1.10
Final R indices [I>2sigma(I)]	R1 = 0.023, wR2 = 0.050
Absolute structure parameter	0.065 (18)
Large diff. peak and hole	1.06 e $Å^{-3}$ and −0.56 e $Å^{-3}$

Table 6.2

Selected Bond Lengths [Å] for $AuP(C_6H_5)_2(C_4H_9)Cl$

Measured Bond	Bond Length [Å]
Au(1)—P(1)	2.2943 (12)
Au(1)—Cl(1)	2.2484 (12)
P(1)—C(1)	1.826 (5)
P(1)—C(7)	1.825 (5)
P(1)—C(13)	1.864 (5)
C(2)—C(1)	1.368 (6)
C(1)—C(6)	1.393 (7)
C(2)—C(3)	1.379 (7)

Table 6.3

Selected Bond Angles [°] for $AuP(C_6H_5)_2(C_4H_9)Cl$

Measured Bond	Bond Angles [°]
P(1)—Au(1)—Cl(1)	176.70 (4)
C(1)—P(1)—Au(1)	109.09 (15)
C(1)—P(1)—C(13)	108.1 (2)
C(7)—P(1)—Au(1)	108.24 (15)
C(7)—P(1)—C(1)	110.6 (2)
C(7)—P(1)—C(13)	107.3 (2)
C(13)—P(1)—Au(1)	113.50 (17)
C(2)—C(1)—P(1)	117.8 (4)
C(6)—C(1)—P(1)	124.6 (4)

Table 6.4

Comparison of selected experimental and theoretical bond angles and lengths using DFT calculations

EXPERIMENTAL BOND LENGTH [Å]		CALCULATED BOND LENGTH [Å]
Au(1)—P(1)	2.2943	2.390
Au(1)—Cl(1)	2.2484	2.332
P(1)—C(1)	1.826 (5)	1.806
EXPERIMENTAL BOND ANGLE [°]		CALCULATED BOND ANGLE [°]
P(1)—Au(1)—Cl(1)	176.70	180.0
C(1)—P(1)—Au(1)	109.09	112.8
C(7)—P(1)—Au(1)	108.24	108.5

6.2.2 Infrared Spectroscopy. All infrared spectra were obtained as potassium bromide (KBr) disc, prepared by compressing the ground mixture of sample and KBr powder, on a Shimadzu IR-PRESTIGE-21 Fourier transform infrared spectrophotometer (4000−300 cm^{-1}). Figure 6.2, 6.3, 6.4, 6.5 and 6.6 shows both experimental and theoretical IR spectrum of the TDMOPP ligand, the mono-, di-, tri- and tetracoordinated TBDPP gold (I) complexes.

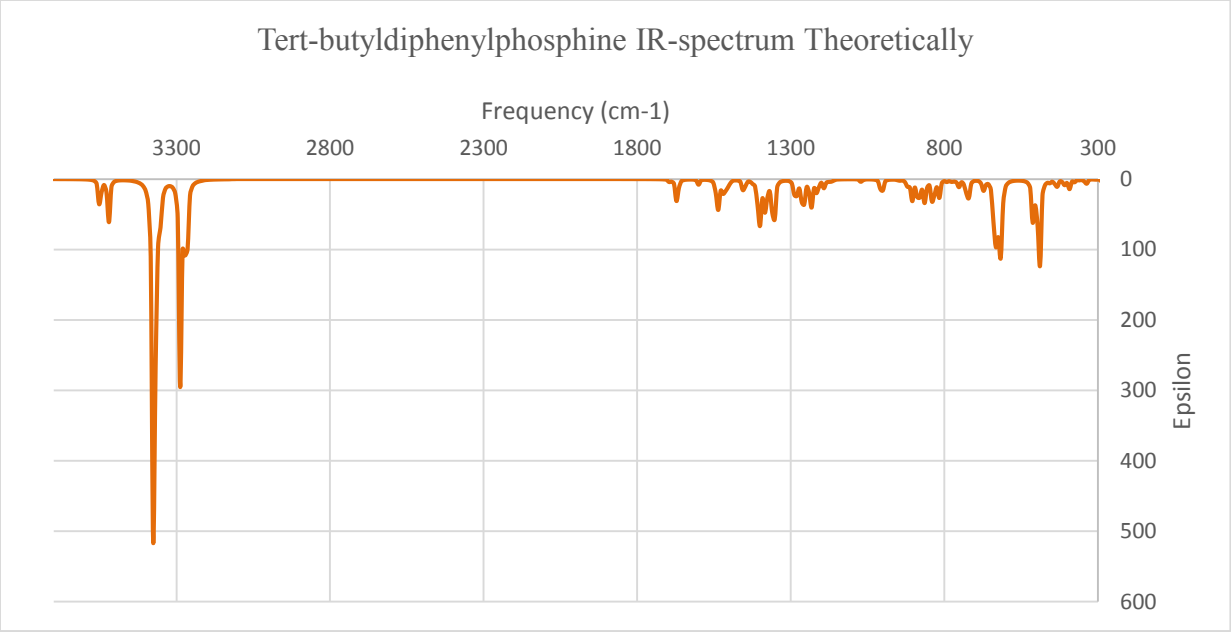

Figure 6.2. Theoretically calculated IR spectrum for $P(C_6H_5)_2(C_4H_9)$ using Gaussian 09 software.

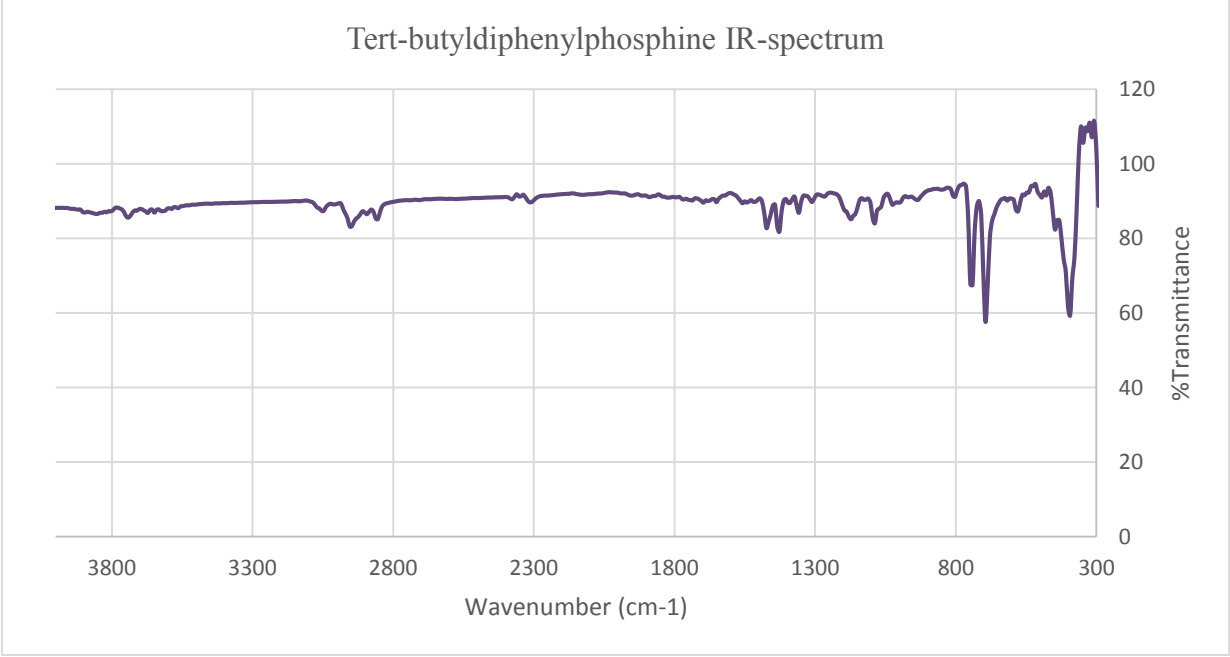

Figure 6.3. IR spectrum for $P(C_6H_5)_2(C_4H_9)$.

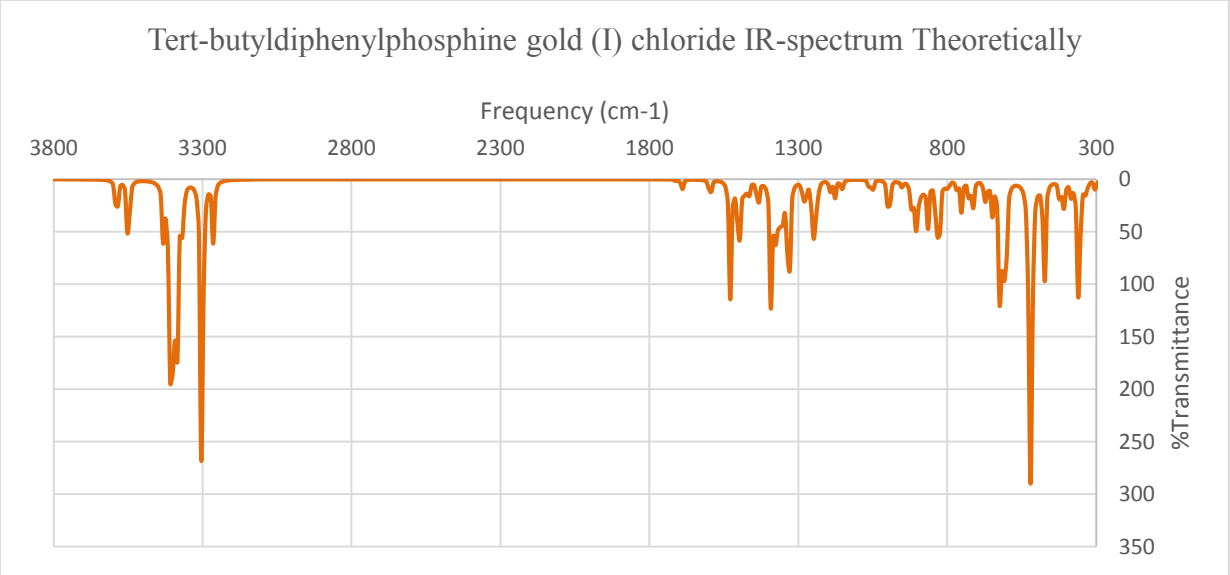

Figure 6.4. Theoretically calculated IR spectrum for $AuP(C_6H_5)_2(C_4H_9)Cl$ using Gaussian 09 software.

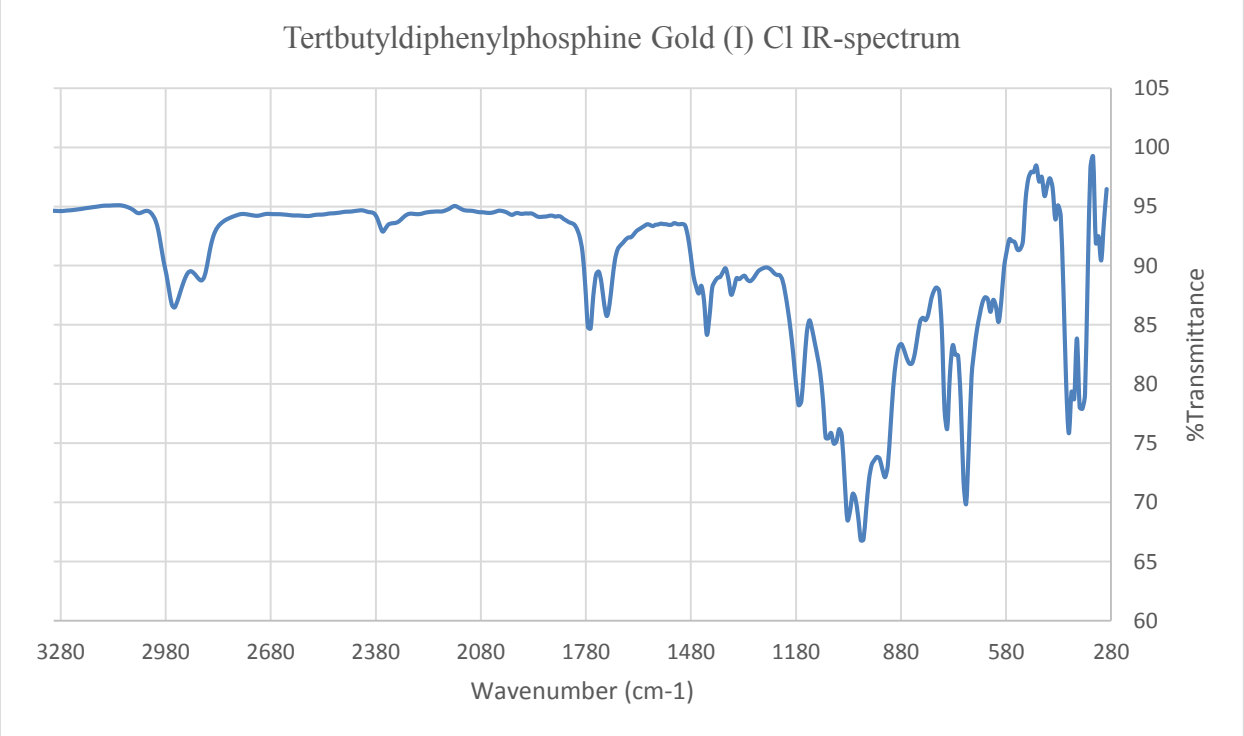

Figure 6.5. IR spectrum for $AuP(C_6H_5)_2(C_4H_9)Cl$.

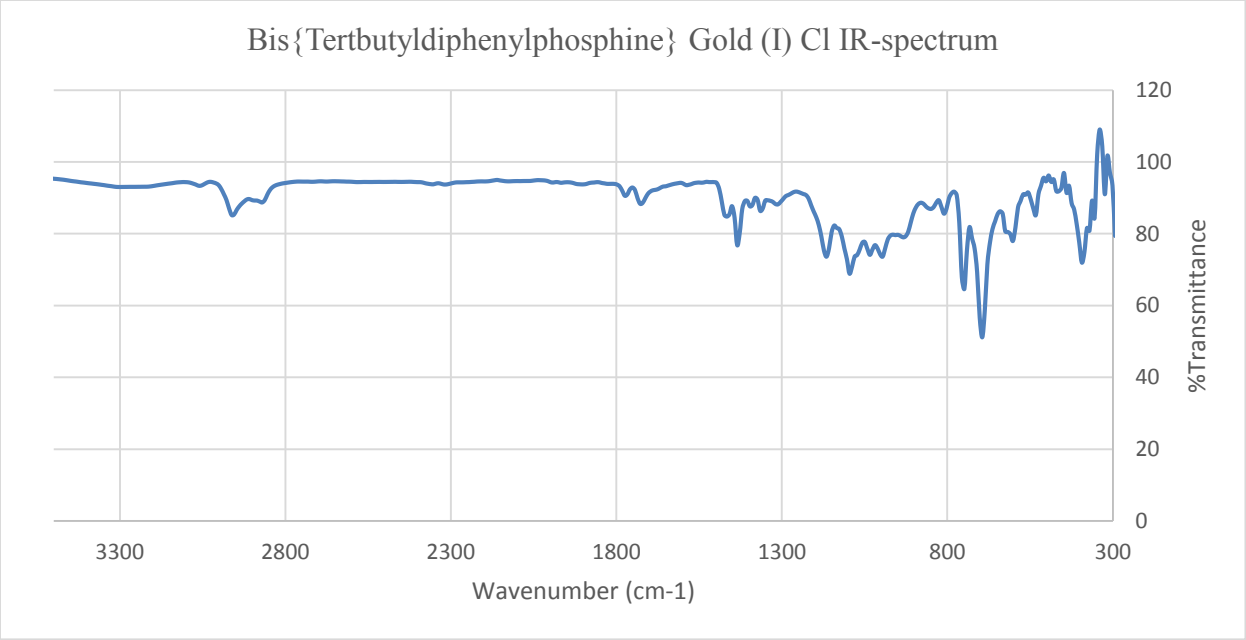

Figure 6.6. IR spectrum for $Au(P(C_6H_5)_2(C_4H_9))_2Cl$.

Table 6.5

Nuclear site group theoretical analysis for $AuP(C_6H_5)_2(C_4H_9)Cl$.

NUCLEAR SITE GROUP ANALYSIS FOR $[(AuP(C_6H_5)_2(C_4H_9)Cl)]$					
ATOMS	Au	P	Cl	C_x	C_y
SITES (16A)	C_1	C_1	C_1	C_1	C_i
VIBRATIONAL (5B)	$3A_g + 3A_u + 3B_g + 3B_u$	$3A_g + 3A_u + 3B_g + 3B_u$	$3A_g + 3A_u + 3B_g + 3B_u$	$3A_g + 3A_u + 3B_g + 3B_u$	$3A_u + 3B_u$
TOTAL CONTRIBUTION = $12A_g + 15A_u + 12B_g + 15B_u$					
ACOUSTIC MODES (5E) = $A_u + B_u$					
OPTICAL MODES = $12A_g + 14A_u + 12B_g + 14B_u$					
IR ACTIVE (5E) = $14A_u + 14B_u$					
RAMAN ACTIVE (5E) = $12A_g + 12B_g$					

6.2.3 Nuclear Magnetic Resonance. The ^{1}H NMR spectral data for the monocoordinated TBDPP gold complex was found in Figure 6.8 showing peaks at 1.3 (3H), 1.5 (6H), 7.3 (2H), 7.6 (2H), 7.9 (1H) ppm and that of the dicoordinated TBDPP gold (I) complex was found in Figure 6.9 showing peaks at 1.4 (3H), 1.6 (6H), 7.4 (2H), 7.6 (2H), 7.9 (1H). The ^{1}H NMR spectral data for the free ligand TBDPP was found in Figure 6.7 showing peaks at 1.2 (3H), 1.4 (6H), 7.2 (2H), 7.5 (2H), 8.0 (1H). The $^{31}P\{^{1}H\}$ NMR spectral data for the ligand, **14** and **15** was found in Figure 6.10, 6.11 and 6.12 showing peaks at 40.0, 56 and 63.0 ppm respectively. Theoretically calculated proton NMR using Gaussian 09 is also shown at Figure 6.13 and 6.14.

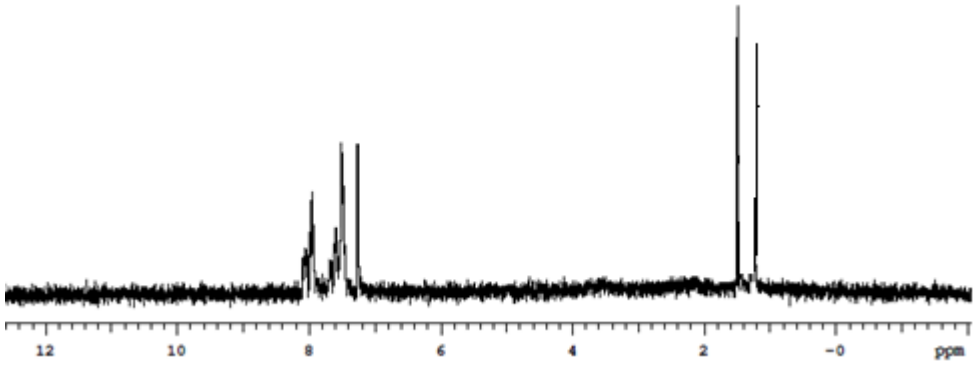

Figure 6.7. ^{1}H NMR spectrum of $P(C_6H_5)_2(C_4H_9)$.

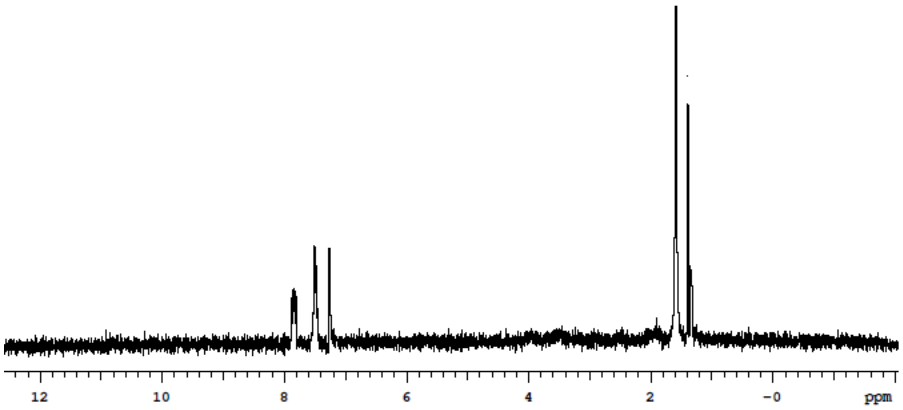

Figure 6.8. ^{1}H NMR spectrum of $AuP(C_6H_5)_2(C_4H_9)Cl$.

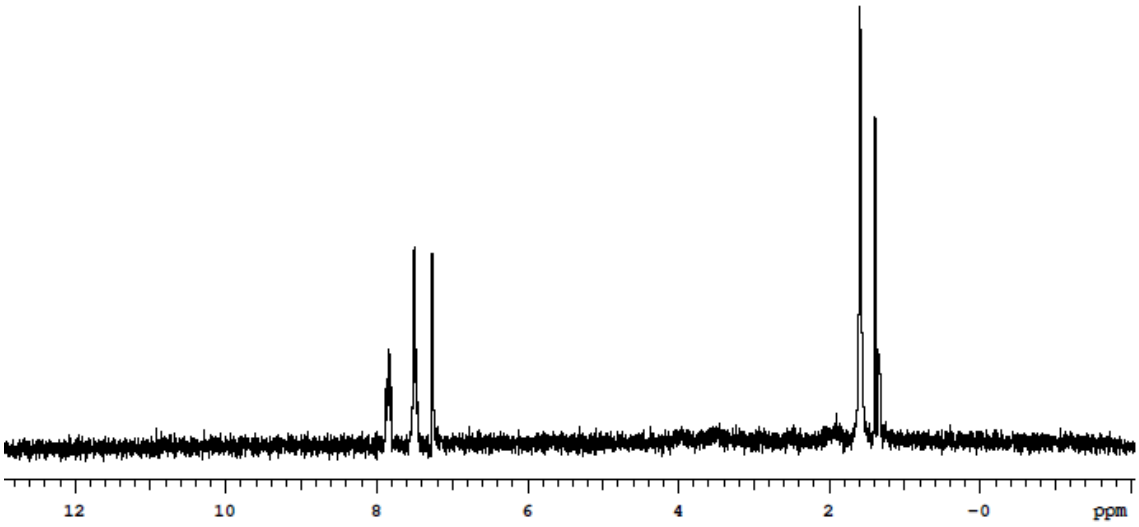

Figure 6.9. ^{1}H NMR spectrum of $Au(P(C_6H_5)_2(C_4H_9))_2Cl$.

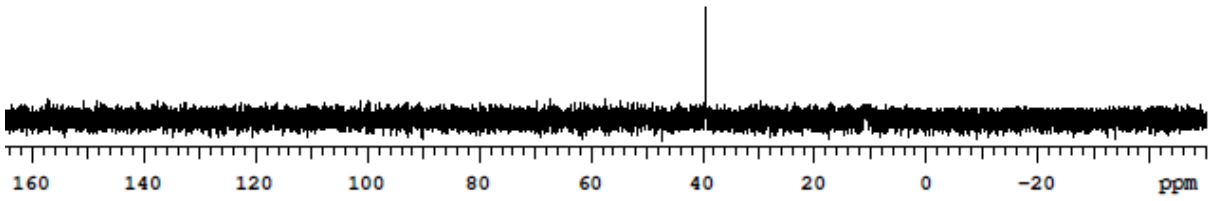

Figure 6.10. $^{31}P\{^{1}H\}$ NMR spectrum of $P(C_6H_5)_2(C_4H_9)$.

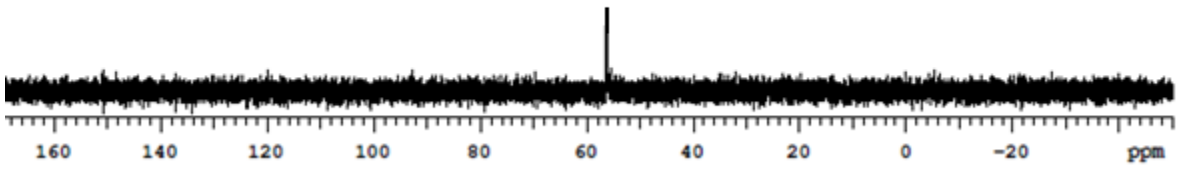

Figure 6.11. $^{31}P\{^{1}H\}$ NMR spectrum of $AuP(C_6H_5)_2(C_4H_9)Cl$.

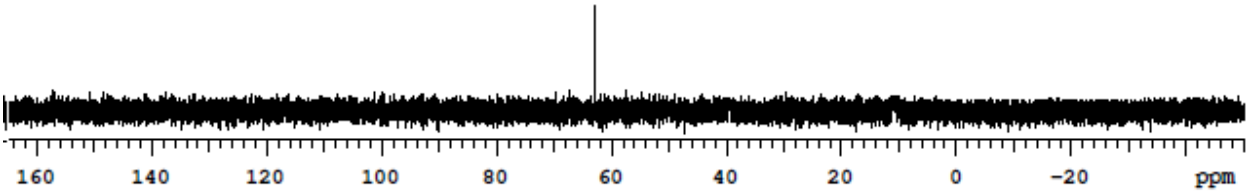

Figure 6.12. $^{31}P\{^{1}H\}$ NMR spectrum of $AuP(C_6H_5)_2(C_4H_9)Cl$.

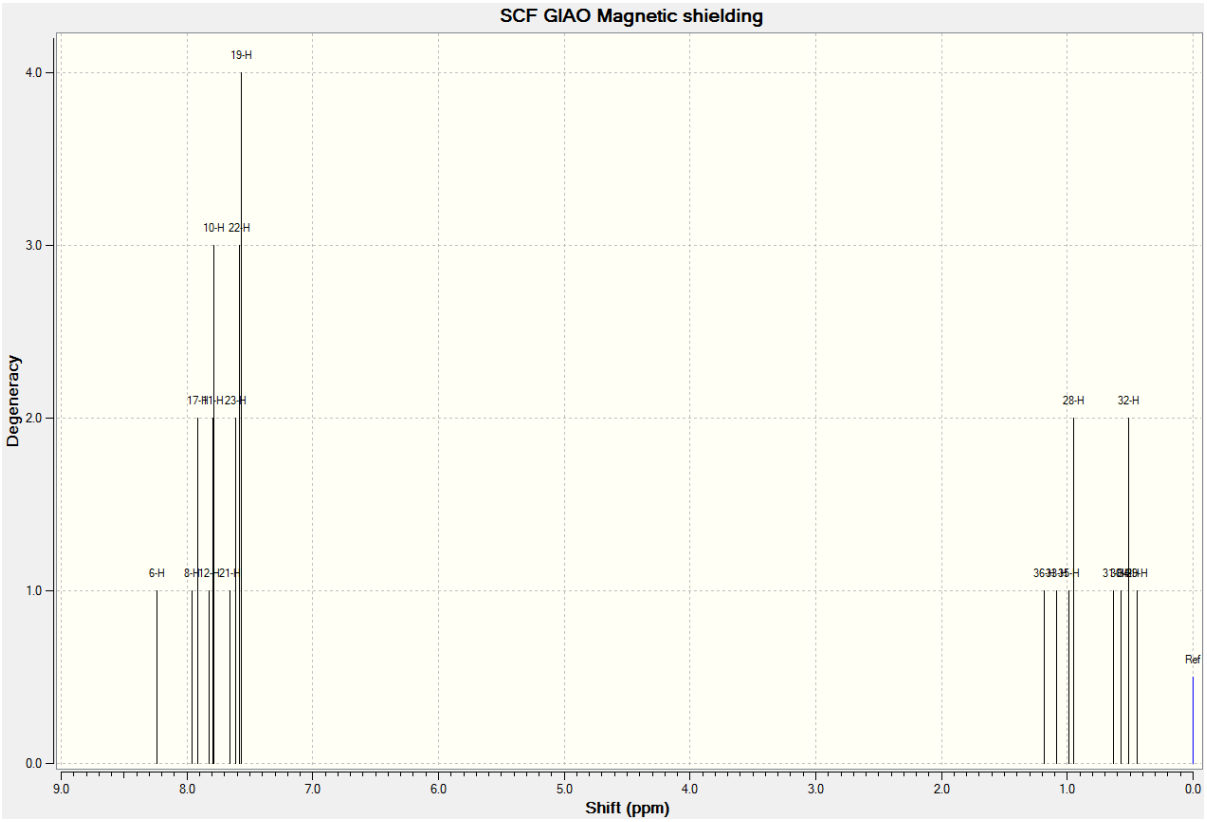

Figure 6.13. Theoretically calculated ^{1}H NMR spectrum of $P(C_6H_5)_2(C_4H_9)$ using Gaussian 09 software.

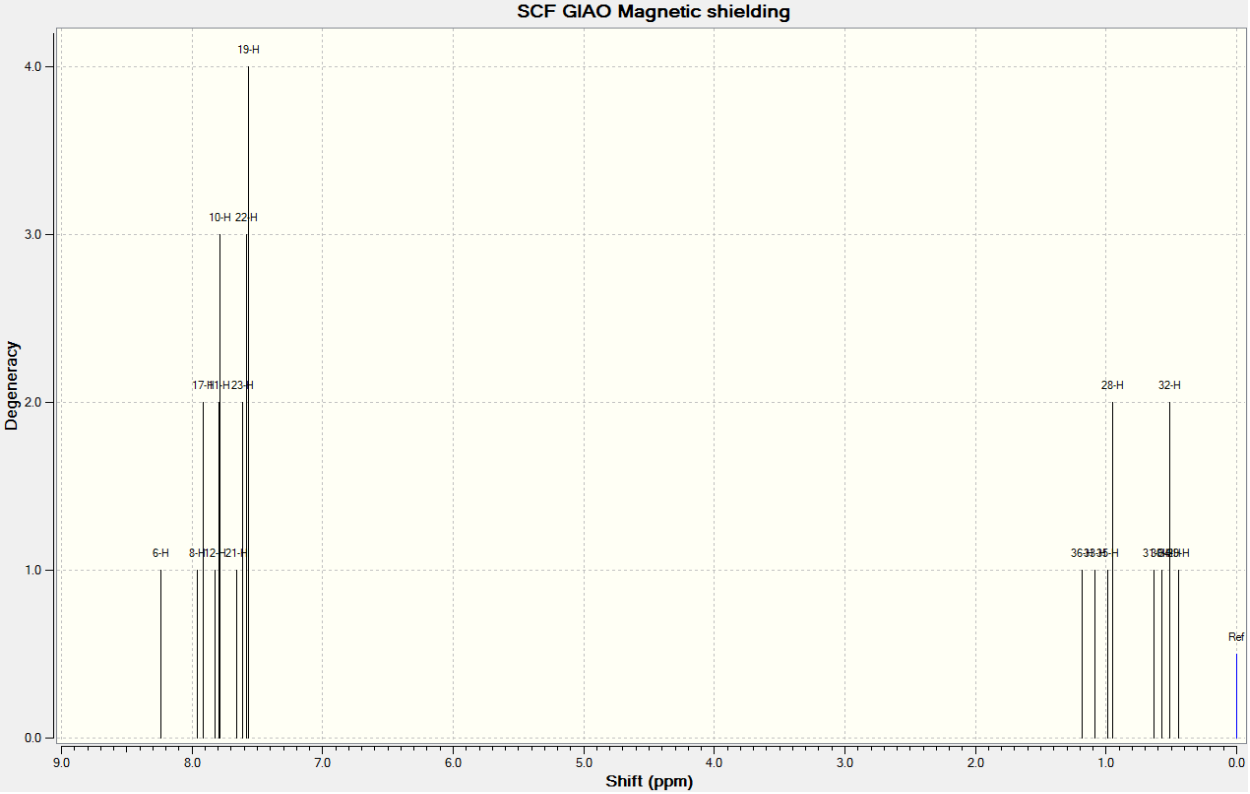

Figure 6.14. Theoretically calculated ^{1}H NMR spectrum of $AuP(C_6H_5)_2(C_4H_9)Cl$ using Gaussian 09 software.

6.2.4 UV-Vis Spectroscopy. All of the samples used for the ultraviolet visible (absorption) experiment, were dissolved in spectroscopic grade acetonitrile (CH_3CN). The TBDPP ligand has a broad absorption spectrum shown at Figure 6.15 that maximizes around 270 nm with a calculated molar absorptivity of 4.32 x 10^4 $M^{-1}cm^{-1}$. The absorption spectrum of **14** shown at Figure 6.16 has a broad absorption profile maximizes at about 240 nm with a calculated molar absorptivity of 7.11 x 10^4 $M^{-1}cm^{-1}$. In Figure 6.17 is shown the absorption profile for **15** which has a band maximum of about 238 nm with a calculated molar absorptivity of 1.20 x 10^5 $M^{-1}cm^{-1}$. The theoretical spectrum using DFT calculations, shows a spectrum at Figure 6.18 and 6.19 with a broad absorption spectrum at 237 nm and 290 for **14** and the TBDPP ligand respectively.

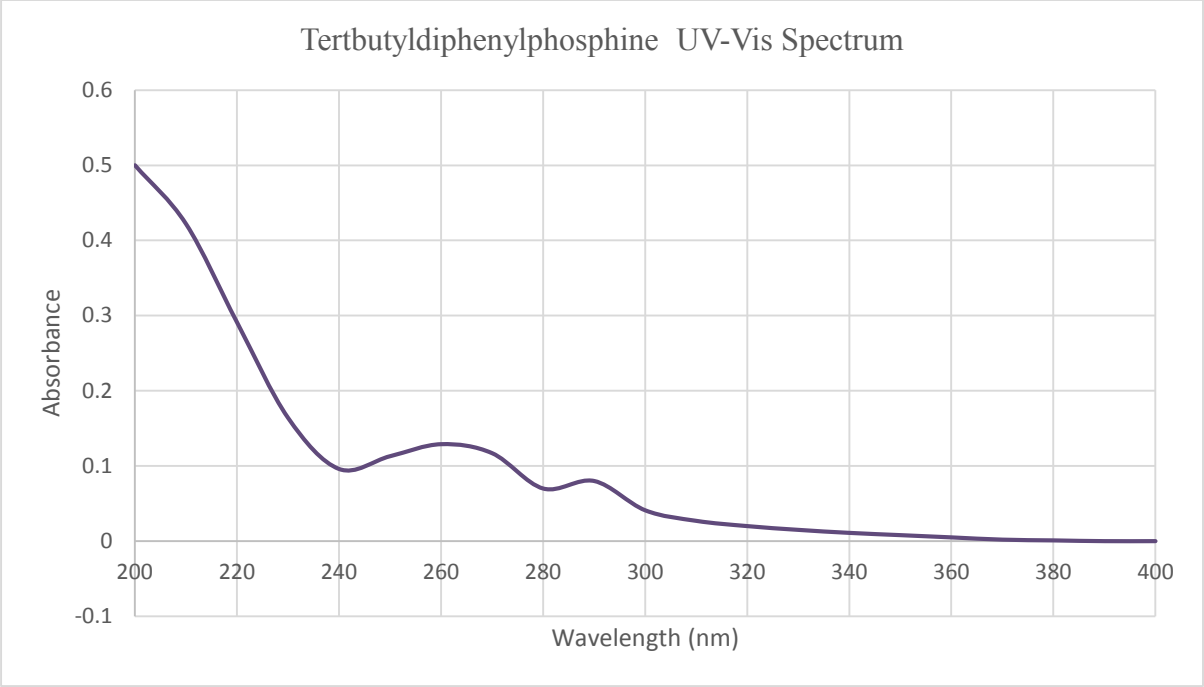

Figure 6.15. UV-Vis spectrum of $P(C_6H_5)_2(C_4H_9)$.

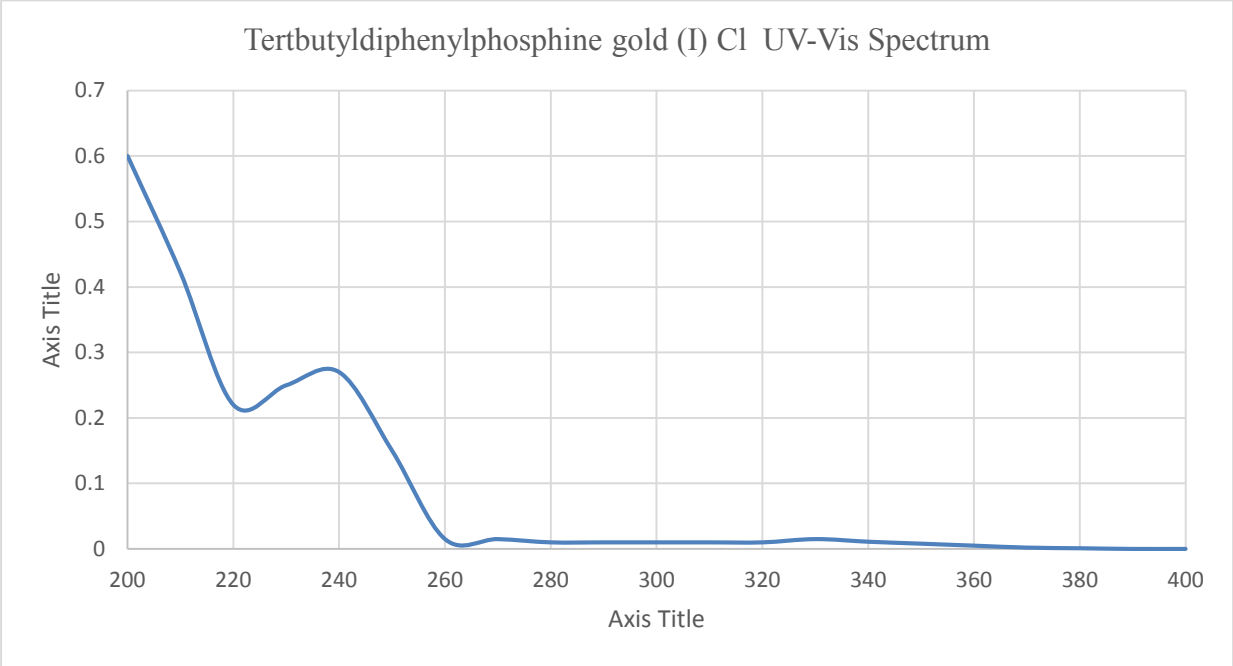

Figure 6.16. UV-Vis spectrum of $AuP(C_6H_5)_2(C_4H_9)Cl$.

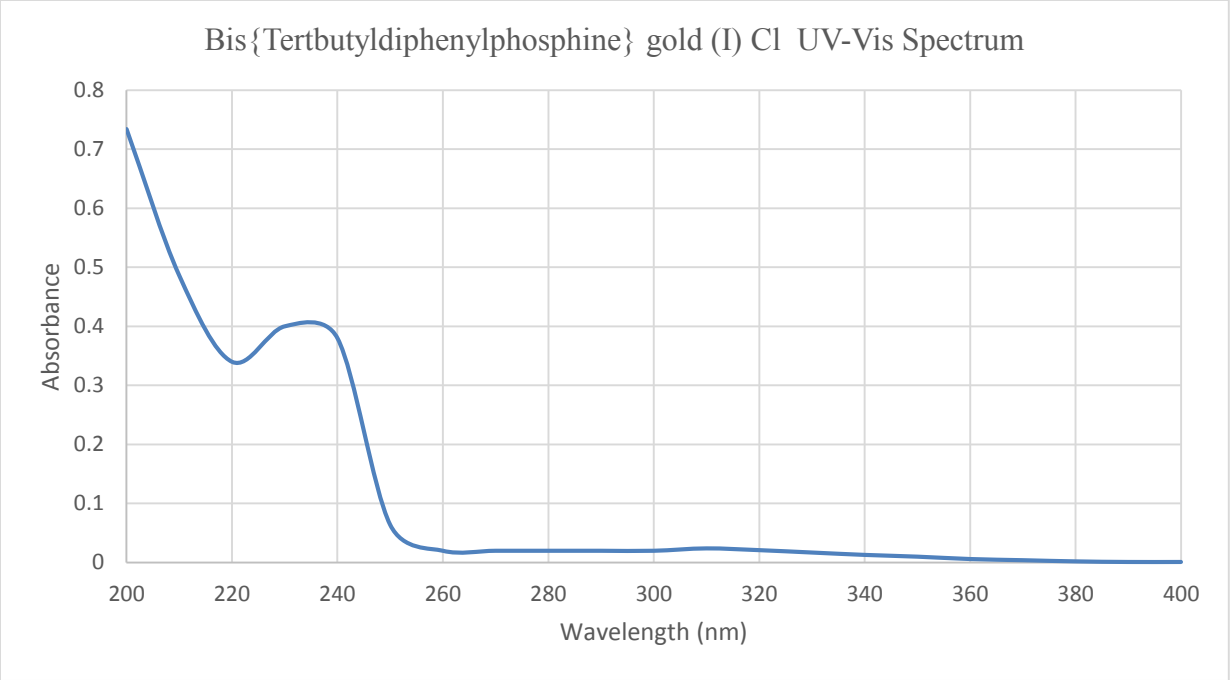

Figure 6.17. UV-Vis spectrum of $Au(P(C_6H_5)_2(C_4H_9))_2Cl$.

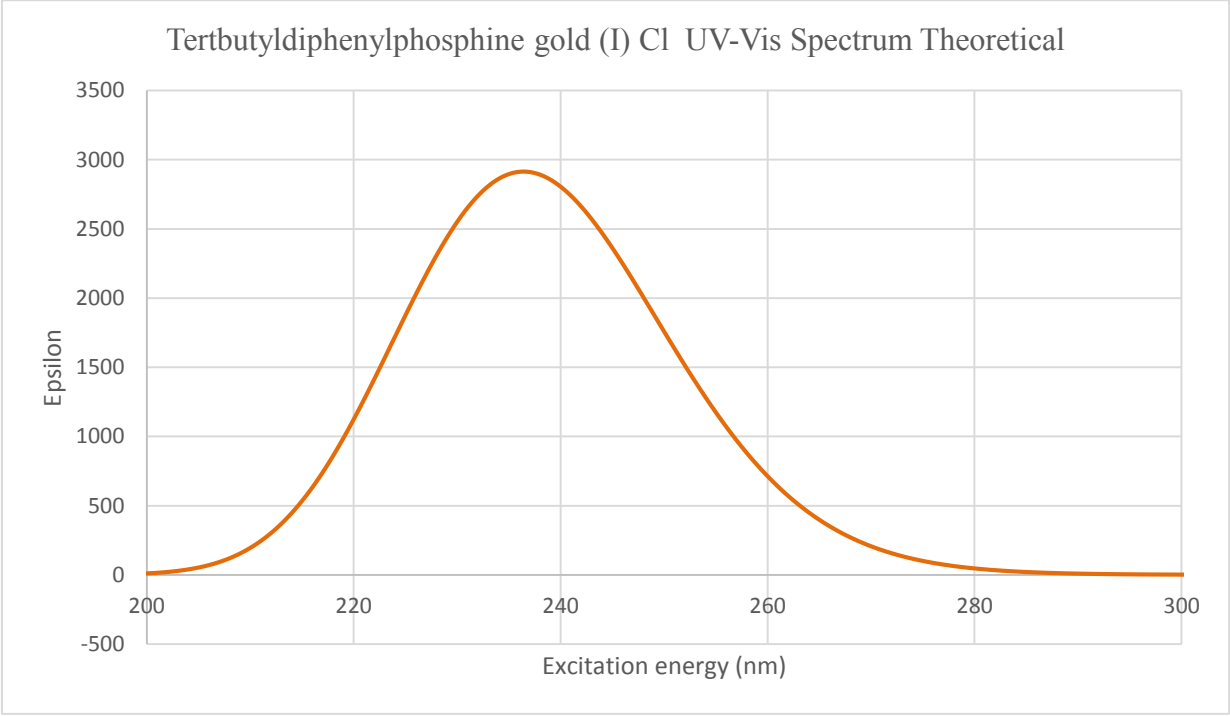

Figure 6.18. Theoretically calculated UV-Vis spectrum of $AuP(C_6H_5)_2(C_4H_9)Cl$ using Gaussian 09 software.

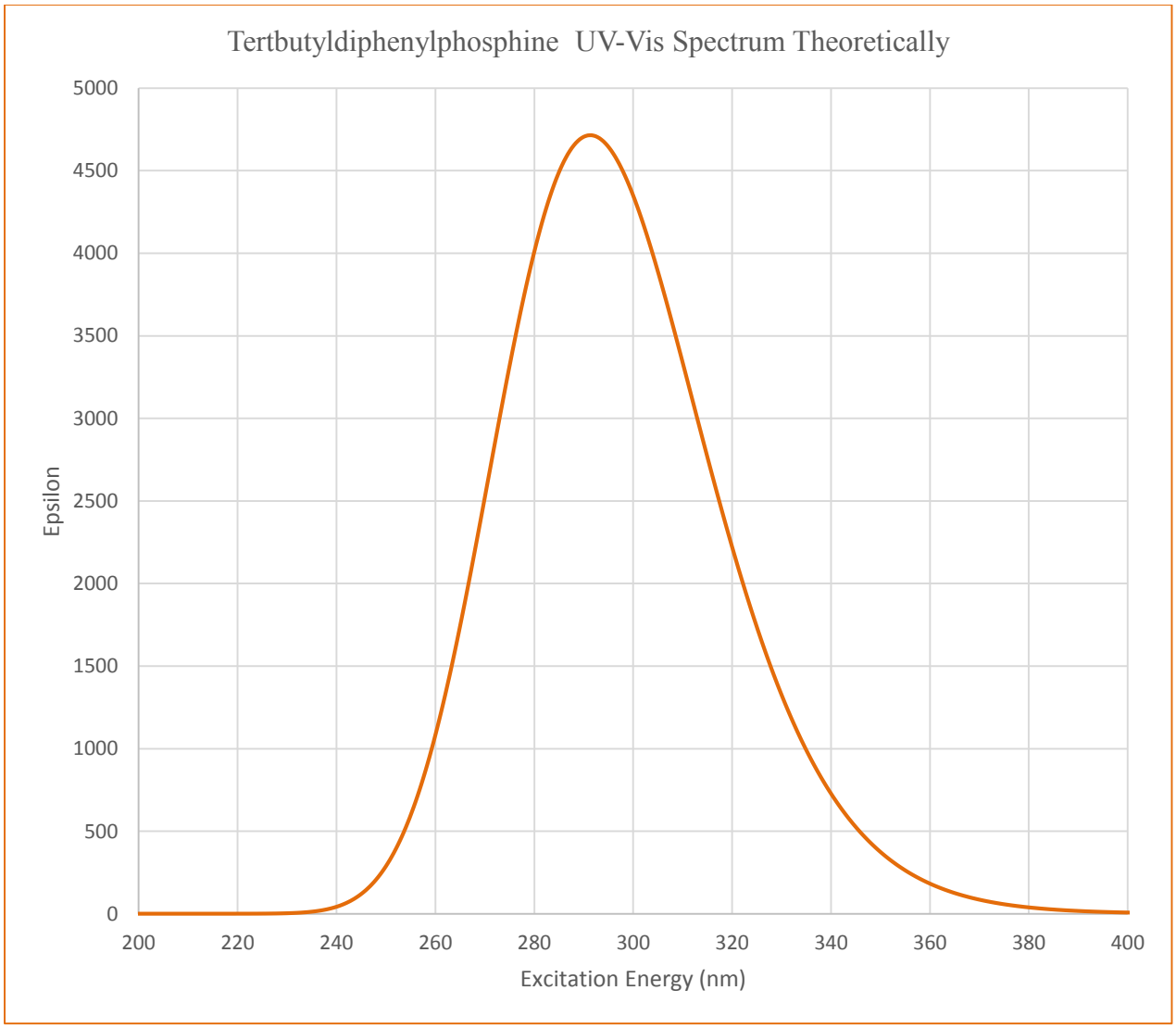

Figure 6.19. Theoretically calculated UV-Vis spectrum of $AuP(C_6H_5)_2(C_4H_9)Cl$ using Gaussian 09 software.

Table 6.6

*TD-DFT generated ground-state to excited-state MO transitions for **14***

TRANSITIONS	CORRESPONDING ORBITALS	% CONTRIBUTION
X	71 → 74	6.52
	71 → 75	8.46
	72 → 74	15.94
	72 → 75	14.84
	72 → 78	6.96
	73 → 74	30.13
	73 → 75	9.36
	73 → 78	7.79
Y	70 → 74	30.11
	70 → 75	10.43
	72 → 74	9.45
	73 → 74	14.40
	73 → 76	20.60
	73 → 77	14.90
Z	70 → 74	8.24
	71 → 74	17.53
	71 → 75	13.23
	71 → 78	6.56
	72 → 74	16.55
	72 → 75	14.46
	72 → 76	5.92
	72 → 78	10.11
	73 → 74	7.38

Table 6.7

*Theoretical results showing the contributions of X, Y, and Z transitions of **14***

Excitation	λcalc. (nm)	%Contribution to the transition		Transition Energy (cm^{-1})	λexp. (nm)
X	237.12				240
Major contribution:					
	73→ 74	30.13		42,173	
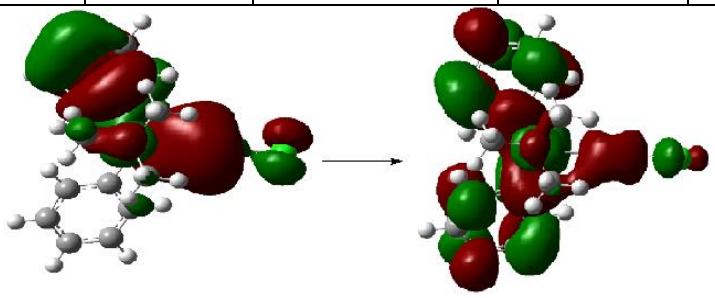					
Y	235.73				
Major contribution:					
	70 → 74	30.11		42,423	
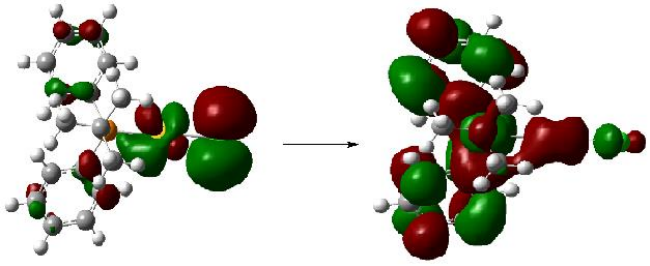					
Z	234.85				
Major contribution:					
	71 → 74	17.53		42,581	
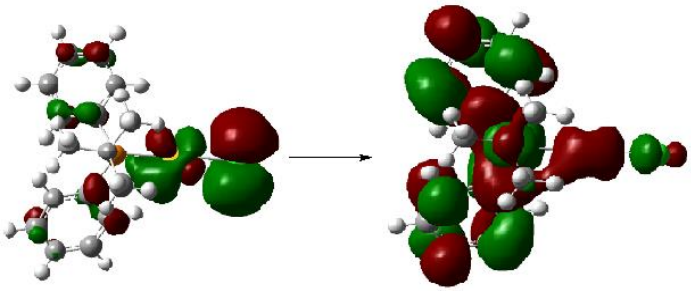					

6.2.5 Luminescence. The TBDPP ligand shows excitation spectrum at room temperature in Figure 6.20. The excitation spectrum for the $AuP(C_6H_5)_2(C_4H_9)Cl$ at room temperature is shown in Figure 6.21, 6.22, 6.23 and 6.24 covering the spectral region from 280 to 430 nm, 280 to 388 nm, 300 to 470 nm, 300 to 447 nm and monitored at an emission band of 450, 424, 490 and 467 nm respectively. The spectrum exhibited vibronic bands at 346, 389 nm monitored at 450 nm; 300, 368 nm monitored at 424 nm; 370, 419 nm monitored at 490 nm; 345, 401 nm monitored at an emission of 467. The excitation spectrum collected in liquid nitrogen is shown in Figure 6.25 and 6.26 covering the spectral region from 280 to 430 nm, 280 to 391 nm, and monitored at an emission band of 450 and 411 nm respectively. The spectrum shows vibronic components at 318, 372, 382 and 392 nm monitored at 450nm; 316, 362, 372 and 382 nm monitored at an emission of 411.The emission spectrum for the ligand collected at room temperature is shown in Figure 6.27. The emission spectrum for both room temperature and liquid nitrogen can be found in Figure 6.28, 6.29, 6.30, and 6.31, 6.32, 6.33, 6.34, respectively.

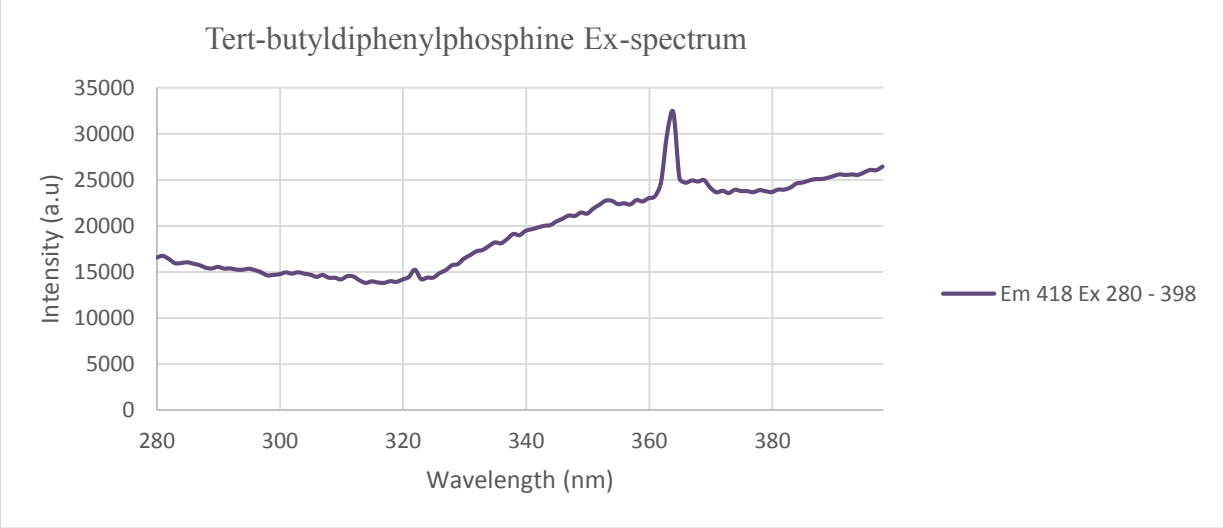

Figure 6.20. Excitation spectrum of $P(C_6H_5)_2(C_4H_9)$ collected at room temperature by monitoring the emission at 418 nm.

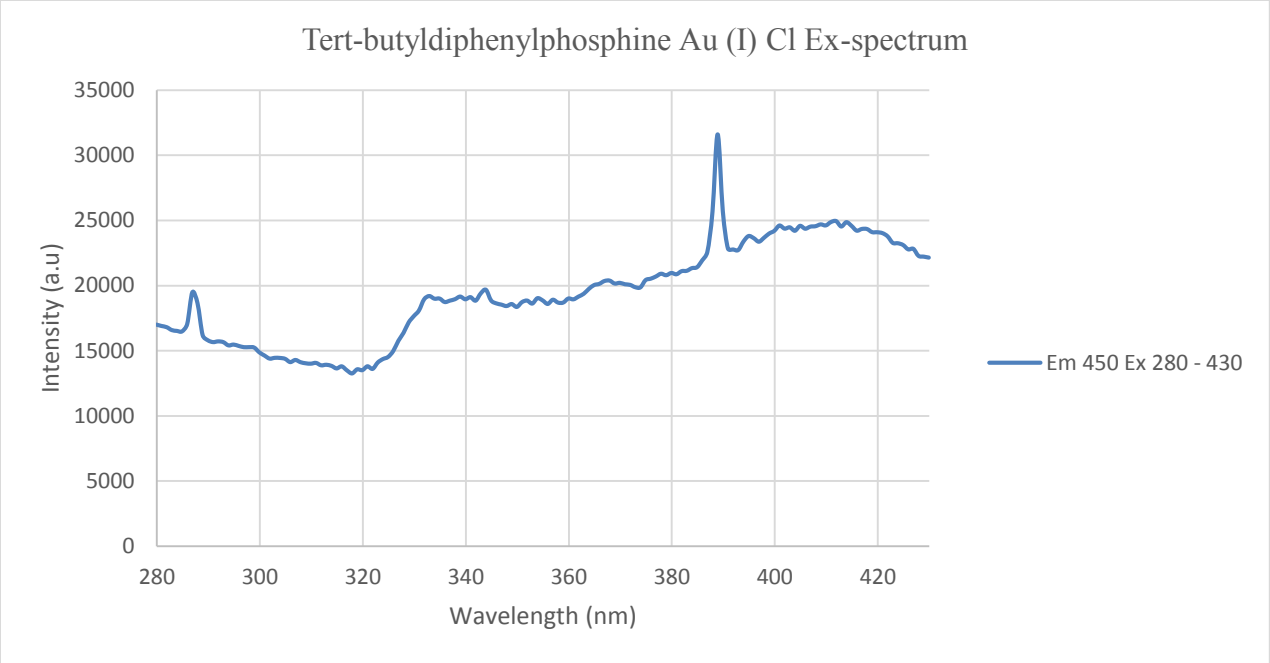

Figure 6.21. Excitation spectrum of $AuP(C_6H_5)_2(C_4H_9)Cl$ collected at room temperature by monitoring the emission at 450 nm.

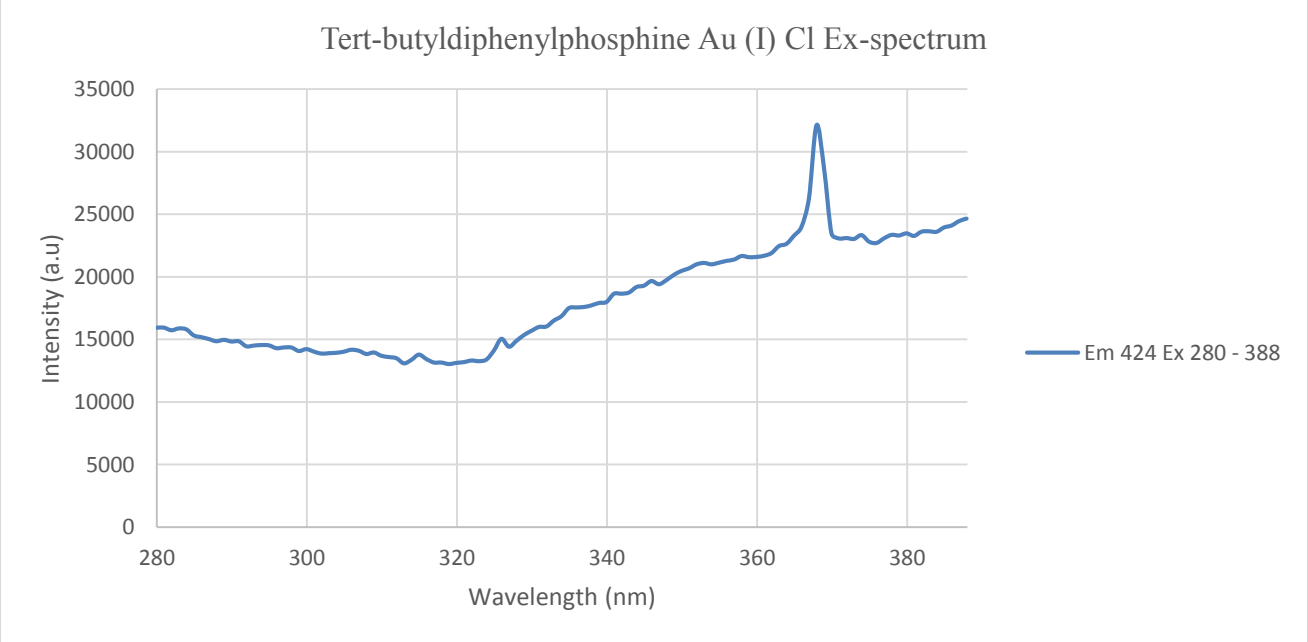

Figure 6.22. Excitation spectrum of $AuP(C_6H_5)_2(C_4H_9)Cl$ collected at room temperature by monitoring the emission at 424 nm.

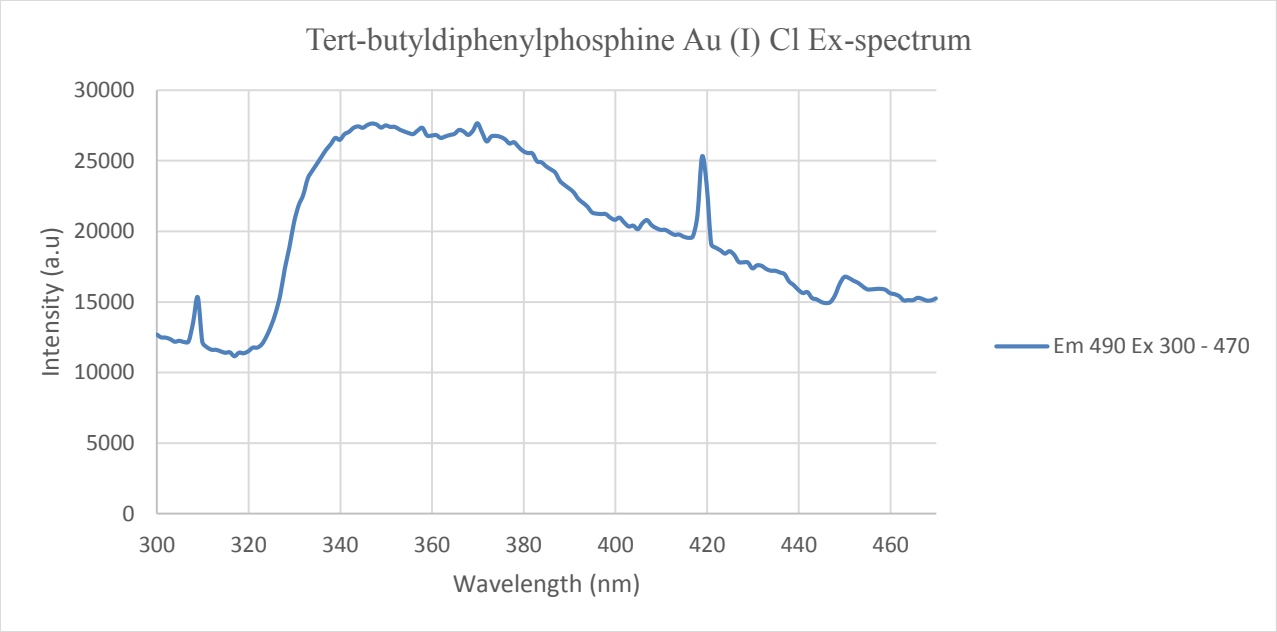

Figure 6.23. Excitation spectrum of $AuP(C_6H_5)_2(C_4H_9)Cl$ collected at room temperature by monitoring the emission at 490 nm.

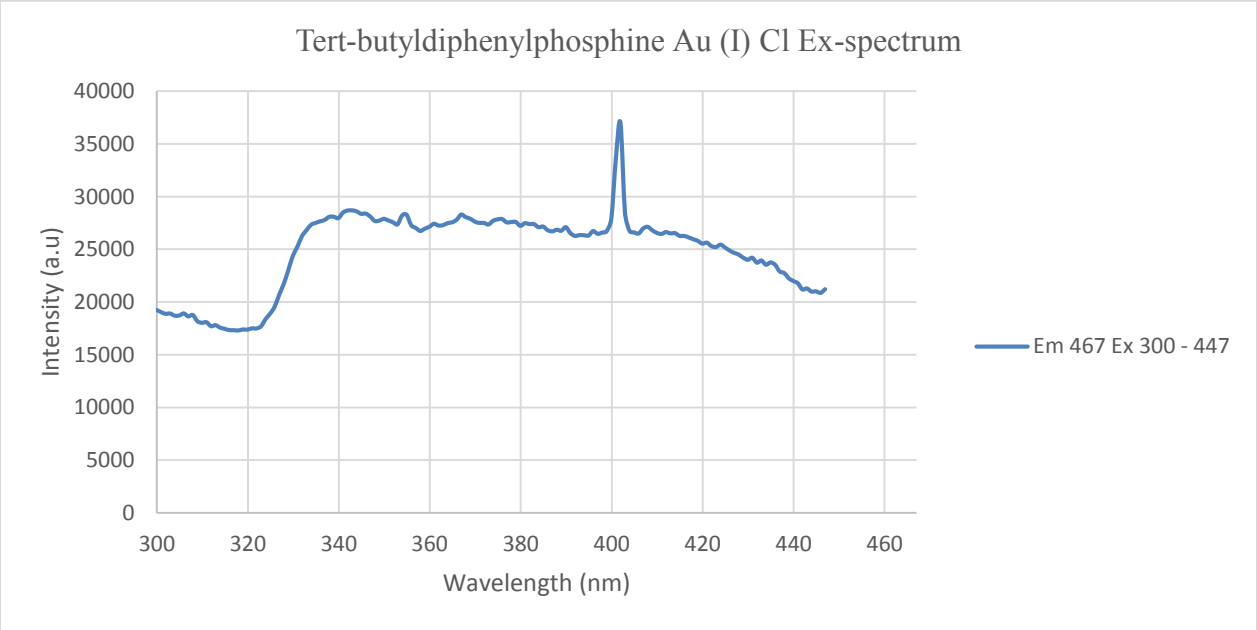

Figure 6.24. Excitation spectrum of $AuP(C_6H_5)_2(C_4H_9)Cl$ collected at room temperature by monitoring the emission at 467 nm.

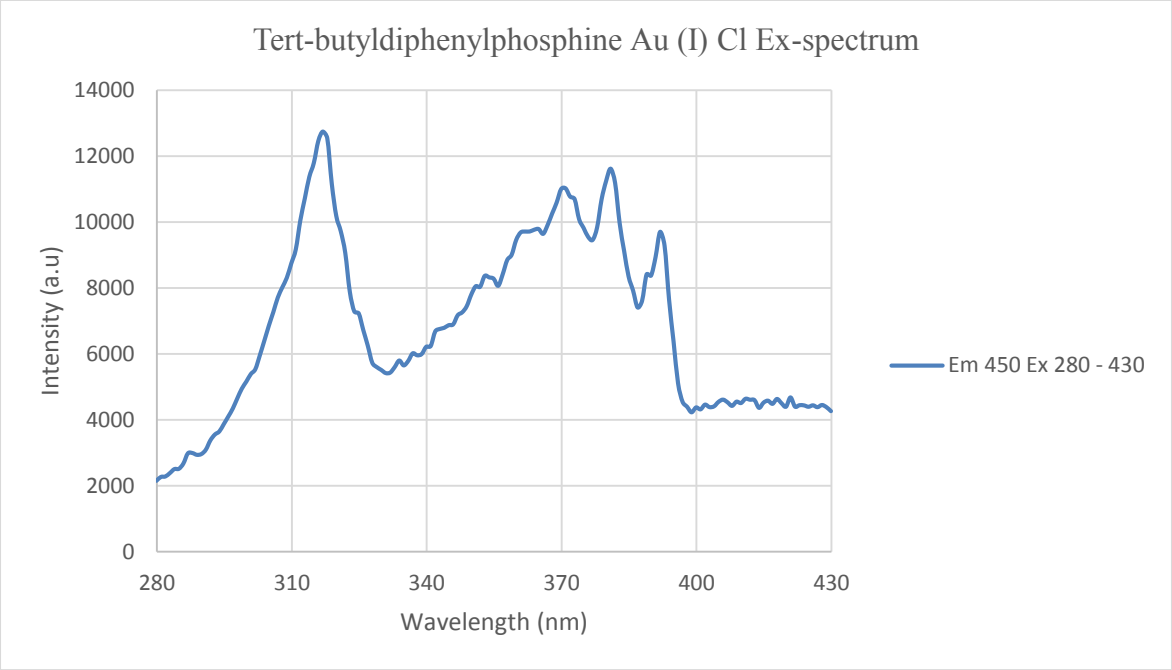

Figure 6.25. Excitation spectrum of $AuP(C_6H_5)_2(C_4H_9)Cl$ collected in liquid nitrogen by monitoring the emission at 450 nm.

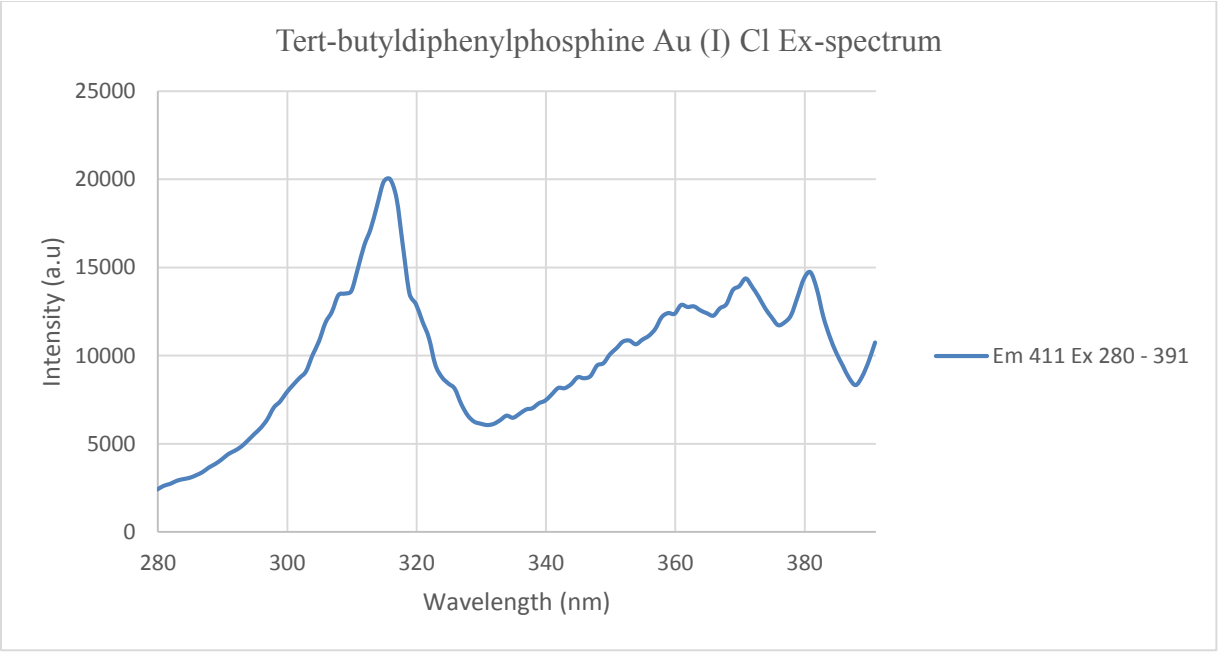

Figure 6.26. Excitation spectrum of $AuP(C_6H_5)_2(C_4H_9)Cl$ collected in liquid nitrogen by monitoring the emission at 411 nm.

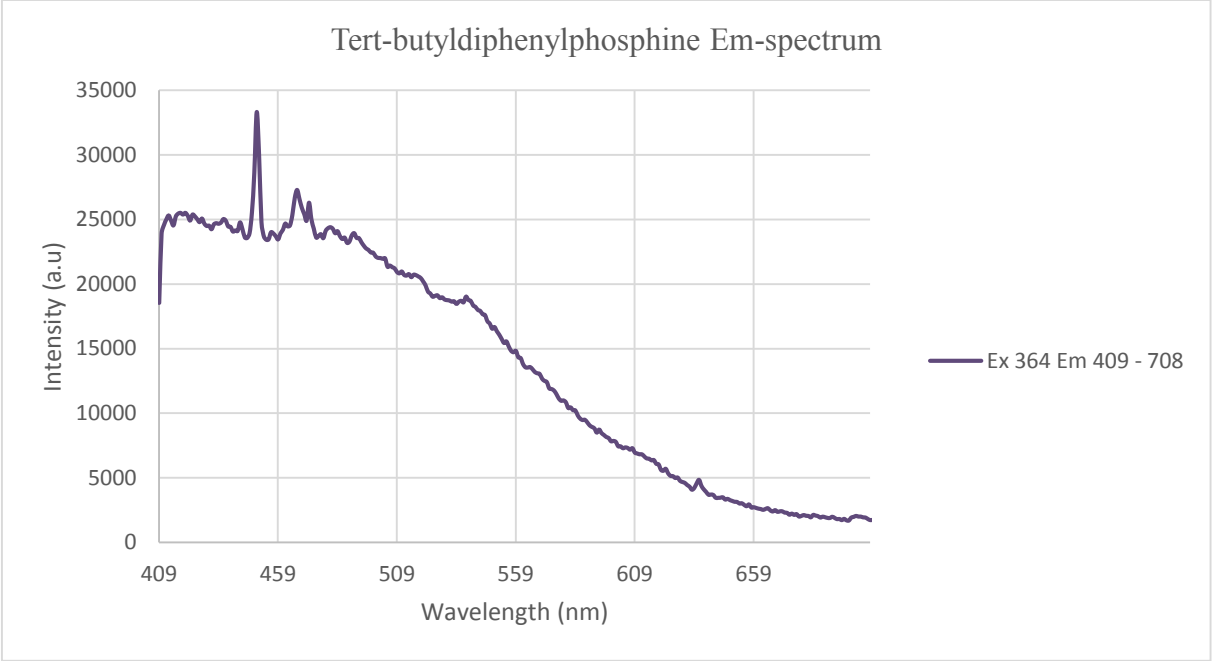

Figure 6.27. Emission spectrum of $P(C_6H_5)_2(C_4H_9)$ collected at room temperature upon excitation at 364 nm.

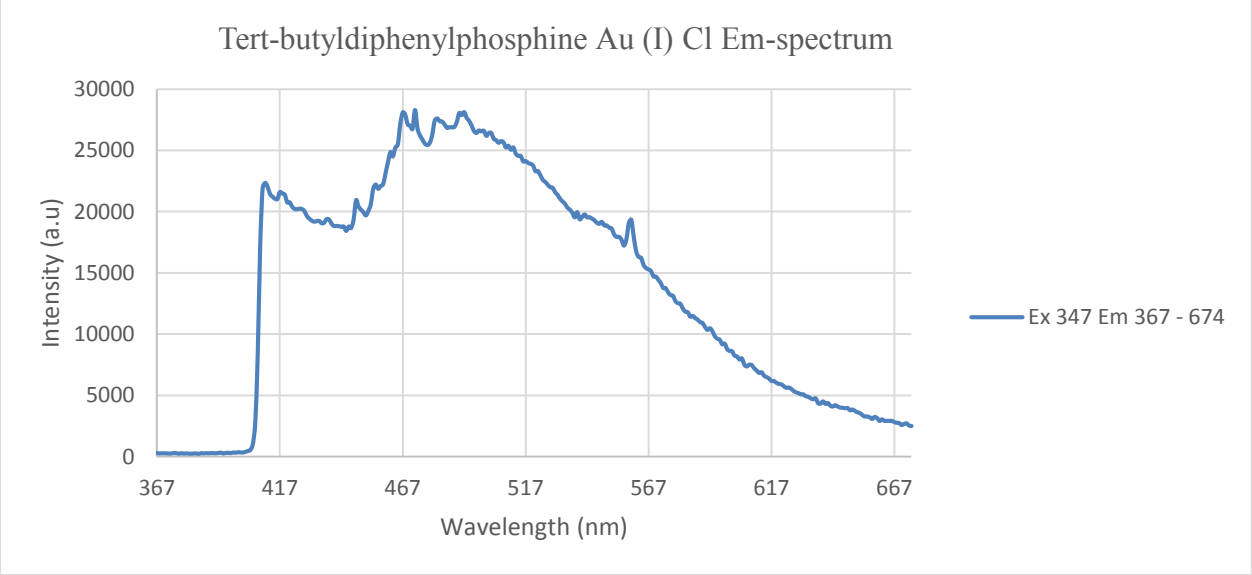

Figure 6.28. Emission spectrum of $AuP(C_6H_5)_2(C_4H_9)Cl$ collected at room temperature upon excitation at 347 nm.

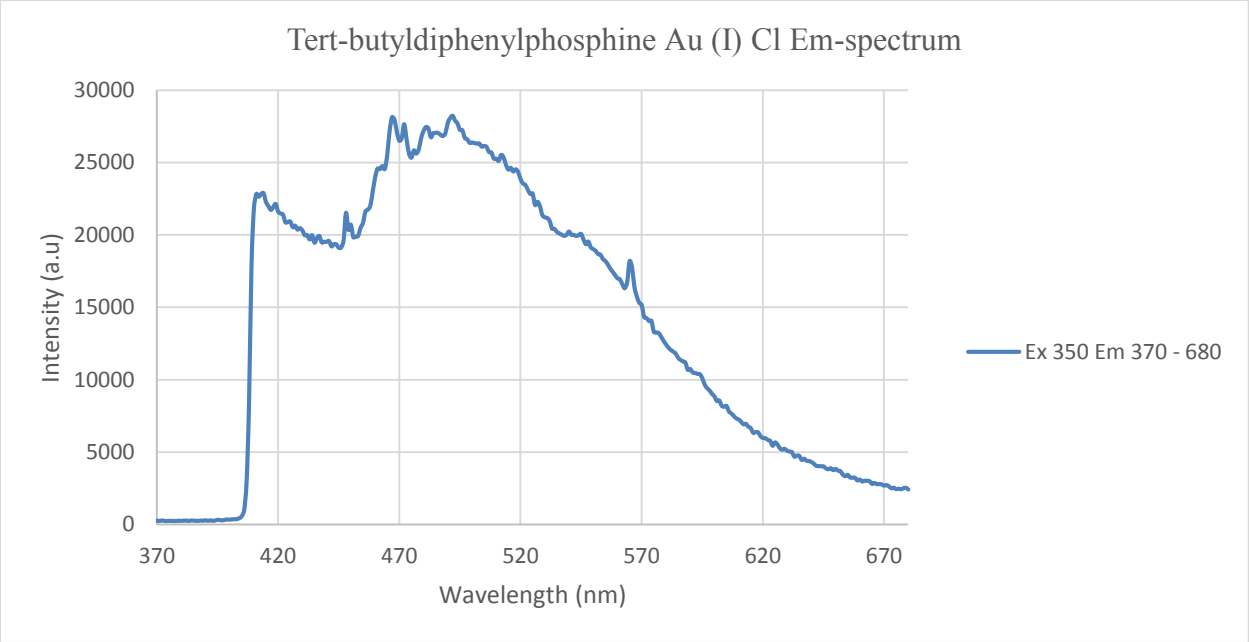

Figure 6.29. Emission spectrum of $AuP(C_6H_5)_2(C_4H_9)Cl$ collected at room temperature upon excitation at 350 nm.

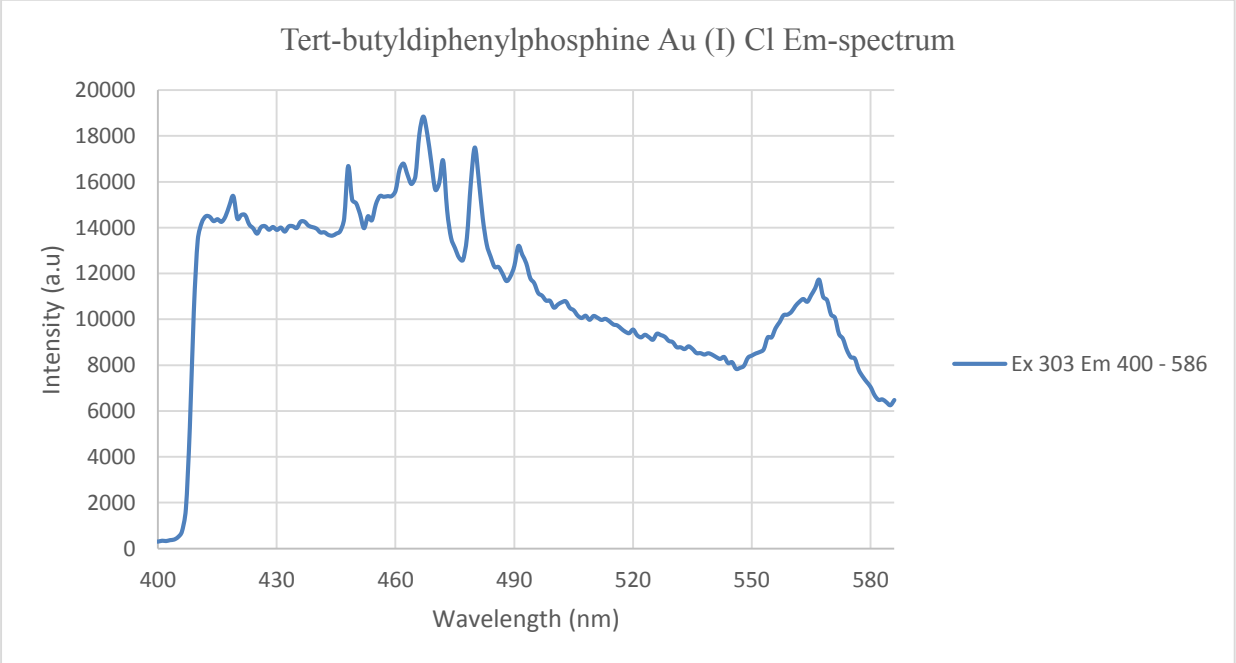

Figure 6.30. Emission spectrum of $AuP(C_6H_5)_2(C_4H_9)Cl$ collected at room temperature upon excitation at 303 nm.

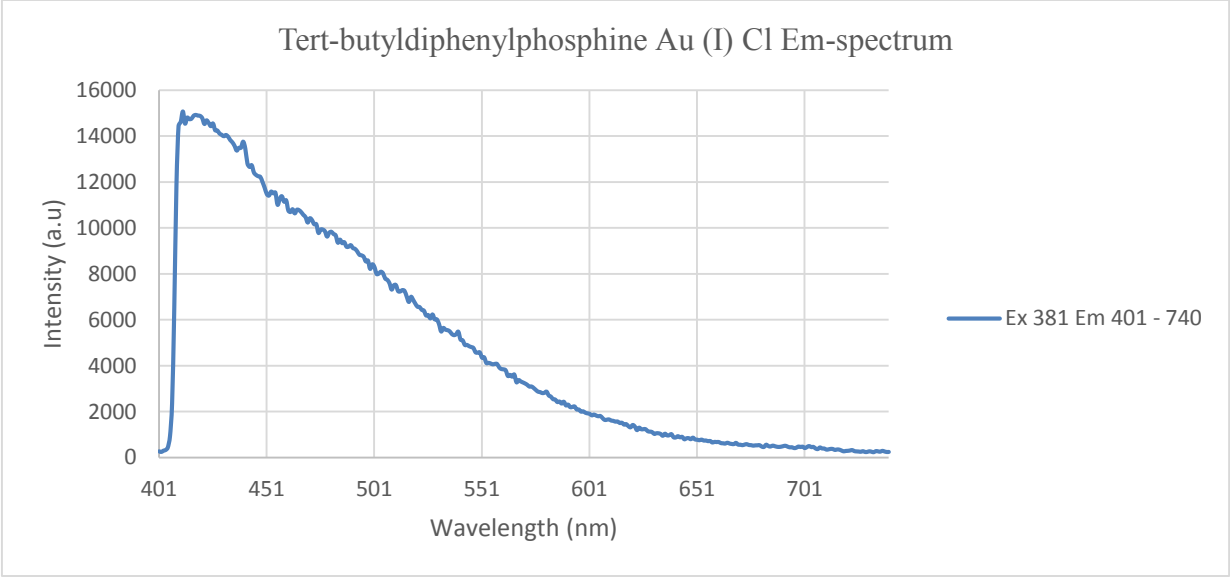

Figure 6.31. Emission spectrum of $AuP(C_6H_5)_2(C_4H_9)Cl$ collected in liquid nitrogen upon excitation at 381 nm.

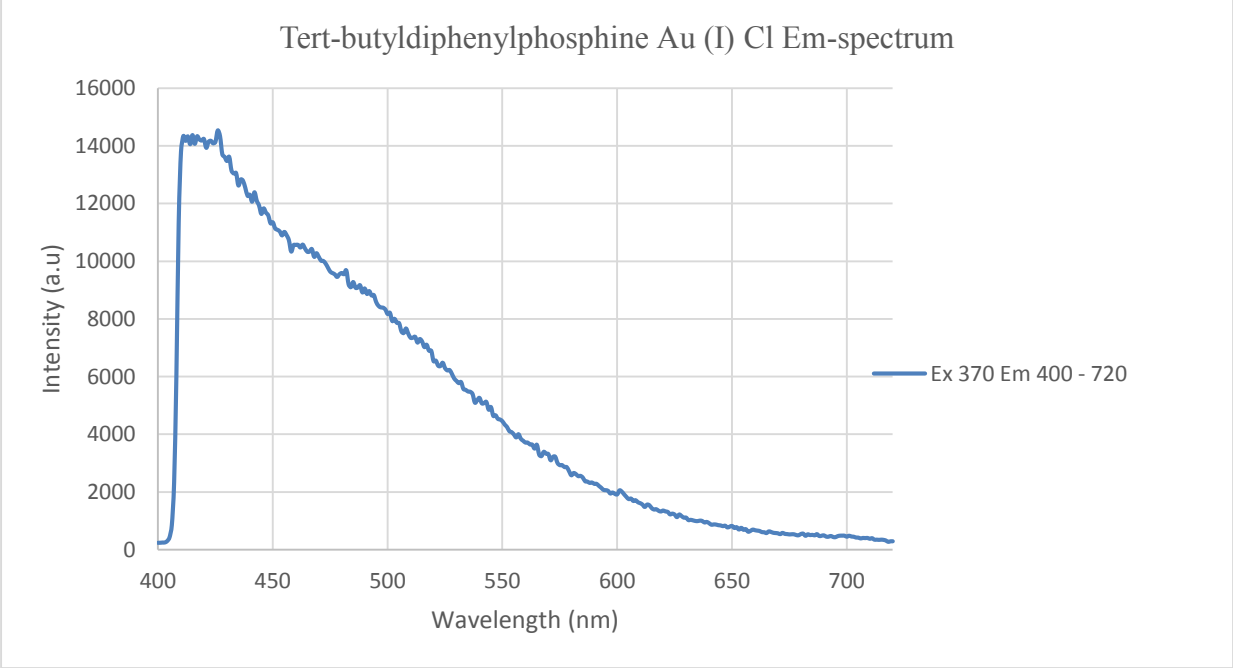

Figure 6.32. Emission spectrum of $AuP(C_6H_5)_2(C_4H_9)Cl$ collected in liquid nitrogen upon excitation at 370 nm.

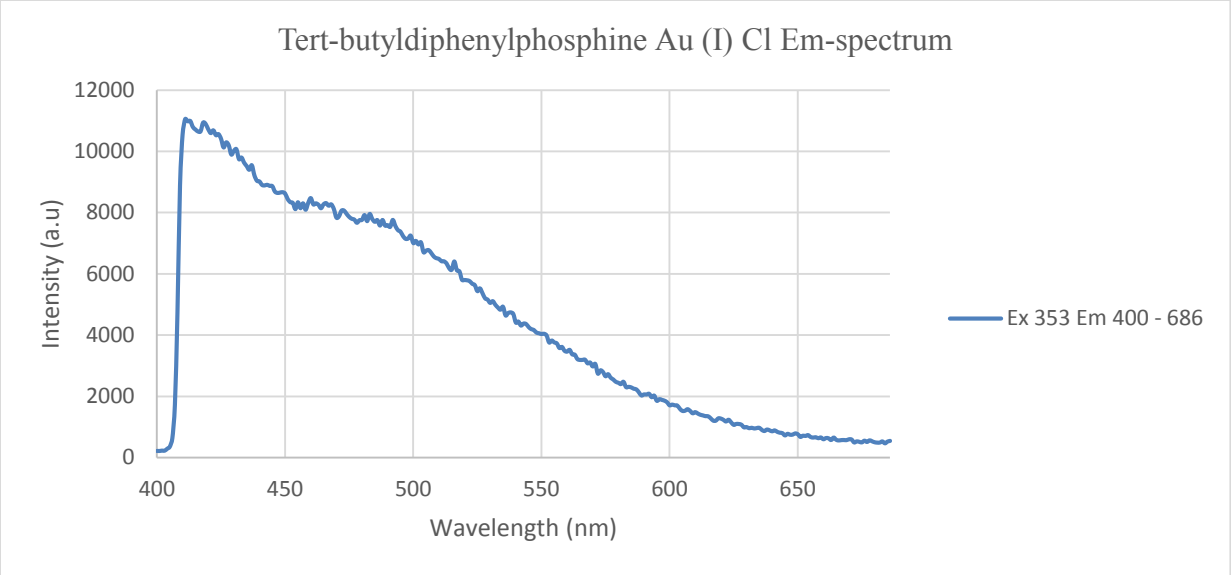

Figure 6.33. Emission spectrum of $AuP(C_7H_7O)_3Cl$ collected in liquid nitrogen upon excitation at 353 nm.

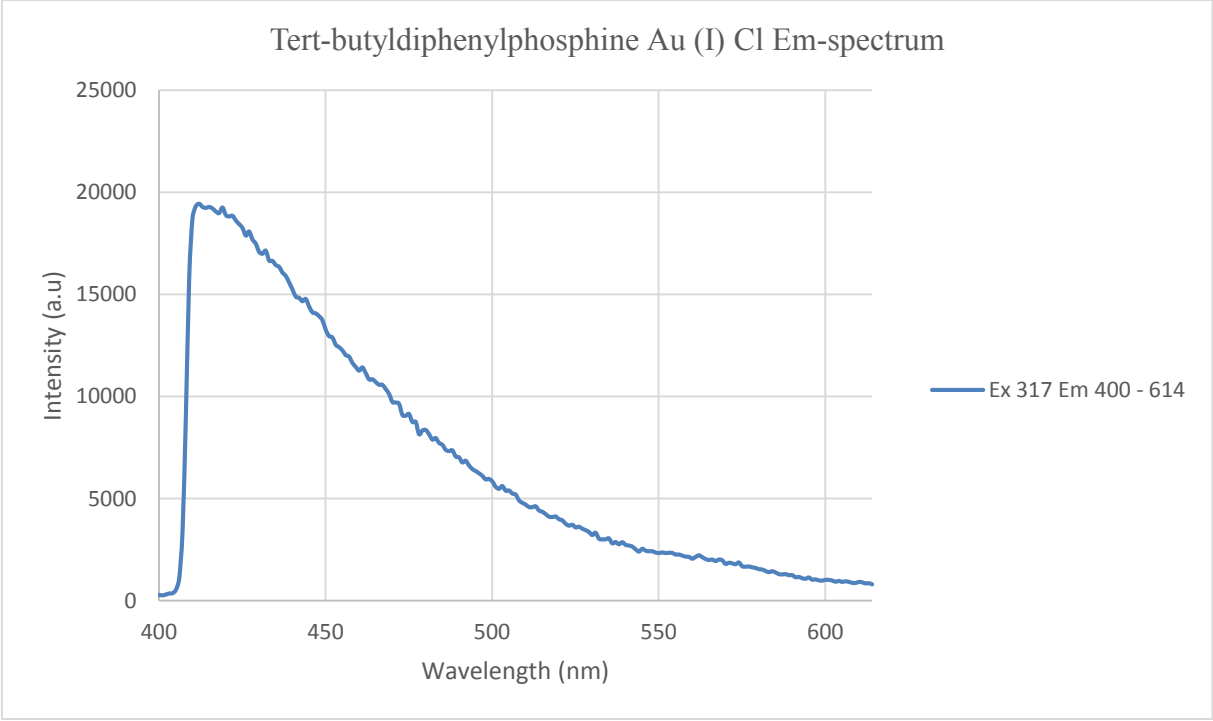

Figure 6.34. Emission spectrum of $AuP(C_6H_5)_2(C_4H_9)Cl$ collected in liquid nitrogen upon excitation at 317 nm.

Table 6.8

*Atomic contributions for the ground state molecular orbitals for compound **14***

ATOMIC CONTRIBUTIONS (%)				
Orbitals	Au	Ligand	P	C
76	18.41	81.59	5.64	75.95
75	21.69	78.31	1.02	77.29
74	6.82	93.18	7.03	86.15
HOMO-LUMO GAP				
73	27.48	72.52	14.18	58.34
72	53.69	46.31	11.38	34.93
71	16.50	83.50	12.14	71.36

Table 6.9

*Atomic Orbital contribution in the ground state for compound **14***

ATOMIC ORBITAL CONTRIBUTIONS (%)				
Orbitals	Au	Ligand	P	C
76	1.99s, 3.06px 10.20py, 3.16pz	19.86s, 9.40px, 17.13py, 35.20pz	1.00px, 4.64py	19.86s, 8.40px 12.49py, 35.20pz
75	2.18px, 7.17py 12.34pz,	8.55s, 6.36px 16.73py, 46.67pz	1.02pz	8.55s, 6.36px 16.73py, 45.65pz
74	1.57s, 1.59px 3.66pz,	9.70s, 6.13px 16.69py, 60.66pz	1.30py, 5.73pz	9.70s, 6.13px 15.39py, 54.93pz
HOMO-LUMO GAP				
73	5.77s, 1.70px 3.08py, 16.93d	7.86s, 19.78px 10.37py, 31.76pz	2.28s, 5.93px 3.22py, 2.75pz	5.58s, 13.85px 7.15py, 31.76pz
72	4.53py, 8.79pz 40.37d	14.84s, 6.81px 6.10py, 19.06pz	3.38px, 3.33py 4.67pz	14.84s, 2.93px 2.77py, 14.39pz 71
6.16s, 1.10px 9.24d	5.38s, 20.26px 57.86pz,	1.74s, 8.29px 2.11pz	3.64s, 11.97px 55.75pz	

6.3 Discussion

6.3.1 X-ray Crystallography. The X-ray crystal structures show a clear distinction between the complexes. The P(1)—Au(1)—Cl(1) bond angle has a linear geometry with a bond angle of 176.70° for the monocoordinated TDMPP gold complex, $AuP(C_6H_5)_2(C_4H_9)Cl$ (**14**). The respective bond angle is in conformity with the linearity expected for sp hybridization found in Au(I) complexes. The Au(1)—P(1) and Au(1)—Cl(1) bond distances in $AuP(C_8H_9)_3Cl$ shown on Table 6.2 are 2.2943 (12) and 2.2484 (12) respectively. The Au(1)—P(1) and Au(1)—Cl(1) bond lengths of **14** shows no significant differences in values with previous data on gold phosphine complexes. The X-ray data also show the lack of intermolecular Au‑Au aggregate formation. The weak aurophilic interactions are prevented due to steric factors as a result of the large cone angle of the TBDPP ligand.

6.3.2 Infrared Spectroscopy (Vibrational Studies). The IR-spectrum of **14** at Figure 6.4 has Twenty Eight (28) distinct bands. It showed the appearance characteristic bands at 3032 cm^{-1} for the aromatic C–H stretching of the phenyl ring, 2908 cm^{-1} and 2847 cm^{-1} for the asymmetric and symmetric aliphatic C–H (CH_3) stretching, 1597 cm-1 and 1450 cm-1 pair for C=C phenyl ring stretching, 1126 cm-1 for the P–Ar stretching, 849 cm-1 for the aromatic C–H bending, 360 cm-1 for the Au-P stretching, 330 cm^{-1} for the Au-Cl stretching. Group Theoretical Analysis (Nuclear site group analysis) for **14** also predicts Twenty Eight (28) IR-active modes. From table 6.1, **14** has a space group $P2_1/n$ with Z = 4. With Z = 4, it means **14** contains four formula units per unit cell. The modes for this unit cell can be found by consulting table 5A [26]. Since there are 64 C-atoms, 4 Au-atoms, 4 Cl-atoms and 4-P atoms, it is immediately seen by inspection of table 5A [26], that the that the Au, Cl, P, the unique aliphatic Carbons (C_x) all must occupy C_1 sites. The remaining aromatic Carbons (C_y) must lie on C_i sites, in two folds

repetitively. From table 5B [26], the vibrational modes of **14** are $3A_u + 3B_u$ for the aromatic C-atom, $3A_g + 3A_u + 3B_g + 3B_u$ for each nucleus on the C_1 sites. The total contribution from C, P, Au and Cl is $12A_g + 15A_u + 12B_g + 15B_u$. From table 5E [26], the acoustic modes are $A_u + B_u$ and the optical modes are $12A_g + 14A_u + 12B_g + 14B_u$. The distribution of the optical modes shows that Twenty Eight (28) ($14A_u + 14B_u$) modes are expected to be IR-active from the selection rule. Comparison of these predictions with the observed and calculated spectra shows that Twenty Eight distinct frequencies are observed for **14**.

6.3.3 Nuclear Magnetic Resonance. The ^{1}H NMR spectrum of **14** shown at figure 6.8 showed splitting at chemical shift at δ = 7.9 (m, 1H, Ar–H), δ = 7.6 (m, 2H, Ar–H), δ = 7.3 (m, 2H, Ar–H), δ = 1.5 (s, 5H, CH_3) and δ = 1.3 (s, 4H, CH_3). The peak intensities of the proton environments corresponds to the number of H-atoms in the respective environments. Comparison of the ^{1}H NMR spectral data between **14** and its free ligand (TBDPP) shows a slight shifting downfield. Peaks for TBDPP ligand found on figure 6.7 showed splitting at δ = 8.0 (m, 1H, Ar–H), δ = 7.5 (m, 2H, Ar–H), δ = 7.2 (m, 2H, Ar–H), δ = 1.4 (s, 5H, CH_3) and δ = 1.2 (s, 4H, CH_3). The slight difference in the position of the peaks between **14** and its ligand is an indication that the ligand has successfully coordinated to the gold center. The ^{1}H NMR spectral data for **15** at Figure 6.9 is slightly different from both the TBDPP ligand and **14**. It showed splitting at chemical shift at δ = 7.9 (m, 1H, Ar–H), δ = 7.6 (m, 2H, Ar–H), δ = 7.4 (m, 2H, Ar–H), δ = 1.6 (s, 5H, CH_3) and δ = 1.4 (s, 4H, CH_3). The ^{31}P{^{1}H} NMR spectral data for the TBDPP ligand, the **14** and the **15** shown at Figure 6.10, 6.11 and 6.12 showed a strong sharp peak at 40.0 ppm, 56.0ppm and 63.0ppm respectively. With the coordination of the mono and the bis, to the gold(I) chloride center the trend of downfield shifting is seen. This is as a result of the weakening of the gold-phosphine bond and consequently de-shielding the electrons and causing the peak to shift to

a larger chemical shift value (downfield). The overall trend appears consistent for gold phosphine complexes where the mono substituted systems usually show smaller chemical shift values than the di, tri substituted complexes. For example, the mono, tris, and tetrakis substituted (TFP)nAuCl compounds have ^{31}P NMR coordination chemical shift (ccs) of 48.4, 66.1, 63.1 respectively [32]. Also, the mono, di, tris, and tetrakis substituted (TPA)nAuCl compounds have ^{31}P NMR values of -51.4, -36.1, -56.1, and -58.0 ppm respectively [27-31]. The increase in the chemical shift value on going from the TBDPP, to the **14** and to the **15** is consistent with the general trend that chemical shift values increases as the coordination number increases. The trend of downfield shifting is also an indication that the ligand has successfully been coordinated to the gold (I) center.

6.3.4 UV-Vis Spectroscopy. The absorption spectral data for the TBDPP ligand, $AuP(C_6H_5)_2(C_4H_9)Cl$ and $Au(P(C_6H_5)_2(C_4H_9))_2Cl$ reveal similarities in their high-energy broad UV absorption profiles. The absorbance maximum for the free TBDPP ligand shown at Figure 6.15 is observed at 270 nm with a smaller less intense band at 290 nm with low energy tail extending all the way to 400 nm. Similarly, all of the TBDPP‑gold(I) complexes also show similar higher energy band maxima near 240 nm . Based on the spectral similarities between the ligand and the complexes as well as the molar absorptivity values of 4.32 x 10^4 $M^{-1}cm^{-1}$, 7.11 x 10^4 $M^{-1}cm^{-1}$ and 1.20 x 10^5 $M^{-1}cm^{-1}$for the TBDPP, $AuP(C_6H_5)_2(C_4H_9)Cl$ and $Au(P(C_6H_5)_2(C_4H_9))_2Cl$ respectively, the 240 nm band is assignable to a $\pi \rightarrow \pi^*$ intraligand transition, which is as result of the presence of double bond in the aromatic phenyl ring. The transition is slightly affected by the coordination with the Au metal. The weaker band at 290 nm which is present in the ligand is absent in the absorption spectra of the complexes **14** and **15** at Figure 6.16 and 6.17 respectively, indicating that the transition is affected by coordination with

the metal. This band is assignable to an n→π* transition and its absence in the absorption spectrum of **14** and **15** is indicative of participation of the lone pair electrons in the bonding scheme of the TBDPP ligand. The higher molar extinction coefficient value of the ligand and the complexes is an indication that the electronic transitions involved as a result of the absorption are statistically probable (said to be 'allowed') due to the fact that their molar extinction **ε** values are in excess of 10 000. It is also interesting to note that the TBDPP ligand, the **14** and the **15** complexes absorbs at similar energies but with the extinction coefficients of **15** about twice more intense than that of **14** and in turn about twice that of the TBDPP ligand . The enhancement of the extinction coefficient in **15** relative to **14** and relative to TBDPP is understandable in view of the presence of two more identical chromophores absorbing at the same region.

6.3.5 Luminescence. The gold(I) complexes and the TBDPP ligand luminescent when excited under UV radiation. The emission spectra of the complexes both at room temperature and in liquid nitrogen have very similar profiles indicating a similar origin for the electronic transitions. The emission spectra of the TBDPP ligand at room temperature shown at Figure 6.27 is characterize by a sharp band and maximizes around 450 nm. The gold complex (**14**) shown at Figure 6.28 to 6.30 also maximizes around 480 nm showing fine vibronic structures arising from the ν(C=C) stretch of the phenyl ring of the ligand, with vibrational progressions with spacings of 1330 cm^{-1}. The shift to the longer wavelength (bathochromic shift) from 450 nm of the TBDPP ligand to 480 nm of $AuP(C_6H_5)_2(C_4H_9)Cl$ is due to the fact that at the excited states, the π→π* transitions of the TBDPP is more polar than their ground states and as a result, a greater charge separation is observed in the excited state. The coordination of the TBDPP to the gold (I) center causes a dipole–dipole interaction which reduces the energy of the excited state more than the ground state, hence making **14** to emit at a longer wavelength. This emission at a longer

wavelength by **14** compare to the ligand is also an indication that the ligand has successfully been coordinated to the gold (I) center. Similar emission bands for **14** in liquid nitrogen were observed at Figure 6.31 – 6.34. The excitation spectrum of the TBDPP ligand and that of **14** at room temperature and in liquid nitrogen shown at Figure 6.20 for TBDPP ligand and Figure 6.21-24 for **14** consists of a well-defined broad band with an average spacing of 1200-1350 cm^{-1}. This spacing is assignable to an electronic transition coupled with vibronic component corresponding to v(C=C) symmetric stretching mode within the phenyl ring. With reference to the previous luminescence studies on tertiary phosphine gold(I) complexes the emission bands at 480 nm in complexes **14** tentatively assigned as derived from excited states of P−> Au ligand-to-metal charge transfer (LMCT) origin. This suggests that the ligand centered transition is responsible for the photoluminescence in **14**.

6.3.6 Computational Studies

6.3.6.1 Structural Comparison. The X-ray crystallographic structure of **14** were compared to theoretical calculations using the GAUSSIAN ‘09 software package. Shown in Table 6.4 are selected bond angles and bond distances of **14**. Although slightly shorter, longer and shorter, the calculated bond distances for Au(1)—Cl(1), Au(1)—P(1) and P(1)—C(1) respectively using the LANL2DZ basis set are in good agreement with the experimental X-ray crystal structures data as given in Table 6.2. The experimental bond distances of 2.248(12) [Å], 2.294(8) [Å] and 1.826(3) [Å] for **14** changes by 0.014 [Å], 0.072[Å] and 0.034 [Å] from the calculated bond distances of (2.332[Å]), (2.390[Å]) and (1.806[Å]) for Au(1)—Cl(1), Au(1)—P(1) and P(1)—C(1) respectively. Similarly the theoretical bond angles of 180.0 [°], 112.8 [°] and 108.5[°] for P(1)—Au(1)—Cl(1), C(1)—P(1)—Au(1) and C(17)—P(1)—C(9) respectively

for **14**, are in agreement with the experimental bond angles of 176.70[°] for P(1)—Au(1)—Cl(1), 109.09[°] for C(1)—P(1)—Au(1) and 108.24[°] for C(7)—P(1)—Au(1).

6.3.6.2 Spectroscopic Comparison. The theoretical calculated IR spectrum of **14** using Gaussian 09 shown at Figure 6.5 also predicts Twenty two (22) distinct bands with a slight shift in the position of some of the individual peaks, but on a whole both the calculated and the experimental spectrum of both the ligand and the complex shows similar IR-spectrum. The theoretical ^{1}H NMR of for both the ligand and the gold complex shown on Figure 6.13 and Figure 6.14 also showed similar splitting patterns and chemical shift values as that of the experimental ones.

6.3.6.3 Electronic Comparison

6.3.6.3.1 Luminescence. The result of the population analysis for **14** is shown in Table 6.8 and 6.9 for the percentage atomic and atomic orbital contributions respectively for the metal and the TBDPP ligand, as well as individual atomic participation for the selected highest three occupied molecular orbitals and lowest three unoccupied molecular orbitals. The third highest occupied molecular orbital (3rd-HOMO), HOMO-71 has the largest contribution from the ligand at 83.50% and the metal at 16.5% followed by the highest occupied molecular orbital, HOMO-72 at 72.52% and 27.48% contributions, respectively. The contribution of the gold atom in the HOMO-71 orbital derives from 5s, 5p_x and 5d_{xz} atomic orbitals at 6.16%, 1.10% and 9.24% contributions, respectively. The atomic contribution of the TBDPP ligand is comprised of phosphorus and carbon with percentage contributions of 5.38s, 78.12p orbitals. However, the gold contribution of the HOMO comes also from 5.77% of the 5s, 1.70% of 5p_x, 3.80% of 5p_y and 16.93% of the 5d_{xz} atomic orbitals with the remaining contribution from the s and p orbitals of the phosphorus and Carbon atoms of the TBDPP ligand. The table also shows

the first three lowest unoccupied molecular orbital (LUMOs) contributions, which are mainly ligand centered contributions. The orbital description as ligand based and partial metal based transitions is thus substantiated to support the observations surrounding the luminescent behavior of **14** and hence the assignment of π→π* transition is in a proper order.

6.3.6.3.2 UV-Vis. The HOMO‑LUMO gap calculated value by the TD-DFT method was 42,173 cm^{-1} corresponding to 237.12 nm. The theoretical calculated spectrum for **14** obtained using TDDFT with the LANL2DZ basis set to identify the orbital(s) contributing to the observed absorption is shown at Figure 6.18. The TD-DFT generated ground-state to excited-transitions is shown on Table 6.6 which summarizes the orbital that took part most in the transitions X, Y, and Z. From Table 6.6, transition Z supports an assignment of the THOMO-71→LUMO-74, a π→π* type transition. This confirms why the n→π* is not present in the experimental UV-Vis spectrum of **14**. The transition X and Y has transitions from the HOMO-73→LUMO-74 and the SHOMO70→LUMO-74 respectively. Table 6.7 summarizes the various transitions pictorially of the theoretically generated ground-state to excited-state transitions for X, Y and Z. These calculated spectrum values are in good agreement with the experimental UV-Vis spectrum of **14**, since both the experimental and calculated spectrum shows a strong absorption maximum around 240 nm.

CHAPTER SEVEN

Synthesis and Characterization of mono-, bis-, tris-, and tetrakis-{tris(4-fluorophenyl)phosphine} gold(I) complexes

7.1 Syntheses

7.1.1 Tris(4-fluorophenyl)phosphine gold (I) chloride (18). Tris(4-flourophenyl)phosphine (0.0200 g, 0.063 mmol) was added to a solution of $(C_4H_8S)AuCl$ (0.0146 g, 0.063 mmol) in dichloromethane (20 ml) at −80 ˚C and the reaction stirred for 2 hours. The solvent was removed by purging nitrogen gas into the solution, until all the solvent dried up. The residue was then recrystallized from CH_2Cl_2/n-hexane mixture for four days. Partial evaporation of the solvent provided quality crystals.

7.1.2 Bis{tris(4-fluorophenyl)phosphine} gold (I) chloride (19). Tris(4-flourophenyl)phosphine (0.0400 g, 0.126 mmol) was added to a solution of $(C_4H_8S)AuCl$ (0.0146 g, 0.063 mmol) in dichloromethane (20 ml) at −80 ˚C and the reaction stirred for 2 hours. The solvent was removed by purging nitrogen gas into the solution, until all the solvent dried up. The residue was then recrystallized from CH_2Cl_2/n-hexane mixture for five days. Partial evaporation of the solvent provided quality crystals.

7.1.3 Tris(4-fluorophenyl)phosphine gold (I) chloride (20). Tris(4-flourophenyl)phosphine (0.0600 g, 0.189 mmol) was added to a solution of $(C_4H_8S)AuCl$ (0.0146 g, 0.063 mmol) in dichloromethane (20 ml) at −80 ◦C and the reaction stirred for 3 hours. The solvent was removed by purging nitrogen gas into the solution, until all the solvent dried up. The residue was then recrystallized from CH_2Cl_2/n-hexane mixture for seven days. Partial evaporation of the solvent provided quality crystals.

7.1.4 Bis{tris(4-fluorophenyl)phosphine} gold (I) chloride (21). Tris(4-flourophenyl)phosphine (0.0800 g, 0.252 mmol) was added to a solution of $(C_4H_8S)AuCl$ (0.0146 g, 0.063 mmol) in dichloromethane (20 ml) at −80 ˚C and the reaction stirred for 3 hours. The solvent was removed by purging nitrogen gas into the solution, until all the solvent dried up. The residue was then recrystallized from CH_2Cl_2/n-hexane mixture for seven days. Partial evaporation of the solvent provided quality crystals.

7.2 Results

7.2.1 X-ray Crystallography. Diffraction-quality crystal structure for $AuP(C_6H_4F)_3Cl$, of the monocoordinated TFFPP gold (I) complex and the crystal structure determination data and selected bond lengths and angles has already been published by Soo Yei Ho and Edward R. T. Tiekink [33]. The di-, tri and the tetra-coordinated have been synthesized under this research.

7.2.2 Infrared Spectroscopy. All infrared spectra data were obtained as potassium bromide (KBr) disc, prepared by compressing the ground mixture of sample and KBr powder, on a Shimadzu IR-PRESTIGE-21 Fourier transform infrared spectrophotometer (4000−300 cm^{-1}). Figure 7.1, 7.2, 7.3, 7.4 and 7.5 show both experimental and theoretically calculated IR spectrum of the mono-, di-, tri- and tetra-coordinated TFFPP gold (I) complexes.

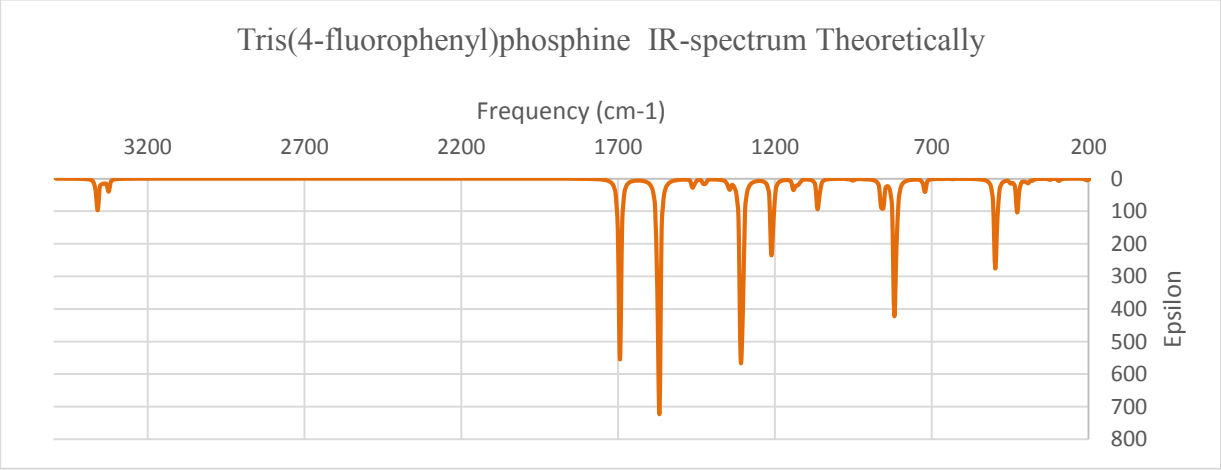

Figure 7.1. IR spectrum for $P(C_6H_4F)_3$ calculated theoretically using Gaussian 09 software.

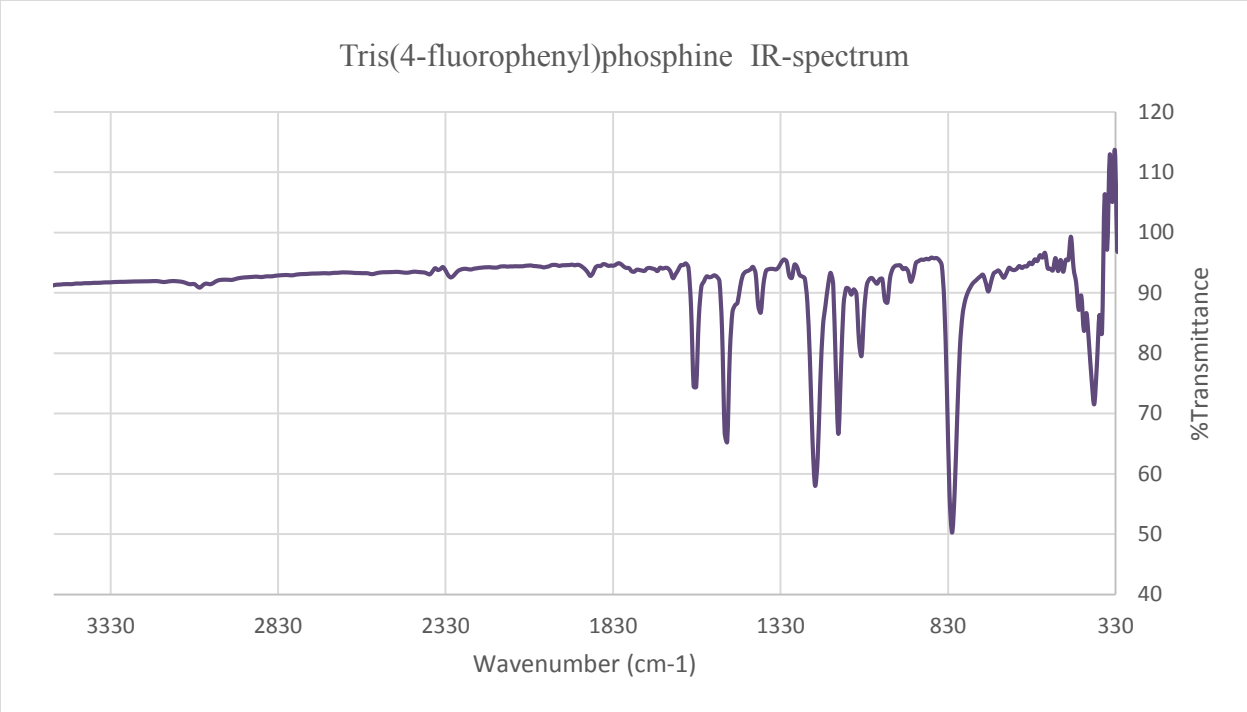

Figure 7.2. IR spectrum for $P(C_6H_4F)_3$.

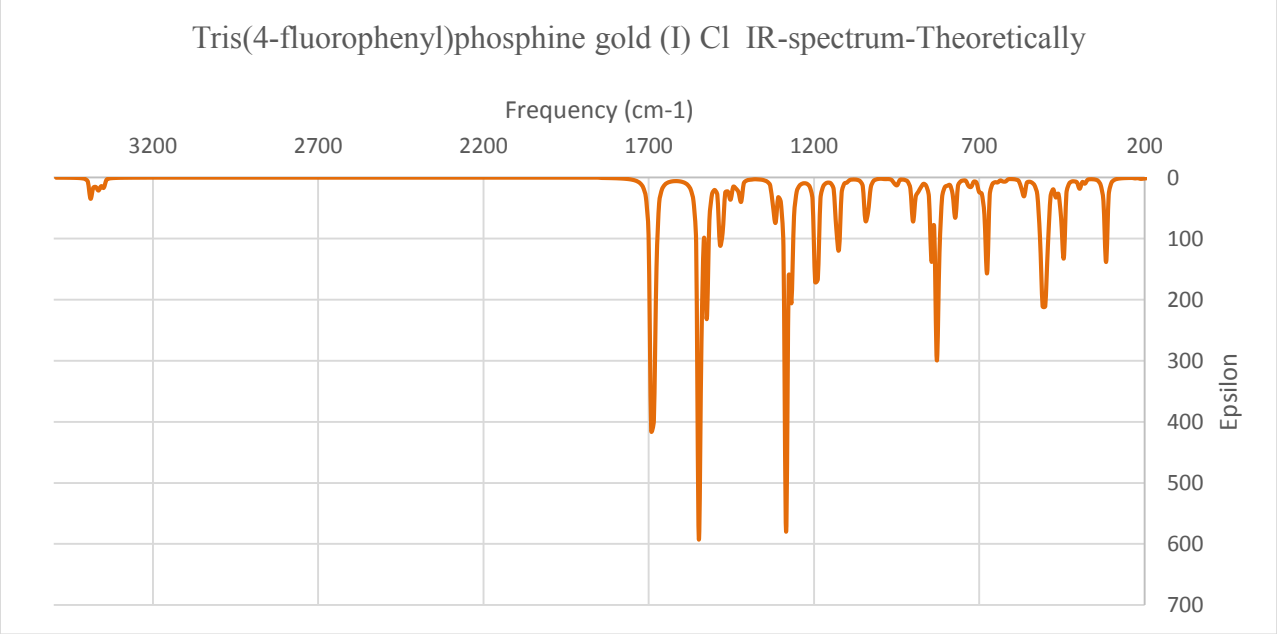

Figure 7.3. IR spectrum for $AuP(C_6H_4F)_3Cl$ calculated theoretically using Gaussian 09 software.

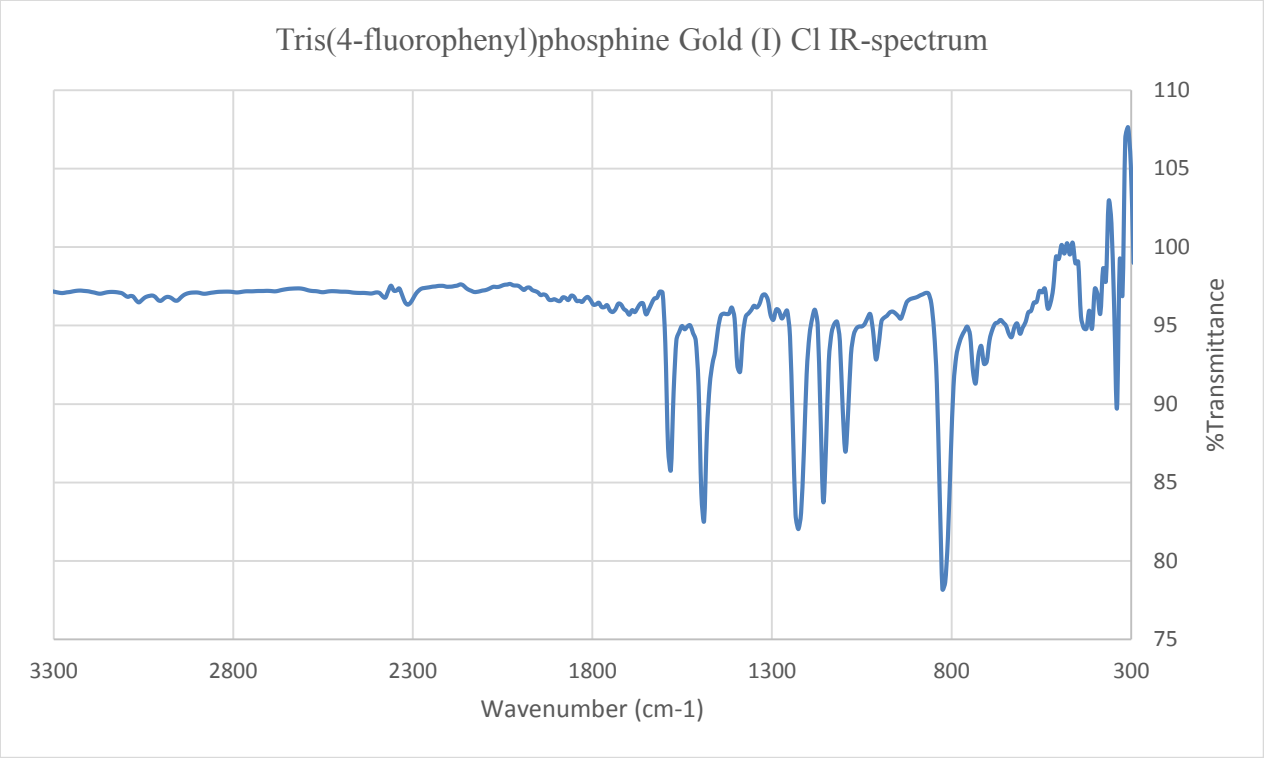

Figure 7.4. IR spectrum for $AuP(C_6H_4F)_3Cl$.

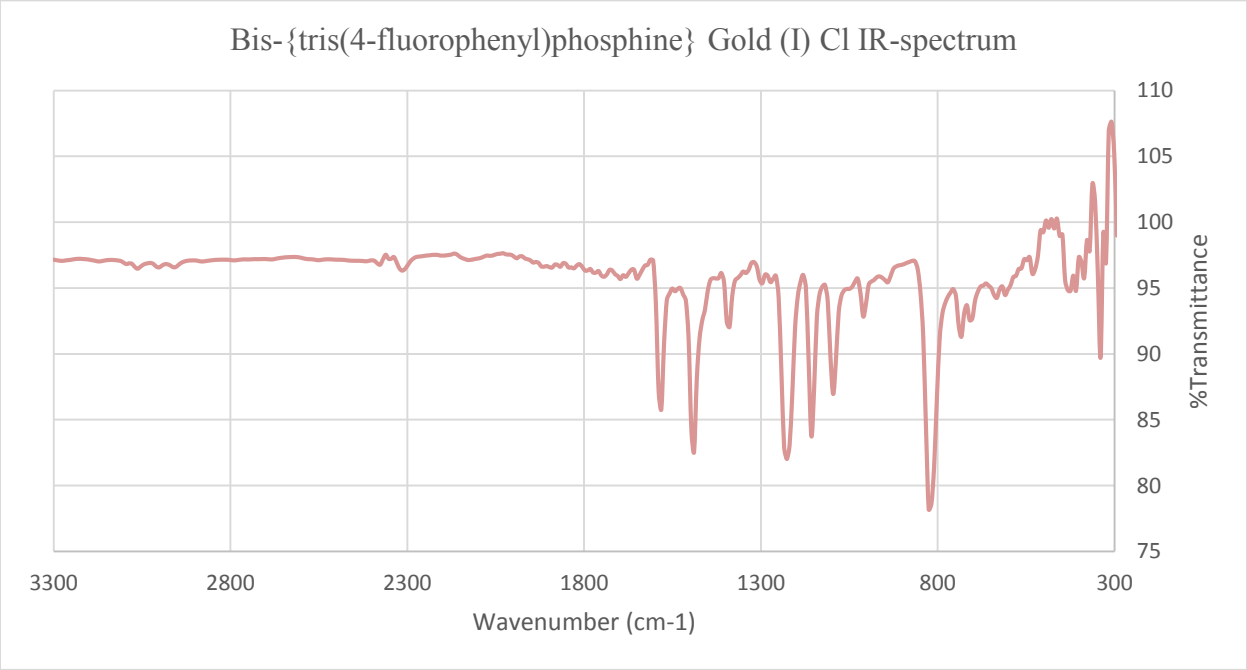

Figure 7.5. IR spectrum for $Au(P(C_6H_4F)_3)_2Cl$.

7.2.3 Nuclear Magnetic Resonance. The ^{1}H NMR spectral data for the monocoordinated TFFPP gold complex was found in Figure 7.7 showing peaks at 7.1 (6H) 7.4 (6H) ppm and that of the dicoordinated TFFPP gold (I) complex was found in Figure 7.8 showing peaks at 7.2 (6H), 7.6 (6H). The ^{1}H NMR spectral data for the free ligand TFFPP was found in Figure 7.6 showing peaks at 7.0 (6H), 7.3 (6H) ppm. The $^{31}P\{^{1}H\}$ NMR spectral data for the ligand, **18** and **19** was found in Figure 7.9, 7.10 and 7.11 showing peaks at 46.0ppm, 59.0 ppm and 74 ppm respectively. Theoretically calculated proton NMR using Gaussian 09 is also shown at Figure 7.12 and 7.13.

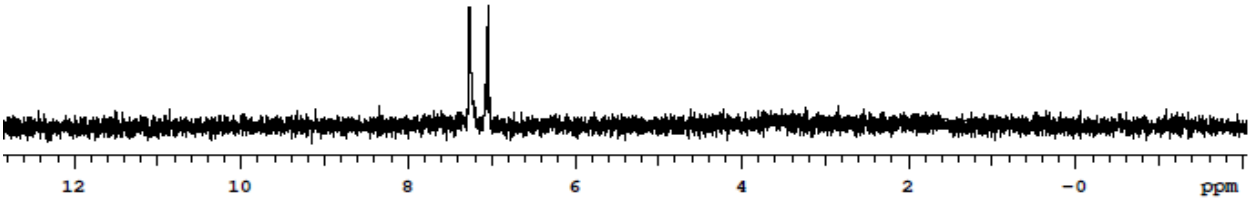

Figure 7.6. ^{1}H NMR spectrum of $P(C_6H_4F)_3$.

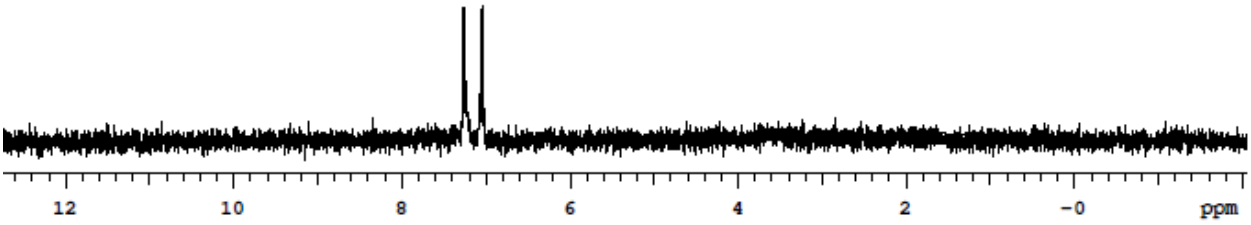

Figure 7.7. ^{1}H NMR spectrum of $AuP(C_6H_4F)_3Cl$.

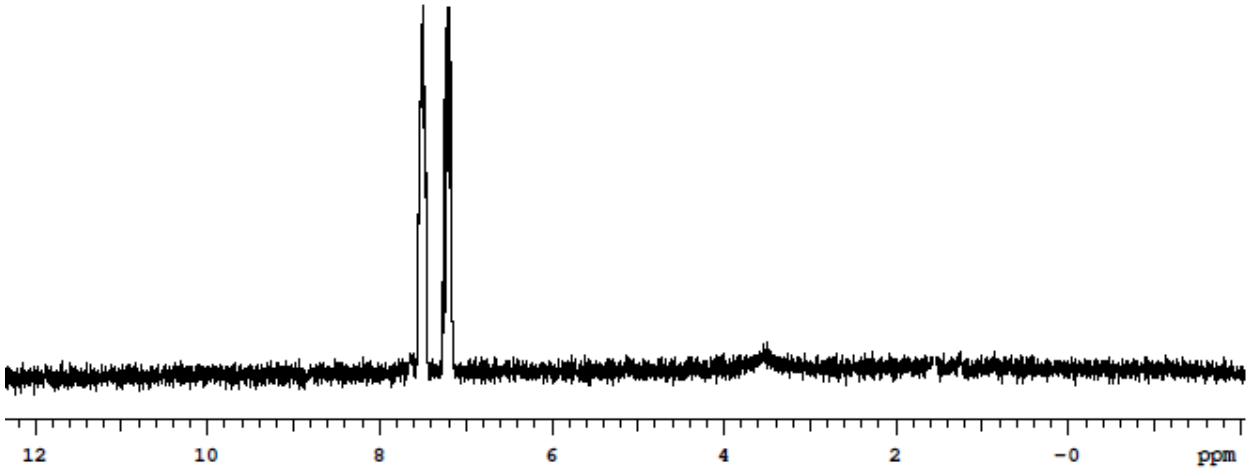

Figure 7.8. ^{1}H NMR spectrum of $Au(P(C_6H_4F)_3)_2Cl$.

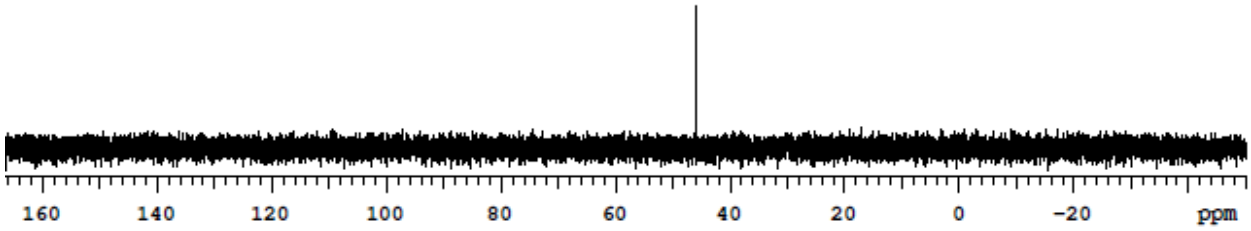

Figure 7.9. $^{31}P\{^{1}H\}$ NMR spectrum of $P(C_6H_4F)_3$.

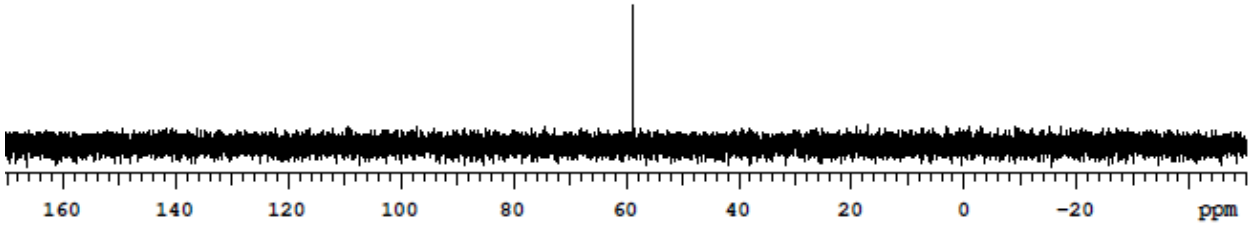

Figure 7.10. $^{31}P\{^{1}H\}$ NMR spectrum of $AuP(C_6H_4F)_3Cl$.

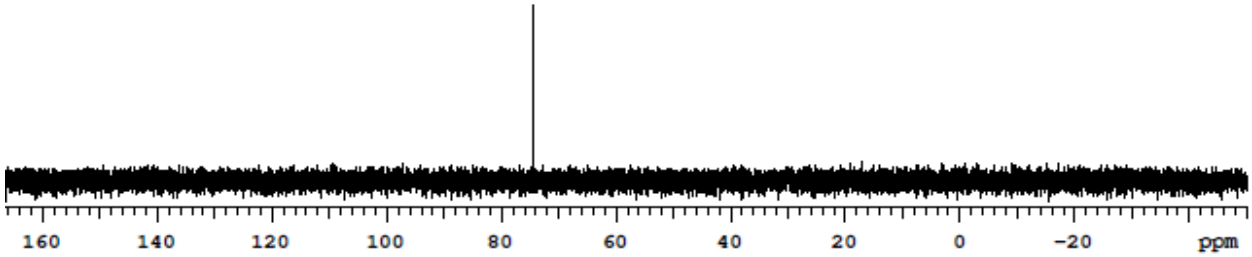

Figure 7.11. $^{31}P\{^{1}H\}$ NMR spectrum of $Au(P(C_6H_4F)_3)_2Cl$.

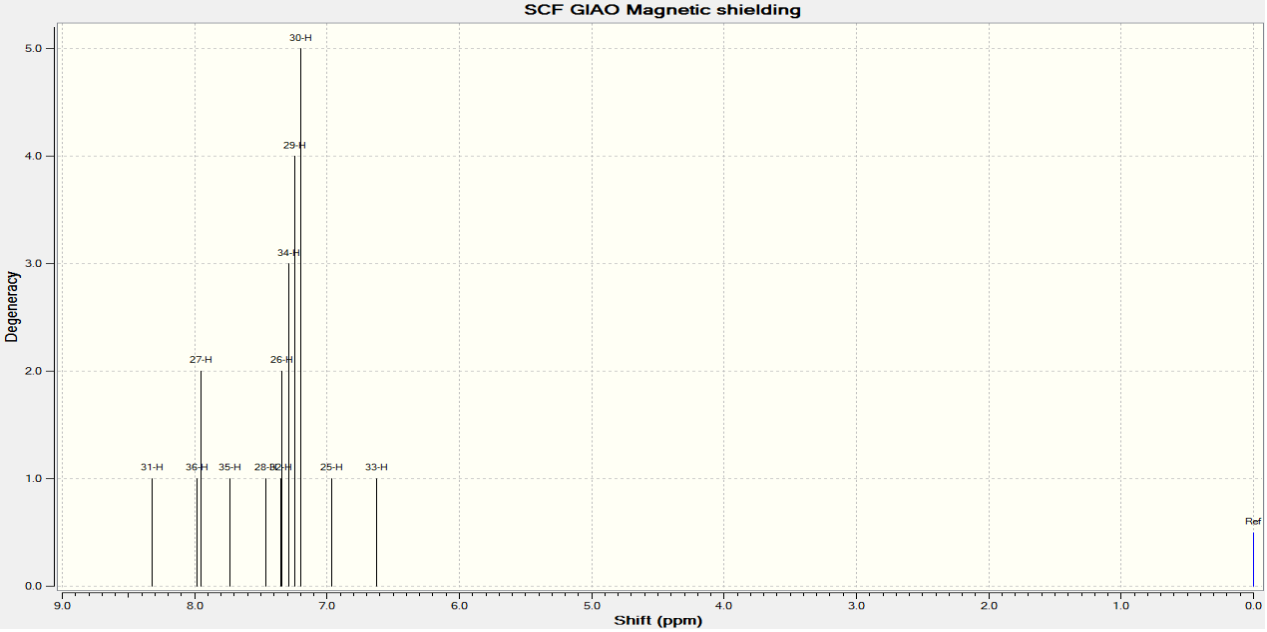

Figure 7.12. ^{1}H NMR spectrum of $AuP(C_6H_4F)_3Cl$ calculated theoretically using Gaussian 09. software.

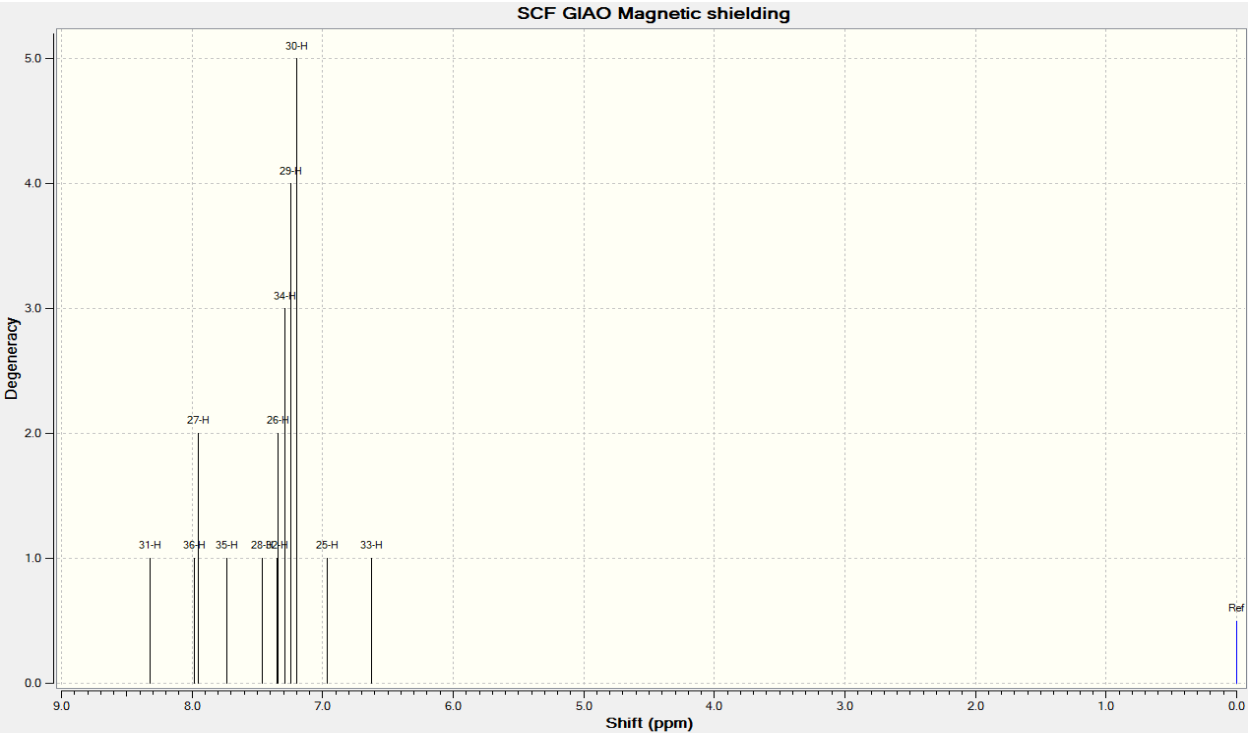

Figure 7.13. ^{1}H NMR spectrum of $P(C_6H_4F)_3$ calculated theoretically using Gaussian 09 software.

7.2.4 UV-Vis Spectroscopy. All of the samples used for the ultraviolet visible (absorption) experiment, were dissolved in spectroscopic grade acetonitrile (CH_3CN). The TFFPP ligand has a broad absorption spectrum shown at Figure 7.14 that maximizes around 260 nm with a calculated molar absorptivity of 5.21 x 10^4 $M^{-1}cm^{-1}$. The absorption spectrum of **18** shown at Figure 7.15 has a broad absorption profile maximizes at about 260 nm with a calculated molar absorptivity of 8.52 x 10^4 $M^{-1}cm^{-1}$. In Figure 7.16 is shown the absorption profile for **19** which has a band maximum of about 260 nm with a calculated molar absorptivity of 1.17 x 10^5 $M^{-1}cm^{-1}$. The theoretical spectrum using DFT calculations, shows a spectrum at Figure 7.17 and 7.18 with a broad absorption spectrum at 249 nm and 258 for **18** and the TFFPP ligand respectively.

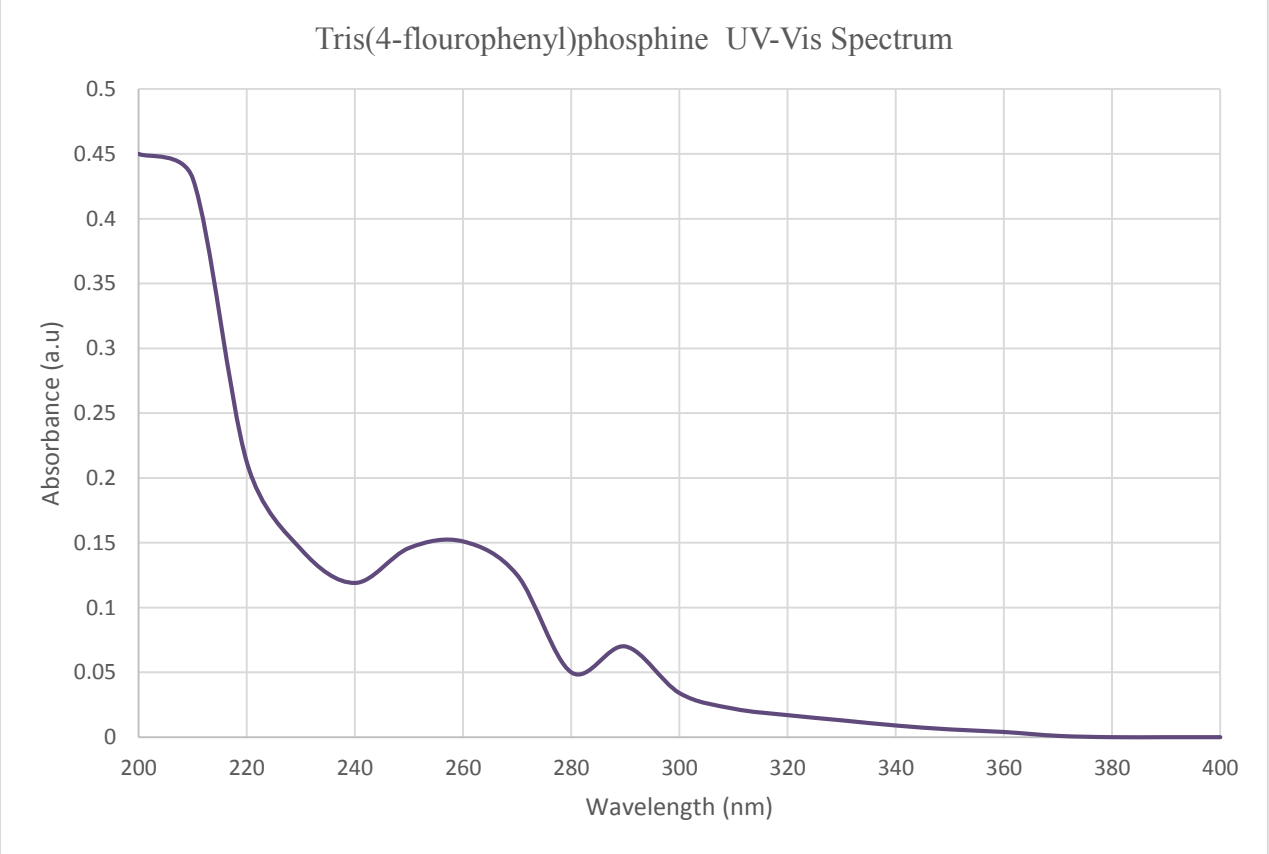

Figure 7.14. UV-Vis spectrum of $P(C_6H_4F)_3$.

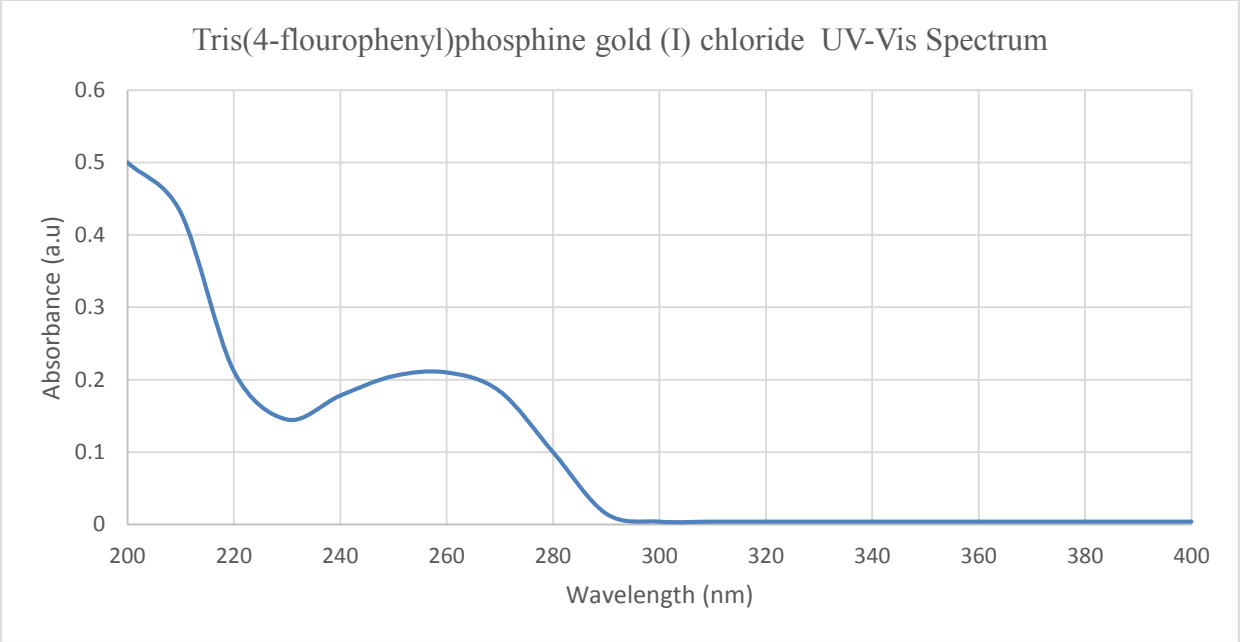

Figure 7.15. UV-Vis spectrum of $AuP(C_6H_4F)_3Cl$.

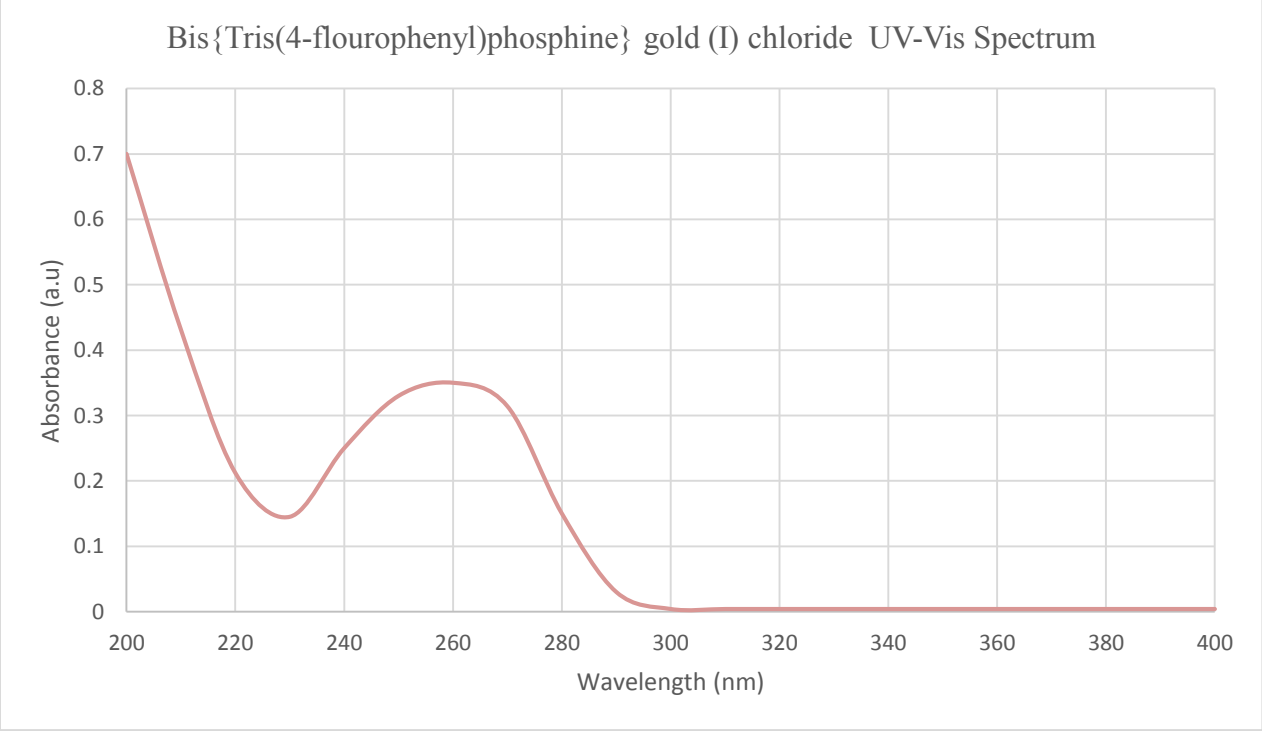

Figure 7.16. UV-Vis spectrum of $Au(P(C_6H_4F)_3)_2Cl$.

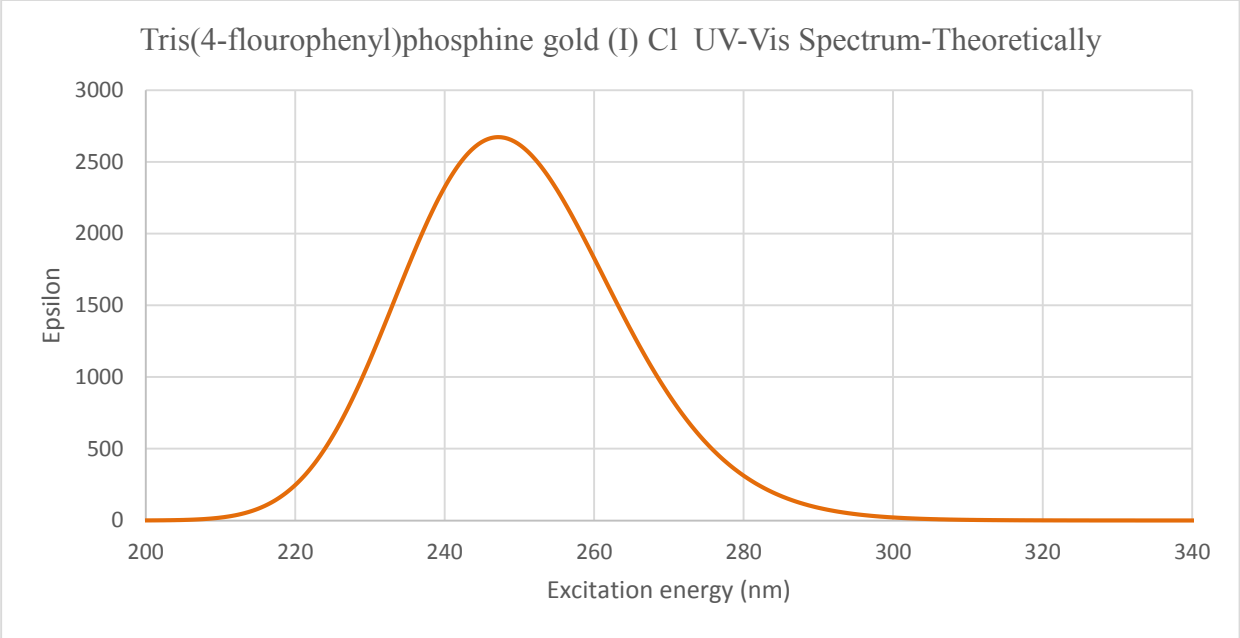

Figure 7.17. UV-Vis spectrum of $AuP(C_6H_4F)_3Cl$ calculated theoretically using Gaussian 09 software.

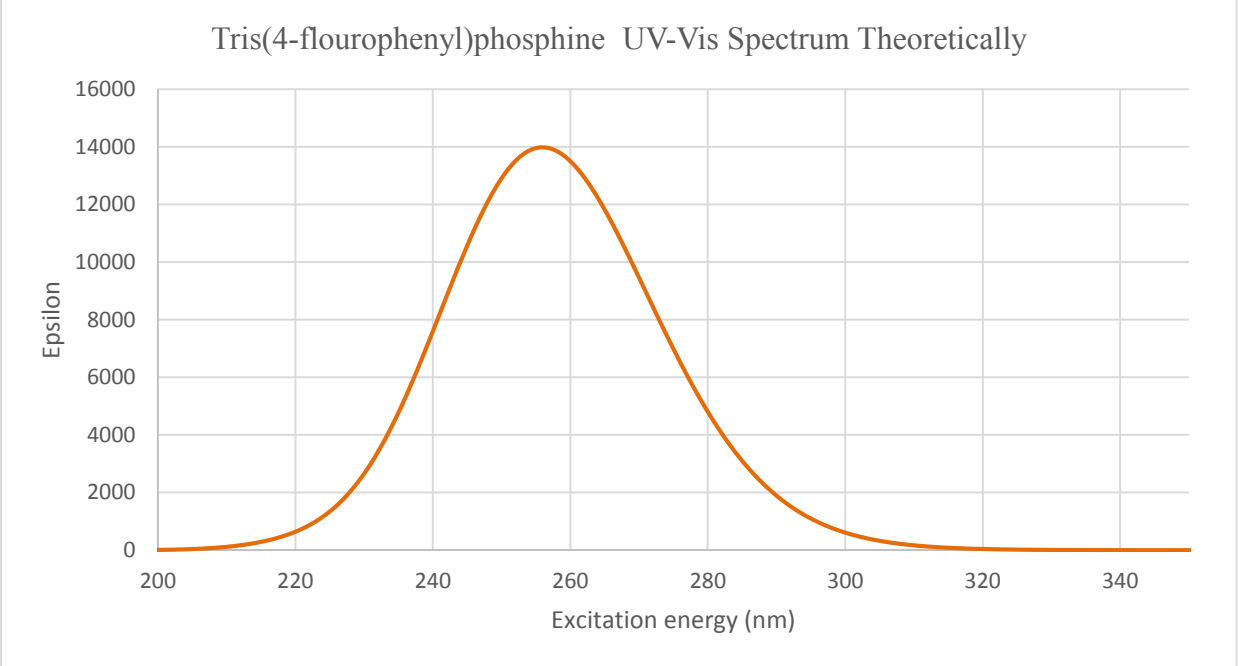

Figure 7.18. UV-Vis spectrum of $P(C_6H_4F)_3$ calculated theoretically using Gaussian 09.

Table 7.1

TD-DFT generated ground-state to excited-state MO transitions

TRANSITIONS	CORRESPONDING ORBITALS	% CONTRIBUTION
X	89 → 90	76.48
	89 → 91	23.52
Y	87 → 90	13.76
	87 → 91	8.58
	88 → 90	29.02
	88 → 91	16.11
	88 → 93	7.79
	88 → 96	9.51
	89 → 91	15.23
Z	87 → 90	35.37
	87 → 91	22.35
	87 → 93	10.14
	87 → 96	12.48
	88 → 90	19.66

Table 7.2

*Theoretical results showing the contributions of X, Y, and Z transitions of **18***

Excitation	λcalc. (nm)	%Contribution to the transition		Transition Energy (cm^{-1})	λexp. (nm)
X	247.74				260
Major contribution:					
	89 → 90	76.48		40,366	
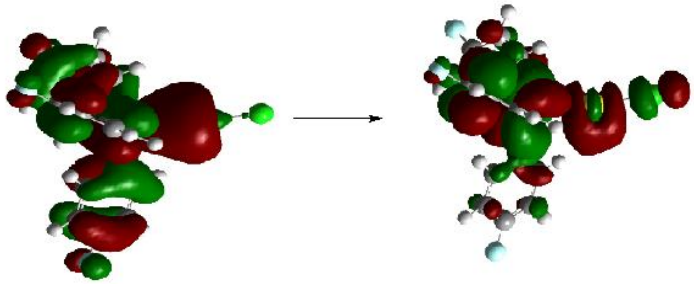					
Y	244.73				
Major contribution:					
	88 → 90	29.02		40,862	
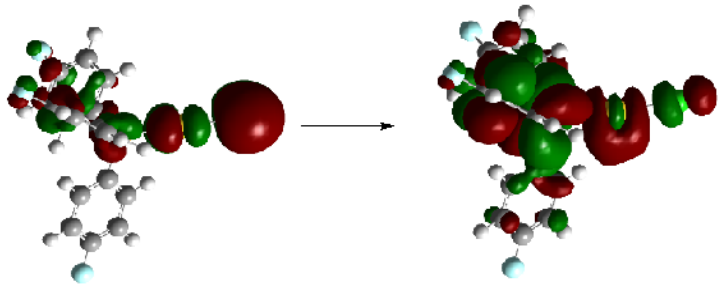					
Z	244.47				
Major contribution:					
	87 → 90	35.37		40,906	
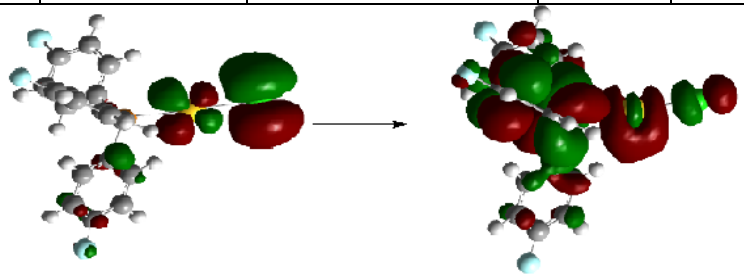					

7.2.5 Luminescence. The TFFPP ligand shows excitation spectrum at room temperature and in liquid nitrogen shown in Figure 7.19 and 7.20 respectively. The excitation spectrum for the $AuP(C_6H_4F)_3Cl$ at room temperature is shown in Figure 7.21 and 7.22 covering the spectral region from 280 to 391 nm, 280 to 430 nm, and monitored at an emission band of 411, and 450 nm respectively. The spectrum exhibited vibronic bands at 358, 317 nm monitored at 411 nm; 389, 287 nm monitored at an emission of 450. The excitation spectrum collected in liquid nitrogen is shown in Figure 7.23 and 7.24 covering the spectral region from 280 to 396 nm, 280 to 430 and monitored at an emission band of 416 and 450 nm respectively. The spectrum shows vibronic components at 356 and 361 nm monitored at 416 nm, 354 and 361 nm monitored at an emission of 450. The excitation spectrum for the $Au(P(C_6H_4F)_3)_2Cl$ at room temperature and in liquid nitrogen is shown in Figure 7.25, 7.26, and 7.27, 7.28, 7.29 respectively. The emission spectrum for the ligand collected at room temperature and in liquid nitrogen is shown in Figure 7.30 and 7.31 respectively. The emission spectrum of **18** and **19** can be found in Figure 7.32 to 7.35 and 7.37 to 7.40, for both room temperature and in liquid nitrogen respectively.

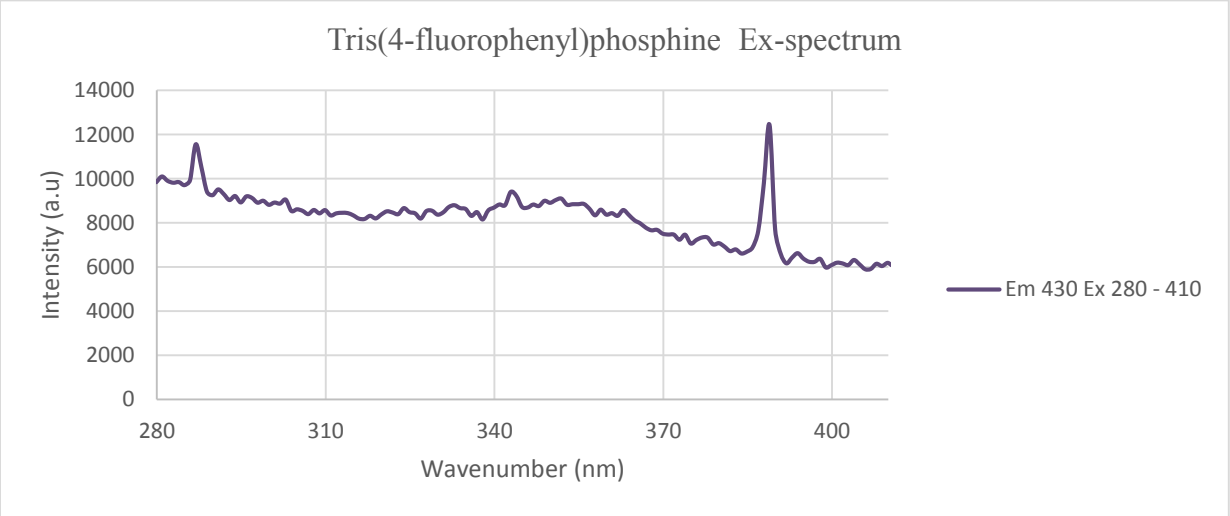

Figure 7.19. Excitation spectrum of $P(C_6H_4F)_3$ collected at room temperature by monitoring the emission at 430 nm.

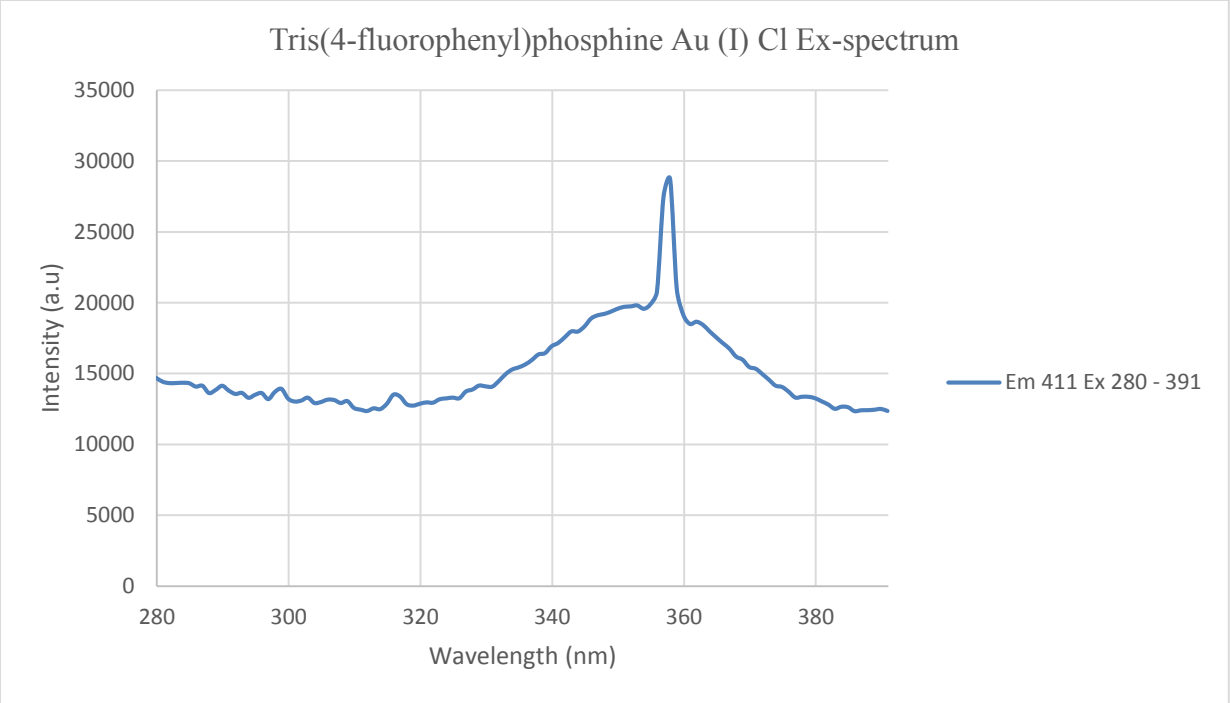

Figure 7.20. Excitation spectrum of $AuP(C_6H_4F)_3Cl$ collected at room temperature by monitoring the emission at 411 nm.

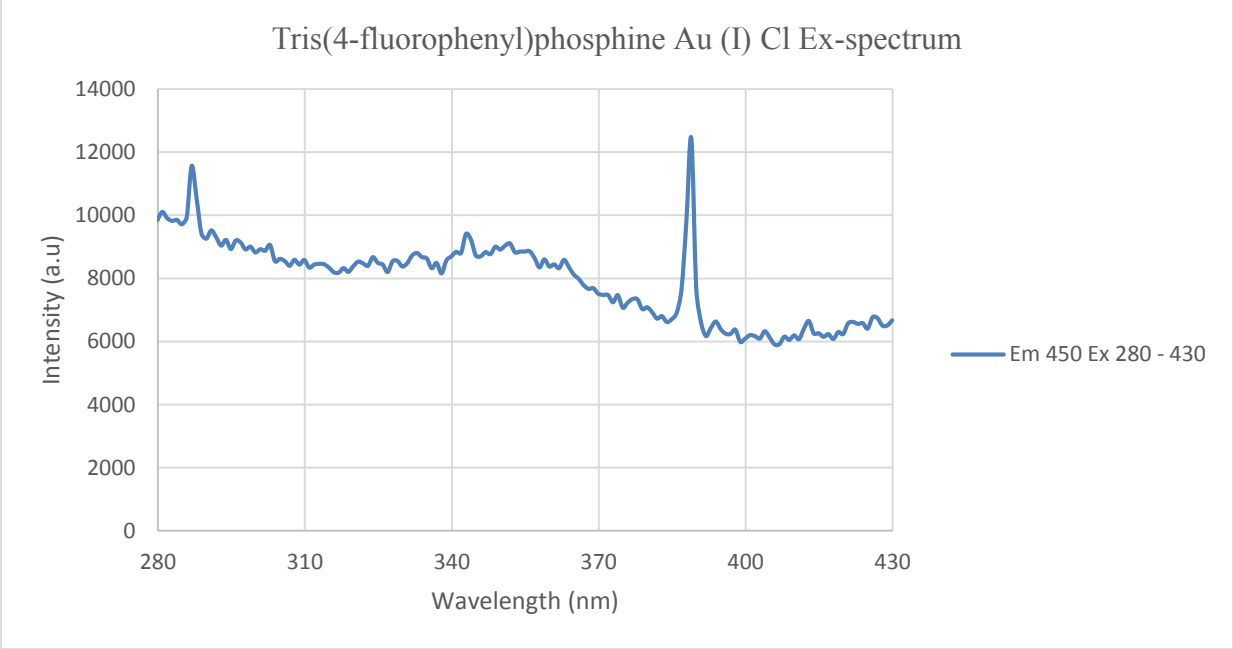

Figure 7.21. Excitation spectrum of $AuP(C_6H_4F)_3Cl$ collected at room temperature by monitoring the emission at 450 nm.

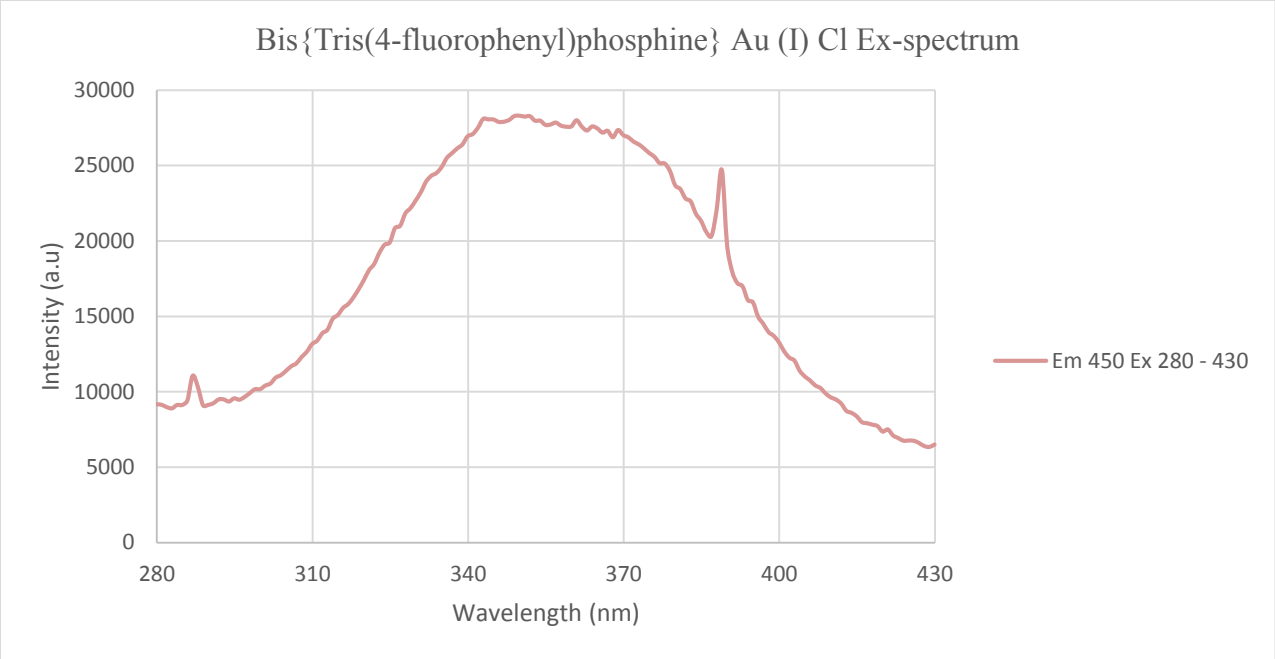

Figure 7.22. Excitation spectrum of $Au(P(C_6H_4F)_3)_2Cl$ collected at room temperature by monitoring the emission at 450 nm.

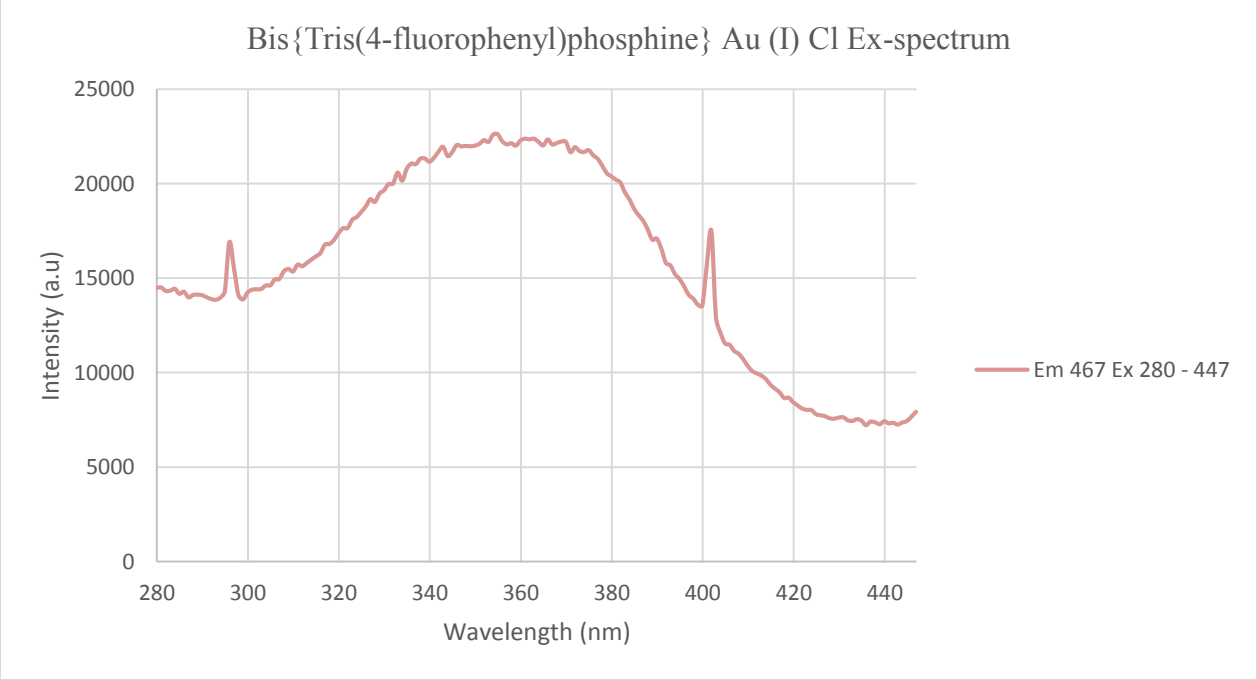

Figure 7.23. Excitation spectrum of $Au(P(C_6H_4F)_3)_2Cl$ collected at room temperature by monitoring the emission at 467 nm.

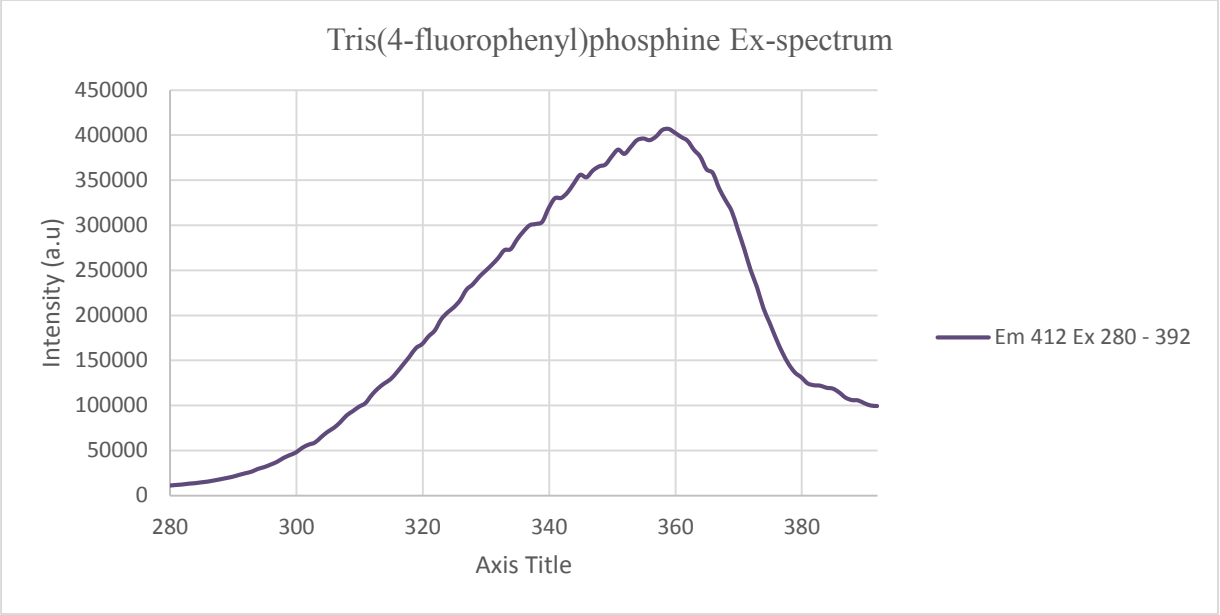

Figure 7.24. Excitation spectrum of $P(C_6H_4F)_3$ collected in liquid nitrogen by monitoring the emission at 412 nm.

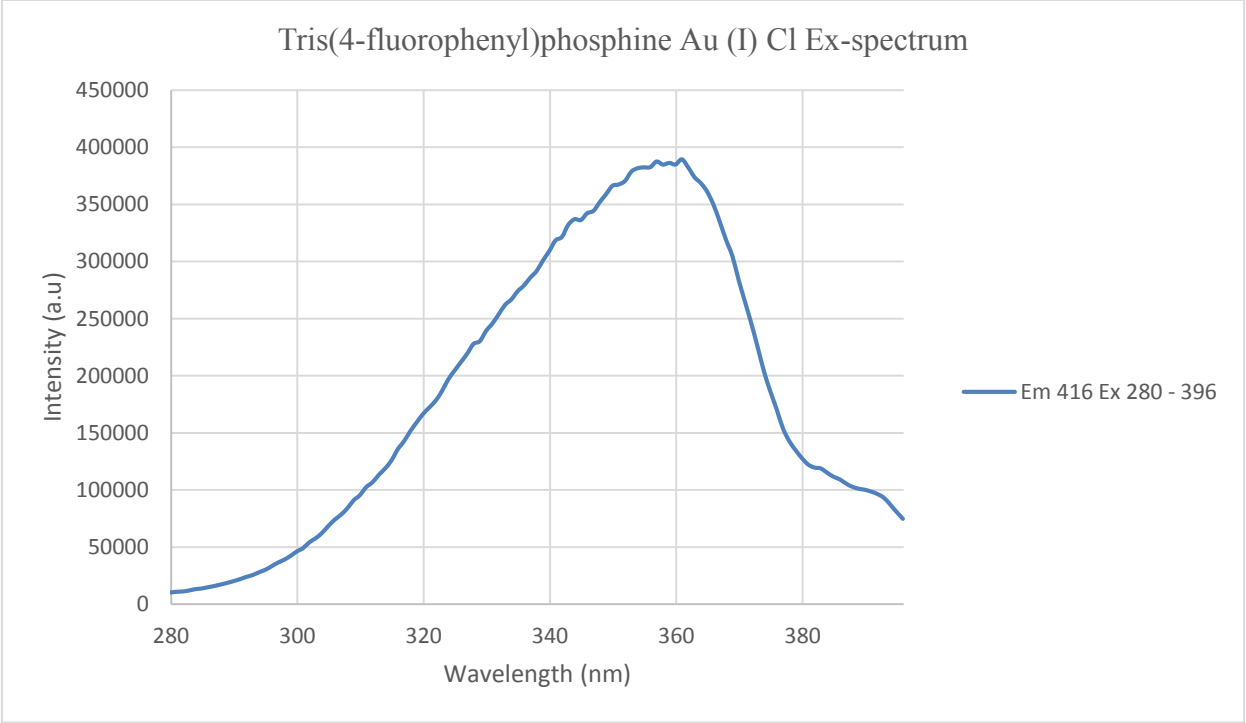

Figure 7.25. Excitation spectrum of $AuP(C_6H_4F)_3Cl$ collected in liquid nitrogen by monitoring the emission at 416 nm.

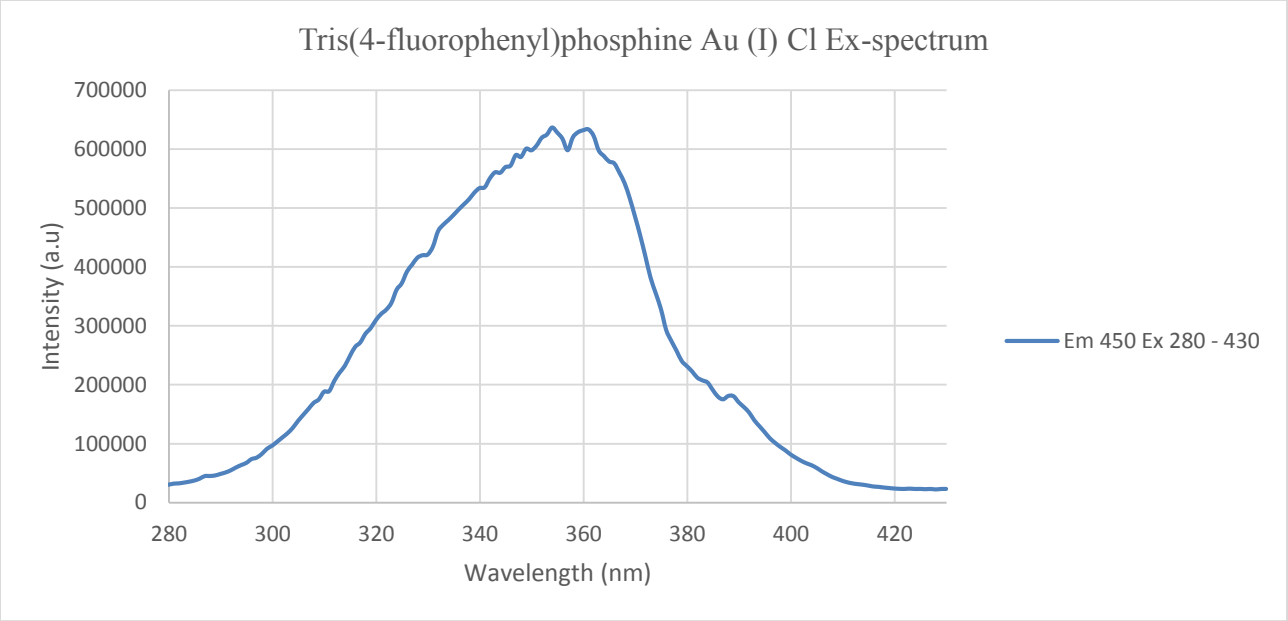

Figure 7.26. Excitation spectrum of $AuP(C_6H_4F)_3Cl$ collected in liquid nitrogen by monitoring the emission at 450 nm.

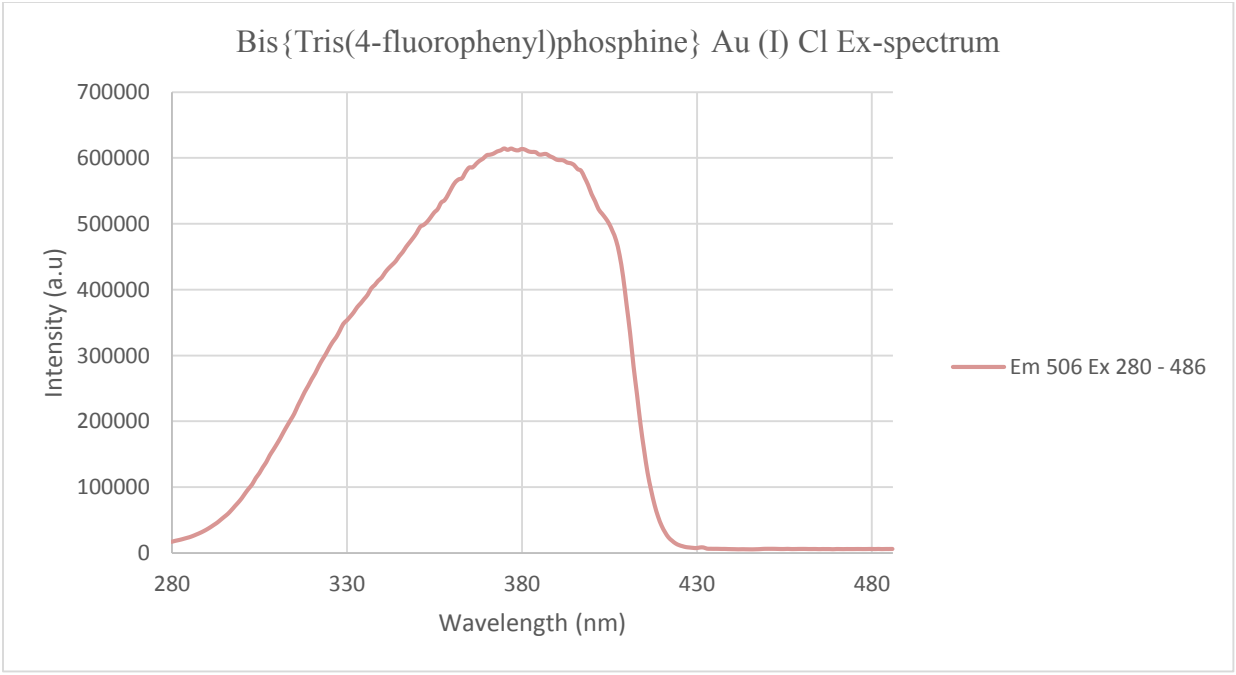

Figure 7.27. Excitation spectrum of $Au(P(C_6H_4F)_3)_2Cl$ collected in liquid nitrogen by monitoring the emission at 506 nm.

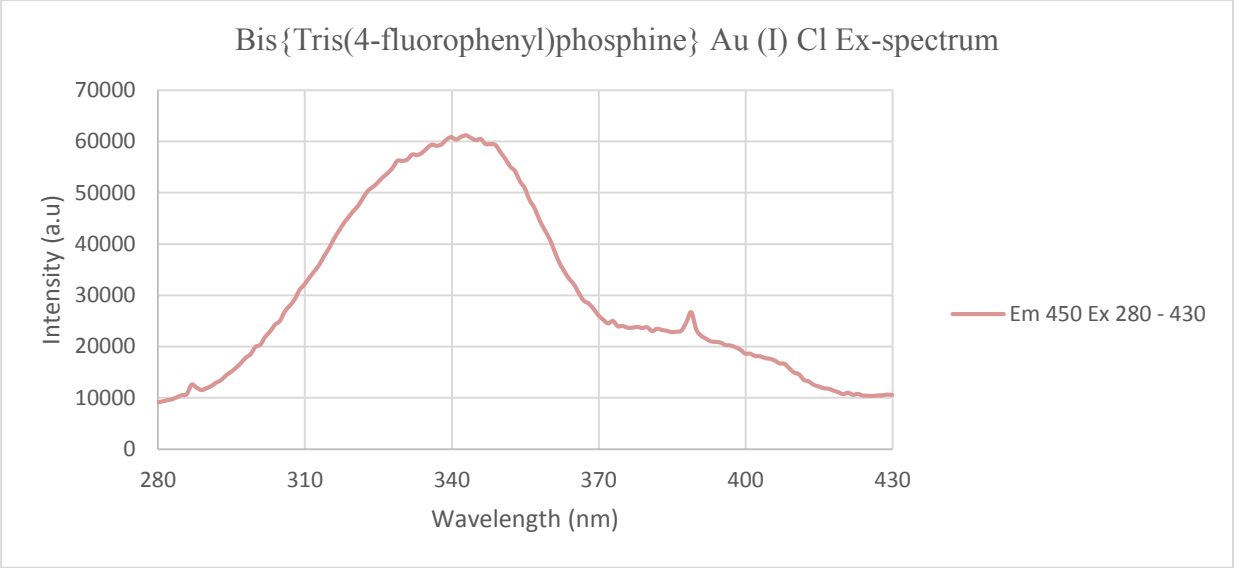

Figure 7.28. Excitation spectrum of $Au(P(C_6H_4F)_3)_2Cl$ collected in liquid nitrogen by monitoring the emission at 450 nm.

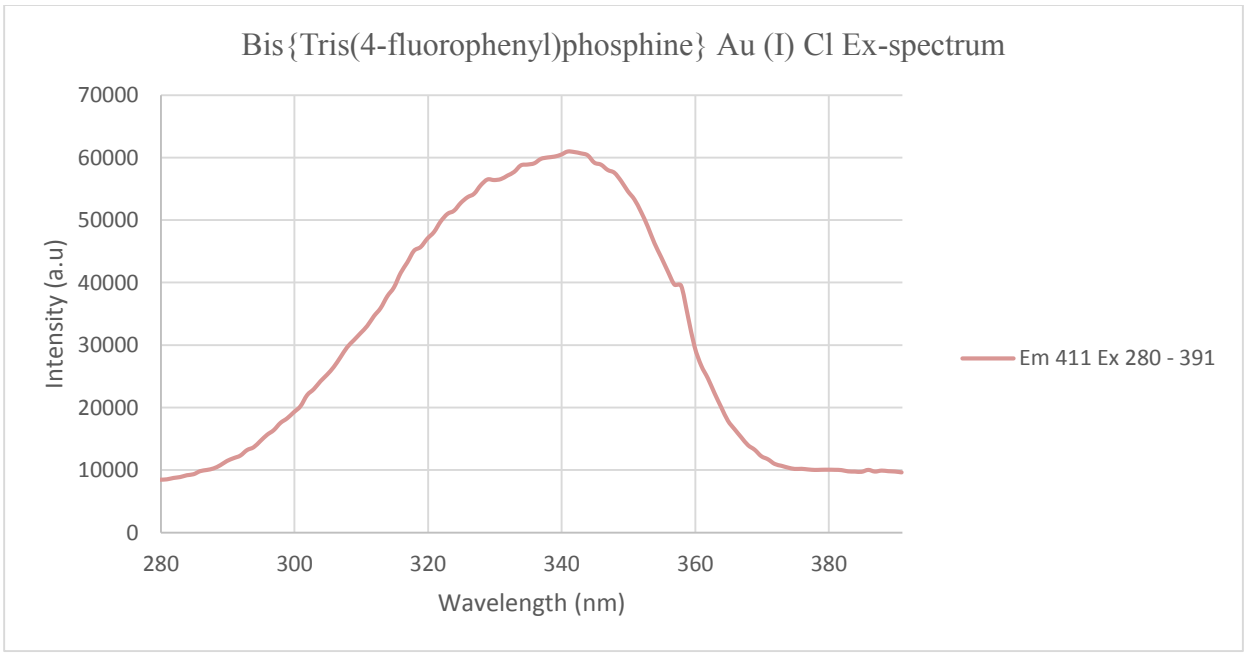

Figure 7.29. Excitation spectrum of $Au(P(C_6H_4F)_3)_2Cl$ collected in liquid nitrogen by monitoring the emission at 411 nm.

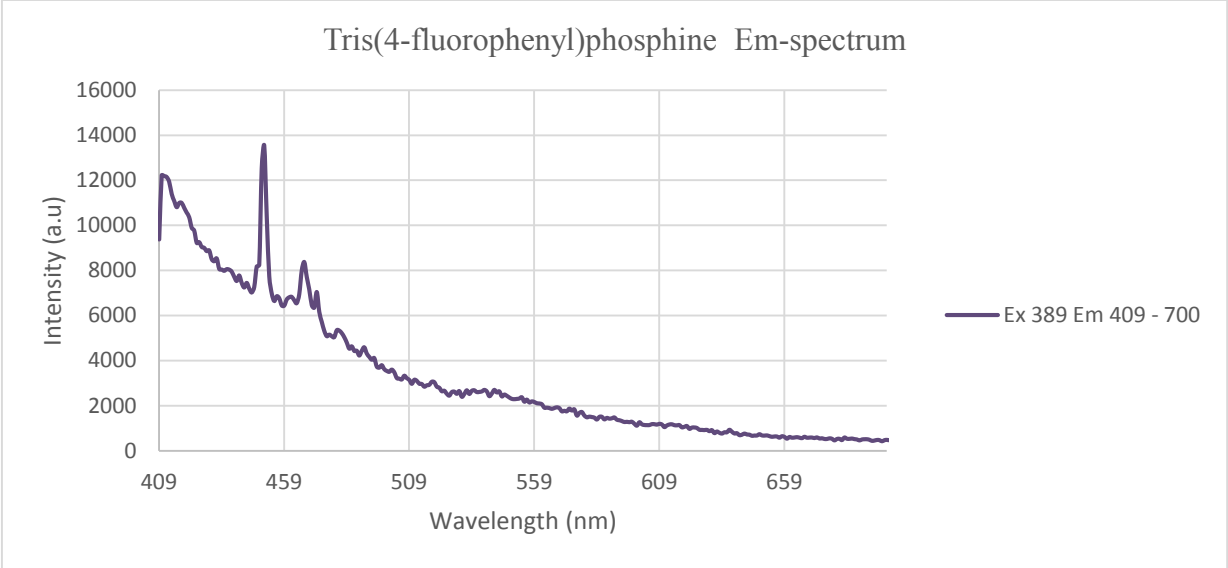

Figure 7.30. Emission spectrum of $P(C_6H_4F)_3$ collected at room temperature upon excitation at 389 nm.

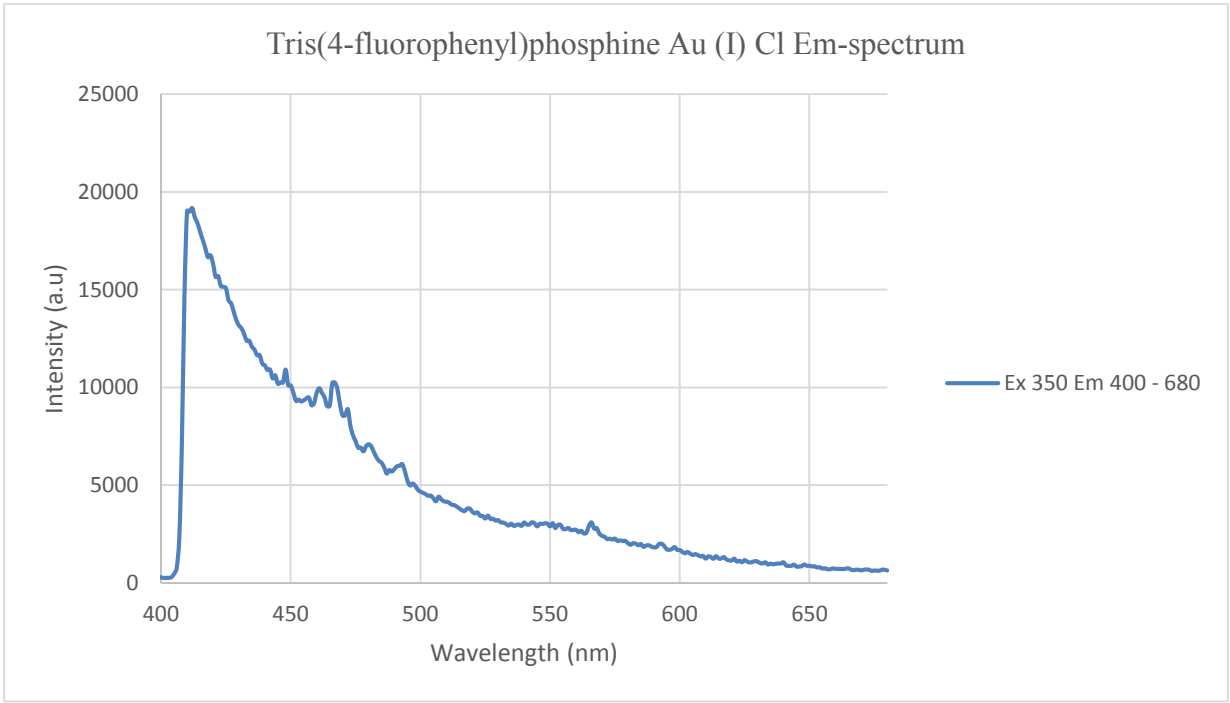

Figure 7.31. Emission spectrum of $AuP(C_6H_4F)_3Cl$ collected at room temperature upon excitation at 350 nm.

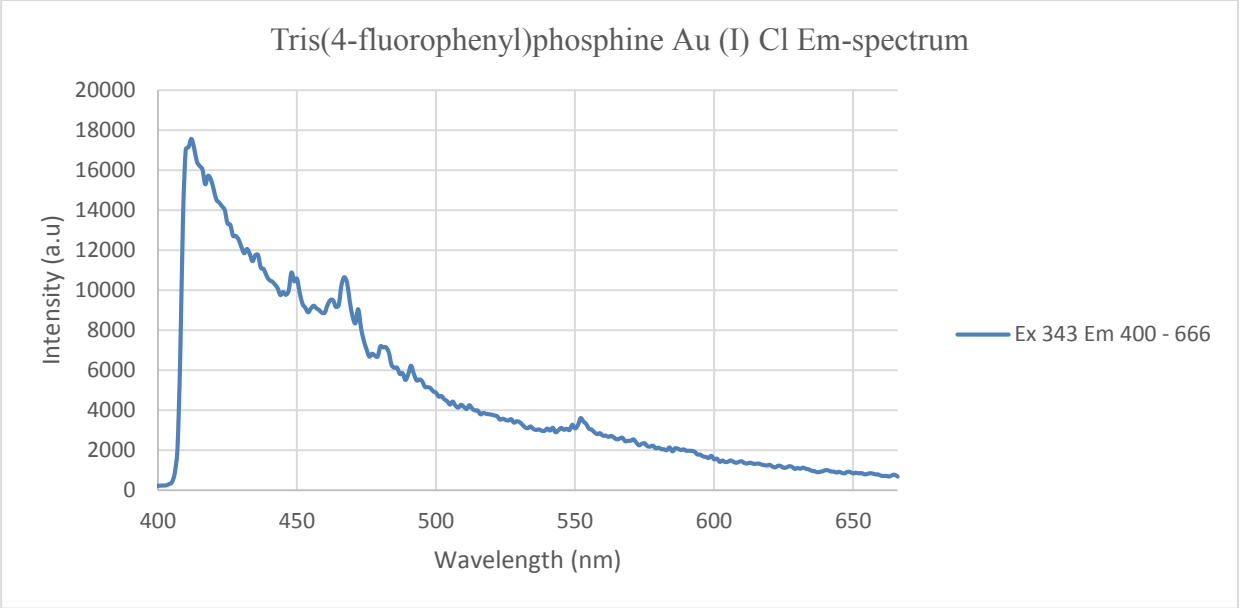

Figure 7.32. Emission spectrum of $AuP(C_6H_4F)_3Cl$ collected at room temperature upon excitation at 343 nm.

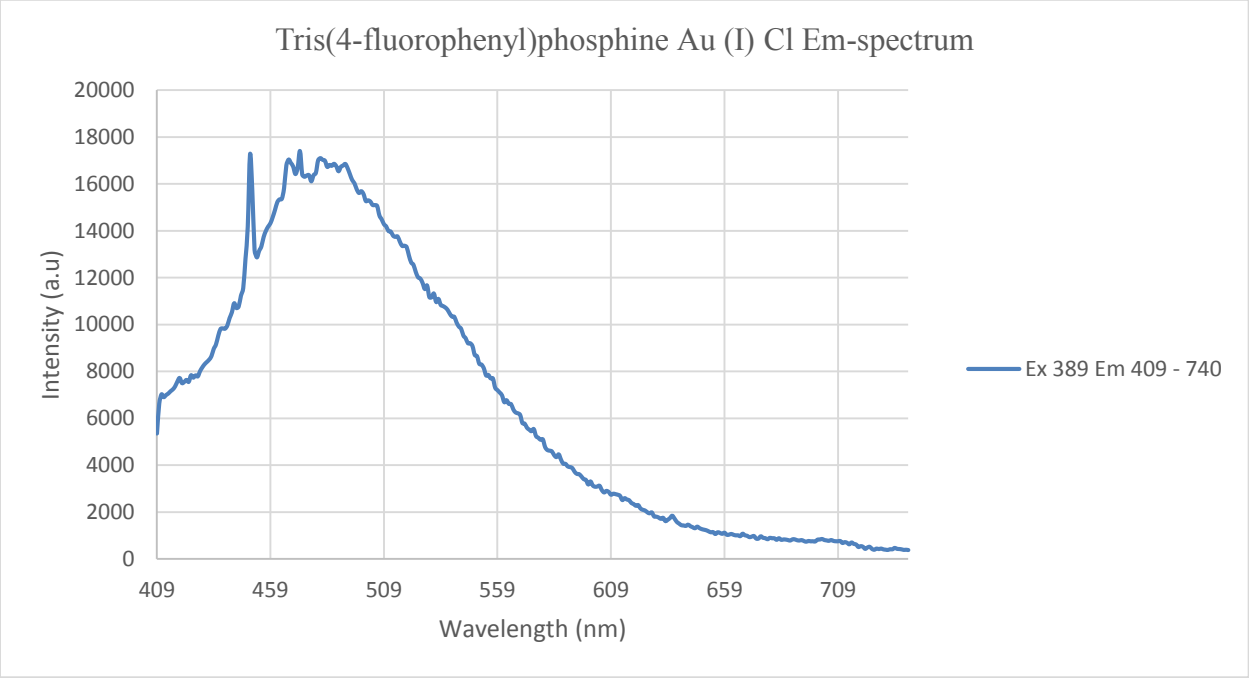

Figure 7.33. Emission spectrum of $AuP(C_6H_4F)_3Cl$ collected at room temperature upon excitation at 389 nm.

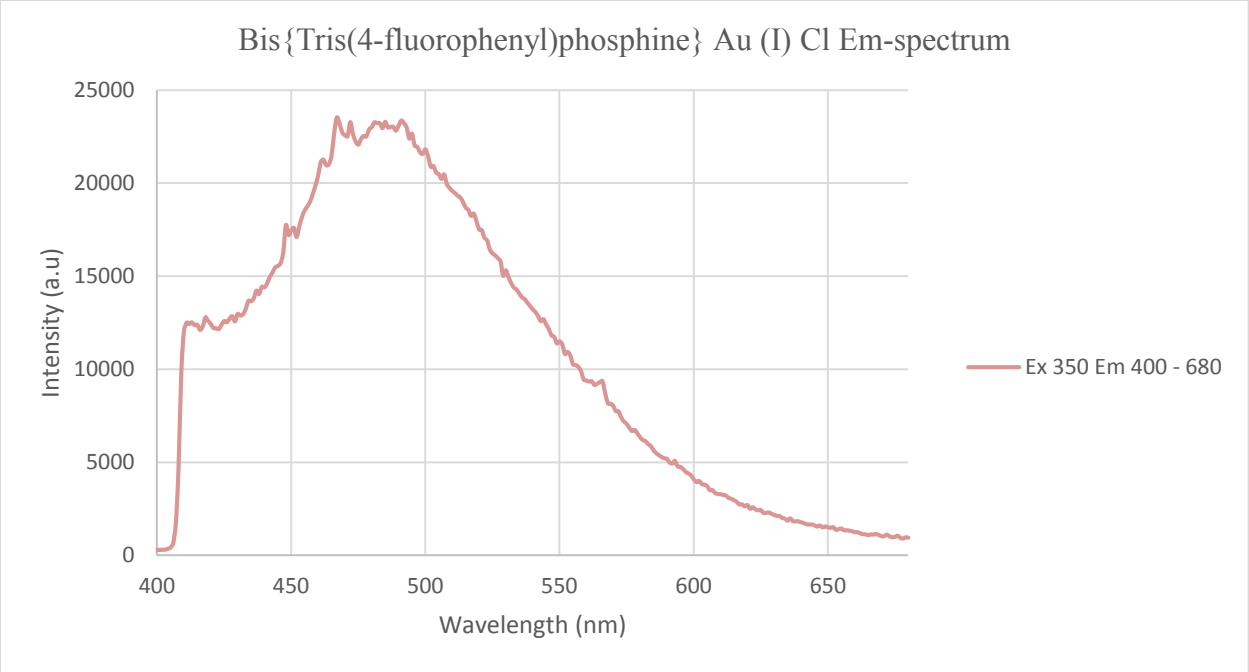

Figure 7.34. Emission spectrum of $Au(P(C_6H_4F)_3)_2Cl$ collected at room temperature upon excitation at 350 nm.

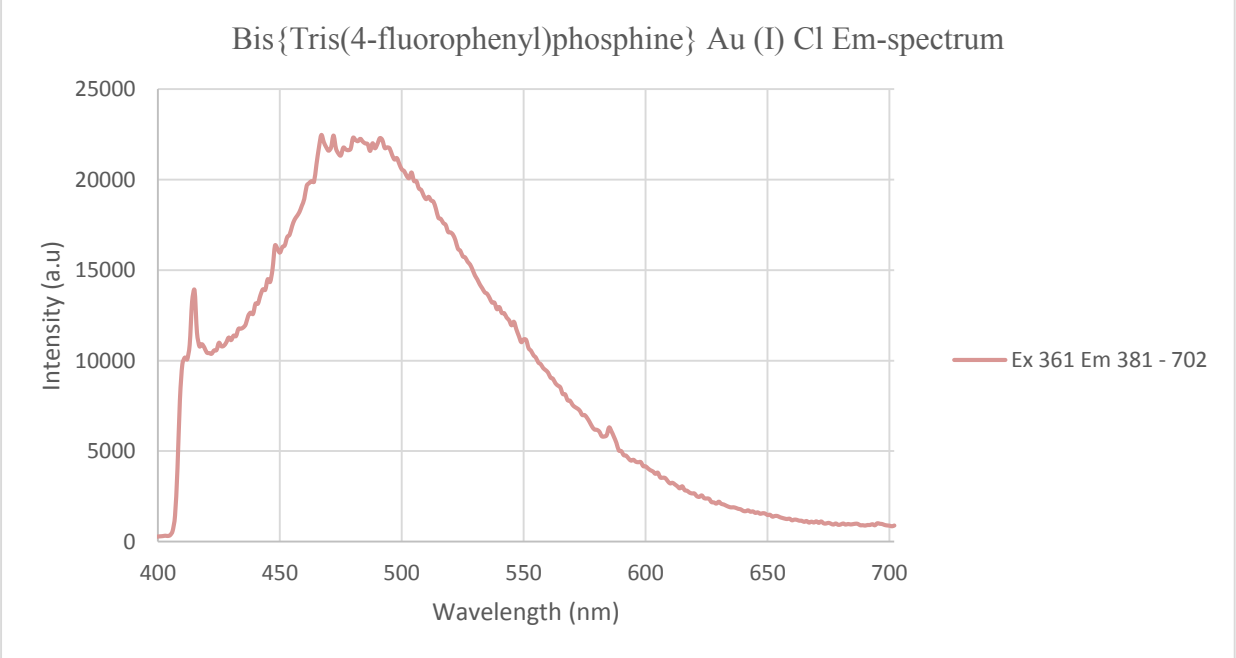

Figure 7.35. Emission spectrum of $Au(P(C_6H_4F)_3)_2Cl$ collected at room temperature upon excitation at 361 nm.

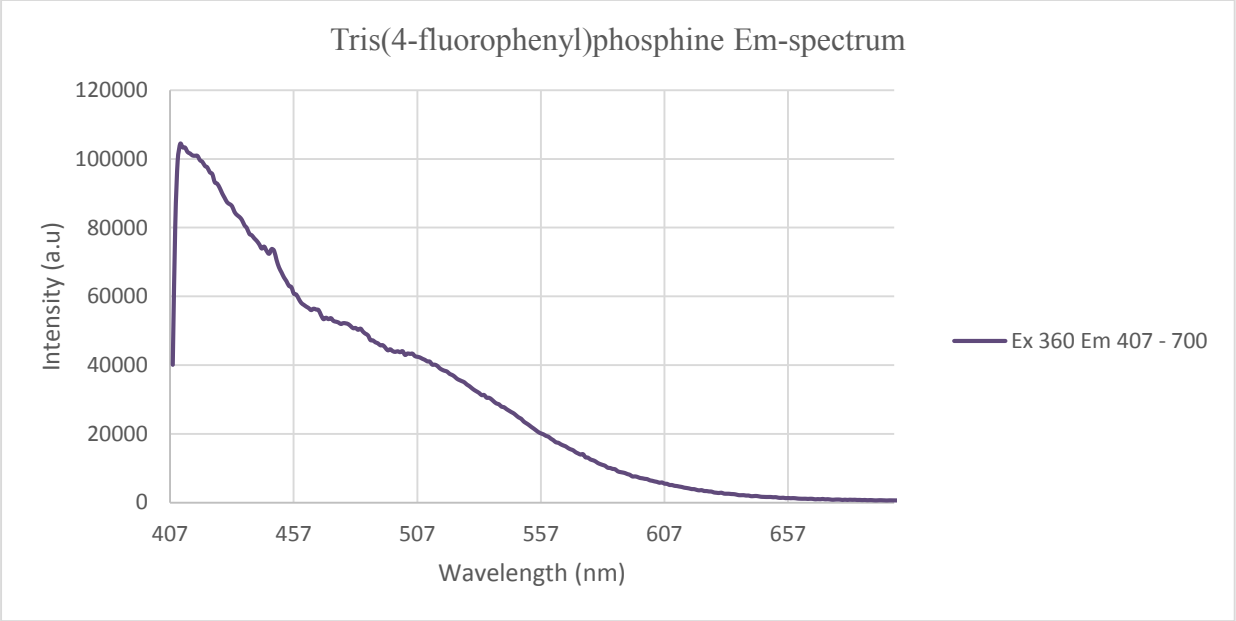

Figure 7.36. Emission spectrum of $P(C_6H_4F)_3$ collected in liquid nitrogen upon excitation at 360 nm.

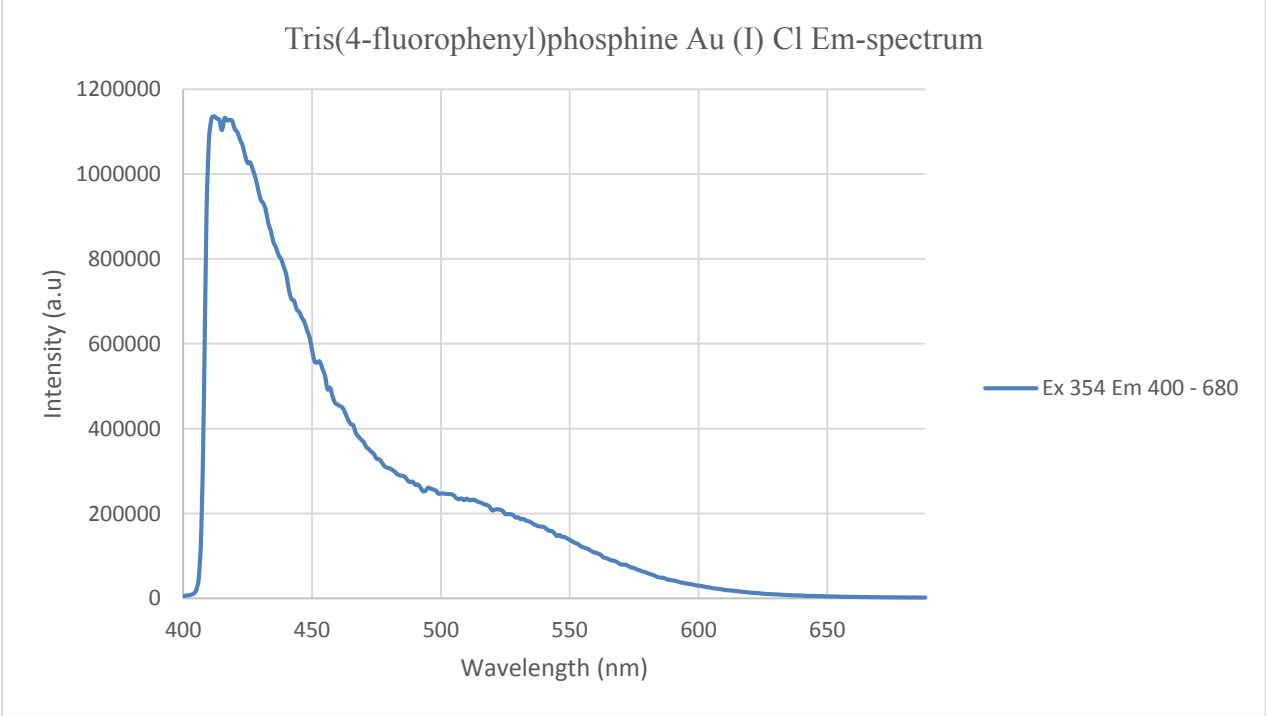

Figure 7.37. Emission spectrum of $AuP(C_6H_4F)_3Cl$ collected in liquid nitrogen upon excitation at 354 nm.

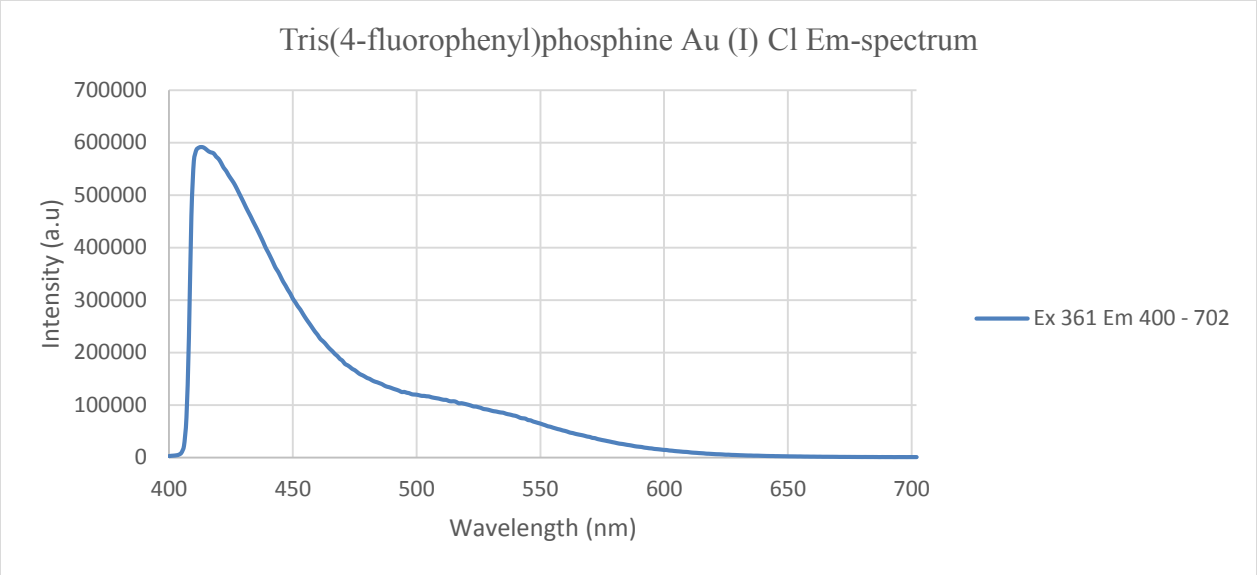

Figure 7.38. Emission spectrum of $AuP(C_6H_4F)_3Cl$ collected in liquid nitrogen upon excitation at 361 nm.

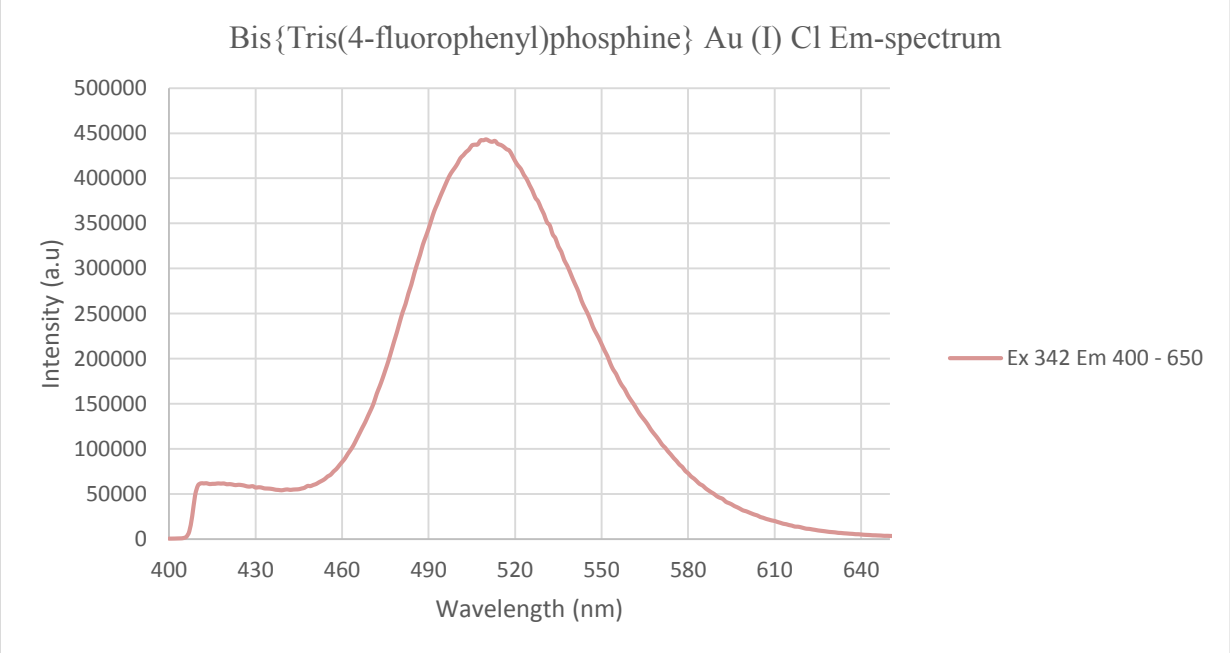

Figure 7.39. Emission spectrum of $Au(P(C_6H_4F)_3)_2Cl$ collected in liquid nitrogen upon excitation at 342 nm.

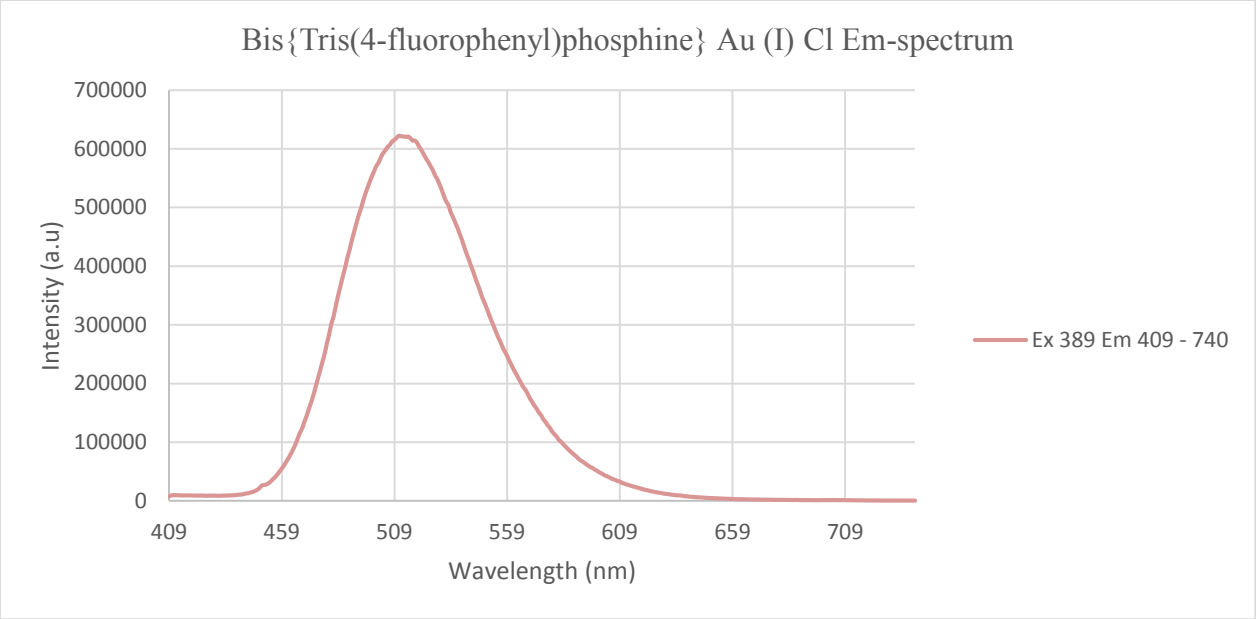

Figure 7.40. Emission spectrum of $Au(P(C_6H_4F)_3)_2Cl$ collected in liquid nitrogen upon excitation at 389 nm.

Table 7.3

Atomic contributions for the ground state molecular orbitals for compound ***18***

ATOMIC CONTRIBUTIONS (%)					
Orbitals	Au	Ligand	P	F	C
92	9.46	90.54	7.36	3.19	79.99
91	8.81	91.19	6.23	2.82	82.14
90	7.55	92.45	6.83	2.49	83.13
HOMO-LUMO GAP					
89	28.29	71.71	6.06	2.46	63.19
88	29.50	70.50	5.15	4.83	60.52
87	10.91	89.09	8.02	8.86	72.21

Table 7.4

Atomic Orbital contribution in the ground state for compound **18**

ATOMIC ORBITAL CONTRIBUTIONS (%)					
Orbitals	Au	Ligand	P	F	C
92	2.41s, 1.53px 2.12py, 4.40pz	11.94s, 33.47px, 24.35py, 20.78pz	1.05s, 2.05px 4.26pz	3.19pz	10.89s, 31.42px 24.35py, 13.33pz
91	2.23s, 1.57px 1.52py, 3.49pz	11.44s, 31.71px 11.71py, 36.06pz	1.09s, 1.41px 3.73pz	2.82pz	10.35s, 30.57px 11.71py, 29.51pz
90	1.68s, 3.78py 2.09pz	9.95s, 23.93px 45.94py, 12.63pz	1.04py, 5.79pz	2.49py,	9.95s, 23.93px 42.41py, 6.84pz
HOMO-LUMO GAP					
89	5.16pz, 23.13d	31.93s, 22.78py 17.00pz	6.06pz	2.46py	31.93s, 20.32py 10.94pz
88	6.78py, 22.72d	23.33s, 21.34py 24.42pz,	4.42py	4.15pz	23.05s, 16.92px 20.27pz
87	4.71s, 2.24px 3.96d	4.52s, 36.53px 19.85py, 28.19pz	2.67s, 5.35py	2.84px, 1.56py 4.46pz	1.85s, 28.34px 18.29py, 23.73pz

7.3 Discussion

7.3.2 Infrared Spectroscopy (Vibrational Studies). The IR-spectrum of **18** at Figure 7.4 has Twenty (20) distinct bands. It shows a weak aromatic C–H stretching of the phenyl ring at 3001 cm^{-1}, the C=C phenyl ring stretching pair at 1574 cm^{-1} and 1462 cm^{-1}, the asymmetric and symmetric C–F (Ar-F) stretching at 1226 cm^{-1} and 1157cm^{-1}, the P–Ar stretching at 1103 cm^{-1}, the aromatic C–H bending at 895 cm^{-1}, the P–C stretching at 775 cm^{-1}, the Au-P stretching at 340 cm^{-1} and the Au-Cl stretching at 324 cm^{-1}. Group Theoretical Analysis (Nuclear site group analysis) for **18** also predicts Twenty (20) IR-active modes. From the x-ray data [33], **18** has a

space group P-1 with Z = 2. With Z = 2, it means **18** contains two formula units per unit cell. The modes for this unit cell can be found by consulting table 2A [26]. Since there are 36 C-atoms, 6 F-atoms, 2 Au-atoms, 2 Cl-atoms and 2 P-atoms, it is immediately seen by inspection of table 2A [26], that the Au, Cl, P, the unique F and C all must occupy C_1 sites. The remaining C and F must lie on C_i sites, in two folds repetitively. From table 2B [26], the vibrational modes of **18** are $3A_g$ + $3A_u$ for those from the remaining C-atoms and F-atoms, and $3A_g + 3A_u$ for each nucleus on the C_1 sites. The total contribution from C, F, P, Au and Cl is $15A_g + 21A_u$. From table 2E [26], the acoustic mode is A_u and the optical modes are $15A_g + 20A_u$. The distribution of the optical modes shows that Twenty (20) ($20A_u$) modes are expected to be IR-active from the selection rule. Comparison of these predictions with the observed calculated spectra shows that twenty distinct frequencies are observed.

7.3.3 Nuclear Magnetic Resonance. The ^{1}H NMR spectrum of **18** shown at figure 7.7 showed splitting at chemical shift at δ = 7.1 (m, 6H, Ar–H), δ = 7.4 (m, 6H, Ar–H). The peak intensities of the proton environments corresponds to the number of H-atoms in the respective environments. Comparison of the ^{1}H NMR spectral data between **18** and its free ligand (TFFPP) shows a slight shifting downfield. Peaks for TFFPP ligand found on figure 7.6 showed splitting at δ = 7.0 (m, 6H, Ar–H), δ = 7.3 (m, 6H, Ar–H). The slight difference in the position of the peaks between **18** and its ligand is an indication that the ligand has successfully coordinated to the gold center. The ^{1}H NMR spectral data for **19** at Figure 7.8 is slightly different from both the TFFPP ligand and **18**. It showed splitting at chemical shift at δ = 7.2 (m, 6H, Ar–H), δ = 7.6 (m, 6H, Ar–H). The ^{31}P{^{1}H} NMR spectral data for the TFFPP ligand, the **18** and the **19** shown at Figure 7.9, 7.10 and 7.11 showed a strong sharp peak at 46.0 ppm, 59.0ppm and 74.0ppm respectively. With the coordination of the mono and the bis, to the gold(I) chloride center the

trend of downfield shifting is seen. This is as a result of the weakening of the gold-phosphine bond and consequently de-shielding the electrons and causing the peak to shift to a larger chemical shift value (downfield). The overall trend appears consistent for gold phosphine complexes where the mono substituted systems usually show smaller chemical shift values than the di, tri substituted complexes. For example, the mono, tris, and tetrakis substituted (TFP)nAuCl compounds have ^{31}P NMR coordination chemical shift (ccs) of 48.4, 66.1, 63.1 respectively [32]. Also, the mono, di, tris, and tetrakis substituted (TPA)nAuCl compounds have ^{31}P NMR values of -51.4, -36.1, -56.1, and -58.0 ppm respectively [27-31]. The increase in the chemical shift value on going from the TFFPP, to the **18** and to the **19** is consistent with the general trend that chemical shift values increases as the coordination number increases. The trend of downfield shifting is also an indication that the ligand has successfully been coordinated to the gold (I) center.

7.3.4 UV-Vis Spectroscopy. The absorption spectral data for the TFFPP ligand, $AuP(C_6H_4F)_3Cl$ and $Au(P(C_6H_4F)_3)_2Cl$ reveal similarities in their high-energy broad UV absorption profiles. The absorbance maximum for the free TFFPP ligand shown at Figure 7.14 is observed at 260 nm with a smaller less intense band at 290 nm with low energy tail extending all the way to 400 nm. Similarly, all of the TFFPP‑gold(I) complexes also show similar higher energy band maxima near 260 nm . Based on the spectral similarities between the ligand and the complexes as well as the molar absorptivity values of 5.21 x 10^4 $M^{-1}cm^{-1}$, 8.52 x 10^4 $M^{-1}cm^{-1}$ and 1.17 x 10^5 $M^{-1}cm^{-1}$for the TFFPP, $AuP(C_6H_4F)_3Cl$ and $Au(P(C_6H_4F)_3)_2Cl$ respectively, the 260 nm band is assignable to a $\pi \rightarrow \pi^*$ intraligand transition, which is as result of the presence of double bond in the aromatic phenyl ring. The transition is slightly affected by the coordination with the Au metal. The weaker band at 290 nm which is present in the ligand is absent in the

absorption spectra of the complexes **18** and **19** at Figure 7.15 and 7.16 respectively, indicating that the transition is affected by coordination with the metal. This band is assignable to an n→π* transition and its absence in the absorption spectrum of **18** and **19** is indicative of participation of the lone pair electrons in the bonding scheme of the TFFPP ligand. The higher molar extinction coefficient value of the ligand and the complexes is an indication that the electronic transitions involved as a result of the absorption are statistically probable (said to be 'allowed') due to the fact that their molar extinction **ε** values are in excess of 10 000. It is also interesting to note that the TFFPP ligand, the **18** and the **19** complexes absorbs at similar energies but with the extinction coefficients of **19** about twice more intense than that of **18** and in turn about twice that of the TFFPP ligand . The enhancement (Hyperchromic shift) of the extinction coefficient in **19** relative to **18** and relative to TFFPP is understandable in view of the presence of two more identical chromophores absorbing at the same region.

7.3.5 Luminescence. The gold(I) complexes and the TFFPP ligand luminescent when excited under UV radiation. The emission spectra of the complexes both at room and liquid nitrogen temperatures have very similar profiles indicating a similar origin for the electronic transitions. The emission spectra of the TFFPP ligand at room temperature and in liquid nitrogen shown at Figure 7.30 and 7.31 is characterize by a sharp band and maximizes around 450 nm and 413 respectively. The emission spectra of the gold complex **18** and **19** at room temperature shown at Figure 7.32 to 7.35 was observed at 468 nm and 486 nm showing fine vibronic structures arising from the v(C=C) stretch of the phenyl ring of the ligand, with vibrational progressions with spacings of 1300 cm^{-1}. The shift to the longer wavelength (bathochromic shift) from 450 nm of the TFMOPP to 468 nm of $AuP(C_8H_9)_3Cl$ and 486 nm of $Au(P(C_6H_4F)_3)_2Cl$ is due to the fact that at the excited states, the π→π* transitions of the TFFPP is more polar than

their ground states and as a result, a greater charge separation is observed in the excited state. The coordination of the TFFPP ligand to the gold (I) center causes a dipole–dipole interaction which reduces the energy of the excited state more than the ground state, hence making the **18** and **19** to emit at a longer wavelength. This emission at a longer wavelength by **18** and **19** compare to the ligand is also an indication that the ligand has successfully been coordinated to the gold (I) center. Similar emission bands for **18** and **19** in liquid nitrogen were observed at 417 nm and 512 nm respectively (Figure 7.37 to 7.40) showing weak vibronic structures arising from the v(C=C) stretch of the phenyl ring of the ligand. The excitation spectrum of the TFFPP ligand, **18** and **19** at room temperature and in liquid nitrogen shown at Figure 7.19 to 7.29 for TFFPP, 18 and **19** consists of a well-defined broad band with an average spacing of 1330 cm^{-1}. This spacing is assignable to an electronic transition coupled with vibronic component corresponding to v(C=C) symmetric stretching mode within the phenyl ring. With reference to the previous luminescence studies on tertiary phosphine gold(I) complexes the emission bands at 468 and 486 nm in complexes **18** and **19** respectively is tentatively assigned as derived from excited states of P−> Au ligand-to-metal charge transfer (LMCT) origin. This suggests that the ligand centered transition is responsible for the photoluminescence in **18** and in **19**.

7.3.6 Computational Studies

7.3.6.1 Spectroscopic Comparison. The theoretical calculated IR spectrum of **18** using Gaussian 09 shown at Figure 7.3 also predicts Twenty (20) distinct bands with a slight shift in the position of some of the individual peaks, but on a whole both the calculated and the experimental spectrum of both the ligand and the complex shows similar IR-spectrum. The theoretical ^{1}H NMR of for both the ligand and the gold complex shown on Figure 7.12 and

Figure 7.13 also showed similar splitting patterns and chemical shift values as that of the experimental ones.

7.3.6.2 Electronic Comparison

7.3.6.2.1 Luminescence. The result of the population analysis for **18** is shown in Table 7.3 and 7.4 for the percentage atomic and atomic orbital contributions respectively for the metal and the TFFPP ligand, as well as individual atomic participation for the selected highest three occupied molecular orbitals and lowest three unoccupied molecular orbitals. The third highest occupied molecular orbital (THOMO), HOMO-87 has the largest contribution from the ligand at 89.09% and the metal at 10.91% followed by the highest occupied molecular orbital, HOMO-89 at 71.71% and 28.29% contributions, respectively. The contribution of the gold atom in the HOMO-87 orbital derives from 5s, 5px and 5dxz atomic orbitals at 4.71%, 2.24% and 3.96% contributions respectively. The atomic contribution of the TFFPP ligand is comprised of Phosphorus, Fluorine and Carbon with percentage contributions of 4.52s, 36.53px, 19.85py and 28.19pz orbitals. However, the gold contribution of the HOMO comes also from 5.16% of the 5pz and 23.13% of the 5dxz atomic orbitals with the remaining contribution from the s and p orbitals of the phosphorus, fluorine and Carbon atoms of the TFFPP ligand. The table also shows the first three lowest unoccupied molecular orbital (LUMOs) contributions, which are mainly ligand centered contributions. The orbital description as ligand based and partial metal based transitions is thus substantiated to support the observations surrounding the luminescent behavior of **18** and hence the assignment of $\pi \rightarrow \pi^*$ transition is in a proper order.

7.3.6.2.2 UV-Vis. The HOMO‑LUMO gap calculated value by the TD-DFT method was 40,366 cm^{-1} corresponding to 247.74 nm. The theoretical calculated spectrum for **18** obtained using TDDFT with the LANL2DZ basis set to identify the orbital(s) contributing to the observed

absorption is shown at Figure 7.17. The TD-DFT generated ground-state to excited-transitions is shown on Table 7.1 which summarizes the orbital that took part most in the transitions X, Y, and Z. From Table 7.1, transition **Z** supports an assignment of the THOMO-87→LUMO-90, a π→π* type transition. This confirms why the n→π* is not present in the experimental UV-Vis spectrum of **18**. The transition X and Y has transitions from the HOMO-89→LUMO-90 and SHOMO-88→LUMO-90 respectively. Table 7.2 summarizes the various transitions pictorially of the theoretically generated ground-state to excited-state transitions for X, Y and Z. These calculated spectrum values are in good agreement with the experimental UV-Vis spectrum of **18**, with a slight red shifting of about 12.26 nm which are within the absorption range of aromatic derivatives.

CHAPTER EIGHT

Synthesis and Characterization of mono-, bis-, tris-, and tetrakis-{tris(pentafluorophenyl)phosphine} gold(I) complexes

8.1 Syntheses

8.1.1 Tris(pentafluorophenyl)phosphine gold (I) chloride (22).

Tris(pentaflouorophenyl)phosphine (0.0200 g, 0.038 mmol) was added to a solution of $(C_4H_8S)AuCl$ (0.00874 g, 0.038 mmol) in dichloromethane (20 ml) at −80 ˚C and the reaction stirred for 2 hours. The solvent was removed by purging nitrogen gas into the solution, until all the solvent dried up. The residue was then recrystallized from CH_2Cl_2/n-hexane mixture for six days. Partial evaporation of the solvent provided quality crystals.

8.1.2 Bis{tris(pentafluorophenyl)phosphine} gold (I) chloride (23).

Tris(pentaflouorophenyl)phosphine (0.0400 g, 0.076 mmol) was added to a solution of $(C_4H_8S)AuCl$ (0.00874 g, 0.038 mmol) in dichloromethane (20 ml) at −80 ˚C and the reaction stirred for 2 hours. The solvent was removed by purging nitrogen gas into the solution, until all the solvent dried up. The residue was then recrystallized from CH_2Cl_2/n-hexane mixture for six days. Partial evaporation of the solvent provided quality crystals.

8.1.3 Tris{tris(pentafluorophenyl)phosphine} gold (I) chloride (24).

Tris(pentaflouorophenyl)phosphine (0.0600 g, 0.114 mmol) was added to a solution of $(C_4H_8S)AuCl$ (0.00874 g, 0.038 mmol) in dichloromethane (20 ml) at −80 ˚C and the reaction stirred for 3 hours. The solvent was removed by purging nitrogen gas into the solution, until all the solvent dried up. The residue was then recrystallized from CH_2Cl_2/n-hexane mixture for seven days. Partial evaporation of the solvent provided quality crystals.

8.1.4 Tetrakis{tris(pentafluorophenyl)phosphine} gold (I) chloride (25).

Tris(pentaflouorophenyl)phosphine (0.0400 g, 0.076 mmol) was added to a solution of $(C_4H_8S)AuCl$ (0.00874 g, 0.038 mmol) in dichloromethane (20 ml) at −80 ˚C and the reaction stirred for 2 hours. The solvent was removed by purging nitrogen gas into the solution, until all the solvent dried up. The residue was then recrystallized from CH_2Cl_2/n-hexane mixture for days. Partial evaporation of the solvent provided quality crystals.

8.2 Results

8.2.1 X-ray Crystallography. Diffraction-quality crystal structure for $AuP(C_7H_7O)_3Cl$, of the monocoordinated TFFPP gold (I) complex and the crystal structure determination data and selected bond lengths and angles has already been published by Hsiao Wei Chen and Edward R. T. Tiekink [34]. The di-, tri and the tetra-coordinated has been synthesized under this research.

8.2.2 Infrared Spectroscopy. All infrared spectra were obtained as potassium bromide (KBr) disc, prepared by compressing the ground mixture of sample and KBr powder, on a Shimadzu IR-PRESTIGE-21 Fourier transform infrared spectrophotometer (4000−300 cm^{-1}). Figure 8.1, 8.2, 8.3, 8.4 and 8.5 show both experimental and theoretically calculated IR spectrum of the mono-, di-, tri- and tetra-coordinated TFFPP gold (I) complexes.

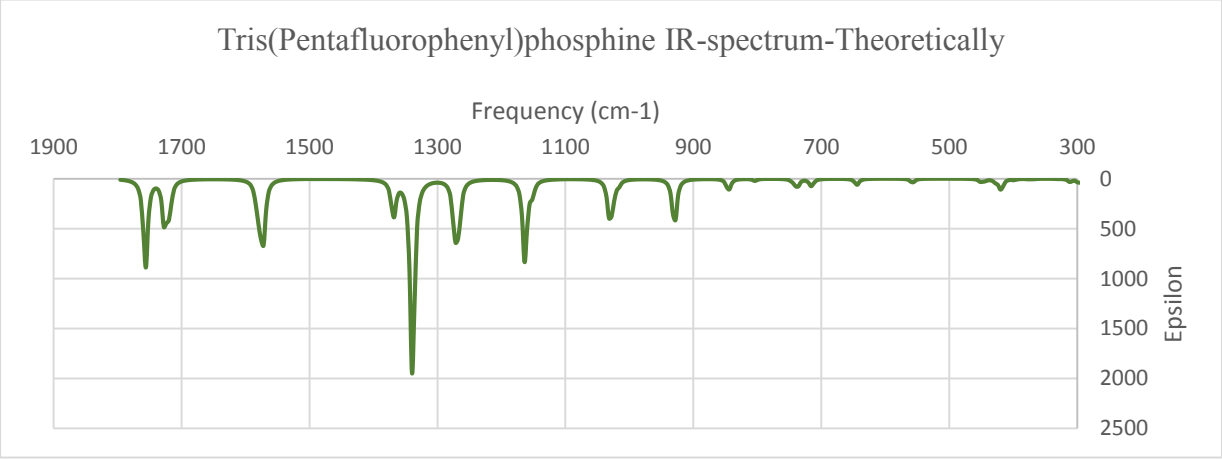

Figure 8.1. Calculated IR spectrum for $P(C_6F_5)_3$ obtained using Gaussian 09 program.

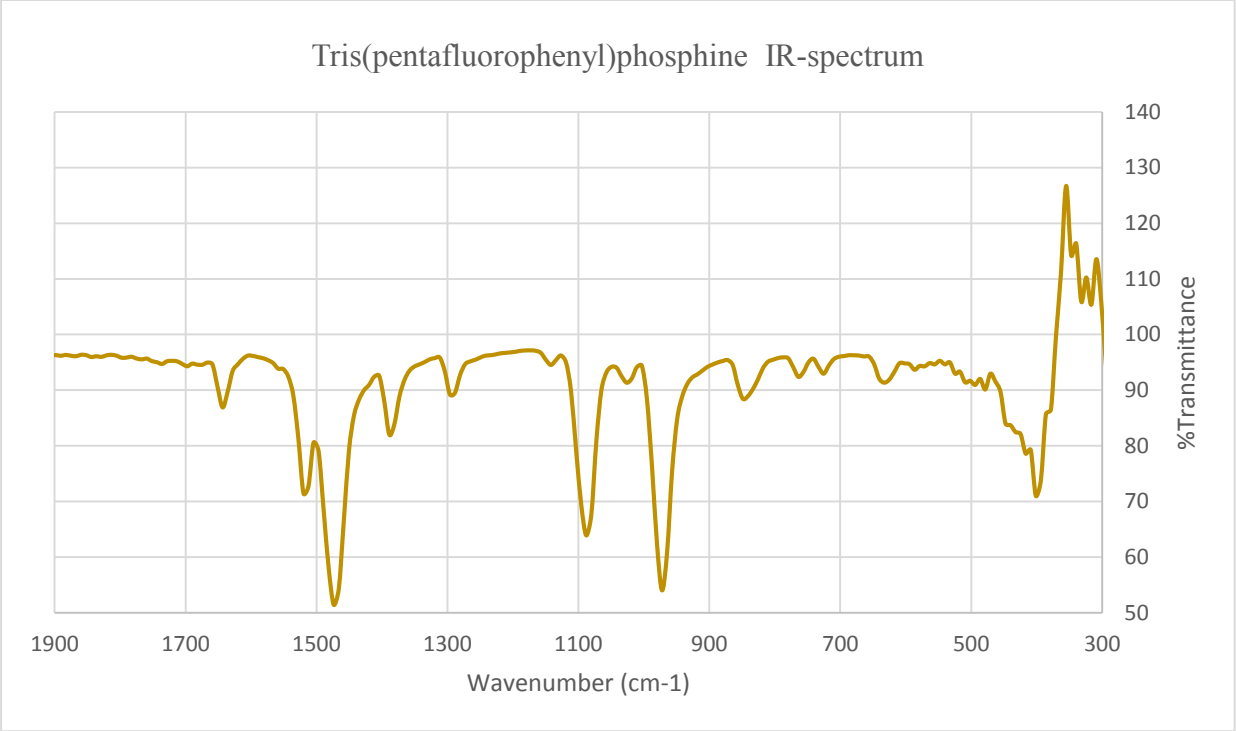

Figure 8.2. IR spectrum for $P(C_6F_5)_3$.

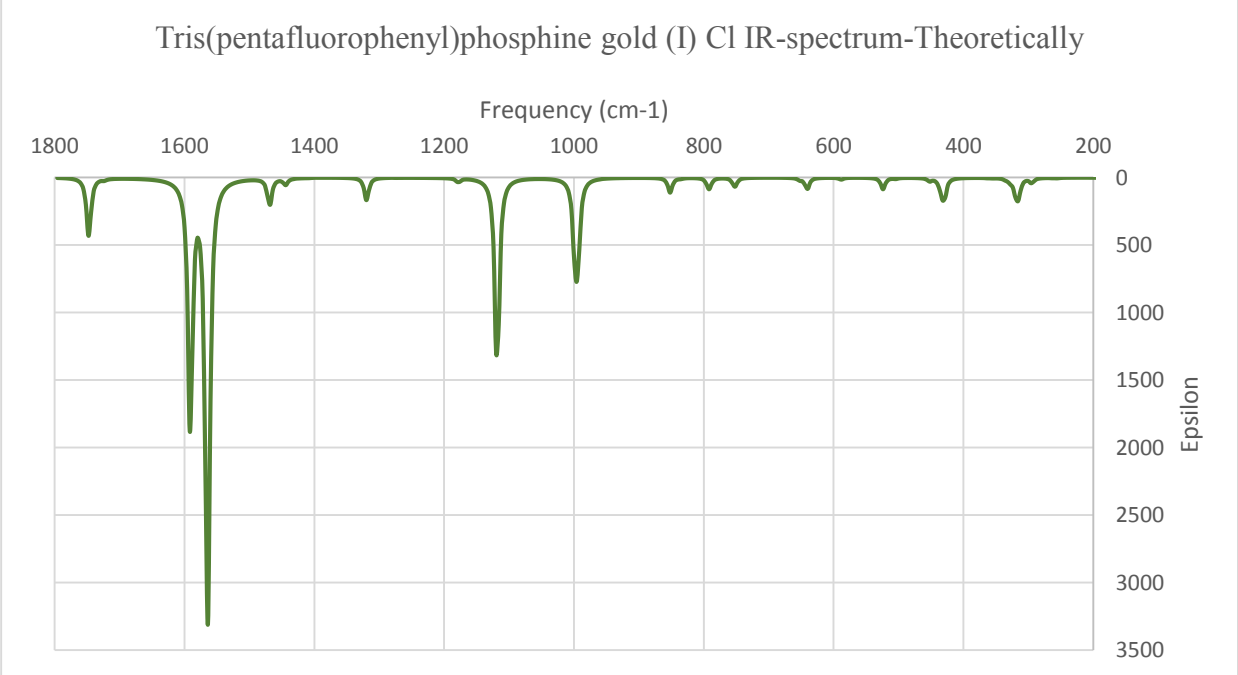

Figure 8.3. Calculated IR spectrum for $AuP(C_6F_5)_3Cl$ obtained using Gaussian 09 program.

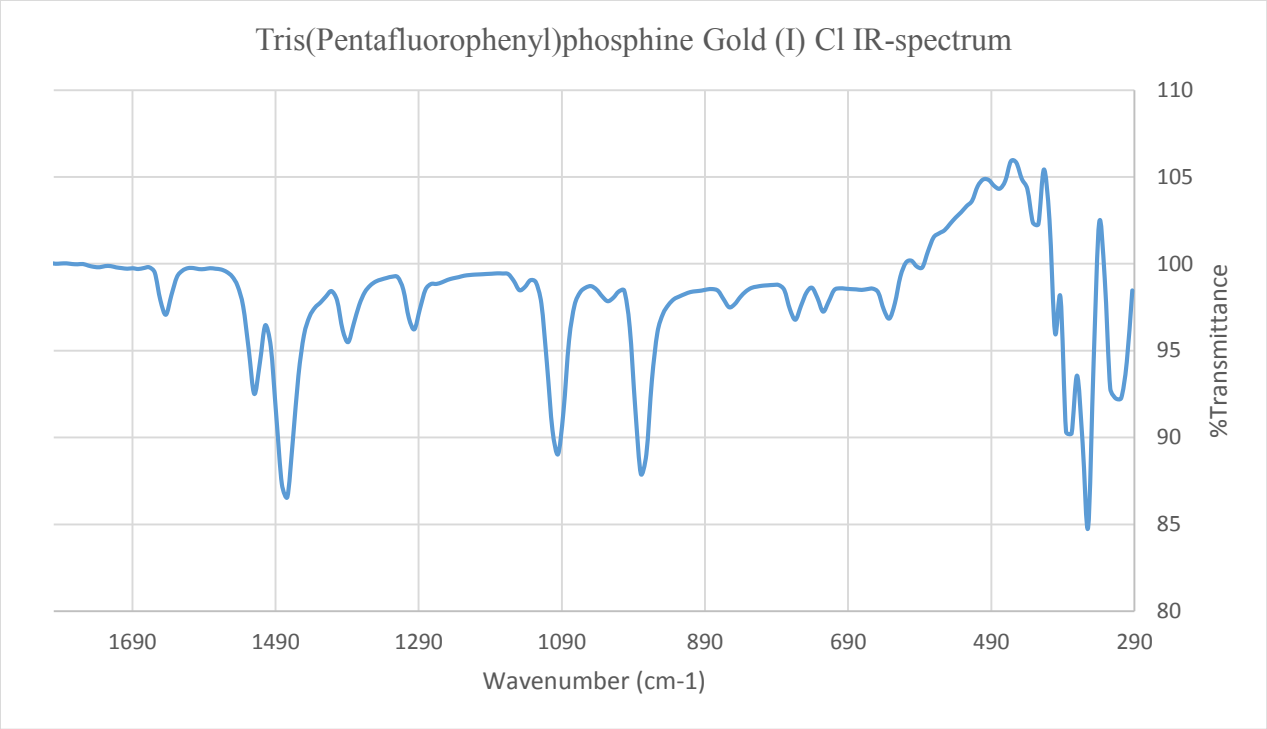

Figure 8.4. IR spectrum for $AuP(C_6F_5)_3Cl$.

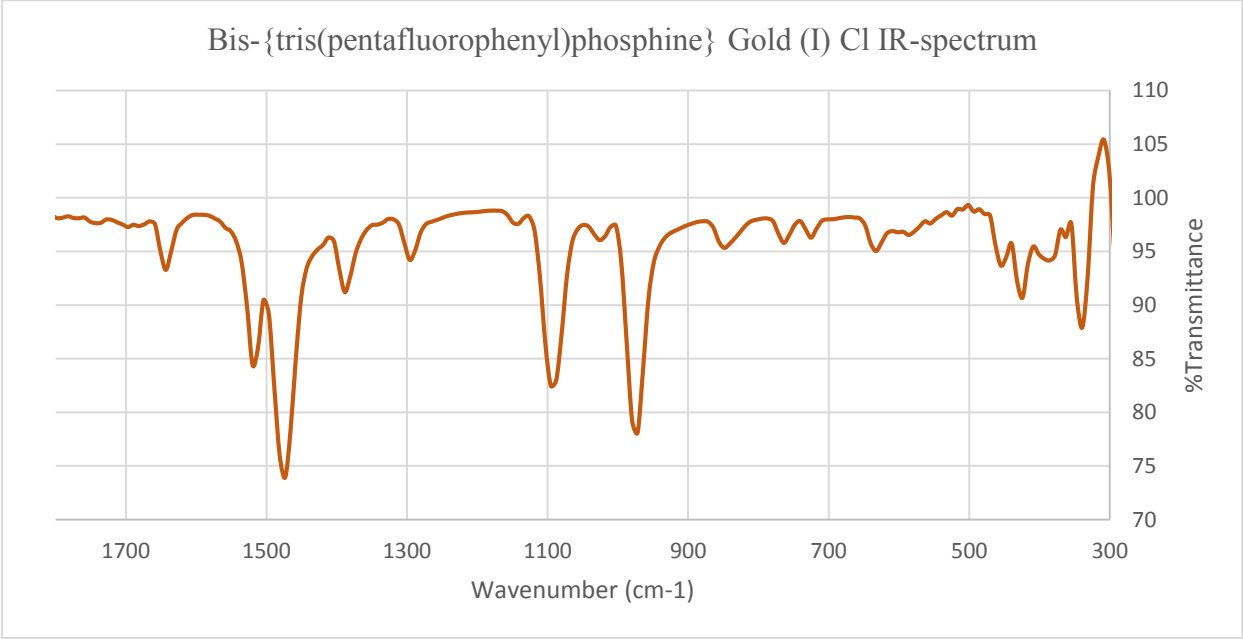

Figure 8.5. IR spectrum for $Au(P(C_6F_5)_3)_2Cl$.

Table 8.1

Nuclear site group theoretical analysis for $AuP(C_6F_5)_3Cl$

NUCLEAR SITE GROUP ANALYSIS FOR $[AuP(C_6F_5)_3Cl]$					
ATOMS	Au	P	Cl	F	C
SITES (16A)	C_s	C_s	C_s	C_1	C_i
VIBRATIONAL (5B)	$2A_g + A_u + B_g + 2B_u$	$2A_g + A_u + B_g + 2B_u$	$2A_g + A_u + B_g + 2B_u$	$3A_u + 3B_u$	$3A_g + 3A_u + 3B_g + 3B_u$
TOTAL CONTRIBUTION = $9A_g + 9A_u + 6Bg + 12B_u$					
ACOUSTIC MODES (5E) = $A_u + B_u$					
OPTICAL MODES = $9A_g + 8A_u + 6B_g + 11B_u$					
IR ACTIVE (5E) = $8A_u + 11B_u$					
RAMAN ACTIVE (5E) = $9A_g + 6B_g$					

8.2.3 Nuclear Magnetic Resonance. The $^{31}P\{^1H\}$ NMR spectral data for the ligand, **22** and **23** was found in Figure 8.6, 8.7 and 8.8 showing peaks at 60.0ppm, 66.0 ppm and 80 ppm respectively.

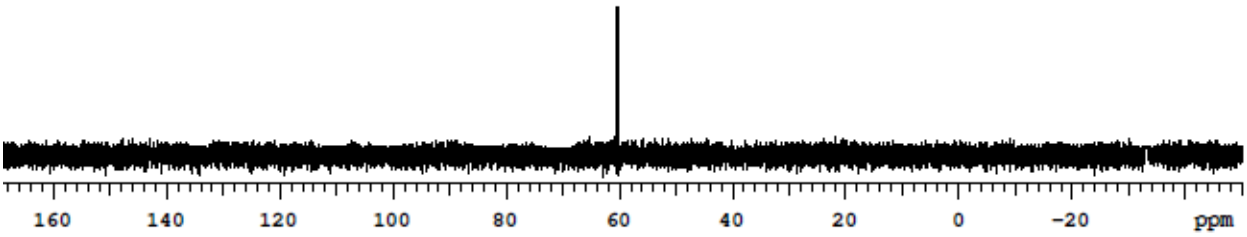

Figure 8.6. $^{31}P\{^1H\}$ NMR spectrum of $P(C_6F_5)_3$.

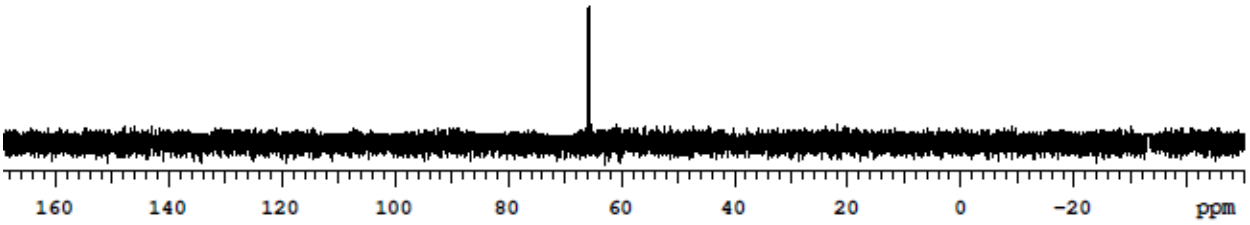

Figure 8.7. $^{31}P\{^{1}H\}$ NMR spectrum of $AuP(C_6F_5)_3Cl$.

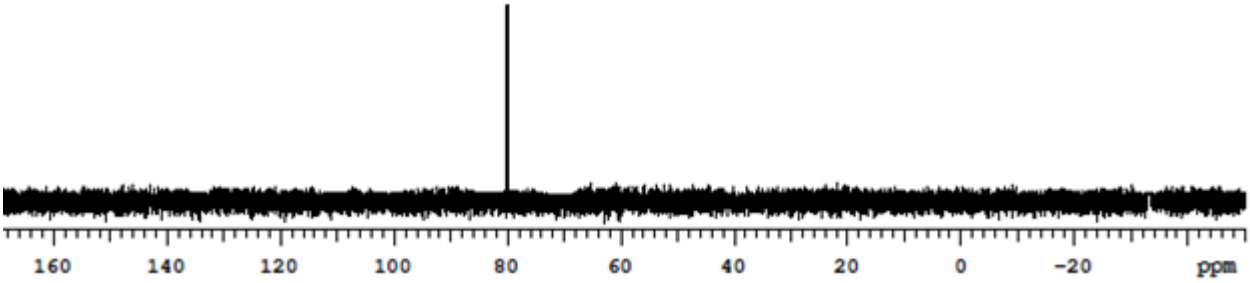

Figure 8.8. $^{31}P\{^{1}H\}$ NMR spectrum of $Au(P(C_6F_5)_3)_2Cl$.

8.2.4 UV-Vis Spectroscopy. All of the samples used for the ultraviolet visible (absorption) experiment, were dissolved in spectroscopic grade acetonitrile (CH_3CN). The TPFPP ligand has a broad absorption spectrum shown at Figure 8.9 that maximizes around 225 nm with a calculated molar absorptivity of 8.54 x 10^4 $M^{-1}cm^{-1}$. The absorption spectrum of **22** shown at Figure 8.10 has a broad absorption profile maximizes at about 225 nm with a calculated molar absorptivity of 1.23 x 10^5 $M^{-1}cm^{-1}$. In Figure 8.11 is shown the absorption profile for **23** which has a band maximum of about 225 nm with a calculated molar absorptivity of 1.85 x 10^5 $M^{-1}cm^{-1}$. The theoretical spectrum using DFT calculations, shows a spectrum at Figure 8.12 and 8.13 with a broad absorption spectrum at 249 nm and 260 for **22** and the TPFPP ligand respectively.

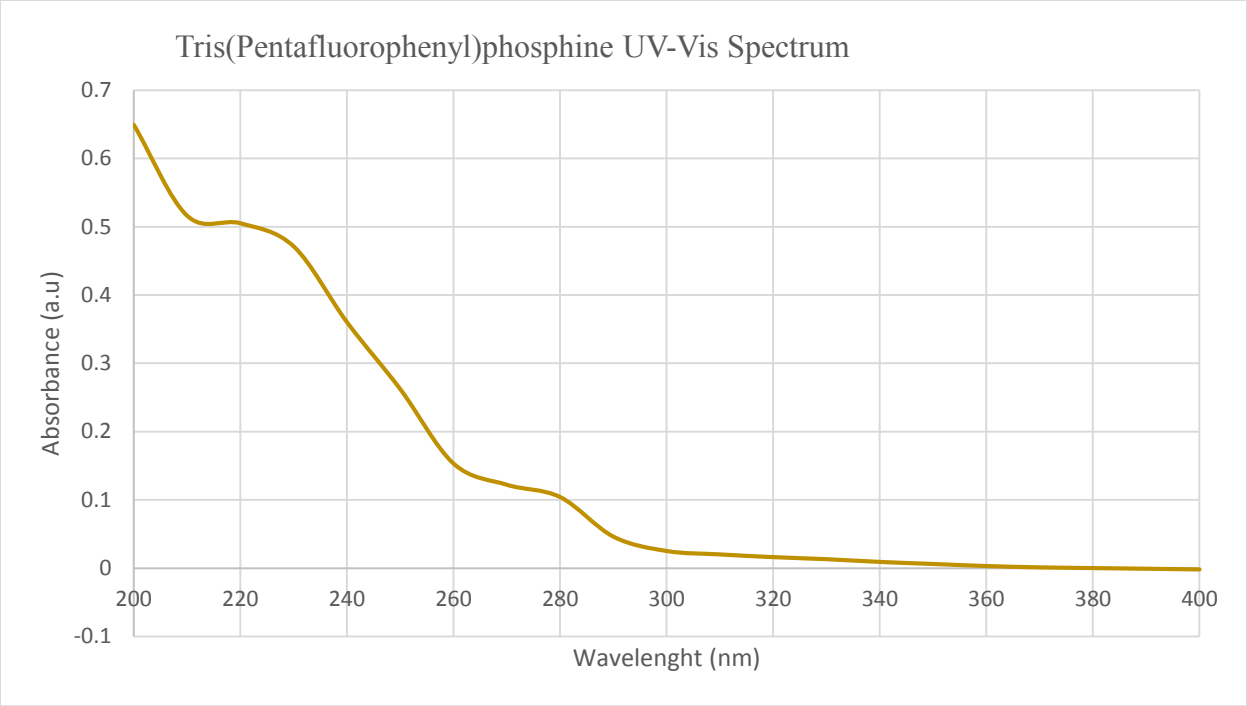

Figure 8.9. UV-Vis spectrum of $P(C_6F_5)_3$.

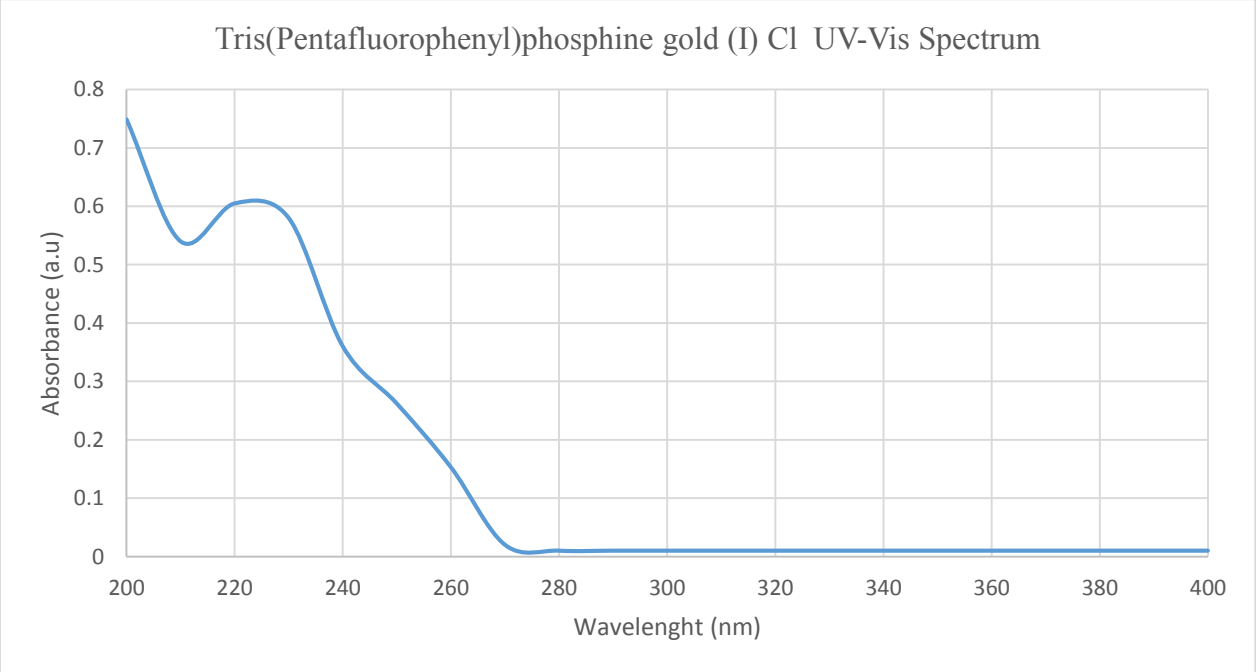

Figure 8.10. UV-Vis spectrum of $AuP(C_6F_5)_3Cl$.

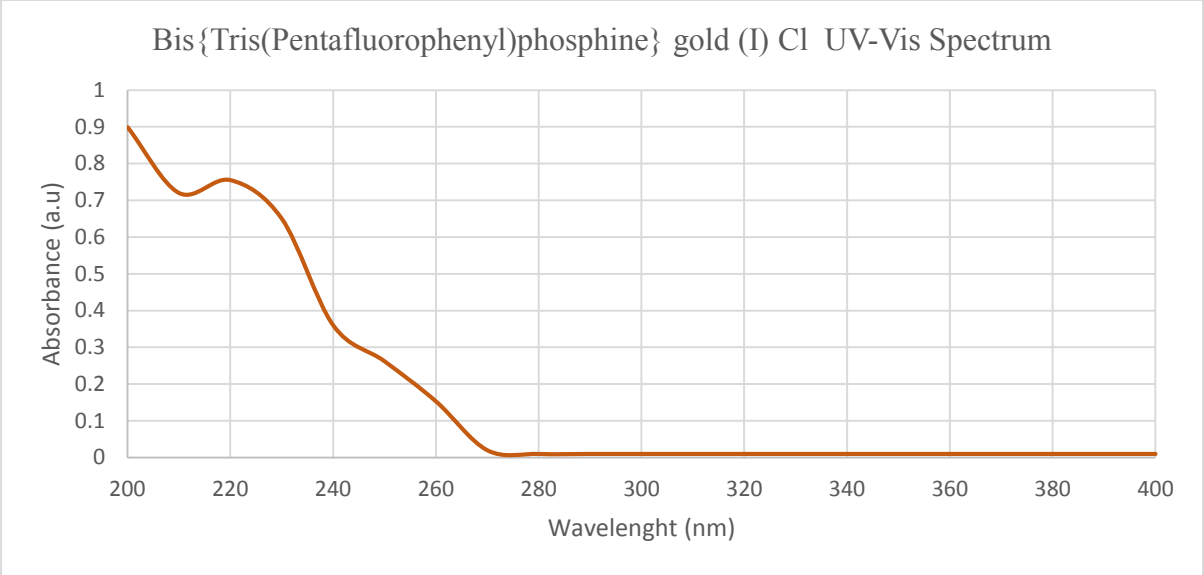

Figure 8.11. UV-Vis spectrum of $Au(P(C_6F_5)_3)_2Cl$.

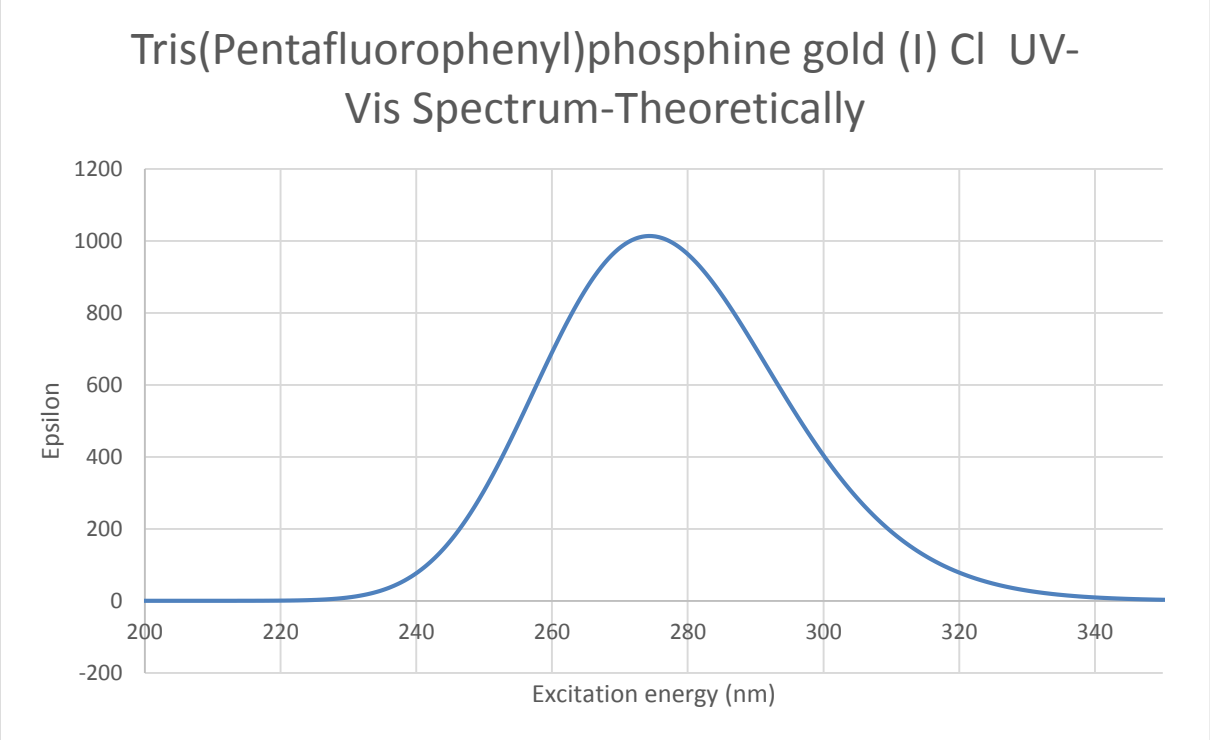

Figure 8.12. Calculated UV-Vis spectrum of $AuP(C_6F_5)_3Cl$ obtained theoretically using Gaussian 09 program.

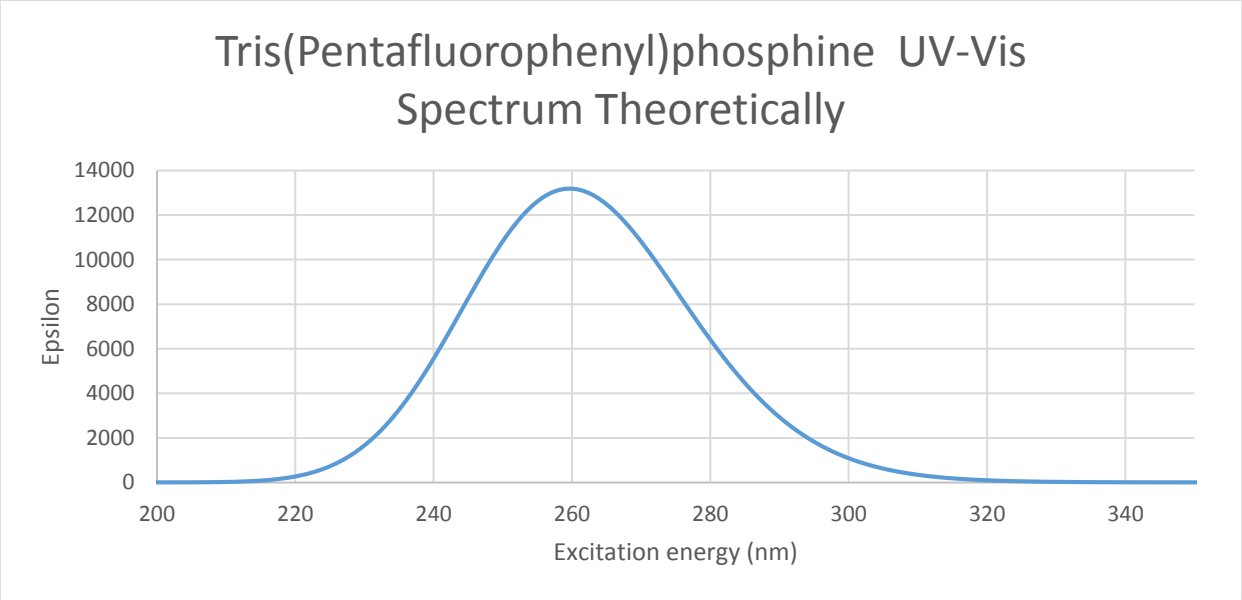

Figure 8.13. Calculated UV-Vis spectrum of $P(C_6F_5)_3$ obtained theoretically using Gaussian 09 program.

Table 8.2

TD-DFT generated ground-state to excited-state MO transitions

TRANSITIONS	CORRESPONDING ORBITALS	% CONTRIBUTION
X	135 → 138	13.41
	136 → 138	27.15
	136 → 140	9.73
	137 → 138	40.04
	137 → 140	9.67
Y	135 → 138	36.50
	136 → 140	16.03
	136 → 141	8.62
	137 → 138	27.38
	137 → 140	11.47
Z	136 → 138	52.72
	136 → 139	13.94
	137 → 140	22.03
	137 → 141	11.31

Table 8.3

Theoretical results showing the contributions of X, Y, and Z transitions of **22**

Excitation	λcalc. (nm)	%Contribution to the transition		Transition Energy (cm^{-1})	λexp. (nm)
X	277.69				225
Major contribution:					
	137 → 138	40.04		36,013	
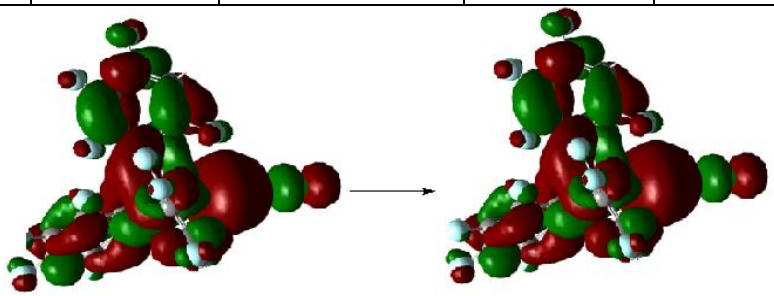					
Y	275.94				
Major contribution:					
	135 → 138	36.50		36,240	
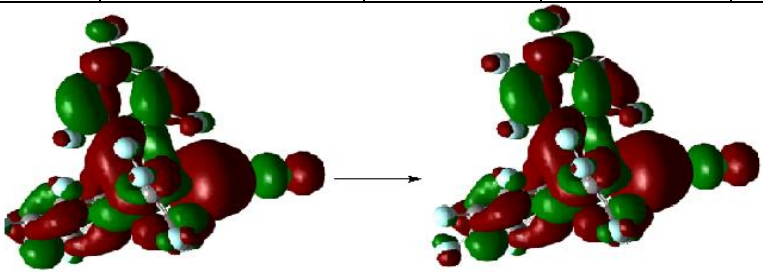					
Z	272.64				
Major contribution:					
	136 → 138	52.72		36,679	
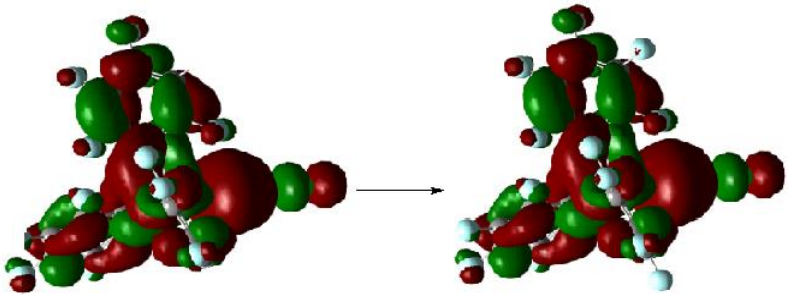					

8.2.5 Luminescence. The TPFPP ligand shows excitation spectrum at room temperature shown in Figure 8.14. The excitation spectrum for the $AuP(C_6F_5)_3Cl$ at room temperature is shown in Figure 8.15 and 8.16 covering the spectral region from 280 to 392 nm, 280 to 430 nm, and monitored at an emission band of 412, and 450 nm respectively. The spectrum exhibited vibronic bands at 359, 318 nm monitored at 412 nm; 389, 287 nm monitored at an emission of 450. The excitation spectrum collected in liquid nitrogen is shown in Figure 8.17 covering the spectral region from 280 to 500 nm, monitored at an emission band of 520. The spectrum shows vibronic components at 341 and 345 monitored at an emission of 520. The excitation spectrum for the $Au(P(C_6H_4F)_3)_2Cl$ at room temperature is shown in Figure 8.18 and 8.19. The emission spectrum for the ligand collected at room temperature is shown in Figure 8.20. The emission spectrum of **22** and **23** can be found in Figure 8.21 to 8.26 and 8.27, for both room temperature and in liquid nitrogen respectively.

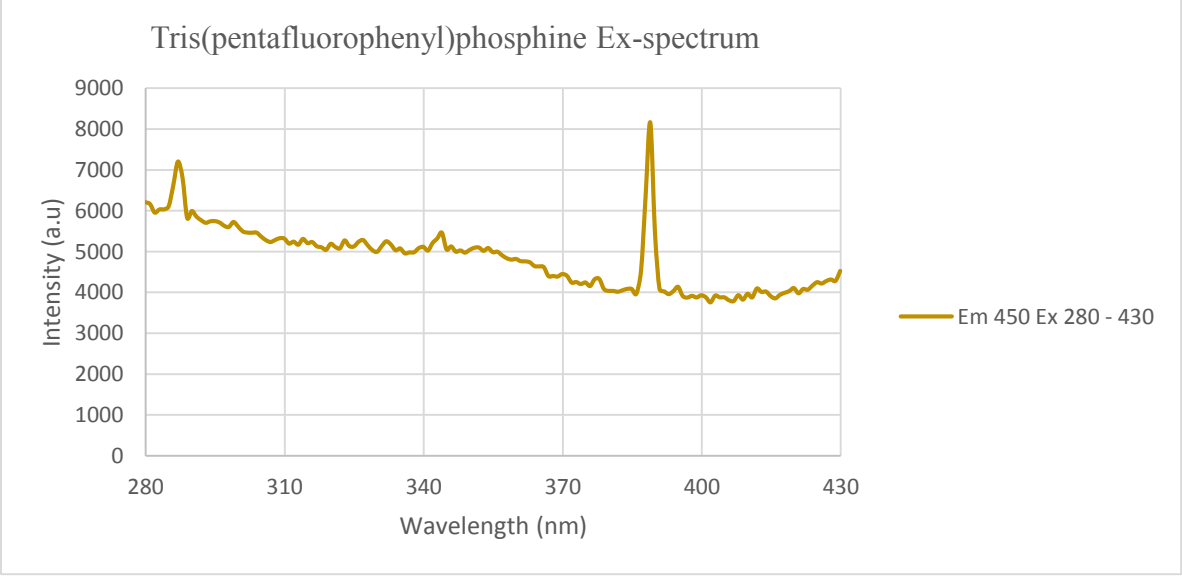

Figure 8.14. Excitation spectrum of $P(C_6F_5)_3$ collected at room temperature by monitoring the emission at 450 nm.

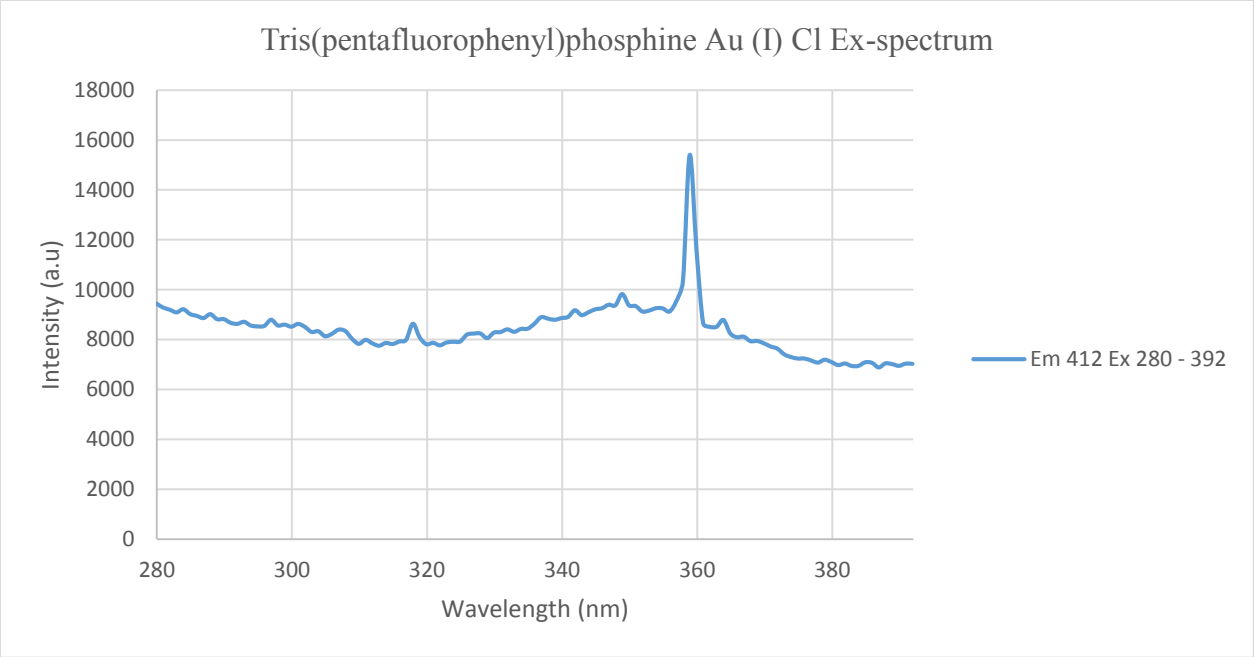

Figure 8.15. Excitation spectrum of $AuP(C_6F_5)_3Cl$ collected at room temperature by monitoring the emission at 412 nm.

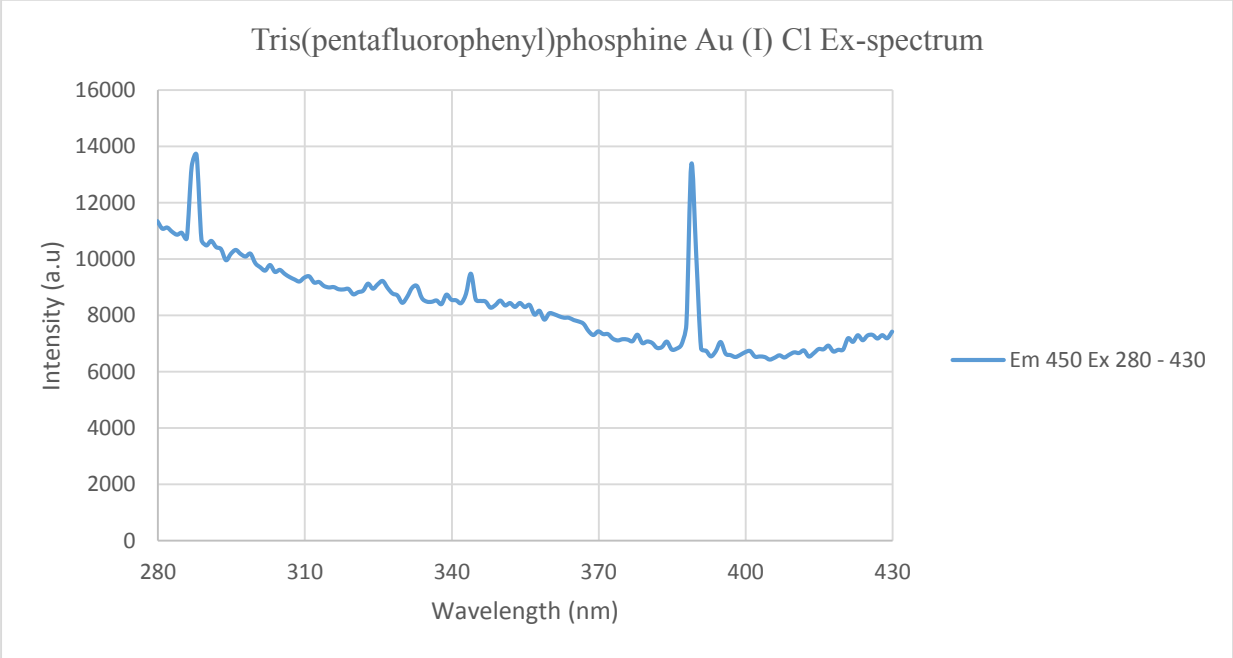

Figure 8.16. Excitation spectrum of $AuP(C_6F_5)_3Cl$ collected at room temperature by monitoring the emission at 450 nm.

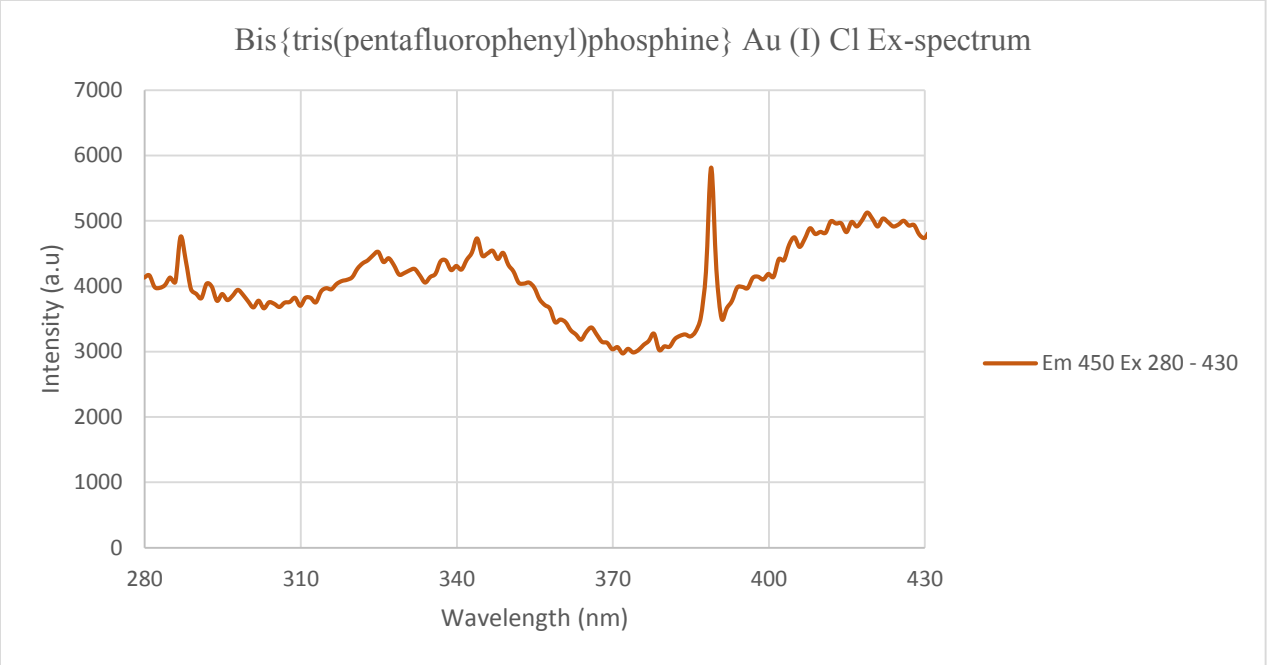

Figure 8.17. Excitation spectrum of $Au(P(C_6F_5)_3)_2Cl$ collected at room temperature by monitoring the emission at 450 nm.

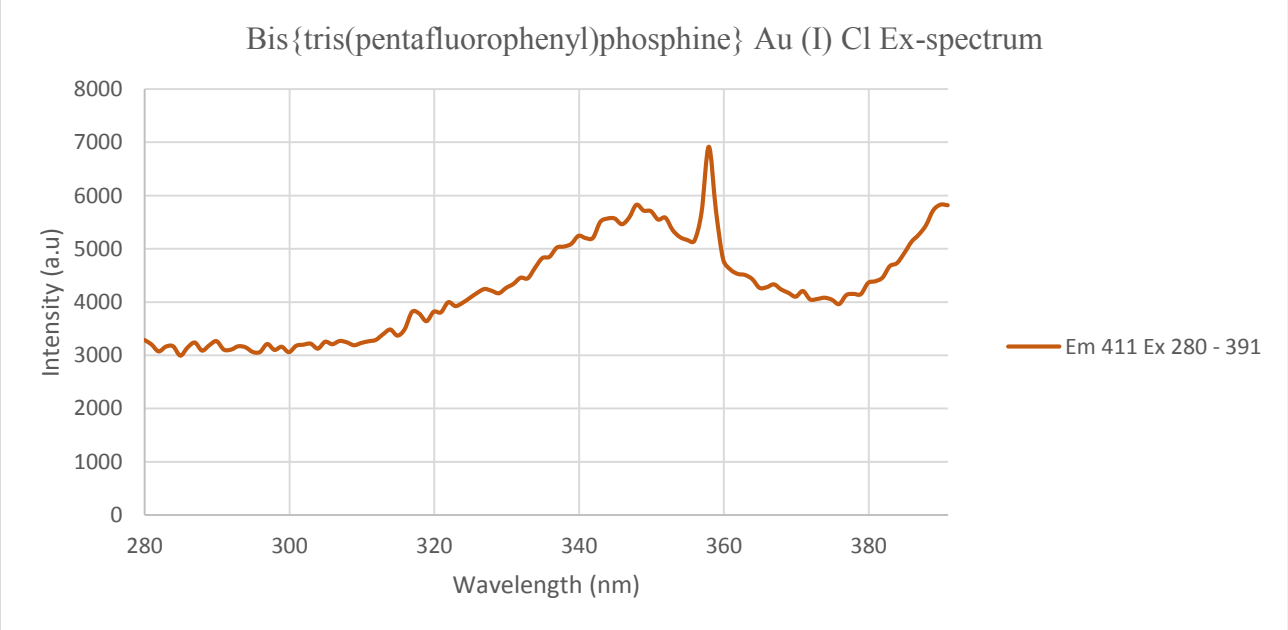

Figure 8.18. Excitation spectrum of $Au(P(C_6F_5)_3)_2Cl$ collected at room temperature by monitoring the emission at 411 nm.

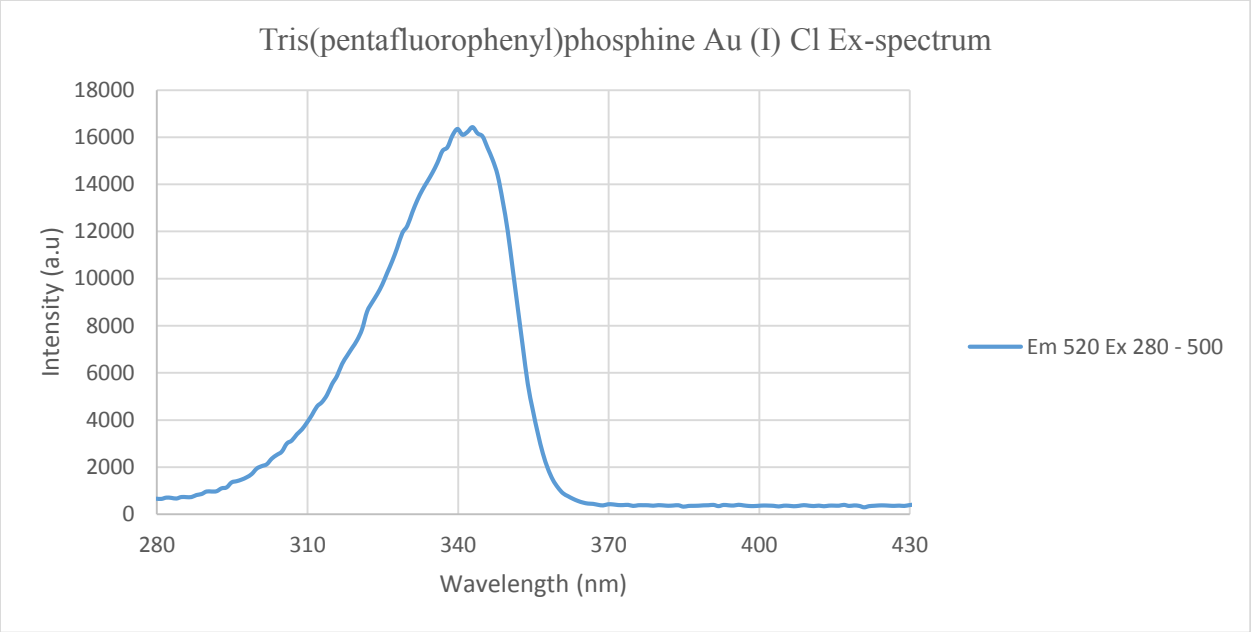

Figure 8.19. Excitation spectrum of $Au(P(C_6F_5)_3)_2Cl$ collected in liquid nitrogen by monitoring the emission at 520 nm.

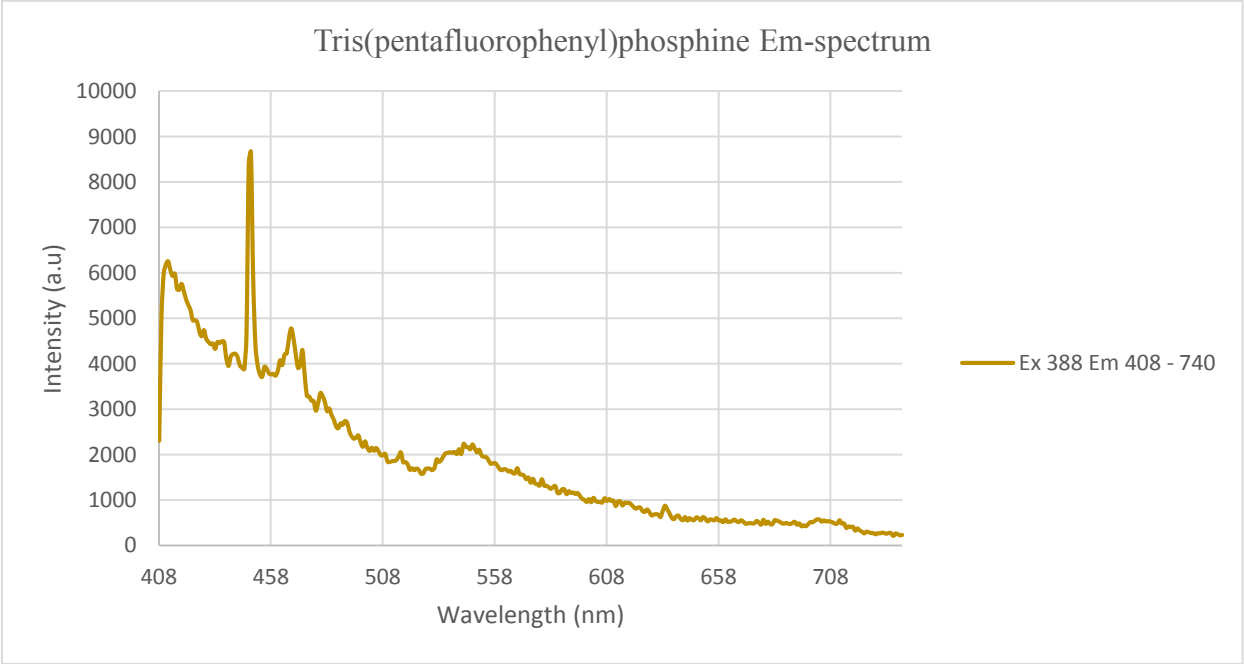

Figure 8.20. Emission spectrum of $(P(C_6F_5)_3$ collected at room temperature upon excitation at 388 nm.

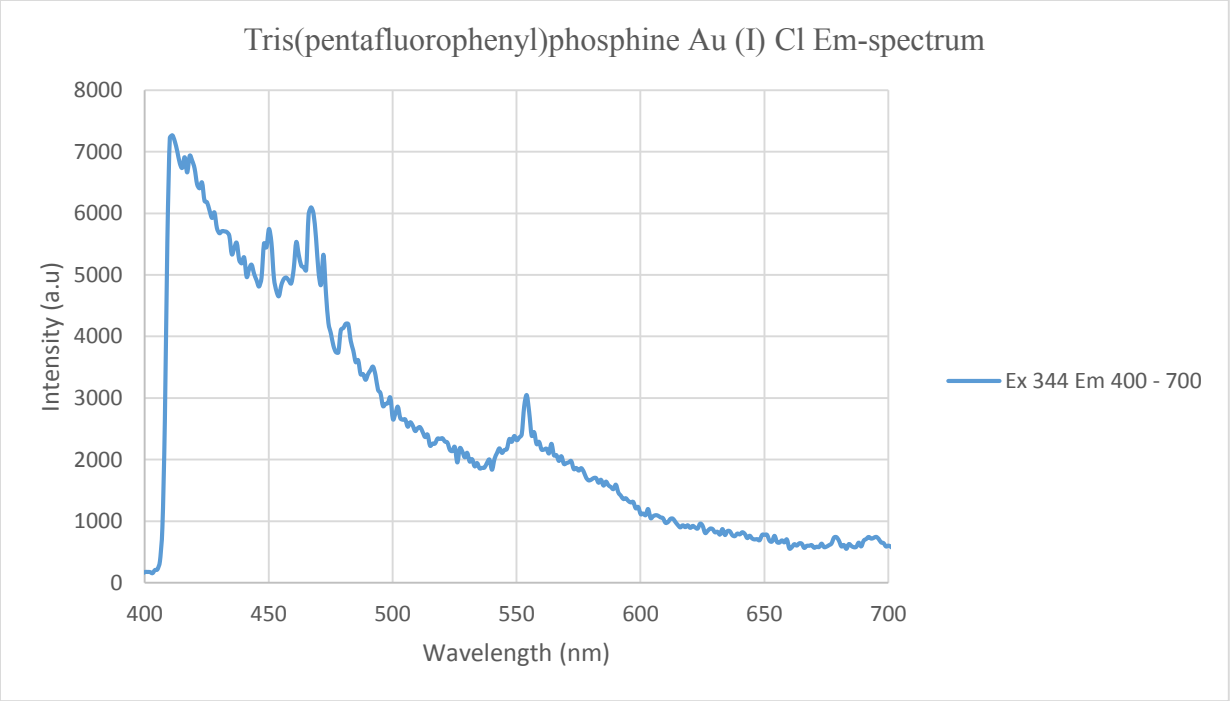

Figure 8.21. Emission spectrum of $AuP(C_6F_5)_3Cl$ collected at room temperature upon excitation at 344 nm.

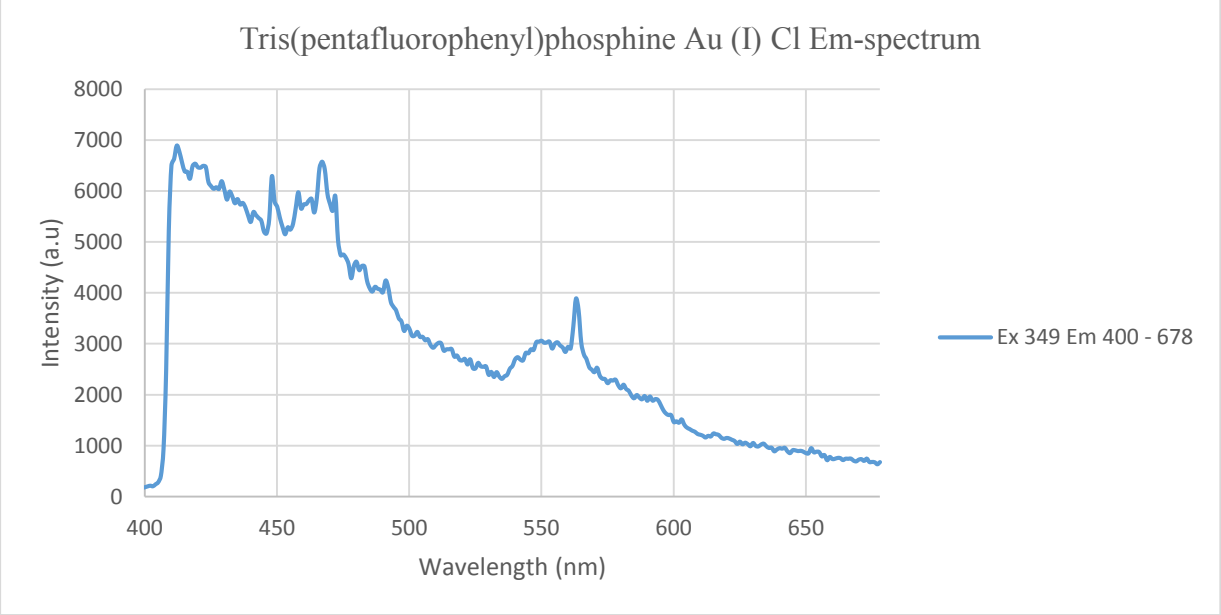

Figure 8.22. Emission spectrum of $AuP(C_6F_5)_3Cl$ collected at room temperature upon excitation at 349 nm.

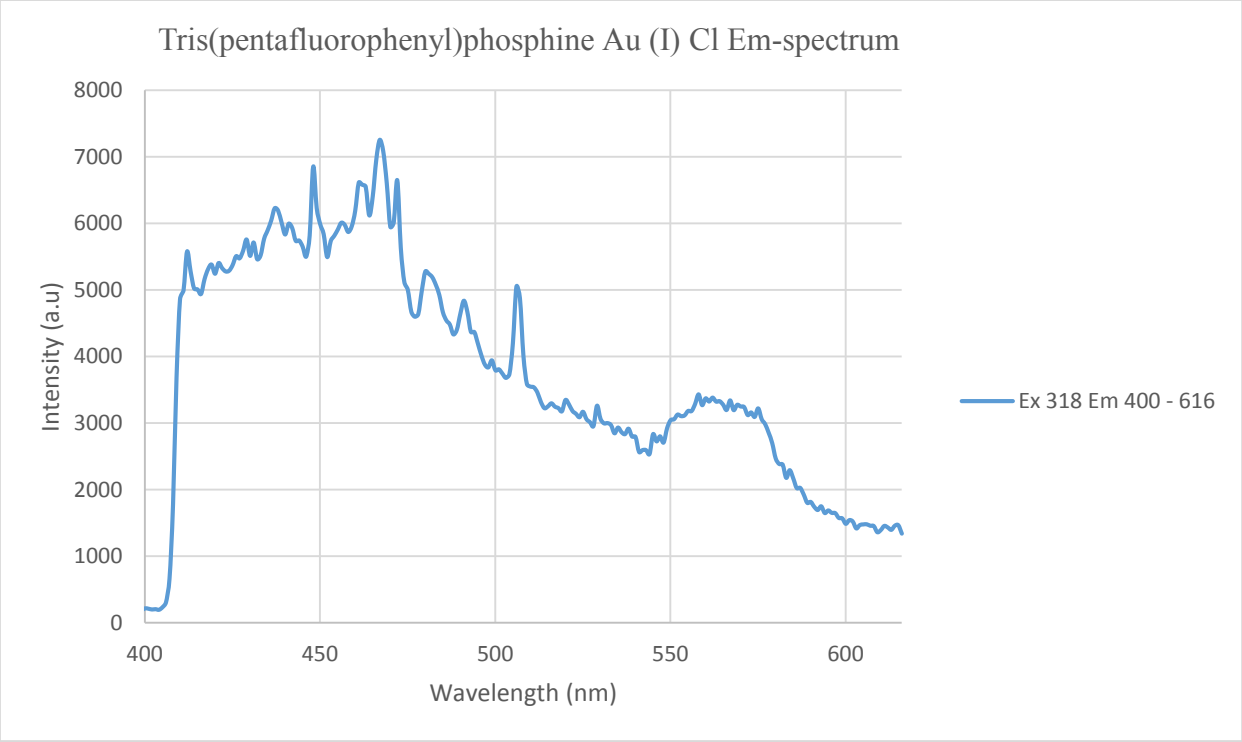

Figure 8.23. Emission spectrum of $AuP(C_6F_5)_3Cl$ collected at room temperature upon excitation at 318 nm.

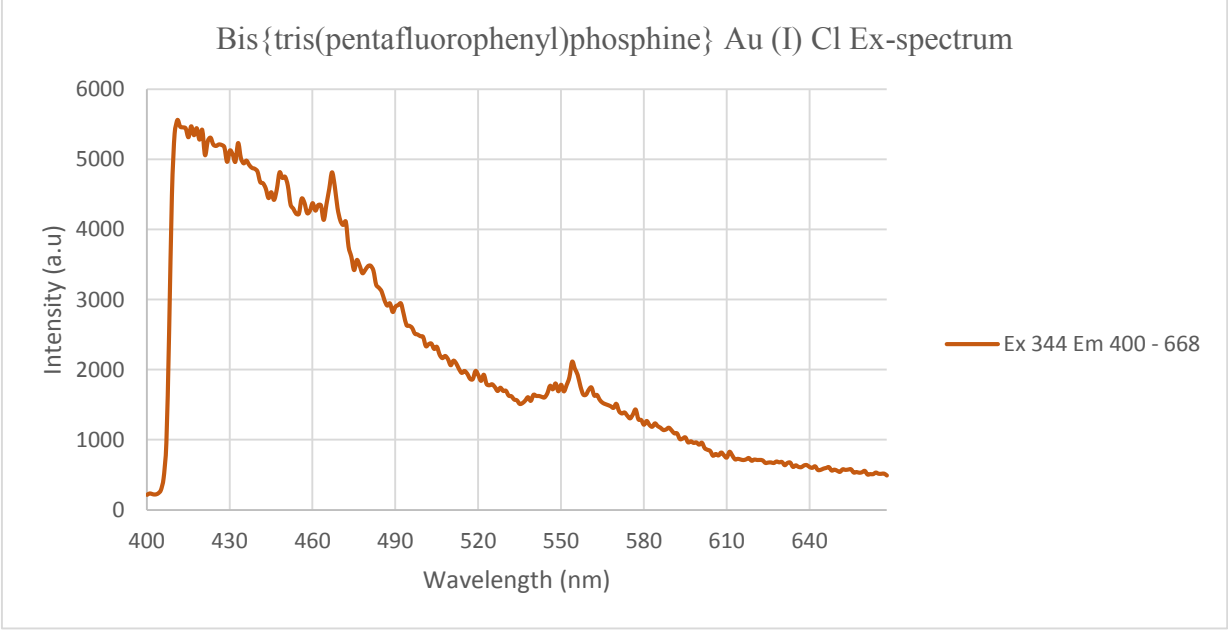

Figure 8.24. Emission spectrum of $Au(P(C_6F_5)_3)_2Cl$ collected at room temperature upon excitation at 344 nm.

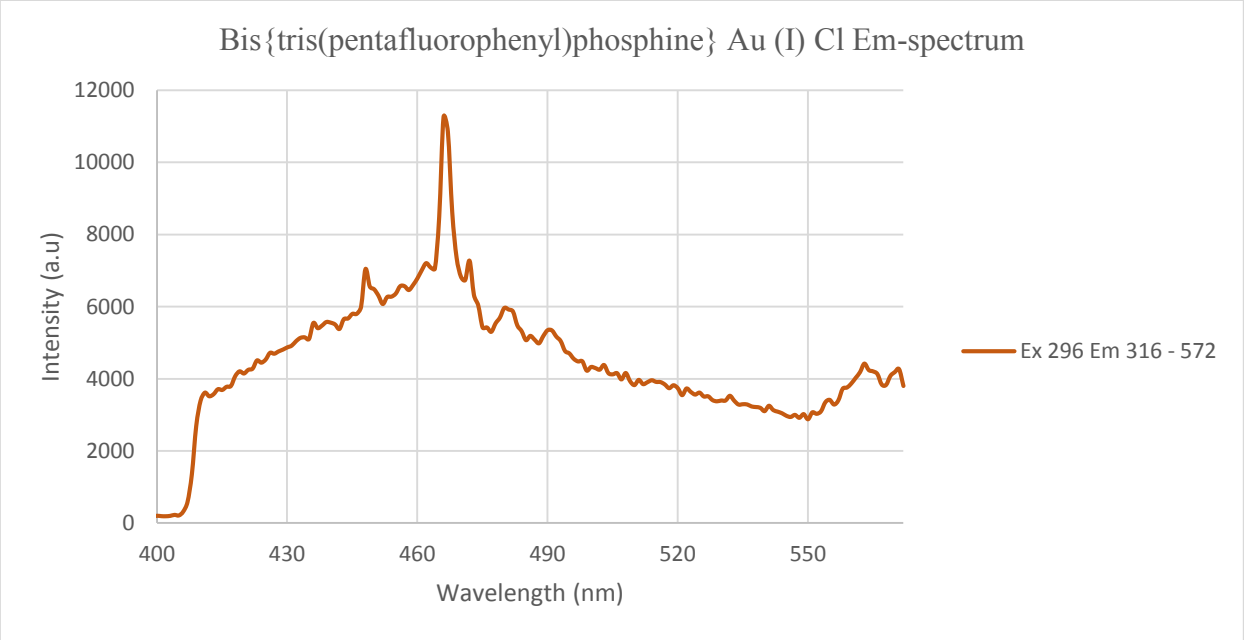

Figure 8.25. Emission spectrum of $Au(P(C_6H_4F)_3)_2Cl$ collected at room temperature upon excitation at 296 nm.

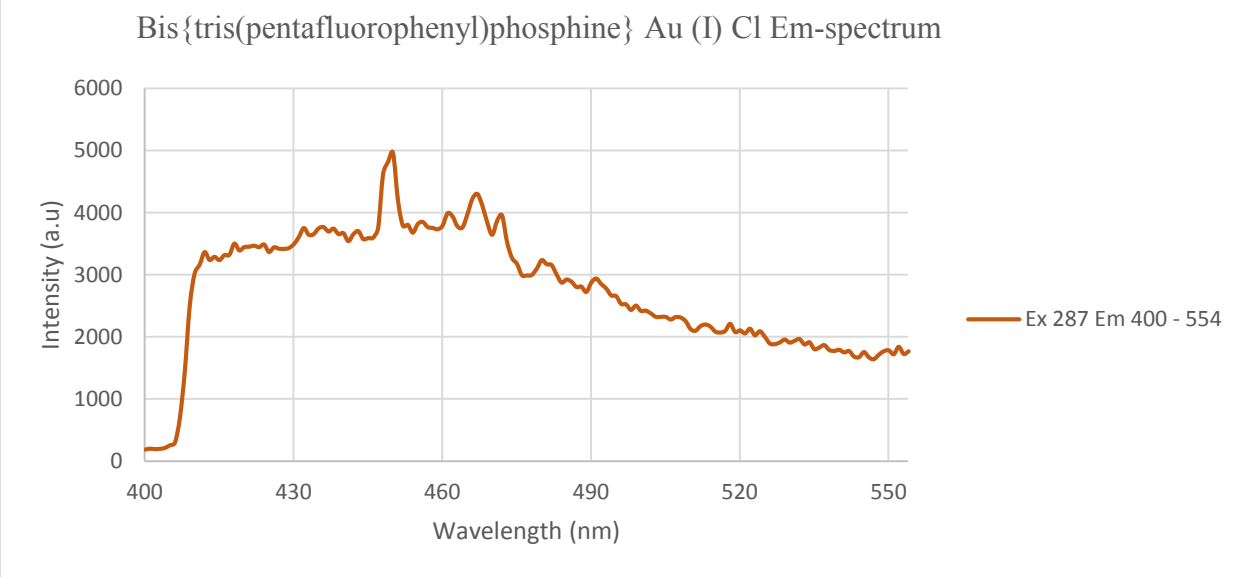

Figure 8.26. Emission spectrum of $Au(P(C_6F_5)_3)_2Cl$ collected at room temperature upon excitation at 287 nm.

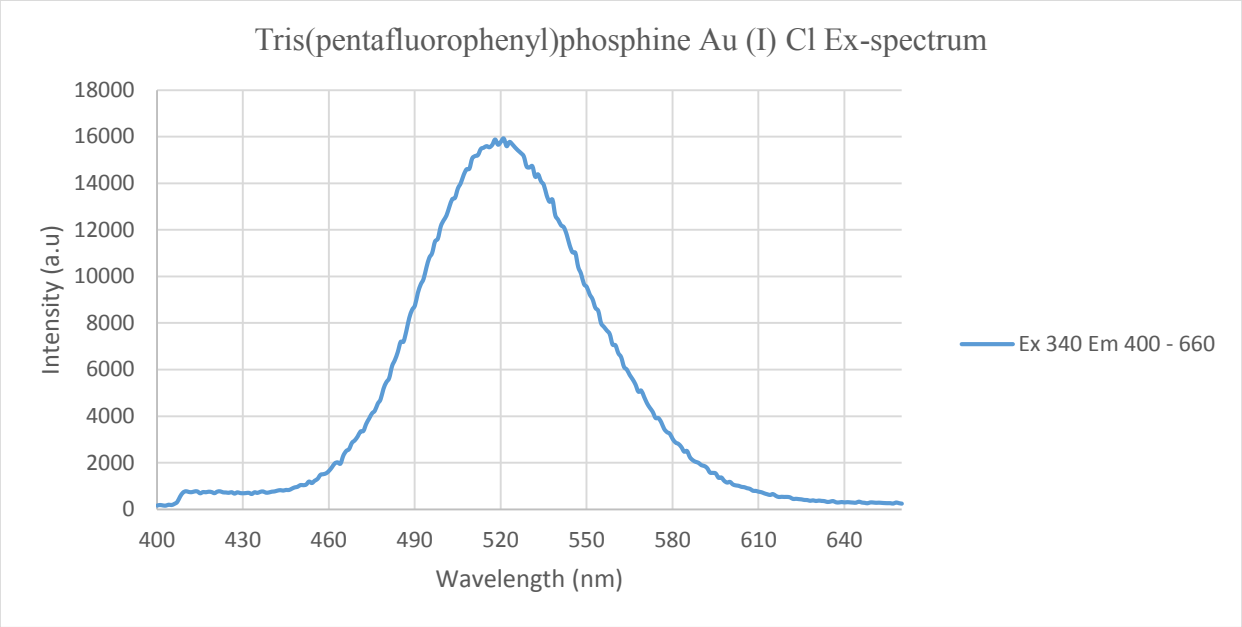

Figure 8.27. Emission spectrum of $AuP(C_6F_5)_3Cl$ collected in liquid nitrogen upon excitation at 340 nm.

Table 8.4

Atomic contributions for the ground state molecular orbitals for compound **22**

	ATOMIC CONTRIBUTIONS (%)			
Orbitals	Au	Ligand	P	C
140	9.46	90.54	10.42	79.99
139	8.81	91.19	9.05	82.14
138	7.55	92.45	9.32	83.13
HOMO-LUMO GAP				
137	21.43	78.57	6.43	72.14
136	21.16	78.84	6.28	72.56
135	72.41	27.59	6.16	21.43

Table 8.5

Atomic Orbital contribution in the ground state for compound **22**

ATOMIC ORBITAL CONTRIBUTIONS (%)				
Orbitals	Au	Ligand	P	C
140	2.41s, 1.53px 2.12py, 4.40pz	11.94s, 33.47px, 24.35py, 20.78pz	1.05s, 2.05px 7.45pz	10.89s, 31.42px 24.35py, 13.33pz
139	2.23s, 1.57px 1.52py, 3.49pz	11.44s, 31.71px 11.71py, 36.06pz	1.09s, 1.41px 6.55pz	10.35s, 30.57px 11.71py, 29.51pz
138	1.68s, 3.78py 2.09pz	9.95s, 23.93px 45.94py, 12.63pz	3.53py, 5.79pz	9.95s, 23.93px 42.41py, 6.84pz
HOMO-LUMO GAP				
137	21.43d	10.55s, 30.09px 33.57py, 4.36pz	3.24px, 3.19py	10.55s, 26.85px 30.38py, 4.36pz
136	21.16d	18.64s, 35.02px 26.44py, 4.92pz	3.14px, 3.14py	12.36s, 31.88px 23.3py, 4.92pz
135	46.78s, 14.82 10.81d	14.20s, 4.67pz 8.72py	6.16s	8.04s, 4.67px 8.72py

8.3 Discussion

8.3.1 Infrared Spectroscopy (Vibrational Studies). The IR-spectrum of **22** at Figure 8.4 has Nineteen (19) distinct bands. It shows a weak aromatic C–H stretching of the phenyl ring at 3001 cm^{-1}, the C=C phenyl ring stretching pair at 1574 cm^{-1} and 1462 cm^{-1}, the asymmetric and symmetric C–F (Ar-F) stretching at 1226 cm^{-1} and 1157cm^{-1}, the P–Ar stretching at 1103 cm^{-1}, the aromatic C–H bending at 895 cm^{-1}, the P–C stretching at 775 cm^{-1}, the Au-P stretching at 340 cm^{-1} and the Au-Cl stretching at 324 cm^{-1}. Group Theoretical Analysis (Nuclear site group analysis) for **22** also predicts Nineteen (19) IR-active modes. From table x-ray data of **22** [26], has a space group $P2_1/n$ with Z = 8. With Z = 2, it means **22** contains Eight formula units per unit

cell. The modes for this unit cell can be found by consulting table 5A [26]. Since there are 144 C-atoms, 120 F-toms, 8 Au-atoms, 8 Cl-atoms and 8 P-atoms, it is immediately seen by inspection of table 5A [26], that the Au, Cl, P, all must occupy C_s sites in two folds repetitively. The C and F must lie respectively on C_1 sites and C_i sites, in four and two folds repetitively. From table 5B [26], the vibrational modes of **22** are $3A_g + 3A_u + 3Bg + 3Bu$ for C-atoms, $3A_u + 3B_u$ for the F-atom and $2A_g + A_u + B_g + 2B_u$ for each nucleus on the C_s sites. The total contribution from C, F, P, Au and Cl is $9A_g + 9A_u + 6Bg + 12B_u$. From table 5E, the acoustic mode is $A_u + B_u$ and the optical modes are $9A_g + 8A_u + 6B_g + 11B_u$. The distribution of the optical modes shows that Nineteen (19) ($8A_u + 11B_u$) modes are expected to be IR-active from the selection rule. Comparison of these predictions with the observed calculated spectra shows that nineteen distinct frequencies are observed.

8.3.2 Nuclear Magnetic Resonance. $^{31}P\{^1H\}$ NMR spectral data for the TPFPP ligand, the **22** and the **23** shown at Figure 8.6, 8.7 and 8.8 showed a strong sharp peak at 60.0 ppm, 66.0ppm and 80.0ppm respectively. With the coordination of the mono and the bis, to the gold(I) chloride center the trend of downfield shifting is seen. This is as a result of the weakening of the gold-phosphine bond and consequently de-shielding the electrons and causing the peak to shift to a larger chemical shift value (downfield). The overall trend appears consistent for gold phosphine complexes where the mono substituted systems usually show smaller chemical shift values than the di, tri substituted complexes. For example, the mono, tris, and tetrakis substituted (TFP)nAuCl compounds have ^{31}P NMR coordination chemical shift (ccs) of 48.4, 66.1, 63.1 respectively [32]. Also, the mono, di, tris, and tetrakis substituted (TPA)nAuCl compounds have ^{31}P NMR values of -51.4, -36.1, -56.1, and -58.0 ppm respectively [27-31]. The increase in the chemical shift value on going from the TPFPP, to the **22** and to the **23** is consistent with the

general trend that chemical shift values increases as the coordination number increases. The trend of downfield shifting is also an indication that the ligand has successfully been coordinated to the gold (I) center.

8.3.3 UV-Vis Spectroscopy. The absorption spectral data for the TFFPP ligand, $AuP(C_6F_5)_3Cl$ and $Au(P(C_6F_5)_3)_2Cl$ reveal similarities in their high-energy broad UV absorption profiles. The absorbance maximum for the free TPFPP ligand shown at Figure 8.9 is observed at 225 nm with a smaller less intense band at 280 nm with low energy tail extending all the way to 400 nm. Similarly, all of the TPFPP‑gold(I) complexes also show similar higher energy band maxima near 225 nm . Based on the spectral similarities between the ligand and the complexes as well as the molar absorptivity values of 8.54×10^4 $M^{-1}cm^{-1}$, 1.23×10^5 $M^{-1}cm^{-1}$ and 1.85×10^5 $M^{-1}cm^{-1}$ for the TPFPP, $AuP(C_6F_5)_3Cl$ and $Au(P(C_6F_5)_3)_2Cl$ respectively, the 225 nm band is assignable to a $\pi \rightarrow \pi^*$ intraligand transition, which is as result of the presence of double bond in the aromatic phenyl ring. The transition is slightly affected by the coordination with the Au metal. The weaker band at 280 nm which is present in the ligand is absent in the absorption spectra of the complexes **22** and **23** at Figure 8.10 and 8.11 respectively, indicating that the transition is affected by coordination with the metal. This band is assignable to an $n \rightarrow \pi^*$ transition and its absence in the absorption spectrum of **22** and **23** is indicative of participation of the lone pair electrons in the bonding scheme of the TPFPP ligand. The higher molar extinction coefficient value of the ligand and the complexes is an indication that the electronic transitions involved as a result of the absorption are statistically probable (said to be 'allowed') due to the fact that their molar extinction **ε** values are in excess of 10 000. It is also interesting to note that the TPFPP ligand, the **22** and the **23** complexes absorbs at similar energies but with the extinction coefficients of **23** about twice more intense than that of **22** and that of the TPFPP

ligand . The enhancement (Hyperchromic shift) of the extinction coefficient in **23** relative to **22** and relative to TPFPP is understandable in view of the presence of two more identical chromophores absorbing at the same region.

8.3.4 Luminescence. The gold(I) complexes and the TPFPP ligand luminescent when excited under UV radiation. The emission spectra of the complexes both at room temperature and in liquid nitrogen have very similar profiles indicating a similar origin for the electronic transitions. The emission spectra of the TPFPP ligand at room temperature shown at Figure 8.20 is characterize by a sharp band and maximizes around 448 nm. The emission spectra of the gold complex **22** and **23** at room temperature shown at Figure 8.21 to 8.26 was observed at 468 nm and 472 nm respectively showing fine vibronic structures arising from the v(C=C) stretch of the phenyl ring of the ligand, with vibrational progressions with spacings of 1310 cm^{-1}. The shift to the longer wavelength (bathochromic shift) from 448 nm of the TPFPP to 468 nm of $AuP(C_6F_5)_3Cl$ and 472 nm of $Au(P(C_6F_5)_3)_2Cl$ is due to the fact that at the excited states, the $\pi \rightarrow \pi^*$ transitions of the TPFPP is more polar than their ground states and as a result, a greater charge separation is observed in the excited state. The coordination of the TPFPP ligand to the gold (I) center causes a dipole–dipole interaction which reduces the energy of the excited state more than the ground state, hence making the **22** and **23** to emit at a longer wavelength. This emission at a longer wavelength by **22** and **23** compare to the ligand is also an indication that the ligand has successfully been coordinated to the gold (I) center. Similar emission bands for **22** in liquid nitrogen were observed at 520 nm (Figure 8.27) showing weak vibronic structures arising from the v(C=C) stretch of the phenyl ring of the ligand.

The excitation spectrum of the TPFPP ligand, **22** and **23** at room temperature and in liquid nitrogen shown at Figure 8.14 to 8.19 for TPFPP, **22** and **23** consists of a well-defined

broad band with an average spacing of 1300 cm^{-1}. This spacing is assignable to an electronic transition coupled with vibronic component corresponding to ν(C=C) symmetric stretching mode within the phenyl ring. With reference to the previous luminescence studies on tertiary phosphine gold(I) complexes the emission bands at 468 and 472 nm in complexes **22** and **23** respectively is tentatively assigned as derived from excited states of P−> Au ligand-to-metal charge transfer (LMCT) origin. This suggests that the ligand centered transition is responsible for the photoluminescence in **22** and in **23**.

8.3.5 Computational Studies

8.3.5.1 Spectroscopic Comparison. The theoretical calculated IR spectrum of **22** using Gaussian 09 shown at Figure 8.3 also predicts nineteen (19) distinct bands with a slight shift in the position of some of the individual peaks, but on a whole both the calculated and the experimental spectrum of both the ligand and the complex shows similar IR-spectrum.

8.3.5.2 Electronic Comparison

8.3.5.2.1 Luminescence. The result of the population analysis for **22** is shown in Table 8.4 and 8.5 for the percentage atomic and atomic orbital contributions respectively for the metal and the TPFPP ligand, as well as individual atomic participation for the selected highest three occupied molecular orbitals and lowest three unoccupied molecular orbitals. The second highest occupied molecular orbital (SHOMO), HOMO-136 has the largest contribution from the ligand at 78.84% and the metal at 21.16% followed by the highest occupied molecular orbital, HOMO-137 at 78.57% and 21.43% contributions, respectively. The contribution of the gold atom in the HOMO-136 orbital derives from 5s and 5p atomic orbitals at 18.64% and 66.38% contributions respectively. The atomic contribution of the TPFPP ligand is comprised of Phosphorus and Carbon with percentage contributions of 18.64s, 35.02px, 26.44py and 4.92pz orbitals. However,

the gold contribution of the HOMO comes also from 21.43% of the 5dxz atomic orbitals with the remaining contribution from the s and p orbitals of the phosphorus, and Carbon atoms of the TPFPP ligand. The table also shows the first three lowest unoccupied molecular orbital (LUMOs) contributions, which are mainly ligand centered contributions. The orbital description as ligand based and partial metal based transitions is thus substantiated to support the observations surrounding the luminescent behavior of **22** and hence the assignment of π→π* transition is in a proper order.

8.3.5.2.2 UV-Vis. The HOMO‑LUMO gap calculated value by the TD-DFT method was 36,013cm^{-1} corresponding to 277.74 nm. The theoretical calculated spectrum for **22** obtained using TD-DFT with the LANL2DZ basis set to identify the orbital(s) contributing to the observed absorption is shown at Figure 8.12. The TD-DFT generated ground-state to excited-transitions is shown on Table 8.2 which summarizes the orbital that took part most in the transitions X, Y, and Z. From Table 8.2, transition **Z** supports an assignment of the SHOMO-136→LUMO-138, a π→π* type transition. This confirms why the n→π* is not present in the experimental UV-Vis spectrum of **22**. The transition X and Y has transitions from the HOMO-137→LUMO-138 and SHOMO-135→LUMO-138 respectively. Table 8.3 summarizes the various transitions pictorially of the theoretically generated ground-state to excited-state transitions for X, Y and Z. These calculated spectrum values are in good agreement with the experimental UV-Vis spectrum of **22**, with a slight red shifting of about 50 nm which are within the absorption range of aromatic derivatives.

CHAPTER NINE

Comparison between the various ligands and their complexes

A series of tertiary phosphine based gold complexes were studied as described in the preceding chapters. The substituents on the phenyl ring of the phosphine ligands vary from electron withdrawing group such as -C_6F_5, 4-CF_3-C_6H_4 to donating groups such as 4-OMe-C_6H_4, 2,6-di-OMe- C_6H_3, 3,5-di-Me-C_6H_3.

9.1 Phosphorus NMR

An analysis of ^{31}P NMR spectra allow an assessment of the strength of the Au-P bond interaction. In this study, it has been noted that the difference in shift between the free phosphine and the Au(I) complex varies as a function of the cone angle of the phosphine. In addition, a larger shift indicates a stronger phosphine-metal interaction. The ^{31}P NMR spectra for the various ligands and their complexes also show that electronic behavior contributed tremendously in determining the how far the electrons in the P→Au bond will be de-shielded. This is seen in the more electronegative TFFPP complexes which happen to appeared downfield for the free ligand, the mono, and the bis respectively complexes as compare with the TDMPP and TDMOPP and the TFMOPP complexes with electron donating substituents. The electronegative fluorine atom on the phenyl ring of the TPFPP and TFFPP complexes withdraw more electrons density, and hence de-shielding more to cause the peaks to appear downfield.

9.2 UV-Vis Spectroscopy

The absorption spectral data for the various ligands and their complexes reveal that electronic feature plays a significant role in the absorption maximum of the individual complexes. The position of the absorption maxima of the various complexes were determined by the groups attached to the phenyl rings. Those with electron withdrawing groups such as -C_6F_5

and 4-CF_3-C_6H_4 absorb at a shorter wavelength (higher energy) when compared with the ligands with the electron donating substituents, such as 4-OMe-C_6H_4, 2,6-di-OMe- C_6H_3, 3,5- di-Me-C_6H_3. The -C_6F_5 adduct with five fluorine groups has an absorption maximum around 220 nm. Similarly the 4-CF_3-C_6H_4 adduct with one fluorine group has an absorption maximum at 260 nm. In contrast the complexes with electron donating groups have red shifted absorption maxima greater than 260 nm. This suggest that the electron withdrawing groups on the conjugated phenyl ring increase the energy difference between the ground and excited states resulting in their absorption at a shorter wavelength. More so, since at the excited state the $\pi \rightarrow \pi^*$ transition is more polar than the ground states, the electron donating groups donate electrons which interacts with the excited state electrons (dipole-dipole interaction) which reduces their energy thereby causing them to absorb at a longer wavelength.

CHAPTER TEN

Conclusion

We have successfully presented a systematic synthetic, X-ray studies and theoretical study of a family of intensely luminescent tertiary phosphine gold (I) complexes. All of the compounds under study luminesce at room temperature and in liquid nitrogen. The emission maxima wavelength reveal a bathochromic shift as more and more ligands are coordinated to the gold(I) center. The UV-visible absorption spectra of the complexes were dominated by intense absorption bands at 220-270 nm in acetonitrile. The high-energy absorption bands were assigned to the $\pi \rightarrow \pi^*$ transitions within the phenyl ring. The low-energy absorption bands were found to be red-shifted around 270-290 nm absorption band. ^{31}P NMR and UV-Vis spectroscopy showed that modifying the groups attached to the phenyl ring can significantly affect both the magnetic and electronic properties of these complexes. The percentage atomic contribution of the frontier orbitals using DFT calculations suggest the electronic transition correspond to a ligand centered transition.

References

1. Harvey, E. N., *A history of luminescence from the earliest times until 1900*. American Philosophical Society: Philadelphia, **1957**.
2. Valeur, B.; Berberan-Santos, M. r. N., A Brief History of Fluorescence and Phosphorescence before the Emergence of Quantum Theory. J. Chem. Educ. **2011**, 88, 731-738.
3. Kitai, A.H. Solid State Luminescence, London: Chapman & Hall, **1993**, pp. 189.
4. Leverenz, H.W. *An introduction to Luminescence of Solids*, New York: Wiley, **1950** pp. 61.
5. (a) Ballhausen, C. J. *Introductoion to Ligand Field Theory*, McGraw Hill, New York, 1962. (b) Jorgensen, C. K. *Absorption Spectra and Bonding in Complexes*, Pergamon, New York, 1962.
6. Higby, G. J. Gold Bull, **1982**, *15*, 130.
7. Bhattacharya, R.; Mukherjee, P.; *Adv. Drug Deliv. Rev*. **2008**, *60*, 1289.
8. Kennedy, L. C.; Bickford, L. R.; Lewinski, N. A.; Coughlin, A. J.; Hu, Y.; Day, E. S.; West, J. L.; Drezek, R. A. Small, **2011**, *7*, 169.
9. Tiekink, E. R. T. *Crit. Rev. Oncol. Hematol*, **2002**, *42*, 225.
10. Fonteh, P., Meyer, D. Metallomics, **2009**, *1*, 427.
11. Pearson, R. G. Science, **1966**, *151*, 172.
12. Melancon, M. P.; Yang, W.; Lu, Z.; Zhang, R.; Cheng, Z.; Elliot, A. M.; Stafford, J.; Olson, T.; Zhang, J. Z. *C. Li, Mol. Cancer Ther*. **2008**, *7*, 1730.
13. Schmidbaur, H. *Gold, Progress in Chemistry, Biochemistry and Technology*, Wiley: Chichester, 1999.

14. Puddephatt, R. J. *The Chemistry of Gold,* Elsevier Sci. Pub., 1978.

15. Gobin, A. M.; Lee, M. H.; Halas, N. J.; James, W. D.; Drezek, R. A.; West, J. L. *Nano Lett*. **2007**, *7*, 1929.

16. Schmidbaur, H.; Cronje, S.; Djordjevic, B.; Schuster, O. *Chem. Phys*. **2005**, *311*, 151-161.

17. Mingos, D. M. P. *Modem Coordination Chemistry*, Royal Society of Chemistry, London, **2002**, pp. 69.

18. Hess, B. A. *Relativistic Effects in Heavy-Element Chemistry and Physics*, Wiley: Chichester, 2003.

19. Hartwig, J. F.; Kawatsura, M.; Hauck, S. I.; Shaughnessy, K. H.; Alcazar-Roman, L. M. *J. Org. Chem*. **1999**, *64*, 5575-5580.

20. Hill, L. L.; Smith, J. M.; Brown, W. S.; Moore, L. R.; Guevara, P.; Pair, E. S.; Porter, J.; Chou, J.; Woltermann, C. J.; Craciun, R.; Dixon, D. A.; Shaughnessy, K. H. Tetrahedron **2008**, *64*, 6920-6934.

21. Forward, J.M.; Assefa, Z.; Fackler, J. P. *J. Am. Chem. Soc*. **1995**, *117*, 9103.

22. Littke, A. F.; Schwarz, L.; Fu, G. C. *J. Am. Chem. Soc*. **2002**, *124*, 6343-6348.

23. Hundertmark, T.; Littke, A. F.; Buchwald, S. L.; Fu, G. C. *Org. Lett***. 2000**, *2*, 1729-1731.

24. Tolman, C. A.; Ittel, S. D.; English, A. D. *J. Am. Chem. Soc*. **1978**,*100*, 4080.

25. Jugé, S.; Merdes, R.; Stephan, M.; Genet, J. P. Phosphorous, Sulphur and Silicon **1993**, 77,199.

26. Rousseau, D. L.; Bauman, R. P.; Porto, S. P. S. *Journal of Raman Spectroscopy*, **1981** *10*, 253-290.

27. Assefa, Z.; Omary, M.A.; McBurnett, B.G.; Mohamed, A.A.; Patterson, H.H.; Staples, R.J.; Fackler Jr, J.P. *Inorg. Chem*. **2002**, *41*, 6274.

28. Forward, J.; Assefa, Z.; Staples, R. J.; Fackler Jr, J.P. *Inorg. Chem*. **1996**, *35*, 16.

29. Assefa, Z.; Staples, R.; Fackler Jr, J.P. *Acta Crystallogr*. **1996**, *C52*, 305.

30. Assefa, Z.; McBurnnet, B.G.; Staples, R. J.; Fackler Jr, J.P. *Inorg. Chem*. **1995**, *34*, 4965.

31. Assefa, Z.; McBurnnet, B.G.; Staples, R. J.; Fackler Jr, J.P.; Assman, B.; Angermaier, K.; Schmidbaur, H. *Inorg. Chem*. **1995**, *34*, 75.

32. Jenkins, D. E.; Sykora, R. E., Assefa, Z. Synthesis, X-ray crystallography, and photoluminescence studies of four coordinate gold(I) complexes with the weak Lewis base tri-2-furyl phosphine ligand. *Inorganica Chimica Acta*, **2013**, *406*, 293- 300.

33. Soo, Y. H.; Tiekink, E. R. T. *Acta Cryst*. **2001**, *57*, 549-550

34. Wei Chen, H.; Tiekink, E. R. T. *Acta Cryst*. **2003**, *59*, 50-52